A Coating Thermal Noise Interferometer for the AEI 10 m Prototype facility

Der QUEST-Leibniz-Forschungsschule
der Gottfried Wilhelm Leibniz Universität Hannover
zur Erlangung des Grades

Doktor der Naturwissenschaften
Dr. rer. nat.

genehmigte Dissertation
von

Dipl.-Phys. Tobias Westphal

2016

Referent:	Prof. Dr. Karsten Danzmann *AEI, Universität Hannover*
Korreferent:	Prof. Dr. Kenneth A. Strain *IGR, University of Glasgow*
Korreferent:	Apl. Prof. Dr. Benno Willke *AEI, Universität Hannover*
Tag der Disputation	15.09.2016

Diese Arbeit wurde angefertigt am

Max-Planck-Institut für Gravitationsphysik (Albert-Einstein-Institut)
und Institut für Gravitationsphysik,
Leibniz Universität Hannover,
Callinstraße 38, 30167 Hannover, Germany

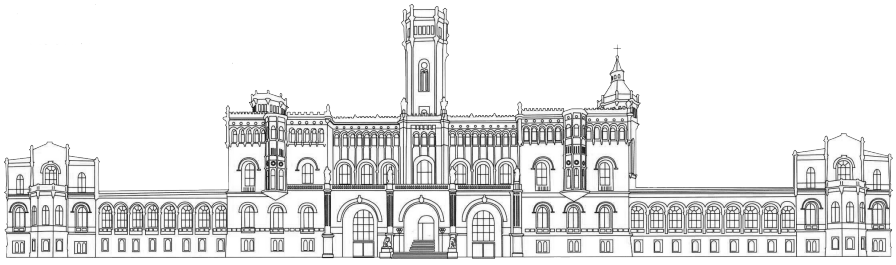

ABSTRACT

Interferometric gravitational wave detectors recently started to unveil a completely new view of our universe. The international community is currently engaged in further increasing the sensitivity of these detectors to bring the field of gravitational wave detection from a discovery mode to a mode of regular astrophysical observation. The AEI 10 m Prototype located in Hannover, Germany, is a dedicated, rapid-prototyping facility for developing and testing new technology, aimed precisely at such research. The read-out of the interferometer arm-length fluctuations is currently limited by thermal noise arising in the highly reflective, multilayer, dielectric coatings. Measuring and understanding this noise source is therefore a crucial step in developing methods to minimize it.

The thermal noise interferometer (TNI), designed and built at the 10 m Prototype, aims at a direct interferometric measurement of Brownian noise of coatings. The free space cavity design of the TNI, with two individually suspended mirrors, allows to continuously explore several cavity geometry related parameters. This includes beam size scaling effects and even mapping of coating inhomogeneities. It is designed to cover a large frequency range, from 20 Hz to beyond 10 kHz, which is the most important band for ground based interferometric gravitational wave detection. The ability to easily replace the flat test mirror allows to rapidly test new experimental coatings. These features enable the exploration of a larger parameter space in coatings than other such instruments in the past.

The design, installation and commissioning of the TNI are covered in this thesis. First a simulation was developed to examine various design considerations. This gave the performance requirements of various subsystems, which constitute the TNI. These subsystems, such as the triple stage suspensions to isolate the cavity mirrors from seismic disturbances, various sensors and actuators to keep the suspended cavity in proper alignment and its length locked to the laser, were developed and installed in the 10 m Prototype facility. Many of these subsystems are also used in a triangular reference cavity (RefC), whose long round-trip length provides a high stability to the facility's laser frequency. Similarly, there are many opportunities for synergy between various subsystems all over the 10 m Prototype.

keywords: Brownian coating noise, interferometry, mirror suspension

KURZFASSUNG

Interferometrische Gravitationswellendetektoren ermöglichen seit kurzem eine völlig neue Sicht auf unser Universum. Nun versucht die internationale Gemeinschaft auch weiterhin die Empfindlichkeit dieser Detektoren zu verbessern, um nicht nur gelegentlich Signale aufzuspüren, sondern eine vollwertige Gravitationswellenastronomie zu etablieren. Der AEI 10 m Prototyp in Hannover ist eine Entwicklungsumgebung, die speziell für die Weiterentwicklung bestehender sowie Erforschung neuer Technologien ausgelegt ist. Mittlerweile ist die Messgenauigkeit höchstpräziser interferometrischer Längenmessungen häufig durch das thermische Rauschen der hochreflektierenden, mehrschichtigen, dielektrischen Beschichtungen begrenzt. Eine experimentelle Überprüfung der bestehenden Vorhersagen ist für die weitere Verbesserung von Spiegelbeschichtungen von entscheidender Bedeutung.

Am 10 m Prototypen wurde daher das TNI Experiment zur direkten interferometrischen Messung von Brownschem Rauschen von Spiegelbeschichtungen geschaffen. Das spezielle Resonatordesign mit seinen zwei einzeln aufgehängten Spiegeln ermöglicht es, die Resonatorgeometrie kontinuierlich zu verändern und Zusammenhänge wie z. B. zwischen thermischem Rauschen und der Strahlgröße zu vermessen, aber auch die Gleichförmigkeit der Beschichtung zu kartieren. Das Experiment wurde speziell darauf ausgelegt, in dem für erdgebundene interferometrische Gravitationswellendetektion wichtigsten Frequenzbereich von 20 Hz bis jenseits von 10 kHz ausschließlich durch das thermische Rauschen begrenzt zu sein. Der flache Testspiegel erlaubt dabei ein einfaches Umrüsten auf neuartig beschichtete Spiegel im experimentellen Stadium. So ist es mit nur einem einzigen Experiment möglich, einen erheblich größeren Parameterraum abzudecken als vergleichbare bisherige Experimente.

Diese Arbeit beschreibt die Konstruktion, Installation und Inbetriebnahme des TNIs. Zuerst wurden verschiedene Designs simuliert. Dies ergab Anforderungen an die verschiedenen Bausteine, aus denen das TNI besteht. Zu den installierten Teilsystemen zählen dreistufige Spiegelaufhängungen, die den Resonator von seismischen Störungen entkoppeln, wie auch verschiedene Sensoren und Aktoren, die eine Überlappung der Resonatormode mit dem einlaufenden Strahl sicherstellen und genutzt werden, um die Resonatorlänge auf die Laserfrequenz zu stabilisieren. Viele dieser Teilsysteme werden auch in dem aus drei Spiegeln bestehendem Referenz-Resonator (RefC) verwendet. Durch seine Länge bietet er eine sehr gute Frequenzreferenz für den Laser. So ergeben sich viele Gelegenheiten für Synergien zwischen verschiedenen Teilsytemen innerhalb des 10 m Prototypen.

Schlagworte: Brownsches Beschichtungsrauschen, Interferometrie, Spiegelaufhängung

CONTENTS

Outline . . . 1
1. the aei 10 m prototype facility . . . 3
1.1. Major objective: SQL Interferometer . . . 3
1.1.1. Reaching the design sensitivity . . . 4
1.2. Vacuum system . . . 5
1.3. Seismic attenuation system (SAS) . . . 6
1.4. Suspension platform interferometer (SPI) . . . 8
1.5. Laser . . . 10
1.6. Frequency stabilization system (FSS) . . . 11
1.7. Digital control and data acquisition system (CDS) . . . 12
1.8. Thermal noise interferometer (TNI) . . . 13
2. mode cleaner cavity (pmc) . . . 15
2.1. Mathematical model for beam geometry fluctuations . 15
2.1.1. Beam geometry changes . . . 17
2.1.2. Mode filtering . . . 20
2.2. Requirements . . . 21
2.2.1. Beam jitter coupling in the SQL interferometer 22
2.3. PMC design . . . 24
2.4. Results . . . 27
3. suspension theory . . . 29
3.1. Seismic noise . . . 29
3.2. Seismic isolation . . . 32
3.2.1. Passive viscous damping . . . 34
3.2.2. Passive structural damping . . . 37
3.2.3. Active damping . . . 38
3.2.4. Coupled oscillators – sequencing isolation stages 40
3.2.5. Damped coupled oscillators . . . 40
3.2.6. Damping a suspension chain . . . 42
3.2.7. Transmissibility in the case of active damping 42
3.2.8. Sensors and actuators . . . 44
3.2.9. Translational vs. rotational damping the radius of gyration . . . 45
3.3. State space modeling . . . 47
4. 850 g triple suspension design . . . 49
4.1. Degrees of freedom . . . 52
4.2. Eigenfrequencies and eigenmodes . . . 53
4.3. Observed resonance frequencies . . . 53
4.4. Support structure: the cage . . . 54
4.5. Local damping & control . . . 55
4.5.1. Shadow sensor – BOSEM sensing units . . . 57
4.5.2. Shadow sensor – readout . . . 60
4.5.3. Shadow sensor – fundamental sensitivity . . . 60

4.5.4. Shadow sensor – readout electronics 62
4.5.5. Shadow sensor – calibration: open light test . 64
4.5.6. Shadow sensor – sensing matrix 66
4.5.7. Shadow sensor – extending the linear range . . 67
4.5.8. Shadow sensor – scattered light 70
4.5.9. Coil actuation – principles 72
4.5.10. Coil actuation – electronics 72
4.5.11. Coil actuation – current sensing resistor . . . 74
4.5.12. Coil actuation – magnet sweet spot 76
4.5.13. Coil actuation – actuation matrix 76
4.5.14. Coil actuation – required strength 77
4.5.15. Local vs. degree of freedom damping 78
4.5.16. Damping filter requirements 79
4.5.17. General damping filter shape 80
4.5.18. Noise projection of the used damping system . 82
4.6. Triple suspension cabling 83
4.7. Temperature, pressure and temporal influences 83
4.7.1. BOSEM calibration changes 84
4.7.2. Cantilever stiffness changes 85
4.7.3. Cantilever length changes 86
4.7.4. Buoyancy change 86
4.8. Horizontal vs. vertical suspension thermal noise 86
5. FREQUENCY REFERENCE CAVITY 89
5.1. Requirements 90
5.2. Optical design 92
5.3. Cavity alignment 94
5.3.1. Alignment acquisition and DC control 95
5.3.2. Spot positioning at the pW level 96
5.3.3. AC alignment control 100
5.3.4. 'Initial' RefC alignment 101
5.4. Noise correlation in a triangular cavity 102
5.5. Common mode rejection 103
5.5.1. alignment to length coupling 106
5.6. Alignment: 2" suspended steering mirrors 108
5.7. RefC design sensitivity 111
5.7.1. Laser frequency noise 113
5.7.2. Laser intensity noise – radiation pressure effect 113
5.7.3. Thermal noise prediction
the Fluctuation Dissipation Theorem 114
5.7.4. Levin pressure formalism 115
5.7.5. Suspension thermal noise 116
5.7.6. Coating thermal noise 117
5.7.7. Substrate thermal noise 120
5.7.8. Seismic noise 122
5.7.9. Control noise 123
5.7.10. Shot noise 124

6. THERMAL NOISE INTERFEROMETER 127
6.1. Features of the TNI 127
6.2. Experimental layout 128
6.3. Juggling reflectivities 133
6.3.1. Impedance matching condition 137
6.4. Optics 138
6.4.1. Commissioning optics 138
6.4.2. IBS silica-tantala test optics 139
6.4.3. Crystalline AlGaAs test optics 140
6.5. Mode matching 141
6.5.1. Changing the cavity mode 142
6.5.2. Mode matching to a changed cavity mode . . 144
6.5.3. Intensity limits: LIDT 145
6.5.4. Measuring the cavity geometry 147
6.5.5. Beyond optical instability 150
6.6. Beam steering 150
6.7. Fixing the beam at the south table 151
6.7.1. Spot position sensors 152
6.7.2. Gouy phase telescopes 152
6.7.3. The optimal spot size 153
6.7.4. Position signal normalization 155
6.8. PDH stabilization 156
6.8.1. Pound Drever Hall signal refinement 158
6.8.2. Voltage controlled phase shifter 161
6.9. Differential wavefront sensing 162
6.10. Auto alignment 163
6.11. Design sensitivity 163
6.11.1. Cavity geometry 164
6.11.2. Seismic noise model 166
6.11.3. SAS isolation model 166
6.11.4. Suspension model 167
6.11.5. Shot noise 167
6.11.6. Radiation pressure noise 168
6.11.7. Suspension thermal noise 168
6.11.8. Substrate Brownian noise 169
6.11.9. Coating Brownian noise 169
6.11.10. Coating thermo optic noise 170
6.11.11. Photo thermal noise 172
6.11.12. Stefan Boltzmann thermo elastic noise 172
6.12. Measured sensitivity 172
6.12.1. Signal readout 173
6.12.2. Actuator characterization 174
6.12.3. Sensor characterization 174
6.12.4. Open loop gain 176
6.12.5. Results 177
6.12.6. PMC as potential frequency reference 178

7. SUMMARY AND OUTLOOK 181
APPENDIX 183
A. MECHANICS 183
A.1. Periscope 183
A.2. 2” steering mirrors 183
A.3. Lens mounts (Kenny) 184
A.4. PBS waveplate assembly 184
A.5. In vacuum spot QPD 185
A.6. Breakout box 185
B. ELECTRONICS 187
B.1. Coil tester 187
B.2. BOSEM tester 187
B.3. RF distribution 188
B.4. BOSEM readout box 189
B.5. BOSEM driver box 190
B.6. Coil driver box 192
B.7. RF QPD aka Quadcam 192
B.8. QPD readout box 193
B.9. Digital IO of CDS 194
C. CABLING 195
C.1. Vacuum feedthroughs 195
C.2. RefC breakout 195
C.3. RefC octopus 196
C.4. 9 pin breakout for EM actuators, BDs, QPDs etc. . . . 196
C.5. 9 pin octopus for EM actuators, BDs, QPDs etc. . . . 197
C.6. Spot-PD 197
D. OTHER STUFF WORTH MENTIONING 201
D.1. UHV compatible beam dump 201
D.2. QPD signal conversion 202
D.3. QPD in $\times$ or $+$ orientation 203
D.4. Suspension wire strength 204
D.5. Generalized CMR of a triangular cavity 207
D.6. A compound mirror – bonding substrates 209
D.7. Slow servo beam shutter 211
D.8. Fast HDD beam shutter 212
D.9. Internal cantilever modes 214
D.10. Phase modulation 214
D.11. Number of coating layers vs. reflectivity 216
D.12. STS2 self noise 218
D.13. Coupling in vacuum noise 218
D.14. Mechanical loss of silica/tantala coatings 220
BIBLIOGRAPHY 233
CURRICULUM VITAE 237
PUBLICATION LIST 240

OUTLINE

Chapter 1 gives an introduction to the AEI 10 m Prototype facility for interferometric studies. An ultra-high-vacuum system reduces air disturbances. Low frequency, passively suspended and actively enhanced optical benches pre-isolate seismic noise. Their relative distance and alignment is measured interferometrically by a suspension platform interferometer and fed back to the tables to form a single virtual rigid system. A Michelson-type SQL interferometer aims at a position sensitivity limited by the uncertainty principle of 100 g test masses.

In **chapter 2** beam geometry fluctuations are investigated mathematically. On this theoretical foundation a very stringent requirement for input beam jitter is deduced for the proposed SQL interferometer. A triangular spatial filter cavity was designed to suppress the beam jitter. This mode cleaner was built and characterized in a master work.

Seismic noise is a limit in large scale interferometry as shown in **chapter 3**. Complex suspension systems isolate test masses (mirrors) from ground motion above their resonances. Active damping allows to reduce resonant enhancement at the eigenfrequencies while maintaining a good noise performance in the interferometric detection band.

A triple stage horizontal suspension chain design with two vertical stages was proposed by Robert Taylor. This system was built and characterized as described in **chapter 4**. Active readout of the upper mass' position and electromagnetic actuation by means of real-time digital feedback loops provides active damping of all major resonances and allows remote positioning of the mirrors in six degree of freedom . The projection of readout and actuation noise terms are realized by a state space model of the suspension.

A high finesse cavity (RefC) with a round trip length of approximately 23 m suspended in vacuum was proposed to satisfy the frequency stability requirement for the laser of the SQL interferometer. The system and its realization are described in **chapter 5**. Projections of various noise terms ensure sufficient noise clearance and deduce a standard sensitivity. The ingoing light is co-aligned with the cavity mode by means of electro-magnetically actuated single stage suspended steering mirrors. A robust remote alignment acquisition procedure was developed and demonstrated.

The TNI described in **chapter 6** is a 10 cm short companion of the RefC. The small beam diameter on the flat test mirror enhances its Brownian coating thermal noise contribution. The free space cavity design allows for easy spot size tuning to investigate scaling laws and spot positioning for mapping coating homogeneity. First results are limited by laser frequency noise and await an improved laser stability.

1

THE AEI 10 M PROTOTYPE FACILITY

The AEI 10 m prototype interferometer facility is currently being constructed at the Albert Einstein Institute in Hannover, Germany. It aims to perform experiments for future gravitational wave detectors using advanced techniques. Seismically isolated benches are interferometrically interconnected and stabilized, forming a low-noise testbed inside a 100 m^3 ultra-high vacuum system. A well-stabilized high power laser will perform differential position readout of 100 g test masses in a 10 m suspended arm-cavity enhanced Michelson interferometer at the crossover of measurement (shot) noise and back-action (quantum radiation pressure) noise, the so-called Standard Quantum Limit (SQL). Such a sensitivity enables experiments in the highly topical field of macroscopic quantum mechanics. This chapter follows [1] to introduce the subsystems employed to achieve such sensitivities.

1.1 MAJOR OBJECTIVE: SQL INTERFEROMETER

The first major goal is to design and build an apparatus able to reach the standard quantum limit (SQL) for a system with macroscopic (100 g) mirrors [1]. Such a system is limited in sensitivity by quantum noise in a wide band around the frequency at which shot noise (the measurement noise) and radiation pressure noise (the back-action noise) are equal. The margin between the sum of the classical noise contributions and the SQL is expected to be at least a factor of 3. This will enable research in quantum mechanics with macroscopic optical components and light fields.

A range of experiments is made possible by a system where classical noise is insignificant. These include the observation of ponderomotive squeezing [2] due to strong opto-mechanical coupling and the entanglement of macroscopic mirrors via light pressure [3]. While it is possible to reach the ground state with micro-mechanical oscillators [4, 5], a macroscopic experiment could reveal underlying decoherence processes such as gravity self decoherence [6]. Furthermore, non-classical interferometry, e.g. frequency dependent squeezed light injection or back-action evasion readout, can be investigated [7].

For the initial configuration, no optical recycling techniques (power-, signal recycling) are foreseen although discussed; mainly to assist the marginally stable interferometer by means of mode-healing. The read-

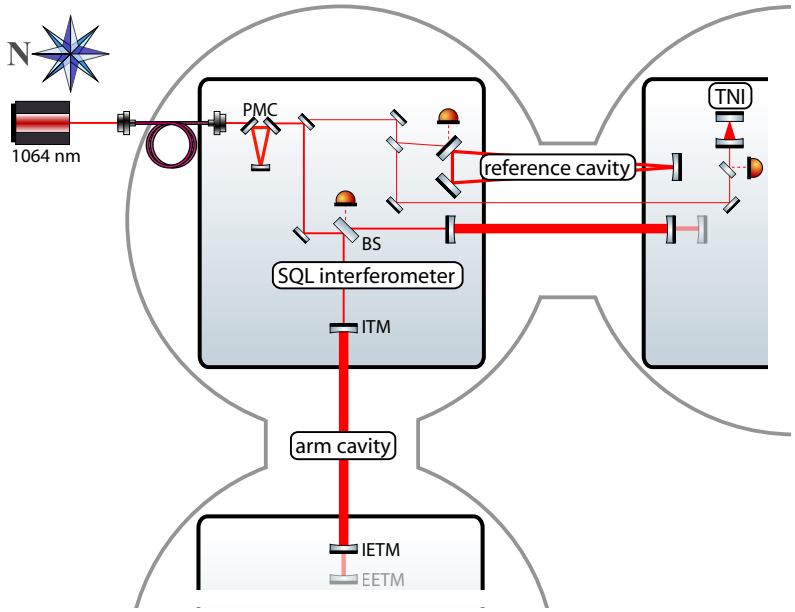

Figure 1.1.: The intended optical layout of the AEI 10 m Prototype facility SQL interferometer is shown. A 1064 nm laser is injected into vacuum via a photonic crystal fiber (PCF). A pre-mode cleaner (PMC) serves spatial filtering. Approximately 250 mW is split off to be stabilized to the length of a 10 m triangular frequency reference cavity (RefC) with a finesse of 3500. Approximately 8 W enter the arm cavity enhanced (finesse 670) Michelson interferometer. The differential arm length is sensed quantum noise limited at the antisymmetric, dark tuned port.

out technique (DC or homodyne) has not yet been decided. However, the local oscillator used to enhance the signal sidebands can be split off in front of the interferometer and locked to an arbitrary readout quadrature for variational readout.

1.1.1 *Reaching the design sensitivity*

Large beam spots on the arm cavity mirrors are required to achieve low mirror thermal noise. This comes at the expense of operating the arm cavities close to instability ($g_{arm} \approx 0.99$). To prevent inoperability of the interferometer, a stepwise approach is planned [13]. Initially, the arm cavities are set up shorter reducing the cavity g-factor with the consequence of a smaller beam size. Therefore, this initial configuration will be limited by coating thermal noise between 100 Hz and 1 kHz. Once realized, the arm length can be increased gradually by moving the end mirrors towards their desired position.

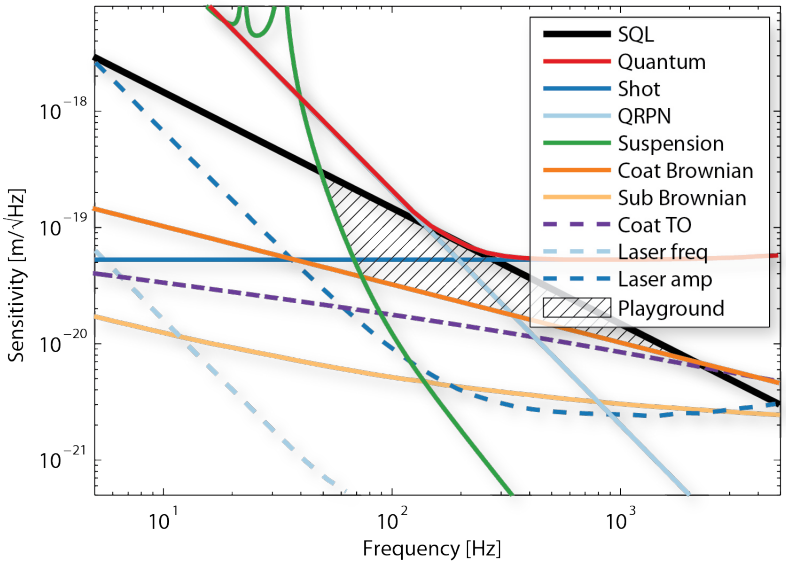

Figure 1.2.: The design displacement sensitivity of the SQL interferometer is optimized to be purely quantum noise limited over a wide frequency range, i.e. photon shot noise at high frequencies (above 200 Hz) and quantum radiation pressure noise at lower frequencies. The margin of ≈ 3 above the total classical noise, dominated by coating thermal noise at the crossover frequency and suspension thermal and seismic noise at the low frequency end, enables the investigation of Heisenberg limited behavior of macroscopic (100 g) test masses. Furthermore, techniques of quantum noise manipulation such as squeezing injection or quantum dense readout can be tested.
The initial SQL interferometer design [8, 9] incorporated Khalili cavities to separate interferometric readout from mechanical losses. Advances in coating technology by means of of crystalline AlGaAs coatings [10] and coherent cancellation of thermo-optic noise terms [11] allow for a classical arm cavity enhanced Michelson interferometer to reach a sufficient margin to the SQL. In contrast to the design study, the actual 100 g suspensions have several high-frequency resonances giving rise to this more realistic noise estimation [12]. Some of the internal suspension resonances might be susceptible to radiation pressure which would change the SQL shape.

1.2 VACUUM SYSTEM

To reduce the influence of air damping, refractive index fluctuations and acoustic coupling, a large ultra-high vacuum system is used. Three tanks of 3.4 m height and 3 m diameter are interconnected by 1.5 m diameter tubes to form an 'L-shape' (see figure 1.3). The center-center distance of the tanks (the arm length) is 11.65 m. To facilitate the hardware installation, the system can be entered through 1 m doors.

The large-aperture beam tubes allow light beams to be sent from any point on a table to any point on its neighbor.

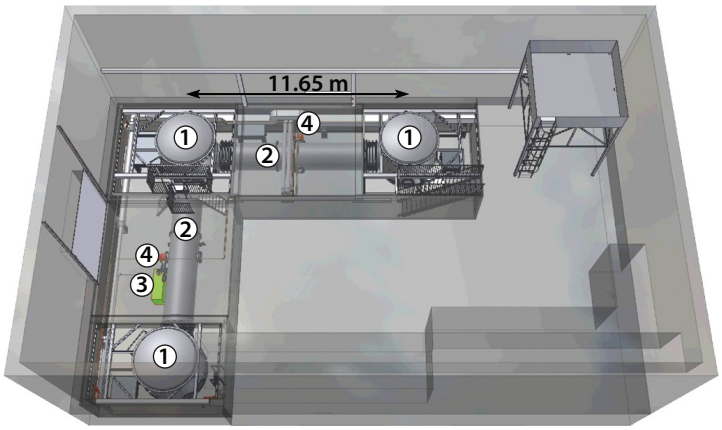

Figure 1.3.: The vacuum system was designed to fit into the basement of the AEI prototype hall. Three 'walk-in' sized tanks (1) are interconnected by 1.5m diameter tubes(2) in an 'L-shaped' configuration of 11.65m arm length. Fast pump down is provided by a screw pump (3). A pressure of $5 \cdot 10^{-8}$hPa is reached with two turbo-molecular pumps (4) attached to the middle of the arm tubes.

A screw pump (175 l/s) evacuates the 100 m^3 system from atmospheric pressure down to 5 Pa within two hours. Then, two turbo-molecular pumps (2400 l/s each) attached to the center of each arm pump down to 10^{-6} hPa, which is sufficient for most experiments, within 10 hours. A pressure of 10^{-7} hPa is reached within one week. The turbo pumps are backed by one scroll pump. Flanges up to 600 mm are sealed by copper gaskets, while bigger ones are sealed by double Viton® O-rings with the gap in between. This gap is separately evacuated by another shared scroll pump to reduce the leak rate by differential pumping. Since these pumps are running during interferometer operation, they are located in a separate room and are seismically decoupled by triple stacks of Sorbothane® hemispheres and granite plates of several hundred kg. A pressure of 10^{-8} hPa was reached before populating the system with experiments, limited by partial pressure of water, since the system cannot be baked out at high temperatures due to the Viton gaskets ($80°C$), NdFeB magnets ($65°C$) and the shear complexity.

1.3 SEISMIC ATTENUATION SYSTEM (SAS)

On a microscopic level the ground is continuously moving driven by natural and anthropogenic sources, requiring the isolation from seismic motion for many experiments. A passively isolated optical bench (1.75m·1.75m) will be installed in each of the three tanks (the central and south tables are in place, the west table is used for testing poten-

tial improvements and is close to installation) [14, 15]. Local sensors are employed to damp eigenmodes and to provide active isolation. The signals of a Suspension Platform Interferometer and optical levers are used to merge the SAS into a single, virtual platform with reduced differential motion down to very low frequencies. The mass of each optical table is 950 kg, including 230 kg ballast, the most part of which can be converted into payload. Inside the vacuum tanks, each table is supported by a vibration isolation system (see figure 1.4) providing passive seismic attenuation in all six degrees of freedom above the corresponding natural frequencies.

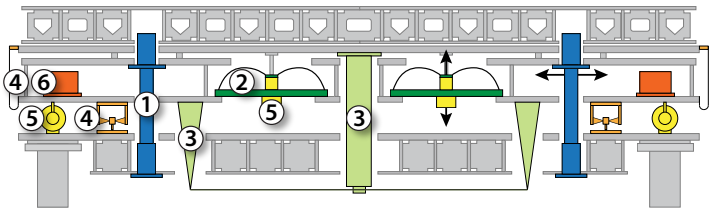

Figure 1.4.: Passively isolating optical benches were developed based on the HAM-SAS design [16]. Inverted pendulum legs (1) provide horizontal isolation from seismic noise starting at low frequencies (0.1Hz). Vertical decoupling is achieved by geometric anti-springs (2) tuned to a resonance frequency of 0.25Hz by means of positive feedback. The so-called tilt stabilization system (3) provides additional elastic restoring torque to the pitch and roll modes which might get unstable due to the soft tuning of the GAS filters in conjunction with the high center of mass positions of the optical tables (including the payload) otherwise. Static position/tilt and thermal drifts are compensated by means of springs driven by stepper motors (4). Linear variable differential transformers (5) and specifically designed accelerometers (6) sense the table's position and acceleration to produce feedback signals for active noise suppression and damping carried out by actuators co-located with the LVDTs.

The isolation system consists of a rigid platform (spring box) mounted on three inverted pendulum (IP) legs providing seismic attenuation for horizontal translation and yaw. The stiffness of the flexures holding the IP-legs is counteracted by an anti-restoring force exerted by gravity, effectively softening the support. The resonance frequency of the inverted pendulum stage is tuned down to 0.1 Hz by loading the spring box (adding ballast).

For the isolation along vertical, pitch and roll degrees of freedom, the spring box hosts three vertical spring systems (filters). To keep the tables compact, the main parts (IP and filters) are interleaved. Since vertical isolators cannot benefit from an anti-restoring gravitational potential, the geometric anti-spring (GAS) approach was chosen; cantilever springs are connected to a common center. There they

are loaded strongly such that they bend. Compression of the blades towards this center creates a tunable anti-spring effect by means of buckling. A shallow potential can be obtained around the working point [17]. By adjusting the compression, the resonance frequency was tuned down to 0.25 Hz. Further electronic tuning by means of positive feedback or magnetic anti-springs might bring the vertical isolation performance closer to that of the horizontal stage. Pitch and roll isolation rely on the vertical and angular compliance of the GAS filters and on the position of the table's center of gravity (COG) which is located several centimeters above the GAS' virtual pivot point. To cope with low frequency tunings of the GAS springs and/or strongly elevated payload an additional tilt stabilization device was implemented. The non-zero moment of inertia of the IP legs and GAS blades would cause the transmissibility to saturate at $\approx$60 dB in both cases called 'center of percussion effect'. Suitable adjustable counterweight systems [18, 19] have been implemented to achieve additional 20 dB improvement.

Each isolator is equipped with voice-coil linear actuators for the control of the optical table in all six degrees of freedom and with local sensors. The horizontal inertial motion of the spring box is measured by three custom designed UHV compatible accelerometers while three commercial L22 vertical geophones (Geospace Technologies) are placed inside the optical tables (into suitable sealed vacuum cans) to monitor their pitch, roll and vertical movement. These are going to be assisted by more sensitive L4C geophones in the near future. Above 1 Hz, passive isolation provides sub-nanometer and sub-nanoradian residual root-mean-square motion, while at lower frequencies the system eigenmodes are actively controlled using local (linear variable differential transformers (LVTD) and accelerometers) and global (interferometric link) sensors. Below the microseismic peak [20], the residual differential motion between the tables would be too high for experiments related to space missions such as LISA or Grace follow-on. Therefore, an additional readout system was developed, as described in the next section.

1.4 SUSPENSION PLATFORM INTERFEROMETER (SPI)

The Suspension Platform Interferometer [21, 22] forms a virtual interferometric interconnection between the center table and each of the end tables (see figure 1.5). The idea is to actively control the positions (and angles) of the tables in the low frequency range, where no passive isolation of the tables takes place. Thereby, it is possible to maintain the center-center distance with a high degree of stability thus creating a unique low-frequency displacement environment. The design goal for the inter-table distance stability was set to $100\,\mathrm{pm}/\sqrt{\mathrm{Hz}}$ between 10 mHz and 100 Hz [21]. For pitch and yaw the goal was set to

$10\,\mathrm{nrad}/\sqrt{\mathrm{Hz}}$. Roll motion about the optical axis between two adjacent tables is not sensed by the SPI.

To carry out the SPI sensing, an Nd:YAG laser beam is split by a beamsplitter. The resulting beams are shifted by 80 MHz−10 kHz by means of acousto-optic modulators and superimposed in a heterodyne Mach-Zehnder setup. One of them, the reference beam, is kept on a plate ($250{\cdot}250{\cdot}30\,\mathrm{mm}^3$) located in the center of the table in the central tank. To this plate, which is made of ultra low thermal expansion glass (Clearceram®-Z HS), all optical components are attached by hydroxide catalysis bonding. The measurement beam, however, is split into four identical copies. Two of those are kept on the central plate. They are brought to interference with the reference beam in interferometers having identical path lengths. One of them, the reference interferometer, measures all differential phase delays introduced upstream, such as phase noise in the fibers feeding the laser beams into the vacuum system. The second, namely the diagnostic interferometer (not shown in figure 1.5 for simplicity), serves for debugging purposes and out-of-loop measurements. Another copy is sent to the west end table where it is bounced off a mirror (radius of curvature -11.8 m) placed in the middle of the table. The beam is redirected back to the central plate under a small angle. There it is interfered with the reference beam. An equivalent interferometer is formed by the fourth beam sensing the south table position. Such interferometers with 23 m arm length mismatch require the laser to be well frequency stabilized. For this reason the iodine reference option for the *Innolight Prometheus* laser was chosen [23]. Quadrant photodiodes are used throughout the whole SPI. Thus, angular misalignments can be detected via differential wavefront sensing [24]. An LTP style phase meter [25] based on field programmable gate arrays (FPGAs) for fast data processing is employed for the photodiode readout which performs single bin discrete Fourier transforms on the signals. A micro controller processes the signals further, sending DC-power and heterodyne amplitude and phase data via Ethernet to the control and data system (see following section). There calibration and subtraction of the reference interferometer signal are carried out digitally in CDS. Furthermore, channels are combined and digitally filtered to produce suitable actuation signals for the table position control.

The recombining beamsplitter of the first long arm (south interferometer) had to be bonded in situ. With this in place, the full length sensitivity could be demonstrated, so that the corresponding relative table positions can be controlled accurately at low frequencies. Tilt motion of the tables, however, directly translates into vertical motion off the axis. The angular sensitivity of the heterodyne interferometer, turned out to be insufficient for active control. Hence, the SPI is being assisted by optical levers. A small fraction of the SPI light is sent to the far table. Its pointing is detected by spot position sensors (QPDs)

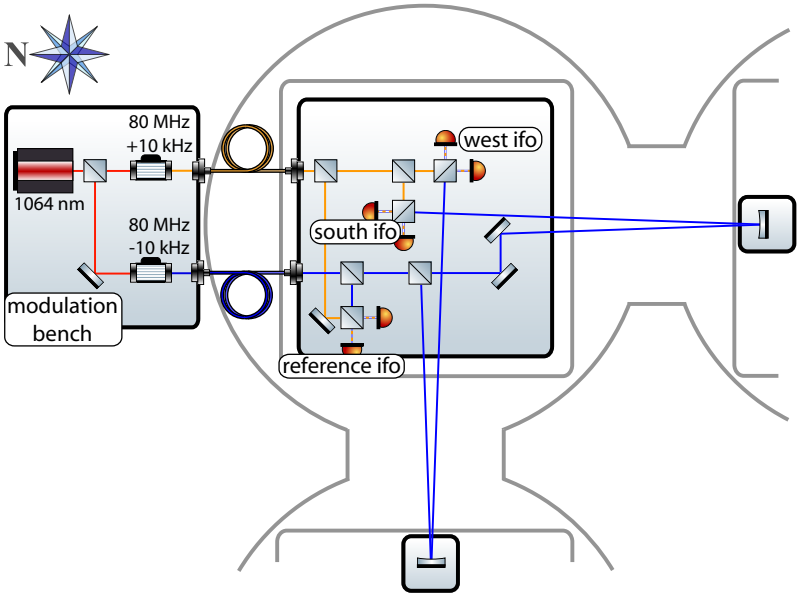

Figure 1.5.: The suspension platform interferometer (SPI) measures the relative position of the optical benches by means of heterodyne Mach Zehnder interferometers. While at high frequencies their passive isolation system delivers decoupling from ground motion, at low frequencies the SPI and local sensors signals are uses to actively stabilize the tables to give a single platform.

which vastly increases the sensitivity for yaw and pitch motion and even enables some limited readout of roll about the optical axis.

1.5 LASER

As the sensitivity of high precision interferometry is often fundamentally limited by the available laser power (i.e. shot noise) a highly stable high power laser is required. A monolithic non-planar ring oscillator (NPRO) provides a highly stable seed for a solid state single pass amplifier. This system supplies 38 W at a wavelength of 1064 nm [26]. While the seed is a well established, commercially available 2 W Innolight Mephisto with Nd:YAG crystal, the amplifier is built after an LZH/AEI design for Advanced LIGO. Four Nd:YVO_4 rods are pumped by fiber coupled diodes at 808 nm with 150 W in total. More than 95% of the 1064 nm light is emitted in the TEM_{00} mode. Mode cleaning as well as injection into vacuum are provided by a 6 m long photonic crystal fiber (type: LMA-15-PM). Its mode shape provides 99% overlap with the fundamental Gaussian mode. The transmitted power was, however, was found to be limited to $\approx$10 W before the onset of stimulated Brillouin scattering [27], while higher power levels have been achieved without being limited by Brillouin scattering [28]. This power level is sufficient for early experiments. Once more power is required,

the power handling capabilities will be investigated in more detail. A different fiber, sectional heating or to use free space coupling of the light into the vacuum system at the expense of an automatic beam alignment system can circumvent the limits. A pre-mode (PMC) cleaner is rigidly mounted to the seismically isolated optical bench inside the vacuum. It provides further spatial mode filtering and beam jitter suppression and serves as fixed spatial reference for experiments. It's design decisions are detailed in chapter 2. The power fluctuations after this point are sensed to establish a feedback loop by means of an intensity stabilization system (ISS) that stabilizes the output to a relative intensity noise of $2{\cdot}10^{-9}$ [29]. Optimization of the incoupling to the fiber is still under investigation to reduce losses in terms of scattered light. About 10 W of highly stabilized light are planned to be allocated for the sub-SQL interferometer and further experiments.

1.6 FREQUENCY STABILIZATION SYSTEM (FSS)

Despite the high inherent stability of the NPRO design, a much better (seven orders of magnitude!) frequency stability is needed. The isolated tables provide a perfect environment to set up a length reference in the frequency range of interest, which is described in more detail in chapter 5. A triangular (ring) optical cavity is formed between three suspended mirrors. The cavity round trip length is 21.2 m, the finesse of the cavity is ≈ 3500, and it is illuminated with 260 mW of input power. To reach the aspired sensitivity of $10^{-4}\,\mathrm{Hz}/\sqrt{\mathrm{Hz}}$ at 20 Hz dropping to below $10^{-6}\,\mathrm{Hz}/\sqrt{\mathrm{Hz}}$ at 1 kHz [30], all three mirrors are suspended by triple cascaded pendulums isolating from lateral seismic motion, while two blade spring stages yield passive vertical isolation above their corresponding eigenfrequencies of approximately 1 Hz as explained in chapter 3. Internal resonances of the suspension system (described in chapter 4) are locally sensed by BOSEM style [31] shadow sensors and controlled by co-located voice coil actuators at the upper stage. The lowest stage wires are heavily loaded (30% of breaking stress) to reduce bending losses for lowering the suspension thermal noise floor and to decrease vertical bounce mode frequencies. A mirror mass of 850 g was chosen to reduce radiation pressure effects as well as substrate thermal noise. A test suspension was set up to verify that the overall weight, including surrounding cage (about 13.5 kg per suspension), is within the payload budget of the tables. Furthermore, it allowed faster commissioning of the feedback and easy access without following cleanliness rules required for in-vacuum use.

A Pound-Drever-Hall (PDH) sensing scheme is used to match the laser frequency to the length of the cavity, always maintaining resonance and thereby full sensitivity. For the chosen cavity parameters, the theoretical shot noise limit of the PDH sensing is below the stability requirement. Below ≈ 1 Hz actuation is carried out by the laser

temperature, up to ≈10 kHz a piezo actuator in the laser can be used while a phase correcting electro optic modulator (EOM) covers the high frequency range up to the aspired unity gain frequency of ≈ 250 kHz. Extensive simulations were carried out to design a stable controller able to achieve the required gain of up to 10^7 within the relevant band of 20 Hz to 100 kHz (see figure 5.1). Differential wavefront sensing (DWS) and subsequent feedback control loops always overlap the ingoing beam with the cavities eigenmode by means of fast steering mirrors [32]. Static cavity misalignment is measured by spot position sensors behind the mirrors and fed to the cavity mirrors. To improve the low frequency sensitivity (i.e. below ≈ 5 Hz) where passive isolation is not effective, the cavity length is stabilized to the frequency of a molecular iodine reference used in the SPI.

Important experimental results, such as the measurement of suspension thermal noise and substrate thermal noise, might already be obtained from this setup even before the installation of the SQL interferometer.

1.7 DIGITAL CONTROL AND DATA ACQUISITION SYSTEM (CDS)

Digital control offers the flexibility that is needed for a prototype facility. To operate the 10 m prototype interferometer, many subsystems have to work together. This is orchestrated by a digital CDS that was developed at Caltech to operate the Advanced LIGO gravitational wave detectors [33]. The CDS front-end computers run more than hundred real-time control loops under a real-time enhanced Linux operating system to e.g. control mirror positions and laser beam parameters. The data of all involved signals can be stored to hard disks for later analysis of experimental results. Together with the data, a precise time stamp derived from a GPS synchronized clock is recorded. The digital control loops are designed graphically from generic digital filters and Simulink®-like blocks. A real-time code generator (RCG) compiles such a model into a Linux kernel module. The module is then assigned to a dedicated CPU core of a front-end computer running the digital loops at an update rate up to 65 kHz whereas full analog/digital loops are limited below 5 kHz for stability reasons (delay/ phase lag) [34]. The digital filter coefficients, switches and parameters of the control loops can be changed online via a graphical user interface (MEDM screens) that sends commands over an EPICS [35] based network protocol. Each CPU core can run dozens of digital filters and the signals can be distributed between CPU cores and front-end computers. The front-end computers are off-the shelf Intel XEON and AMD Opteron servers. To digitize analog signals from the sensors, 16 bit ADC PCI-X cards[1] with 32 differential channels each are housed in separate I/O-

1 General Standards Corporation 16AI64SSC

chassis. 16 bit DAC PCI-X cards[2] are located in the same chassis to drive the actuators, each with 16 differential output channels. The ADC and DAC cards are clocked externally with a GPS-locked 2^{16} Hz (65536 Hz) timing signal. For the 10 m prototype interferometer, well beyond 500 analog channels will be installed. In addition to these fast (up to 65 kHz) channels, several hundred slow (a few Hertz) EPICS channels will be used; for example, environmental sensors and computers monitoring the system-wide DC power supplies provide their data via EPICS channels. For fast communication and data sharing between real-time modules, the front-end computers are connected via a low-latency Myrinet fiber network. According to the overall status of the project, about half of the CDS is installed and working.

1.8 THERMAL NOISE INTERFEROMETER (TNI)

Brownian coating thermal noise is expected to limit the current generation of gravitational wave detectors in their most sensitive frequency range. Yet the underlying theory is not very well tested experimentally due to a lack of sufficiently sensitive measurement devices.

The TNI described in chapter 6 targets to fill this gap as a versatile system. It was designed to be limited within an extremely wide band between 20 Hz and 20 kHz by this coating thermal noise. This allows the investigation of the frequency dependence by means of direct thermal noise observation. The TNI consists of a 10 cm long linear free space cavity. The hemispheric cavity geometry results in a small spot on the flat test-mirror which dominates the noise and a larger spot on the curved in-coupler. Tuning the length closer towards optical instability allows to investigate the spot size dependence of the noise. The test-mirror can be exchanged easily to test various experimental coatings [36, 10, 37], even when they cannot be manufactured on curved surfaces yet. Furthermore, no transmission is required to lock the cavity.

The TNI is the shorter twin of the frequency reference cavity. This gives plenty margin for laser frequency noise. Both its mirrors are suspended by the same triple suspension used for the RefC. They are supported by a single, rigid cage structure giving a high mechanical common mode rejection. The length is locked by means of a Pound-Drever-Hall scheme using the RefC sidebands. All optically relevant degrees of freedom can be sensed by means of in vacuum spot sensors augmented by out of vacuum differential wavefront sensors.

2 General Standards Corporation 16AO16

2

MODE CLEANER CAVITY (PMC)

The pre-mode cleaner (PMC) was designed to provide a clean Gaussian fundamental TEM_{00}-mode inside vacuum. It suppresses static beam deformations caused by the photonic crystal fiber (PCF) guiding the laser into vacuum, attenuates residual light in the wrong polarization and reduces pointing, i.e. beam jitter. Furthermore, it serves as an ultimate position reference inside vacuum and provides a beam suitable to feed the SQL interferometer without additional focusing elements aside from a collimating mirror used under a small angle of incidence.

The first section 2.1 of this chapter introduces the mathematical framework following and extending [38, 39] to describe laser beams, their geometry fluctuations and the suppression of these fluctuations. Section 2.2 gives stability requirements arising from the SQL interferometer. Based on these, in section 2.3 a design for a PMC fulfilling the requirements of the prototype facility is deduced. The realization and characterization of this design is described in [39]. A summary of this is given in section 2.4.

2.1 MATHEMATICAL MODEL FOR BEAM GEOMETRY FLUCTUATIONS

The Maxwell equations give the most fundamental classical description for the propagation of electromagnetic fields. They lead to the Helmholtz equation, the wave equation for light. Plane waves and Bessel waves are sets of general solutions, which are more of theoretical interest as they carry an infinite amount of energy for a given intensity at the center. Finding an applicable set of solution requires an approximation: the transverse profile of a beam may not change quickly along its propagation axis. This is called paraxial approximation. It allows to factor out the simplest solution of the wave equation, a plane wave

$$\vec{E} = E_0 \cdot \vec{e}_{\mathrm{pol}} \cdot u(x, y, z) \cdot \mathrm{e}^{-i(kz-\omega t)} \tag{2.1}$$

with a frequency of ω propagating along the z-axis. Here $\vec{e}_{\mathrm{pol}}$ is one of two orthonormal polarization vectors which are orthogonal to the direction of propagation. This leads to a reduced beam shape u whose z-dependence is basically caused by diffraction effects. In the following it is used to compare a few of the huge set of possible solutions of the

paraxial wave equation. Gaussian shaped transverse beam profiles are of special interest in laser interferometry as they are eigenfunctions of Fraunhofer diffraction. Therefore, they represent the field distribution of a single mode laser very well. Two transverse modulations of the Gaussian profile are discussed in more detail in the following sections.

Hermite Gauss modes

Hermite Gauss modes are well suited for axially symmetric problems. These actually dominate the situations experienced in everyday lab work (see chapter 2.1.1). The three dimensional field distribution of any mode of order m propagating along the z-axis

$$u_m(x,z) = \left(\frac{\sqrt{2/\pi}}{2^m m! w_0}\right)^{1/2} \left(\frac{q_0}{q(z)}\right)^{1/2} \left(\frac{q_0}{q_0^*}\frac{q^*(z)}{q(z)}\right)^{m/2} \times H_m\left(\frac{\sqrt{2}x}{w(z)}\right) \exp\left(-i\frac{kx^2}{2q(z)}\right) \tag{2.2}$$

contains the complex beam parameter q. It can be rewritten in the form

$$u_m(x,z) = \sqrt{\frac{w_0}{w(z)}}\, H_m\left(\frac{\sqrt{2}x}{w(z)}\right) \times \exp\left(-\frac{x^2}{w^2(z)} - i\frac{kx^2}{2R(z)} + i\frac{2m+1}{2}\zeta(z)\right) \tag{2.3}$$

which is much more intuitive after comprehending the meaning of all its contributions. It contains the wave number $k = 2\pi/\lambda$, the size of the beam

$$w(z) = w_0 \sqrt{1 + \left(\frac{z}{z_\mathrm{R}}\right)^2}, \tag{2.4}$$

which is called the waist size $w_0 = w(0)$ at the narrowest point, a radius of curvature of the wavefronts

$$R(z) = z\left(1 + (z_\mathrm{R}/z)^2\right), \tag{2.5}$$

an order index m,n for the modulating Hermite polynomials $H_{m/n}$ and an additional phase

$$\zeta = \arctan\left(z/z_\mathrm{R}\right) \tag{2.6}$$

called Gouy phase. Here $z_\mathrm{R} = \pi w_0^2/\lambda$ is a length called Rayleigh range which marks the boundary between near field (plane waves) and far field (spherical waves). Note that the transversely oriented modes can be obtained by exchanging $x \to y$ and introducing another independent order index $m \to n$. The total beam shape can be obtained by means of $u_{mn}(x,y,z) = u_m(x,z) \cdot u_n(y,z)$ and adding all the contributing modes up $u(x,y,z) = \sum_{n,m} u_{mn}(x,y,z)$

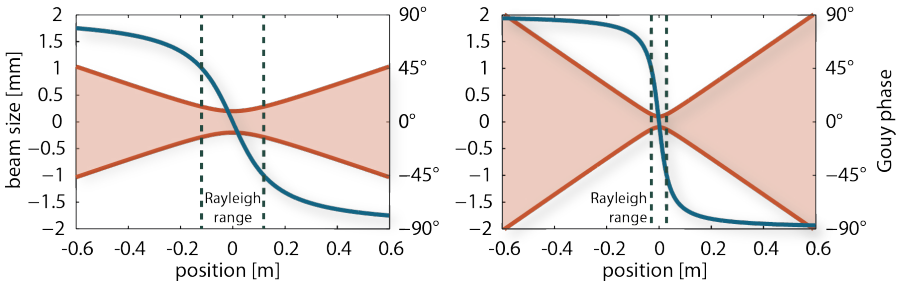

Figure 2.1.: The beam size $w(z)$ of a fundamental Gaussian mode is depicted in red, the corresponding Gouy phase $\zeta(z)$ is shown in blue for two differently diverging beams: on the left is a waist size z_0 (smallest beam size) of 200 µm, on the right it is only 100 µm big. The Rayleigh reaches from $-z_R$ to $+z_R$. The Rayleigh distance $\pm z_R$ can be estimated in terms of beam size increase by $\sqrt{2}$ or Gouy phase of 45° relative to the waist position. The wavefront curvature (not shown) is the strongest at this point.

Laguerre Gauss modes

Laguerre Gauss modes are better suited for describing radially symmetric problems. In addition to the parameters described already, their three dimensional field distribution

$$u_{l,p}(r,\phi,z) = \frac{C_{lp}^{\mathrm{LG}}}{w(z)}\left(\frac{r\sqrt{2}}{w(z)}\right)^{|l|}\exp\left(-\frac{r^2}{w^2(z)}\right)L_p^{|l|}\left(\frac{2r^2}{w^2(z)}\right)\times \exp\left(ik\frac{r^2}{2R(z)}\right)\exp(il\phi)\exp\left(i(|l|+2p+1)\zeta(z)\right) \tag{2.7}$$

contains the generalized Laguerre polynomials L_p^l with the radial ($p \geq 0$) and the azimuthal (l) order index.

Both modal systems, same as any other, form a complete set of modes, a basis for paraxial light fields. The full beauty of their choice can only be admired when looking at their influence on common beam deformations.

2.1.1 *Beam geometry changes*

The fundamental non-astigmatic Gaussian mode ($m,n=0$) with a fixed polarization has got seven degrees of freedom:

- lateral shift in two dimensions
- tilt in two dimensions
- waist size determining the angle of divergence
- macroscopic longitudinal waist position
- microscopic longitudinal phase shift

Another two degrees of freedom are introduced when allowing more general, astigmatic beams. These 'suffer' from two independent divergence angles and waist positions. They are implicitly covered by the Hermite Gauss formalism and are therefore not treated separately in this document.

To understand the influence of the six macroscopic beam geometry fluctuations listed above, the first terms of the fields' Taylor expansions are given in the next sections [39].

lateral shift

A coordinate transformation to $x' = x + \Delta x$ is equivalent to a transverse shift in x-direction. If the shift $\Delta x \ll w_0$ is small compared to the waist size, the shifted mode can be approximated by

$$E_{00}(x + \Delta x)\Big|_{x\approx 0} \approx E_{00}(x) + \frac{1}{\sqrt{2}} E_{10}(x) \frac{\Delta x}{w_0} \tag{2.8}$$

or

$$E_{00}(y + \Delta y)\Big|_{y\approx 0} \approx E_{00}(y) + \frac{1}{\sqrt{2}} E_{01}(y) \frac{\Delta y}{w_0} \tag{2.9}$$

respectively – a simple addition of HG_{10} or HG_{01}-mode.

tilt

To describe the tilt of a fundamental Gaussian mode by an angle $\alpha \ll \theta$, a slightly more complex coordinate transformation is required: $x' = x - \alpha z$, $z' = z + \alpha x$. Then the approximation for a mode tilted little in units of divergence angle reads as

$$E_{00}(x - \alpha z, z + \alpha x)\Big|_{\substack{x\approx 0 \\ z\approx 0}} \approx E_{00}(x, z) + i\sqrt{2}\, E_{10}(x, z) \frac{\alpha}{\theta} \tag{2.10}$$

and

$$E_{00}(y - \alpha z, z + \alpha y)\Big|_{\substack{y\approx 0 \\ z\approx 0}} \approx E_{00}(y, z) + i\sqrt{2}\, E_{01}(y, z) \frac{\alpha}{\theta} \tag{2.11}$$

where $\theta \simeq \frac{\lambda}{\pi w_0}$ is the divergence angle with respect to the optical axis. In comparison to a beam shift, a beam tilt is achieved by adding an imaginary HG_{10} or HG_{01}-mode, i.e. the same but shifted by 90° microscopic phase. It should be pointed out that due to the Gouy phase of 90° being accumulated between waist and far field the role of shift and tilt exchange roles.

size change

The derivation of a beam size change by $\Delta w_0 \ll w_0$, which is small compared to the actual beam size itself, leads to a field distribution described by

$$\begin{aligned} E_{00}(w_0 + \Delta w_0) \approx E_{00}(w_0) + E_{00}(w_0)\, \frac{w_0}{\Delta w_0} \\ + \frac{1}{4}\, \left[E_{20}(w_0) + E_{02}(w_0)\right]\, \frac{w_0}{\Delta w_0}\,. \end{aligned} \tag{2.12}$$

The beam profile is widened or narrowed by adding or subtracting second order HG modes. Some additional E_{00} content must be added, probably to compensate for power loss.

longitudinal shift

A macroscopic longitudinal waist shift by $\Delta z \ll z_R$, which is small compared to the Rayleigh range, changes the field distribution to

$$\begin{aligned} E_{00}(z + \Delta z)\Big|_{z \approx 0} \approx E_{00}(z) + \frac{i}{2}\, (1 + exp(2i\zeta(z)))\; E_{00}(z)\, \frac{\Delta z}{z_R} \\ + \frac{i}{8}\, \left[E_{20}(z) + E_{02}(z)\right]\, \frac{\Delta z}{z_R}\,, \end{aligned} \tag{2.13}$$

so again some fundamental mode needs to be added to account for intensity changes but the more interestingly the actual shift can be achieved by adding some HG_{20} and HG_{02} mode in quadrature (i.e. again 90° shifted). Also the Gouy phase term must be corrected by adding some fundamental mode in quadrature to refer the Gouy phase to the waist position. And again it should be noted that the second order mode accumulates 180° Gouy phase when propagating from the focus to the far field. Therefore, it's sign changes and an initially enlarged beam goes through a region where the size is the same but the radius of curvature is different, i.e. imaginary second order mode at the Rayleigh distance, to the far field, where the mode is shrunk now, i.e. second order mode with opposite sign compared to waist.

It is astounding that the first two higher orders of HG-modes suffice to characterize the most common beam geometry changes. In practice the changes described by the first order modes are referred to as alignment of the beam. The deformation caused by the second order modes is especially important in mode matching of a cavity mode to the eigenmode of another optical cavity.

PCF mode

A beam geometry change specific to the prototype facility is investigated in this section. As the laser is sent into vacuum via a photonic crystal fiber, it passes a prominent hexagonal structure. This structure

is partly imprinted onto the laser beam being coupled out in vacuum (compare figure 2.2).

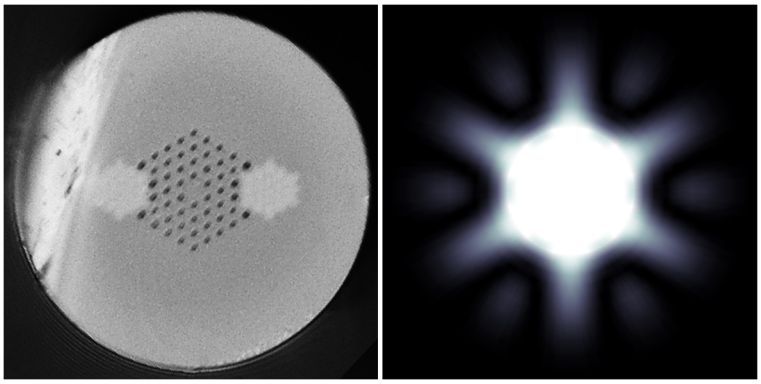

Figure 2.2.: The hexagonal structure of the photonic crystal fiber (photo taken by Patrick Oppermann) imprints onto a laser beam. The transmitted mode can be described by a sum of a fundamental mode plus some LG_0^6 content as shown on the right, where the intensity in the center of the beam is clipped.

This deformation is of higher order with a sixfold rotational symmetry. Therefore, the system of Laguerre Gauss modes is well suited for its description. For visualization, a fundamental mode with about 7% LG_0^6 mode amplitude content is plotted next to the structure. Note the similarity to the mode measured by means of detuning the PMC from resonance figure 2.8. Yet the mode height in the scan suggests only 4..5% content. For good alignment of the PMC, this mode is actually dominant as can be seen from the scan and therefore shows similarities to the light reflected by the PMC in lock.

As one usually works with the fundamental mode in interferometry, all higher order modes are often referred to as 'junk light' and need to be attenuated as described in the next section. They can be static like beam deformation, imperfect alignment or mode matching or dynamic as for beam jitter also called pointing, i.e. sideways or angular wiggle.

2.1.2 *Mode filtering*

Every stable optical cavity serves as a mode filter. Depending on its geometry, it prefers to pass through a certain field distribution while others are reflected for a given microscopic length. For the following discussion it is important that the length is usually stabilized or scanned slowly, so that the light field inside the cavity is in a static/equilibrium state.

In most experiments the length of a cavity is only scanned microscopically. This is assumed to change only the round trip phase and not the geometry and Hence, the shape of the eigenmode. The pattern of transmitted/reflected light then repeats after the additionally

accumulated round trip phase reaches 2π- a quantity referred to as free spectral range (FSR). The attenuation of any mode at a given detuning from its resonance is given by the Airy formula[1]

$$I_{\text{trans}} = \frac{(t^2)^2}{(1-r^2)^2 + 4r^2 \sin^2 \phi} \ , \tag{2.14}$$

where ϕ is the length detuning from resonance in radians. When looking at equation 2.3 or 2.7, higher order modes experience an additional phase shift $(1+m+n)\zeta(z)$ compared to the fundamental mode $\zeta(z)$ when propagating. This additional phase is called Gouy phase. It must be computed section-wise between mode converting, z_R-changing, i.e. focusing or defocussing, optics. It never equals an integer multiple of 2π in any stable resonator. This shifts the resonances of higher order modes away from the fundamental mode, i.e. reduces the possible degenerate of modes. In addition, mirroring of the mode happens at every reflection in a cavity. Therefore, each modes experiences an additional round trip phase shift of π, i.e. half an FSR, according to its parity.

This is of special importance in planar cavities with an uneven number of mirrors as in the PMC with three mirrors in a horizontal plane and modes that are antisymmetric about the normal axis of the plane, in this case about the vertical axis. Bear in mind that this affects modes with a horizontal antisymmetry, so where m, which is the index for horizontal field nodes, is odd) as well as horizontally polarized modes. In this case only modes with even 'm' are affected. The opposite of the higher order mode suppression, i.e. the higher order mode transmission can be found in figure 2.7.

2.2 REQUIREMENTS

Highly sensitive interferometric experiments are usually operated at or close to the dark fringe, where very little DC light reaches the readout port. This method relies on destructive interference of different beam paths at a beam splitter/combiner. For equally long matching beam paths, the interferometer should not be sensitive to beam jitter as both split beams are moving in the same way. In reality, however, the lengths can be vastly different[2] and specific couplings can occur anticorrelated in the paths like misaligned mirrors, astigmatism etc.. The deduction of the beam jitter requirements for the sub-SQL interferometer concentrates onto the latter effect caused by imperfectly aligned mirrors in the interferometer. These cause the arm cavity modes to be misaligned

1 Airy assumed a Fabry Perot interferometer, i.e. exactly two mirrors, and the amplitude reflectivities (r) and transmissivities (t) of the mirrors to match each other. For a more generalized case please refer to equation 6.29.

2 Imagine the case of a long Fabry Perot cavity as the 10 m Reference Cavity, different effective lengths of arm cavities due to imperfect finesse matching or Schnupp asymmetry in a Michelson interferometer.

against the ingoing beam and couple into power fluctuations at the jitter frequency at the interferometers dark port.

2.2.1 *Beam jitter coupling in the SQL interferometer*

The calculation of beam jitter requirements for the sub-SQL interferometer follows a method described in [40]. The laser, or in the Prototype's case the photonic crystal fiber, is assumed to put out a perfect single frequency TEM_{00}. Initially it is aligned and mode matched optimally to the PMC mode and more important to the interferometer, especially the arm cavities and another cavity called output mode cleaner (OMC)[3]. Some of these alignments are static, others are established by auto alignment loops. Now in reality seismic motion moves all components. In the following discussion the eigenmodes of the well aligned arm cavities propagated back to the beamsplitter serve as the spatial reference for the TEM_{00} mode. The beamsplitter is assumed to be inertially free, same as the arm cavity input test mass (ITM) and end test mass (ETM), because it will be well suspended as well. Now the input beam into the interferometer may jitter in displacement or tilt. According to equation 2.9 and 2.11 this can be described by converting some light from the fundamental to first order modes at sideband frequencies of the motion at the interferometer's input. Now there are

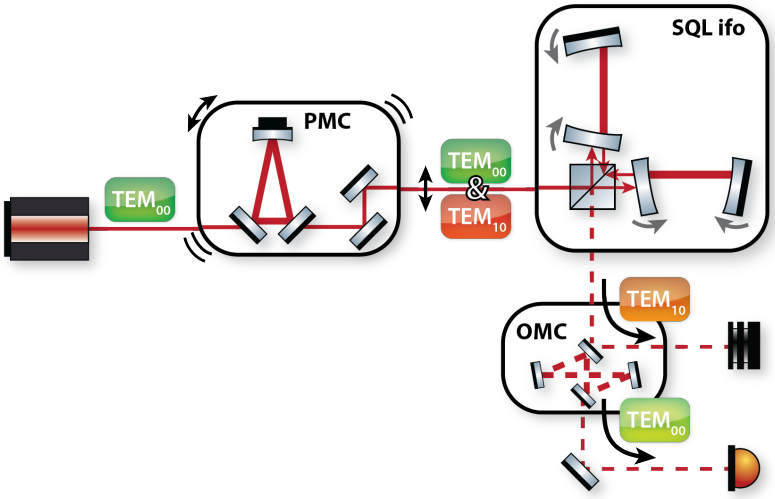

Figure 2.3.: The laser/fiber moves relative to the SQL interferometer. This causes the beam to jitter in the beamsplitter's frame which creates first order HG modes at sideband frequencies of the motion. Imperfect alignment of interferometer mirrors will mix the modes again by down-converting first order modes. This causes power fluctuations indistinguishable from arm length signals even though an OMC is removing the higher order modes.

3 The OMC is required to remove junk light not carrying any signal but contributing power on the detection photodiode and therefore adding shot noise.

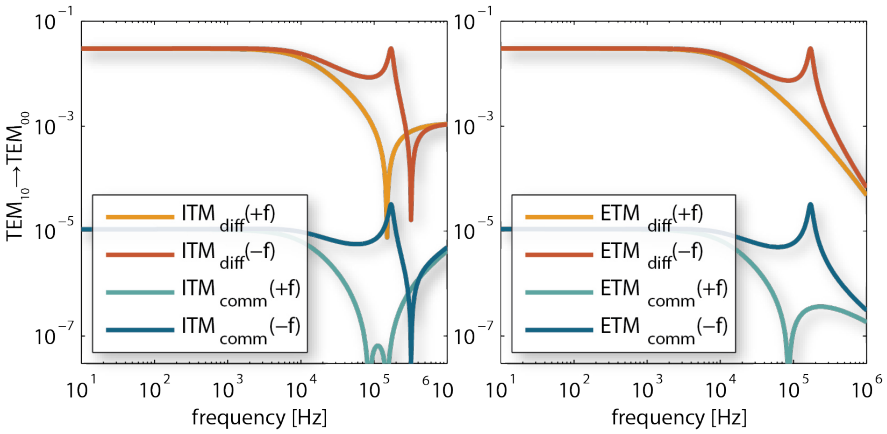

Figure 2.4.: The coupling of fundamental and first order modes in the SQL interferometer is simulated by means of a matrix formalism. The coupling of each building block (i.e. beamsplitter, mirrors, propagation) is described by a particular coupling matrix. Their combination gives the coupling of the whole interferometer. Only first order effects ($TEM_{10} \rightarrow TEM_{00}$) are covered. The degrees of freedom are common/differential misalignment of the ITMs and ETMs. The common mode barely contributes to the coupling as it is easy to achieve the angular alignment of an extremely divergent beam. Hence, it is neglected in the following calculations. The couplings of upper (+f) and lower sidebands (-f) are calculated separately because of different resonance conditions (Gouy phase shift).

three main effects leading to interferometer input beam jitter:

- A jitter of the fiber output mode, either originating from the incoupling of the laser into the PCF, created inside the PCF itself or caused by the unsupported fiber end.
- Motion of interferometer input optics couples to beam jitter similar as PMC motion but with different coupling factors due to differing beam geometries.

The laser is installed on the moving ground. It's jitter is supposed to be filtered by the photonic crystal fiber guiding it to the seismically isolating, yet moving SAS table. Motion of the table, acoustic effects or others However, may cause fiber output mode jitter. This effect could not be fully quantified yet. Therefore, the PMC was designed to have a moderately high finesse. In the case that the suppression is not high enough, a second PMC must be added. Motion of the PMC or input optics relative to the interferometer's inertial frame also couples to beam jitter noise. The allowable PMC motion can be quantified and is given in figure 2.5 on the right vertical axis. Using the PMC design parameters, the measured ground motion can be projected into the allowable TEM_{10} mode. The SAS tables suffer from internal resonances in the measurement band above 100 Hz. The achievable isolation can

barely be quantified. A factor of 30 isolation is required at 100 Hz. It is important to mention that the vertical isolation will probably be worse due to a higher resonance frequency, an isolation plateau which is increased on the long term a way more complicated GAS filter design with internal resonances and tilt to vertical coupling. If it turns out that PMC motion is too large, a simple single stage suspension in horizontal as well as in vertical should be sufficient for an optional, additional mode cleaner.

In principle the requirement can be calculated for beam shift and beam tilt independently. In practice, however, both couplings can be correlated but it is reported that they both mix up pretty quickly. Therefore, the final result in figure 2.5 is simplified to

$$\epsilon = \sqrt{\left(\frac{\Delta x}{w_0}\right)^2 + \left(\frac{\alpha}{\theta}\right)^2} \quad . \tag{2.15}$$

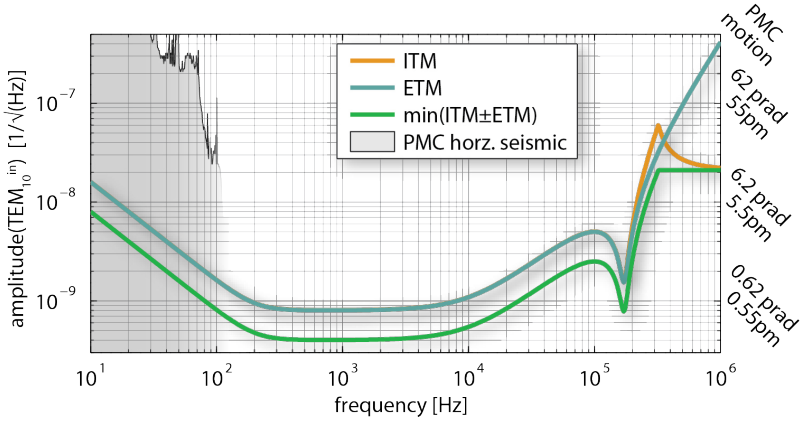

Figure 2.5.: The results from figure 2.4 are used to project the SQL interferometer's quantum noise limited sensitivity backwards to equivalent beam jitter. Here a safety factor of 10 is taken into account, a value every classical noise source should stay below the quantum noise. ITM and ETM misalignment are assumed to occur independently, so the worst possible configuration which is the minimum of 'common' or differential mode of relative ITM-ETM misalignment must serve as a requirement. Below 200 Hz the interferometer sensitivity is dominated by radiation pressure effects which relaxes the requirements, at high frequencies its sensitivity is limited by the arm cavity bandwidth. The dip in the requirement is caused by the resonance condition of the lower sidebands of the TEM_{10} mode. The second y-axis is calibrated in equivalent motion of a PMC with the proposed design.

2.3 PMC DESIGN

The photonic crystal fiber, which is used to couple the light into vacuum, already shows some mode cleaning effect. However, it also imprints its hexagonal structure onto the transmitted light. Furthermore,

it is dynamically bent from thermal and acoustic couplings and when the SAS table moves relative to ground. Therefore, another mode filter was required. As a further advantage, it serves as a mode reference inside vacuum in case the delicate fiber breaks or must be exchanged.

In order to construct a good mode cleaner, the cavity geometry must be chosen in a way that good attenuation for the low order modes is provided. These are higher in content in the beam [41] and have a stronger coupling to interferometer readout noise. At the same time some higher order mode suppression should be maintained. Also it is beneficial, especially for the use after a (not perfectly) polarization maintaining fiber, to add a polarization selective element, i.e. go for a three mirror design. To calculate the throughput of an arbitrary input field one has to decompose it into the modal system of the mode cleaner by calculating the overlap integral of the incident beam with each mode. Results for the lowest order beam deformations are given in chapter 2.1.1.

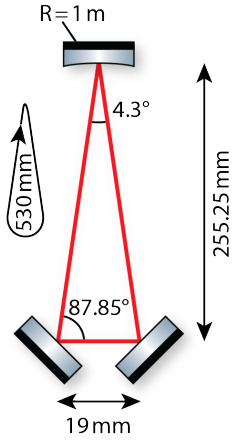

Figure 2.6: The specified radius of curvature of the end mirror in conjunction with the desired g-factor determines the required optical round trip length. The distance between in- and outcoupler is limited by the 1" mirror size. The opening angle of incidence at the curved mirror results in some minor astigmatism: its effective radius of curvature is 0.7 mm bigger in vertical and 0.7 mm smaller in horizontal. This is on the order of surface deviations at the $\lambda/20$ scale which is small compared to typical mirror specifications.

The actual mode suppression is calculated by substituting the Gouy phase shift $\zeta(z)$ plus the geometric phase shift $c \cdot \pi$ into equation 2.14. Here it comes in handy that the Gouy phase shift accumulated over one round trip can be calculated by means of

$$\zeta = \arccos\left(\sqrt{g}\right) \tag{2.16}$$

from the g-factor directly. The result is visualized in figure 2.7. The design value of $g = 0.735$ for the PMC gives a good ratio of mode suppressions. The actual overall suppression can be improved further by increasing the finesse as can be seen from equation 2.14. For the PMC the finesse should not be too high which would decrease the locking stability. Also 8 W of laser power already result in 1 MW/cm^2 with a finesse of 950. Instead further mode filtering could be provided by simply adding a second, possibly suspended PMC in line.

The g-factor $g = 1 - L/R$ fixes only the ratio of round trip length to mirror radius of curvature. The length as a free parameter is chosen in a way that the waist size is 386 µm. Then the output beam has a size

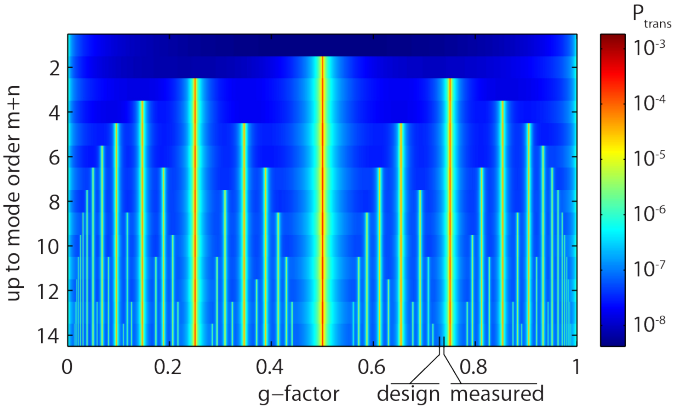

Figure 2.7.: The transmission of higher order modes through a cavity with varying g-factor is shown. The region around $g = 0.735$ provides high low order suppression as well as sufficient higher order attenuation. It was chosen as design value for the mode cleaner cavity for the AEI 10 m prototype facility. For more details see figure 5.2

of $r = 9.7$ mm after freely propagating 11 m between two tables without further optical elements. On the far table it can be collimated by means of a concave mirror for the steering into the SQL interferometer. This scheme has a small enough beam to put optics such as an EOM or a Faraday isolator behind the PMC. At the same time it expands the SQL input beam to the correct size without any further lenses which would introduce beam deformations and scattering. The collimating mirror is used under a narrow angle of incidence to provide negligible astigmatism.

In contrast to gravitational wave detectors, where the mode cleaners are usually composed of individually suspended mirrors, the 10 m prototype design follows the rigid spacer philosophy [42]. Recently, many of these fixed spacer cavities use length tuning by means of temperature using Peltier elements as a low noise high range actuator. This solution is not vacuum compatible. A big challenge in vacuum, especially in a suspended system, is to get rid of heat. On the other hand, low frequency drifts, like tides, which have large amplitudes, are mostly common between the three SASs.[4] Thermal expansion of the foundation and/or vacuum system is measured by the SPI. These low frequency disturbances can be compensated by the long range SAS actuators. Therefore, the PMC spacer was manufactured from a material reacting very little to temperature changes, SuperInvar. Its thermal expansion ($CTE = 350 \cdot 10^{-9}$) is only 10 times that of ULE glass ($CTE = 30 \cdot 10^{-9}$), but it is easier to machine. The residual temperature to round trip length coupling is $0.17\lambda/\mathrm{K}$.

4 Relative SAS motion defines cavity lengths (RefC, SQL arms...) and thereby the required frequency tuning of the laser

For microscopic length tuning, a long range piezo (NAC2125-H12-C01) is used to tune the curved end-mirror. It provides a maximum range of 13.3 µm or 80 K in terms of spacer temperature change across a voltage range of $-40..+200$ V. This comes at the drawback of lower frequency resonances and a reduced control bandwidth compared to a thinner model. The thermal stability inside vacuum allows to stay in lock over hours without any re-locks even when driving the piezo only with a less noisy $-15..+50$ V HV amplifier.

2.4 RESULTS

Manufacturing and specification tolerances lead to the situation that the built PMC does not match the design exactly. A mode scan is a good tool to find out the actual g-factor by means of Gouy phase separation. From figure 2.8 a Gouy phase of $\zeta = 0.170 FSR$ was deduced resulting in an actual $g = \cos^2(\zeta) = 0.741$ compared to a design value of $g = 0.735$. The measured value is shifted towards increased LG_0^6 transmissivity (about 3 times as much) but suppresses the star mode still well enough. Normally the accuracy would not be very trustworthy,

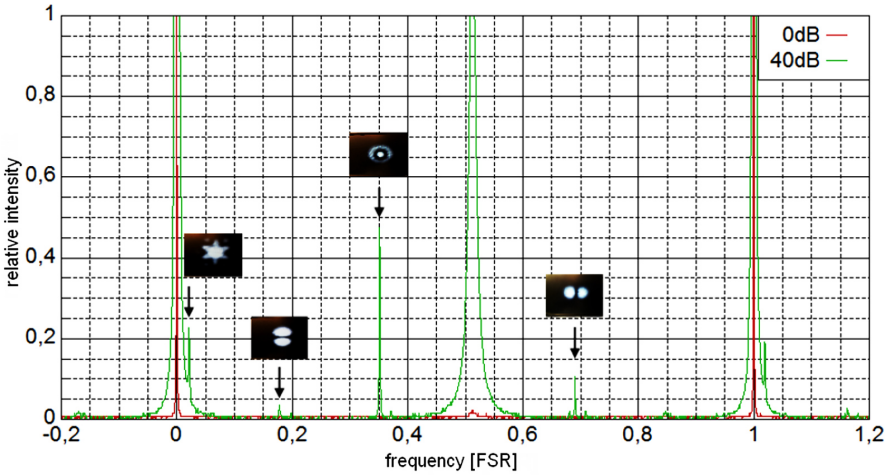

Figure 2.8.: A longitudinal scan of the PMC cavity [39] selects higher order modes to be transmitted while the fundamental mode is attenuated. The beam coming out of the PCF is already rather clean. Residual misalignment (1st order modes) shows up shifted by half an FSR with respect to each other due to the triangular cavity geometry. Mode mismatch (2nd order modes) appears at twice the frequency shift. The star mode arising from the PCF structure experiences six times the TEM_{01}'s Gouy phase and appears close to the next order fundamental mode. Residual p-polarization shows up close to half an FSR. Actually, it is slightly shifted due to different path length arising from the different reflection condition inside the coatings of the mirrors.

as PZTs usually suffer from nonlinear behavior. However, the sixth order 'star-mode' is quite close to the next order fundamental mode,

which reduces the impact of nonlinearities strongly. Therefore, the Gouy phase of the sixth order mode can be measured very accurately and is divided by six to obtain the first order Gouy phase with high precision.

When increasing the circulating power, the heat dissipated in the coatings could heat them locally and cause a radius of curvature change same as the thermal lens in the in- and outcoupler. However, thermal effects seem to play a comparably small role: When the input power is raised from 200 mW to 8 W, the Gouy phase of the sixth order mode changes only by 0.16% (1.7 miliFSR). This is equivalent to a g-factor increase from 0.741 to 0.742 which should be acceptable.

parameter	PMC
T_{input}	3300 ppm
T_{output}	3300 ppm
T_{curved} (HR)	20 ppm
add. loss	guess: 200 ppm per round trip[5]
$Finesse_{s\text{-}pol}$	937 ± 28 (design: 950)
$Finesse_{p\text{-}pol}$	≈ 77
FSR	566.04 ± 0.11 MHz
FWHM	604 ± 18 kHz
$P_{in,max}$	12 W tested
$P_{trans,max}$	95.3 ± 2.1 %
R_{curved}	1 m
w_0	386 µm
g-factor	0.735 design, 0.741 measured
$l_{round\ trip}$	530 ± 0.1 mm
f_{mod}	35.5 MHz
modulation depth	1.5 mrad

Table 2.1.: The construction and characterization of the PMC is described in [39]

5 The measured finesse agrees to about 40 ppm round trip loss in addition to T_{curved}

3

SUSPENSION THEORY

One of the biggest noise terms in ground based interferometry is ground motion also known as seismic noise. In addition to strong but short earthquake events there are weaker but way more frequent micro tremors and an everlasting 'grumble'. But also other sources induce motion of the ground which is usually not recognized in every day life.

Some origins and the frequency distribution along with the temporal variability are described in section 3.1. In section 3.2 the simplest method of isolating the measurement apparatus, i.e. cavity mirrors, from the seismic disturbances is described: the harmonic oscillator. This approach can be improved by stacking multiple stages as shown in section 3.2.4. Such complicated systems suffer from resonant enhancement at some frequencies which can be damped according to section 3.2.1 and 3.2.3 either passively or actively. Sections 3.2.8 and 3.2.9 discuss the active damping in more detail. The actual design of the damping system for a system with many modes requires a sophisticated modeling which is explained in section 3.3. The practical realization of two differently complex systems is then depicted in chapter 5.6 and 4.

3.1 SEISMIC NOISE

Seismic noise is the inherent motion of the ground. It's floor changes over the course of days as depicted in figure 3.1 but is also strongly dependent on the season as shown in figure 3.2. Various natural as well as artificial effects contributing are described in the following.

- Tides move the ground. However, the prototype facility is relatively small so that displacements usually occur in common. Yet they also tilt the ground which leads to a modulation of the direction of the gravitational acceleration g. This then shows up as horizontal displacement of test masses at low frequencies [43].

- Barometric pressure modulates the force exerted onto ground in the few mHz region. Again tilt dominates [44].

- Earthquakes all around the world release low frequency bursts and therefore cause broadband noise. The STS2 seismometer

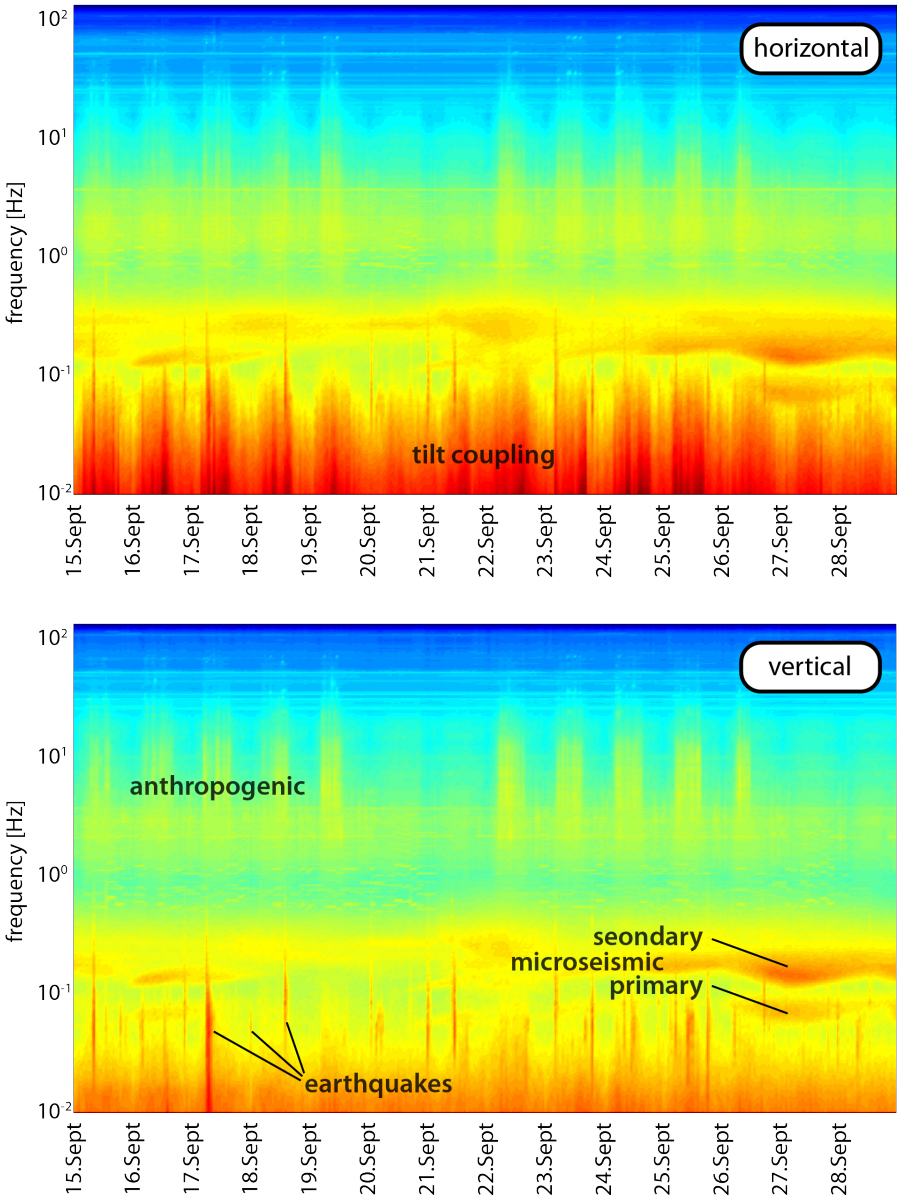

Figure 3.1.: The horizontal and vertical motion of the ground next to the experiment was measured with a Streckeisen STS2 seismometer. The spectrogram shows the variability of the seismic ground motion. At low frequencies (about 0.1 Hz) the horizontal measurement is spoiled by ground tilting. Anthropogenic noise changes on a diurnal and weekly basis while microseism changes slower ($\approx$2..3 days) and earthquakes all around the world down to $\approx$5 mag contribute broadband low frequency bursts.

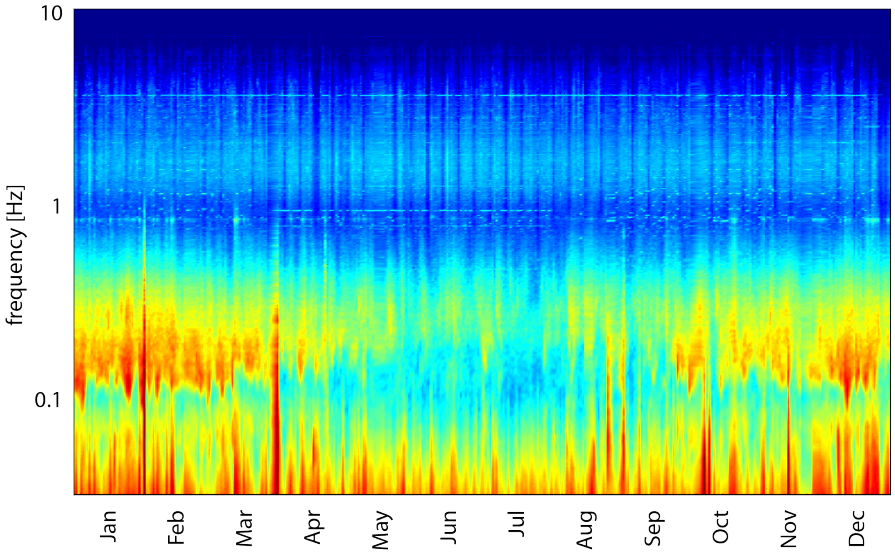

Figure 3.2.: The variability of seismic noise was monitored over the course of a year. Each day in 2014 a 1 hour horizontal seismic spectrum was taken, starting at 3:00 a.m., when the human influence is the lowest. Yet the anthropogenic 7-day cycle is visible in the few Hz band. More prominent is the strong seasonal variation of the microseism in the few tens of mHz region. During wintertime, the season of storms, the microseismic peak is more than an order of magnitude higher, while sometimes almost vanishing during summertime. September which was chosen for figure 3.1 provides a good average.

which is used to measure the ground motion of the experiment, easily can resolve 5 mag earthquakes all around the world (see vertical low frequency lines in figure 3.1, e.g. between March and April).

- Wind on shallow waters causes waves. These can interact with the seabed (primary microseismic peak at 40-170 mHz) or with each other (secondary microseismic peak at 80-340 mHz) resonantly to cause seismic motion. This noise is correlated with the swell along nearby coastlines [45] and varies over the course of a few days. The size of the microseismic peak in Hannover depends mostly on the wind conditions in the North Sea. However, the associated wavelength are big (tens of km) so that effect is usually common mode in small detectors (< 100 m) and thereby for our experiment less dominant than in gravitational wave detectors [20].

- Wind pushes against buildings and causes turbulences. This shows up at 0.5..60 Hz [46].

- At the AEI, civilization dominates ground motion in the range of 1..30 Hz and tilt in the 10..100 mHz region during daytimes. Cars,

trams, industry etc. cause a diurnal variation. Figure 3.1 shows that there are mostly two distinct states: anthropogenic noise is increased during weekdays and reduced in nighttimes and on weekends. Sensitive measurements which don't require long-term observation, are optimally run in nighttime or on weekends.

- From a few Hz towards high frequencies there is typically a roll-off of the order $1/f^{1}.5$ to $1/f^{2}$ (figure 3.3).

For easier further use, the seismic data needed to be condensed into a single seismic spectrum. Unlike gravitational wave detectors [47], the AEI 10 m Prototype is not built to achieve high duty cycles on a 24/7 basis. Therefore, it is sufficient to reach requirements under quiet seismic conditions. The seismic variability is covered by the probability density function as found in figure 3.3. Seismic data of two weeks in September was evaluated.

3.2 SEISMIC ISOLATION

In table top experiments a lot of noise can be avoided by measuring at high frequencies in the MHz range. Earthbound interferometric gravitational wave detectors, however, are limited to the audio frequency band. Below that, the noise rises quickly (e.g. seismic wall, gravity gradient noise) while above, the weakness of sources requires even better detection sensitivities (lower shot noise). As the Prototype facility with it's subsystems, e.g. Reference Cavity and the TNI described in chapters 5 and 6 respectively, are designed for research and development for gravitational wave detectors, the aspired displacement sensitivity and frequency range and therefore the techniques used are similar.

In a lab environment, seismic noise is usually rather correlated. Yet mechanical responses of optical components to ground motion never match each other perfectly. When e.g. a mirror moves, this modulates the phase of the reflected light. Thereby it produces signals which are indistinguishable from common measurement quantities such as laser frequency, space-time deformation and many others. For this reason seismic noise needs to be attenuated by several orders of magnitude for highly sensitive measurements. It is important that this happens in a wide band: at low frequencies to maintain the working condition (usually the resonance of an optical cavity) and at high frequencies to avoid direct noise coupling into the desired measurement quantity. Seismic decoupling is equivalent to silencing the sensitive optics in an inertial frame. There are two approaches to achieve this:

Active seismic isolation

Active seismic isolation of a test mass requires inertial sensors. Their signals are used to apply forces that counteract the forces exerted onto

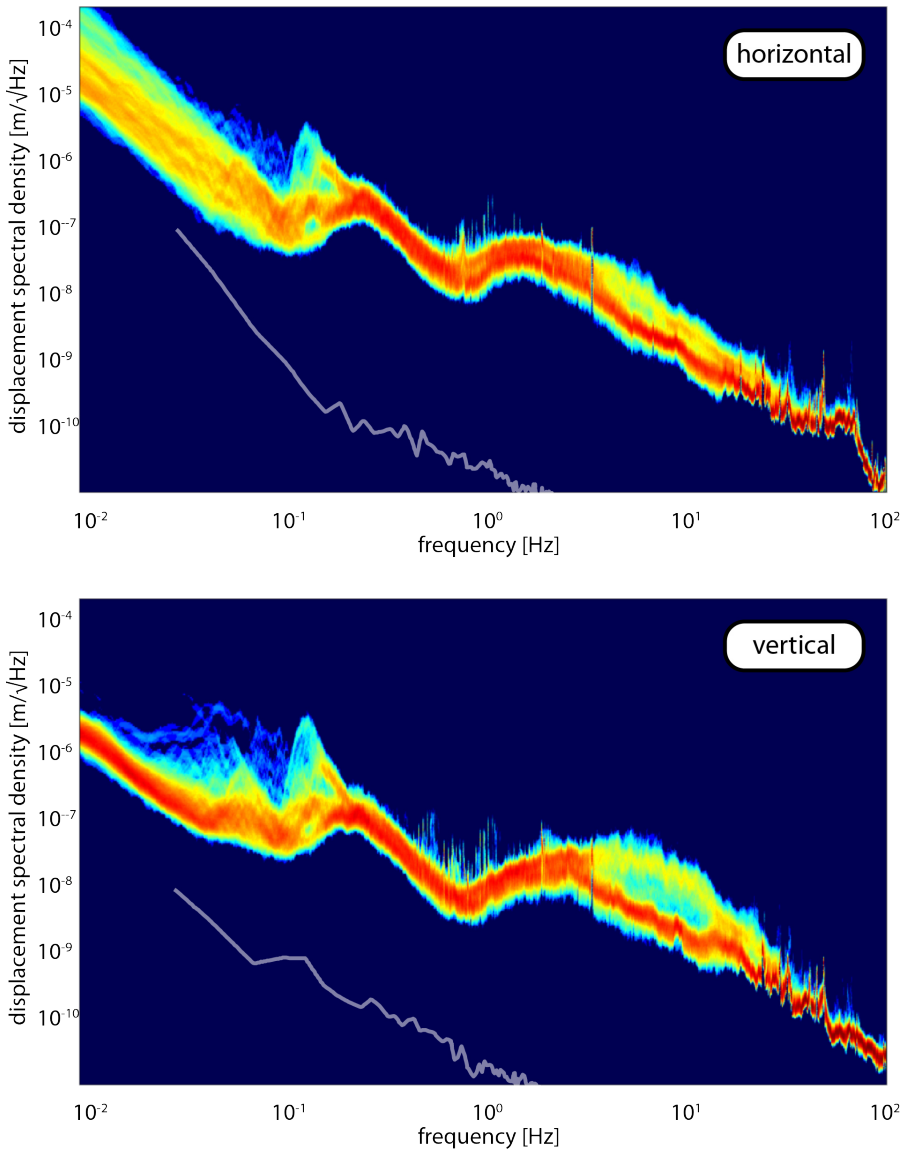

Figure 3.3.: The probability density distribution of horizontal (a) and vertical (b) displacement spectral density of the ground next to the experiment is shown. It describes the probability to obtain a certain spectral density within a 1 dB band during two weeks in September 2014. Around 0.1 Hz the microseismic peak varies while anthropogenic noise manifests around 10 Hz and below 0.1 Hz, latter mostly in horizontal direction as tilt. for comparison, the STS2 instrument noise from figure D.18 is given.

the test mass by the environment, either by means of feedback (sensor on the test mass) or feed forward (sensor on ground). This method can only be as good as the noise floor of the sensor. With existing sensors active isolation can only serve as pre-isolation (the lowest stage of a multiple stage isolation system), mainly to reduce the low frequency contributions [48, 49].

Passive seismic isolation

Passive seismic isolation relies on the $1/f^2$ decay of the mechanical susceptibility of a harmonic oscillator (later referred to as pendulum) above it's resonance frequency (compare figure 3.4). The ideal (mathematical) horizontal oscillator can be realized almost perfectly by suspending an optic close to its center of mass from a thin (and thereby almost massless) wire. Alternatively it can be suspended from several parallel wires attached to its circumference. Vertical isolation can be provided by hanging the optic from springs. It turned out that it is beneficial to decouple vertical and horizontal isolation stages. Therefore, horizontally stiff cantilever springs also called blade springs are used instead of for example coil springs.

Often more isolation at lower frequencies is demanded. This can be achieved by reducing the eigenfrequency

$$\begin{aligned} \omega_{\text{pend}} &= \sqrt{\frac{g}{l}} \\ \omega_{\text{spring}} &= \sqrt{\frac{g}{\Delta z}} \end{aligned} \tag{3.1}$$

of the suspension where l is the pendulum length and Δz is the loaded extension of the spring compared to the unloaded rest position. From this equation it can be seen that classical low frequency suspensions would get too large. New techniques, such as inverted pendulums (IP) and magnetic/geometric anti spring (MAS, GAS) filters [50], however, increase the complexity of the isolation system and are only used in pre-isolation. A simpler alternative for mirror suspensions is stacking several pendula, each of which is providing its $1/f^2$ transmissibility above the resonance frequency (which is usually of the order of 1 Hz). Then, significant isolation can be achieved in the audio range above some ten Hertz.

3.2.1 *Passive viscous damping*

Passive isolation systems come at the drawback of amplified transmissibility (frequency response of the suspended mass' motion to suspension point motion) at their resonances. This increases the rms displacement of a test mass depending on their mechanical quality factor (see section 3.2.4). Hence, the resonances need to be damped.

A damped harmonic oscillator is described by

$$\begin{array}{llll} F_{\text{inertia}} & + F_{\text{damp}} & + F_{\text{restore}} & = F_{\text{ext}} \\ m\ddot{x} & + b\dot{x} & + \kappa x & = F_{\text{ext}} \end{array} \tag{3.2}$$

where m is the mass, b is the damping coefficient and κ is the spring constant of the oscillator at the position $x(t)$. F_{ext} is the force acting onto the oscillator. The equation still holds for multiple coupled oscillators as described in chapter 4. Then x and F must be expanded to vectors, and m, b and κ to matrices (compare equation 3.24). The second line already assumes the most common form: viscous damping. In the Fourier domain, the time derivative simplifies to

$$\begin{aligned} \tilde{F}_{\text{damp}} &= b\dot{\tilde{x}} \\ &= i\omega b\tilde{x} \ , \end{aligned} \tag{3.3}$$

where ω is the angular frequency. The i is symbolic for the 90° lag of the damping force behind the position. It is reduces the velocity (i.e. extracts kinetic energy $E_{\text{kin}} = 1/2m\dot{x}^2$). High peaks in the transfer function are associated with high velocities and Hence, experience a bigger damping force. Therefore, resonances are flattened out while the off-resonant floor is influenced only little. This can be seen well in the frequency response

$$\begin{aligned} \frac{F_{\text{ext}}}{m} &= \ddot{x} + 2\gamma\dot{x} + \omega_0^2 x \\ \frac{\tilde{F}_{\text{ext}}}{m} &= (\omega_0^2 - \omega^2 + 2i\gamma\omega) \cdot \tilde{x} \\ \frac{\tilde{x}}{\tilde{F}_{\text{ext}}/m} &= \frac{1}{(\omega_0^2 - \omega^2 + 2i\gamma\omega)} := \frac{H_F}{m} \\ \left|\frac{\tilde{x}}{\tilde{F}_{\text{ext}}/m}\right| &= \sqrt{\frac{1}{(\omega_0^2 - \omega^2)^2 + (2\gamma\omega)^2}} \\ \text{phase}\left(\frac{\tilde{x}}{\tilde{F}_{\text{ext}}/m}\right) &\overset{1}{=} \arctan\left(\frac{2\gamma}{\omega_0}\frac{1}{\frac{\omega}{\omega_0} - \frac{\omega_0}{\omega}}\right) \end{aligned} \tag{3.4}$$

of the oscillator position x to a force F_{ext} exerted onto it which is plotted in figure 3.4. Here the damping constant $\gamma = b/2m$ was introduced. The Q-factor $Q = \omega_0/(2\gamma) = m\omega_0/b$ is another, experimentally more convenient way, to express the damping. For $Q \gg 1$ it gives the amount of enhancement on resonance compared to the off-resonant floor (see figure 3.4 and 3.5). A damping with $Q = 1/2$ is called 'critical'.

In practice, seismic isolation systems are usually carefully designed to have little inherent damping. They need to be damped artificially, e.g. by means of eddy current damping. Magnets and conducting cups are attached to the suspended mass and the surrounding mounting

1 The phase of a complex number H is calculated by means of $\text{phase}(H) = \arctan(\text{Im}(H)/\text{Re}(H))$

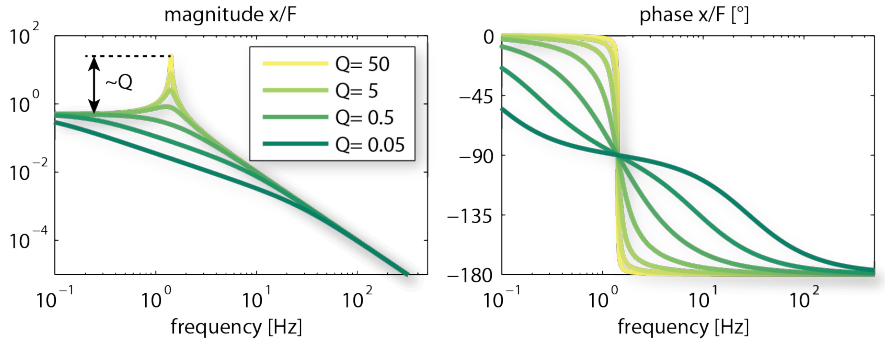

Figure 3.4.: The amplitude and phase response plots show the susceptibility $H_F(f)$, sometimes denotes as $\chi(f)$ of different damped harmonic oscillators to an external force. The quality factor (Q) is determined by the strength of the damping which is viscous in many cases. As the inherent damping of a well engineered pendulum is low, it has be replaced by controlled means of eddy current damping (magnet on the test mass, conduction cup on the ground or vice versa). Beyond the resonance, the response decreases as $1/f^2$.

structure called the cage.[2] However, the damping force cannot distinguish between oscillator movement and ground motion. Therefore, it is important to distinguish between the susceptibility (the transfer function $F_{\text{ext}} \to x$) illustrated in figure 3.4 and the transmissibility (the frequency response of the oscillator to ground motion $x \to x_0$)

$$\begin{aligned} 0 &= \ddot{x} + 2\gamma(\dot{x} - \dot{x_0}) + \omega_0^2(x - x_0) \\ (\omega_0^2 - \omega^2 + 2i\gamma\omega)\tilde{x} &= (\omega_0^2 + 2i\gamma\omega)\tilde{x}_0 \\ \frac{\tilde{x}}{\tilde{x}_0} &= \frac{\omega_0^2 + 2i\gamma\omega}{\omega_0^2 - \omega^2 + 2i\gamma\omega} := H_x \\ \left|\frac{\tilde{x}}{\tilde{x}_0}\right| &= \sqrt{\frac{w_0^4 + (2\gamma\omega)^2}{(\omega_0^2 - \omega^2)^2 + (2\gamma\omega)^2}} \\ \text{phase}\left(\frac{\tilde{x}}{\tilde{x}_0}\right) &= \arctan\left(\frac{2\gamma}{\omega_0}\frac{1}{\frac{\omega}{\omega_0} - \frac{\omega_0}{\omega}}\right) + \arctan\left(\frac{2\gamma}{\omega_0}\frac{\omega}{\omega_0}\right) \quad , \end{aligned} \tag{3.5}$$

which is illustrated in figure 3.5.

At high frequencies, i.e. a factor of Q above resonance, the ω-proportional F_{damp} dominates the frequency independent restoring force. The transfer function only decays with $1/f$ because seismic noise is bypassed through the viscous damper. For a better comparison both, the transfer function and the transmissibility, are shown along each other in figure 3.6.

2 If the magnets are mounted to the mass, then a coil wound onto the damping cup can exert forces to align it the suspended mass.

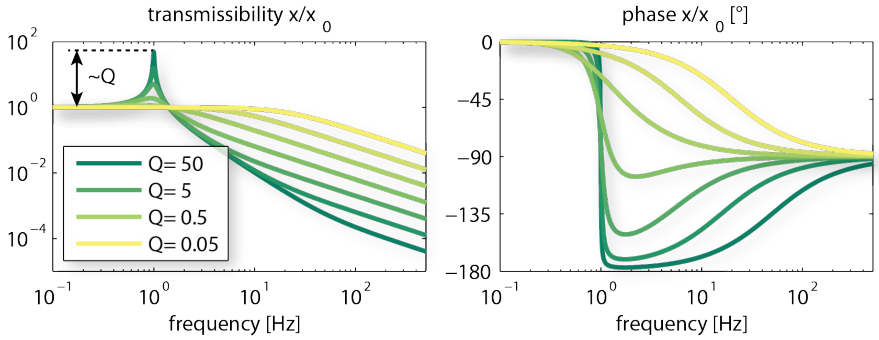

Figure 3.5.: The transmissibility of various damped harmonic oscillator is shown. Different viscous (velocity proportional) damping strengths are realized by feeding back the test mass velocity relative to the suspension point. In contrast to a force to displacement transfer function, the transmissibility levels off with $1/f$ towards higher frequencies as the damping bypasses ground motion to the test mass with a $1/f$ slope. Usually a Q-factor of 3 to 10 is aimed for to obtain sufficient isolation with reasonable ring-down times.

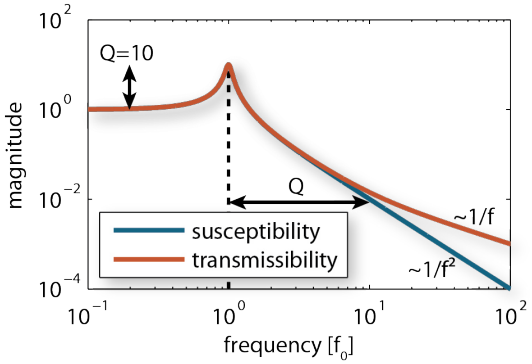

Figure 3.6.: The force to displacement susceptibility rolling of as $1/f^2$ towards higher frequencies is shown in blue. Compared to it, the roll-off of the suspension point to displacement transmissibility shown in red is getting shallower a factor of Q above the resonance. This is explained by the damping which bypasses the isolation of the harmonic oscillator.

3.2.2 *Passive structural damping*

Beyond viscous damping, there are other kinds of dissipation. Passive damping effects can be described more generally including the damping in equation 3.2

$$\begin{array}{llll} F_{\text{inertia}} & + F_{\text{damp}} & + F_{\text{restore}} & = F_{\text{ext}} \\ m\ddot{x} & + i\kappa\tan(\phi)x & + \kappa x & = F_{\text{ext}} \end{array} \tag{3.6}$$

as an imaginary part of the spring constant. For small loss angles $\tan(\phi) \to \phi$ can be applied

$$m\omega^2 + \kappa(1 + i\phi) = F_{\text{ext}}/x \ . \tag{3.7}$$

Viscous damping is now a special case

$$\phi_{\text{visc}}(\omega) = \frac{b\omega}{\kappa} \ , \tag{3.8}$$

showing that the loss angle can in fact be frequency dependent (compare viscous, structural or thermoelastic damping, latter even has a dissipation peak). This potential frequency dependence, i.e. the exact fundamental loss mechanism, is still poorly known for many systems. This prompts it's measurement across a broad frequency range (compare chapter 6).

3.2.3 *Active damping*

The damping described in chapter 3.2.1 is realized by a velocity-proportional force. Such a feedback can also be applied actively. This requires a sensor for the state of motion of the oscillator $x(t)$ and an actuator to exert a force F_{damp} onto it. In practice the position of the oscillator is measured. It is passed through a function $D(\omega)$ which infers the velocity and fed back by acting a force onto the oscillator.

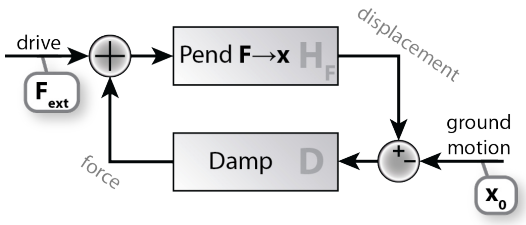

Figure 3.7.: Damping can be seen as a feedback force F_{damp} which is depending on the state of motion x_{osc}. Usually in mirror suspensions the position relative to ground is measured and fed back by means of electromagnetic actuation, whether actively or by means of eddy currents. The pendulum transfer functions $H_F(x)$ can be as simple as equation 3.4 or far more complicated and only experimentally measurable.

Assuming that the equation of motion of the initial, not actively damped, pendulum is solved by the transfer function

$$\frac{\tilde{x}}{\tilde{F}} = \frac{1}{m(i\omega)^2 + bi\omega + \kappa} := H_F(\omega) \tag{3.9}$$

as described by equation 3.2, it's actively damped transfer function can be deduced from figure 3.7. Additional to the external force determining the pendulum motion, another term $\tilde{F}_{\text{damp}}$ is acting onto it

$$\begin{aligned} \frac{1}{H_F(\omega)} \cdot \tilde{x} &= \tilde{F}_{\text{ext}} + \tilde{F}_{\text{damp}} \\ &= \tilde{F}_{\text{ext}} + D(\omega) \cdot \tilde{x} \ . \end{aligned} \tag{3.10}$$

The closed loop force to displacement transfer function

$$\frac{\tilde{x}}{\tilde{F}_{\text{ext}}} = \frac{1}{\frac{1}{H_F(\omega)} - D(\omega)} \tag{3.11}$$

directly follows from this.

When the allowance for payload is big, as in the SAS (chapter 1.3), accelerometers or geophones can be used to measure inertial motion. For mirror isolation systems, a lighter variant is used: the mirror displacement is measured by a sensor fixed to ground x_0 (compare chapter 4.5.1). The suspension point is fixed to ground as well. Then the equation of motion reads in the Fourier domain as

$$\begin{array}{llll} \tilde{F}_{\text{inertia}} & + \tilde{F}_{\text{damp}} & + \tilde{F}_{\text{restore}} & = \tilde{F}_{\text{ext}} \\ (i\omega)^2 m\tilde{x} & + D \cdot (\tilde{x} - \tilde{x}_0) & + \kappa \cdot (\tilde{x} - \tilde{x}_0) & = \tilde{F}_{\text{ext}} \ , \end{array} \tag{3.12}$$

where the damping inherent to the oscillator is left out for simplicity – the damping is assumed to be dominated by the active feedback.

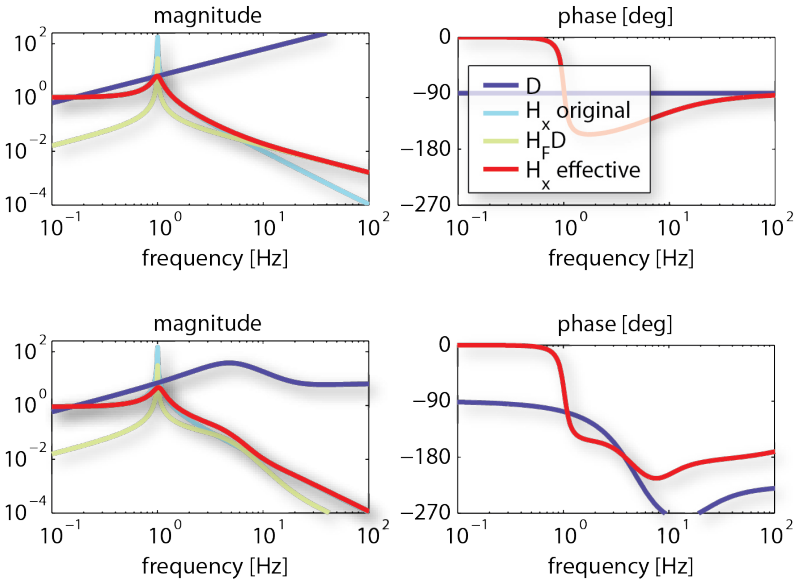

Figure 3.8.: The upper graphs show the contributions to the effective transmissibility (red line) of a viscously damped oscillator (compare figure 3.5). Towards higher frequencies the feedback (light green) is limiting. The lower graphs show that a fairly simple reduction of the feedback (violet) in this region can reduce the unintentionally fed back ground motion to almost recover the full (undamped) transmissibility (light blue) at the slight expense of a weak servo bump.

In reality, there are some limitations on $D(\omega)$. Firstly, it must be a causal function. Secondly, it should be a linear, time invariant function of the state. This means, it can always be represented by a separation into (complex) poles and zeros plus a delay [51]. Stability requires the phase of the open loop gain to stay away from 180° in the vicinity of

unity gain [52]. Therefore, 'D' must be similar to velocity proportional, i.e. well between constant and f^2-slope close to unity gain, around the resonances which should be damped.[3] In regions where the open loop gain is well below unity, the servo can be shaped quite freely to achieve minimal noise coupling into the detection band. An example is given in figure 4.24.

3.2.4 *Coupled oscillators – sequencing isolation stages*

Often space requirements do not allow for a single oscillator providing the required isolation (e.g. strong horizontal isolation requires long pendula). This fact can be overcome by stacking several isolation stages. In case of a pendulum, each stage will be shorter compared to the single pendulum case, which increases the individual (uncoupled) eigenfrequencies. On the other hand, each stage provides a $1/f^2$ transmissibility above its resonance frequency. The stacking causes the restoring forces onto the 'inserted' oscillators to depend on the position of the surrounding ones. The differential equations, that describe the full system, become coupled (off-diagonal κ-terms in equation 3.2). The equations of motion then are not solved analytically but instead numerically (see chapter 3.3). Hence, the understanding is more observational based than theoretically founded. Nevertheless, a few properties are be discussed in the following sections.

The describing differential equations can be decoupled into the eigenmodes. This results in frequency splitting and shifting in the coupled system. In the frequency response ($F_m \to x_n$), oscillators that are inside the measurement path (between F_m and x_n) show up as resonances. The associated quality factors determine their widths and also the steepness of the 180° phase loss. If additional oscillators are coupled to the measured system, they also show up as resonances. But furthermore, they produce antiresonances at frequencies where their recoil onto the measured system is out of phase with the driving force. At these antiresonances, the 180° phase loss across the resonance is recovered.

3.2.5 *Damped coupled oscillators*

When considering unequally damped coupled oscillators, not only are their frequencies are coupled, but also their dampings. A double pendulum serves as a good example. It is shown in figure 3.9. The upper stage of a pendulum is assumed to dominate the energy loss of the system (uncoupled $Q_1 = 10$). The lower stage is weakly damped against the upper stage (uncoupled $Q_2 = 10^9$). This resembles the longitudinal degree of freedom of a real double stage mirror isolation quite well: Energy is extracted at the top stage to reduce the test mass motion while

3 Bear in mind that the pendulum provides a $1/f^2$ drop across the resonance.

the lower stage's Q is intentionally high for suspension thermal noise reasons (see chapter 5.7.5).

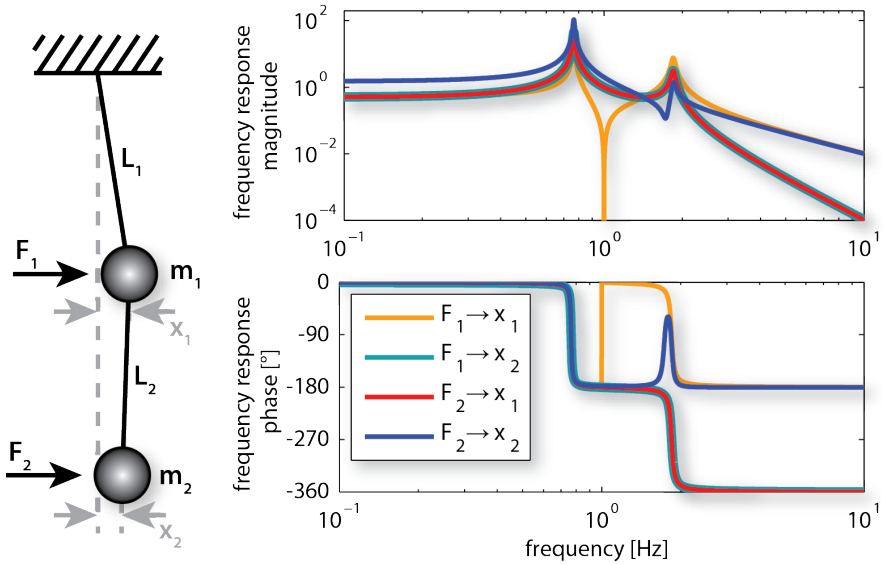

Figure 3.9.: If several oscillators are stacked to obtain higher isolation, their motions couple to each other. The frequency response to forces exerted onto either oscillator of the coupled system is shown ($L_1 = L_2$, $m_1 = m_2$ and individual quality factors $Q_1 = 10$, $Q_2 = 10^9$). Even by measuring only the susceptibility of x_1 to a force F_1 exerted onto m_1, information about further oscillators coupled to it can be obtained. An antiresonance (dip in magnitude) develops when an oscillator, which is coupled to the measured system, moves out of phase with the excitation (see figure 4.23).

It turns out that the antiresonances observed at an oscillator x_n yield valuable information about a simpler system: They develop at frequencies, where the rest of the system, usually the stages hanging below, would have a resonance if the system was held in place at the observation point x_n. In case of the simple double pendulum shown in figure 3.9, there is an antiresonance in $F_1 \to x_1$ at 1 Hz. As the mass m_1 does not move at this frequency, the motion of the system cannot be influenced by its properties. Hence, at 1 Hz there must the resonance of the uncoupled lower pendulum. Moreover, only the lower mass' loss (in this case it is known that Q_2 is high compared to Q_1) can determine the width of the antiresonance and the steepness of the 're-gain' in phase.

The same can be found for the $F_2 \to x_2$ transfer function: There is another antiresonance (dip and 90° phase retrieved) at 1.7 Hz ($\sqrt{3}Hz$). This agrees to the resonance of the upper mass with the lower mass fixed in place.

3.2.6 *Damping a suspension chain*

Active damping of a suspension is usually applied to the upper mass. There are two reasons for this: First, the readout of the state is always noisy. This noise couples into the actuation signal and Hence, to displacement of the actuated mass. The closer to ground this is in a suspension, the more this noise is filtered by the lower suspension stages as can be seen from x_2-motion in figure 3.10. The second reason is that most damping systems measure the state of motion relative to ground. As the latter is moving, one would unintentionally feed this ground motion back and thereby bypass the upper stages. Again, this effect is filtered better, the further at the top of the suspension chain the actuation is applied. The motion of the test mass itself is then only damped via its coupling to the motion of the upper mass.[4] This situation is illustrated in figure 3.10 and 3.11, where the lower mass has little inherent damping $Q_2 \approx 10^4$) against the upper mass. The masses are assumed to be equal for simplicity. The wires have the same lengths. With little damping (uncoupled $Q_1 \ll 1$), both modes are showing up with high peaks. When overdamping the upper mass ($Q_1 \gg 1$, the lower mass motion shows resonant enhancement again. In this case the upper mass is held at rest (relative to ground), so lower mass motion cannot couple to it, once energy reaches the mirror. To obtain efficient energy transfer of noise coupling into the test mass (represented by the F_2 in figure 3.11), the damping of the upper stage must be tuned. Usually a $Q_1 \approx 3..10$ is chosen to reduce the feedback noise compared to the optimal energy transfer case $Q_1 \approx 1/2$ [53].

However, the graph also shows another effect mentioned before: The damping happens relative to ground. But unlike in many other cases, the ground cannot be treated as an inertial frame (compare figure 3.3). Dependent on the strength of the damping, the transmissibility flattens out at a $1/f$ slope ($\lim_{f\to\infty} mag = f_0/(fQ)$). This means compared to the ideal n-staged harmonic oscillator ($\lim_{f\to\infty} mag = (f_0/f)^{2n}$) additional ground motion is transmitted to the test mass. This is of importance because (especially when applied to a lower stage of a multi stage suspension system) this effect would bypass the isolation. In principle the slope of a passive damping system could be modified to overcome the seismic shortcut. However, this would require mechanical systems with specially designed transfer functions ruining the advantage of passive damping: simplicity.

3.2.7 *Transmissibility in the case of active damping*

In the more general case of frequency dependent (active) damping and ground noise in conjunction with force noise, the situation of

4 In the design of a suspension chain it is essential to provide enough coupling to damp all modes sufficiently.

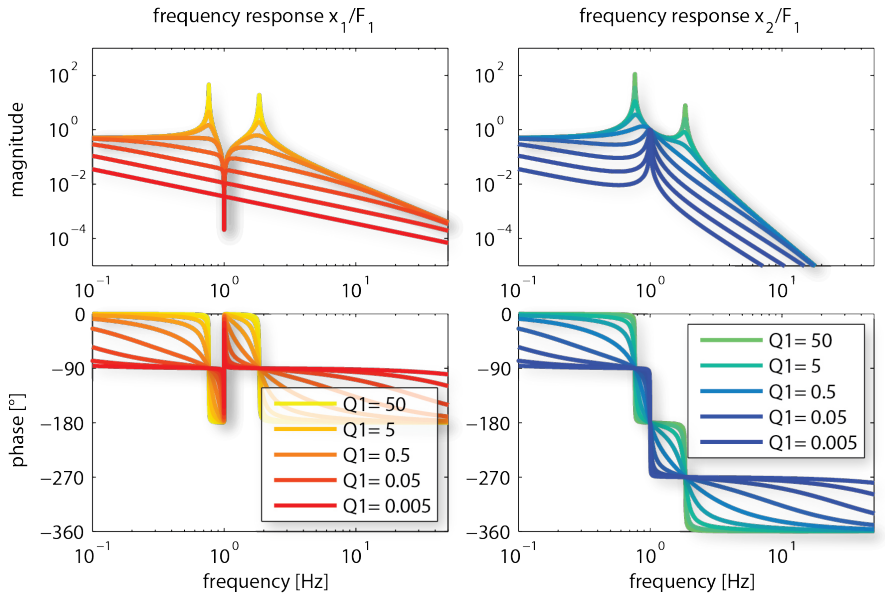

Figure 3.10.: The frequency response of two coupled oscillators (stacked pendula) to a force applied at the upper mass is shown. This represents force noise coupling in via the upper mass, e.g. actuation or seismic noise. Bear in mind that ground motion coupling depends on the Q-factor as well (see figure 3.5). When damping only the upper stage, there is an optimum around critical damping ($Q = 1/2$) for motion of the lower 'test mass'.

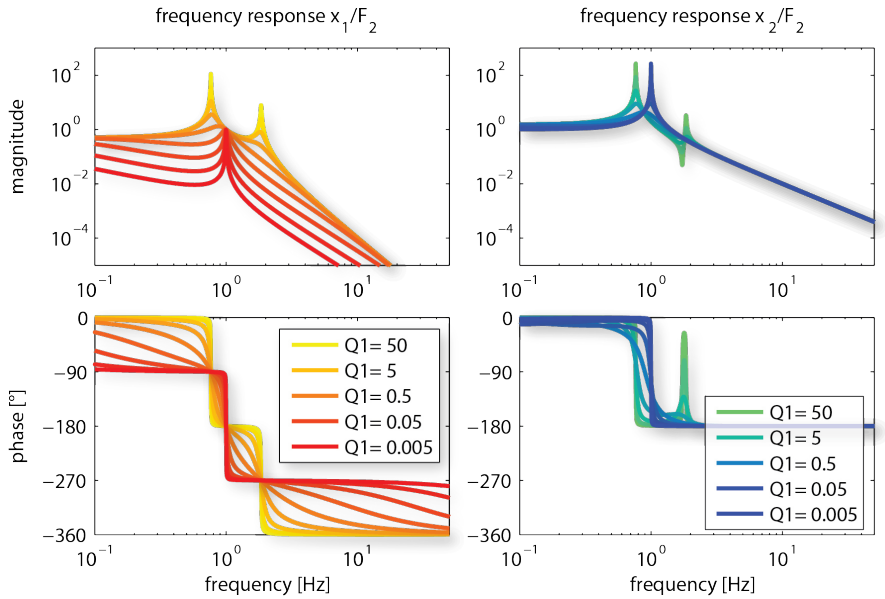

Figure 3.11.: The frequency response of two coupled oscillators, in contrast to 3.10 to a force applied at the lower stage, is shown. While damping only the upper stage, there is an optimum around critical damping ($Q = 1/2$) for motion of the lower 'test mass'.

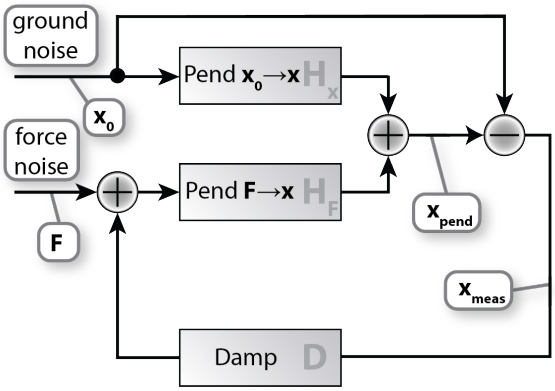

Figure 3.12.: This flow chart describes the coupling of suspension point noise x_0 and an external force F_{ext} into the position x_{pend} of an actively damped pendulum. H_x and H_F refer to the transmissibility and the force transfer function respectively.

the last section gets more complicated. Imagine the active damping to measure the pendulum position x_{pend} relative to the ground x_0: $x_{\text{meas}} = x_{\text{pend}} - x_0$. This error signal is processed by a damping controller with transfer function D. Together with the force noise F the resulting feedback signal acts onto the pendulum with a force to displacement transfer function H_F. At the same time the pendulum is driven by the ground noise via the transmissibility H_x. Figure 3.12 can be translated into the equation

$$x_{\text{pend}} = H_F F_{\text{ext}} + H_F D\,(x_{\text{pend}} - x_0) + H_x x_0 \tag{3.13}$$

and resolved for the pendulum position

$$x_{\text{pend}} = \frac{H_F F_{\text{ext}} + (H_x - H_F D)\, x_0}{1 - H_F D} \quad . \tag{3.14}$$

In the case of no driving force $F = 0$ this reduces to the generalized transmissibility

$$\frac{x_{\text{pend}}}{x_0} = \frac{H_x - H_F D}{1 - H_F D} \tag{3.15}$$

while for no ground motion $x_0 = 0$ it can be simplified to the generalized susceptibility

$$\frac{x_{\text{pend}}}{F_{\text{ext}}} = \frac{H_F}{1 - H_F D} \quad . \tag{3.16}$$

3.2.8 *Sensors and actuators for active damping*

Active feedback requires sensors and actuators. To minimize introduced noise, both should work contact free. Optimally, there would be inertial position sensors. In practice, performance must be sacrificed as the payload of a suspension is limited. Therefore, the position is usually measured relative to ground (the implications are described in

chapter 3.2.7). This is accomplished electromagnetically (LVDT, capacitively), or optically by shadow sensors (BOSEM) or interferometrically (Euclid).

The actuation method must provide forces to the suspension without spoiling the performance (i.e. reduce parasitic noise couplings). For strong actuation, electromagnetic actuators (magnet and coil) are commonly used. The magnets are attached to the suspension to avoid wires running to it, which would cause unwanted damping, seismic shortcutting and crosstalk between different degrees of freedom. These magnets are oriented in a way that their overall magnetic moments cancel in the sensitive degrees of freedom. In cases where weaker actuation is required but which are more sensitive in terms of introduced noise, as the lowest mass of a multi stage suspension, either much smaller magnets or a different actuation schemes such as electrostatic forces [54] or radiation pressure [55] are used.

3.2.9 *Translational vs. rotational damping – the radius of gyration*

Six rigid body degrees of freedom require at least six dampers in order to dampen all modes. The question arises, where to apply the dampers. To answer this question, the problem of a six degree of freedom oscillator is divided into six one dimensional oscillators: three translational degrees (usually vertical, perpendicular to the test masses surface and sideways are chosen) and three rotational degrees (either about the principal axes or about the eigenmodes axes).

In a single translational dimension x the equation of motion of a damped harmonic oscillator is

$$F_{\text{ext}} = m\ddot{x} + b\dot{x} + \kappa x \tag{3.17}$$

according to equation 3.2. Its general solution without an external force ($F_{\text{ext}} = 0$) is

$$x(t) = A_x \exp\left(-\frac{b}{2m}t\right)\cos\left(\omega_x t + \phi_x\right) \ , \tag{3.18}$$

where A_x is a given amplitude and ϕ_x is a phase factor, both determined by the starting conditions [56] (eq. 11.17a). For weak damping the eigenfrequency ω_x can be approximated by $\omega_x = \sqrt{\kappa/m}$.

For a torsional damped harmonic oscillator the equation of motion reads similar

$$\tau_{\text{ext}} = I\ddot{\theta} + \Gamma\dot{\theta} + \mu\theta \tag{3.19}$$

with the mass moment of inertia I, the torsional damping factor Γ and the restoring spring constant μ. In this case the general solution without a driving torque $\tau_{\text{ext}} = 0$ is

$$\theta(t) = A_\theta \exp\left(-\frac{\Gamma}{2I}t\right)\cos\left(\omega_\theta t + \phi_\theta\right) \tag{3.20}$$

where the eigenfrequency can be approximated by $\omega_\theta = \sqrt{\mu/I}$. In equation 3.19 the term $\tau_{\text{damp}} = \Gamma\dot{\theta}$ describes the torque exerted by the damping mechanism. In suspension damping, the torque $\tau = rF$ arises from a force F applied at distance r away from the rotation axis. In case the same damper is used for translational as well as for rotational damping, the induced damping matches, the damping force $F_{\text{damp}} = b\dot{x}$ of the linear oscillator from equation 3.17. The local velocity $\dot{x} = r\dot{\theta}$ can be expressed by the angular velocity . Now combining the latter four equations yields

$$\tau_{\text{damp}} = \Gamma\dot{\theta} \stackrel{!}{=} r^2 b\dot{\theta} \tag{3.21}$$

which contains the free parameter r. It turns out that the radius of gyration

$$r_g = \sqrt{I/m} \tag{3.22}$$

is a good choice for this. Mathematically the radius of gyration is the root mean square distance of an object's elements away from a given rotation axis. Physically any body behaves the same in rotation as the one which got the same mass concentrated in a shell at a distance r_g from the rotation axis. Inserting equation 3.22 into 3.21 gives the important result

$$\frac{\Gamma}{2I} = \frac{b}{2m} \ , \tag{3.23}$$

which shows that the decay time in equation 3.18 and 3.20 are the same. Therefore, the ring-down of all the different modes takes the same time, independent of the frequencies of the eigenmodes or other parameters like the mass.

In practice one has to take care to counteract the center of percussion effect. Using only one off-axis damper for a rotational degree of freedom would couple translation and rotation which is highly undesired. Usually two dampers are used on opposite sides of the rotation axis. Sometimes it is beneficial due to the geometry of a suspension to rearrange the dampers (many upper masses are wide to accommodate cantilevers and flat). In the case of the triple suspension described in chapter 4, there are three dampers at the top of the upper mass covering vertical, pitch and roll and only one damper at the side at the height of the roll axis to not introduce roll motion when acting sideways (compare figure 4.4). In this configuration the dampers B and C have to compensate only half of the torque exerted by A. Then according to equation 3.21 they have to be located $r/\sqrt{2}$ away from the rotation axis.

However, when using active damping (see section 3.2.3), all dampers might be moved as far away from the axis as possible. This assures maximal sensitivity in the sensing of rotational degrees of freedom. Lever arm imbalances can be compensated for by different feedback gains easily.

3.3 MODELING A COMPLEX SUSPENSION SYSTEM THE STATE SPACE

Around its rest position any complex suspension system can be simplified as structure of coupled harmonic oscillators. Hence, the compound system is described by multiple coupled quadratic differential equations ([56] equation 11.22a)

$$\mathbf{m}\ddot{\mathbf{x}} + \mathbf{b}\dot{\mathbf{x}} + \boldsymbol{\kappa}\mathbf{x} = \mathbf{F}_{\text{ext}}(t) \tag{3.24}$$

similar to the 1D harmonic oscillator in equation 3.2, but this time in vector notation. They are cumbersome to derive for each degree of freedom of a realistic suspension system [57]. Using a few tricks, they can be simplified:

Each of the 2nd order differential equations can be decomposed into two linear differential equations

$$\begin{aligned} \dot{\mathbf{x}} &= \mathbf{v} \\ \dot{\mathbf{v}} &= -\mathbf{m}^{-1}\mathbf{b}\mathbf{v} \; - \mathbf{m}^{-1}\boldsymbol{\kappa}\mathbf{x} \; + \mathbf{m}^{-1}\mathbf{F}_{\text{ext}}(t) \;\; . \end{aligned} \tag{3.25}$$

When performing a Laplace transform ($\mathcal{L}x(t) \to \tilde{x}(s)$),

$$\begin{aligned} s\tilde{\mathbf{x}} &= \tilde{\mathbf{v}} \\ s\tilde{\mathbf{v}} &= -\mathbf{m}^{-1}\mathbf{b}\tilde{\mathbf{v}} \; - \mathbf{m}^{-1}\boldsymbol{\kappa}\tilde{\mathbf{x}} \; + \mathbf{m}^{-1}\tilde{\mathbf{F}}_{\text{ext}}(t) \;\; , \end{aligned} \tag{3.26}$$

the whole system simplifies to a set of linear algebraic equations. So it is easy to solve in state space. The answer in time domain can be obtained by applying an inverse Laplace transform in conjunction with proper starting conditions. These last steps, however, need to be repeated for any adjustment of the system, driving force or starting conditions.

In proper arrangement,

$$\begin{pmatrix} \mathbf{x} \\ \dot{\mathbf{x}} \end{pmatrix} \to \bar{\mathbf{x}}\,, \quad \begin{pmatrix} \dot{\mathbf{x}} \\ \ddot{\mathbf{x}} \end{pmatrix} \to \dot{\bar{\mathbf{x}}} \tag{3.27}$$

equation 3.25 can be used as A and B matrices of the state space formalism

$$\begin{aligned} \dot{\bar{\mathbf{x}}} &= \mathbf{A}\bar{\mathbf{x}} + \mathbf{B}\bar{\mathbf{u}} \\ \bar{\mathbf{y}} &= \mathbf{C}\bar{\mathbf{x}} + \mathbf{D}\bar{\mathbf{u}} \;\; . \end{aligned} \tag{3.28}$$

The characteristic of this is that the measurable state $\bar{\mathbf{y}}$ is influenced by internal states $\bar{\mathbf{x}}$. These are not observable but predictable from the knowledge of the structure of the system and input $\mathbf{u}$. The A-matrix already contains all the properties of the non-driven system ($\bar{\mathbf{u}} = \mathbf{0}$). Its eigenvectors show the shape of the eigenmodes. The corresponding eigenvalues are the eigenfrequencies of the modes. While [57] sets the direct input to output coupling $\mathbf{D}$ to zero, nonzero values come in handy to simulate sensors measuring for example positions relative to

the driving ground (compare section 3.2.7). The full state space system can be solved only numerically. Matlab contains a lot of built in functionality for such systems, thereby offloading the work of solving the differential equations to the computer. There are fast routines to calculate for example the step response or the spectral response. Even active feedback loops can be simulated effectively by feeding sensor signals $\bar{\mathbf{y}}$ back via force actuators $\bar{\mathbf{u}}$.

4

850 G TRIPLE SUSPENSION DESIGN

Isolating the interferometer from ground noise requires suspended optics (compare chapter 3 for the theory). The design of the RefC suspension system was stimulated by the GEO600 input mode cleaner suspensions. A 100 mm diameter, 50 mm thick mirror has the optimal 2:1 aspect ratio for minimizing substrate thermal noise [58, 59]. Nevertheless a BK7 substrate would limit the RefC sensitivity by Brownian substrate noise (compare figure 5.20) which is why low mechanical loss fused silica mirrors (Suprasil 2 Grade A) are used. Those weigh approximately 850 g each. This size is easier to manipulate and is lower cost compared to several tens of kg masses as used in aLIGO. The suspension system is less delicate than mini-suspensions such as for the 100 g SQL mirrors. The 1 kg class of mirror also results in reasonable inertias to give low frequency rotational resonances.

The upper mass serves as a feedback point for damping internal modes and for slow alignment actuation. A triple system has two more stages below, which efficiently isolate the test mass from unavoidable actuation noise with $1/f^6$ as seen in figure 4.25. Thin steel wires are loaded close to their breaking strength to ensure low suspension thermal noise and high frequency internal violin modes [60]. Well defined bending points are provided by means of wire clamps which are specially hardened to reduce the wear on the long term [61, 62].

The sensitivity of the interferometric readout to vertical motion as well as other degrees of freedom is small. A generic 1:1000 coupling is assumed [63], either directly by means of tilted mirrors or indirectly by mechanical coupling to longitudinal motion in the suspension system. This is equivalent to the $1/f^2$ provided by a single stage at 30 Hz when assuming a resonance frequency of 1 Hz. Therefore only two vertical isolation stages are implemented: one in the very top holding the horizontal suspension point which can be seen in figure 6.2 and one hidden inside the upper mass consisting of two relatively long cantilevers each. Those are pre-curved during manufacturing to flatten out perfectly in their loaded state, providing optimal decoupling from the horizontal isolation. Their triangular shape ensures a homogeneous stress distribution along the cantilever. The artificially aged maraging steel (Marvel18) has extremely low creep noise [64]). For protection against environmental influences, especially hydrogen embrittlement,

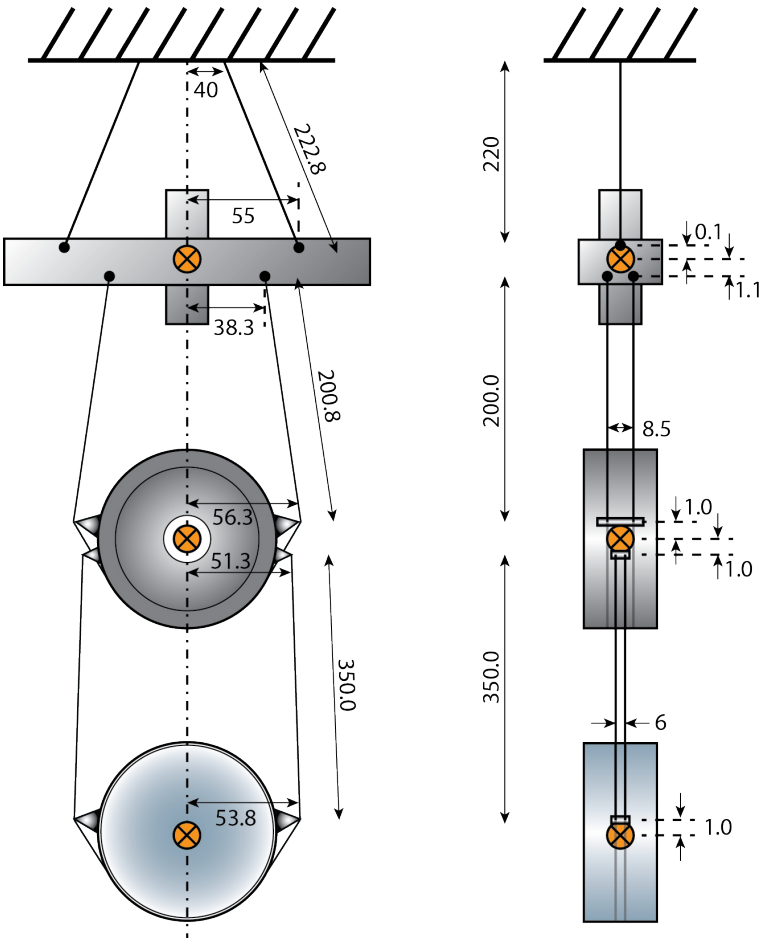

Figure 4.1.: The geometrical design measures of the 850 g triple suspensions as encoded in the function `build_pend.m` are visualized for ease of use (the effective values, e.g. effective bending point of wires differ). Vertically isolating cantilevers are not depicted for graphical simplicity. All of them were slightly ($< 10\%$) reshaped (plastically deformed by hand) to level out under the nominal load. Suspension wire lengths and positions inside clamps are defined by jigs to better than 0.1 mm during the assembly. The positions of wires on the break-off prisms had to be adjusted by eye and might deviate by 0.5 mm. Each suspension chain is designed to be almost symmetrical about two planes: the one parallel to the mirror surface through the masses' centers and the other orthogonal to the mirror surface through the masses' centers. Only the upper mass deviates from this due to the nested cantilevers inside. The biggest unknowns are the position of the intermediate stage break-off point inside the upper mass; the deflection of the cantilevers strongly depends on the load. Also the height of the upper masses center of mass is uncertain; additional ballast was added in order to level out the upper stages cantilevers.

their surface is protected with a nickel layer. The blades were tested in an FEM simulation. As a side-product, their internal modes are simulated as well (see chapter D.9). In future, the internal modes of the blades might need additional eddy current damping. Finally the shape of the blade was EDM cut from sheet material and annealed in the pre-bent state.

quantity	symbol	design value
total effective length	l_{total}	774.2 mm
total mass	m_{total}	2714 g
upper mass	m_{upper}	995 g
intermediate mass	m_{interm}	873 g
lower mass	m_{lower}	846 g
upper stage wire diameter	d_{upper}	152.4 µm
intermediate wire diameter	d_{interm}	101.6 µm
lower stage wire diameter	d_{lower}	55.2 µm
vertical stiffness top stage	k_{top}	$2 \cdot 60.5$ N/m
vertical stiffness upper stage	k_{upper}	$2 \cdot 137$ N/m

Table 4.1.: Summary of the key triple suspension parameters

The dimensions of the suspension (see figure 4.1 and table 4.1 for the key parameters) define their resonance frequencies. Using a full state space model, an effective energy transfer from the test mass to the upper mass was ensured. Passive damping for pitch was not sufficient for this suspension as the dimensions wouldn't allow for a sufficiently long lever arm (compare chapter 3.2.9). The employed active damping comes at the drawback of increased complexity as described in section 4.5 but also at the benefit of knowledge about the upper mass' orientation and the ability to redistribute noise out of the detection band.

Four equal triple suspension system were built for the RefC: three mirror suspensions (RC1a, RC2a, RC2b) and one optional reaction pendulum (RC1b). The latter is reserved to be installed closely behind RC1a which posed constraints for the design of the whole suspension chain. It can be used as a suspended actuation point in order to introduce less noise when actuating onto the test mass directly for fast control.

Two more identical suspensions (TNI-A, TNI-B) were built for the TNI and another one (TNI-C) prepared as reaction pendulum. A comparison of the different suspensions is presented in table 4.2.

The first built suspension of this kind, called the *toy model*, was never cleaned for in vacuum use but mainly used for easily accessible damping tests. Another, very similar suspension was built in collaboration with the *modern controls group* at the AEI [65] to investigate modern feedback loop design on a not fully observable MIMO system, i.e. not all degrees of freedom can be sensed. Here the state space model is not

used a priori but might be used for the physical interpretation of the controller in the end.

4.1 DEGREES OF FREEDOM

Each rigid body has six degrees of freedom. In suspension applications they are usually called

- longitudinal along the optical axis or normal to a mirror surface
- vertical along with the gravitational acceleration
- sideways, horizontally transverse to the mirror normal
- pitch (or tilt) around the sideways-axis, pointing a reflected beam up or down
- yaw around the vertical axis, pointing a reflected beam sideways
- roll, around the longitudinal axis, having the least influence onto a beam

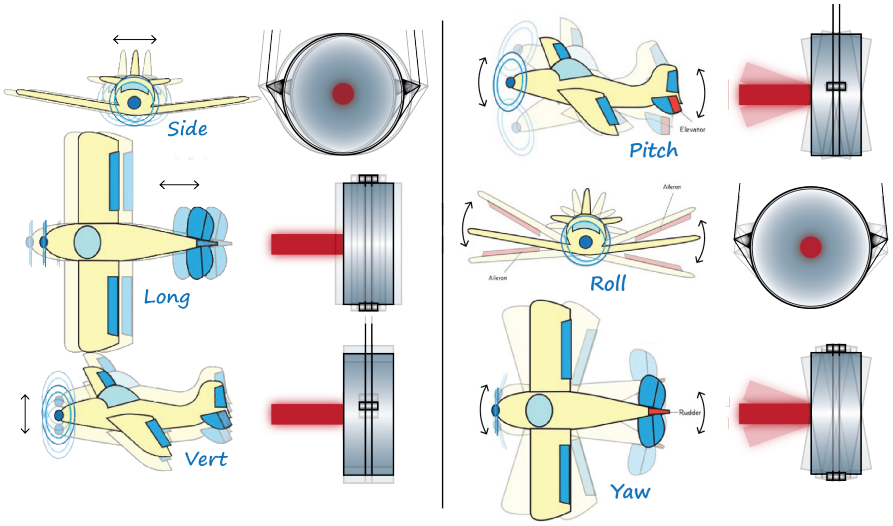

Figure 4.2.: A rigid body has six degrees of freedom, three translational (left) and three rotational (right). For a suspended mass these are the same as for an aircraft. They are aligned related to a specific geometry, usually along the principle axes of inertia: pitch rotates around the sideways axis is moving the reflected beam up and down, roll rotates around the longitudinal axis which shows the least (optimally no) influence onto the reflected beam and yaw rotates around the vertical axis which tits the beam sideways.

In a system of coupled pendulums, the individual modes couple to each other. In mirror suspensions this coupling is enforced specifically in order to obtain a well dampable system. The degrees of freedom, however, are kept well separated from each by the construction. This reduces

the influence of not perfectly damped modes onto the readout, which is by definition only sensitive to longitudinal mirror motion. Usually a parasitic coupling of 1:1000 from other degrees of freedom into longitudinal is assumed [63], either by direct influence onto reflected phase via imperfect mirror alignment or by residual coupling to longitudinal mirror motion.

4.2 EIGENFREQUENCIES AND EIGENMODES

Each oscillator has natural frequencies, the eigenfrequencies. In a system of coupled oscillators, the individual modes couple and result in eigenmodes. If an eigenmode of a weakly damped system[1] is excited, then the oscillators either move in phase with the excitation or exactly out of phase (180° shifted). The equations of motion for the individual masses are

$$\mathbf{x}(t) = \mathbf{A}_0 \exp\left(\frac{-\omega_0}{2Q}t\right)\sin(\omega_0 t) \ . \tag{4.1}$$

The amplitudes $\mathbf{A}_0$, may be different and even negative for some of the participating oscillators. But the characteristic frequency ω_0 and the damping Q are inherent properties of the eigenmode.

4.3 OBSERVED RESONANCE FREQUENCIES

A comparison of all suspensions in use is shown in table 4.2. The undamped eigenfrequencies can be identified in transfer function measurements as shown in figure 4.23. The frequencies are then measured exactly in spectra of long time series without damping and compared to the initial model. One finds that roll modes and the differential yaw modes are softer than expected. This is actually beneficial as a lower resonance frequency results in more attenuation in the detection band. For the fundamental roll mode, the non-flatness of the cantilevers matters the most (see figure 4.1). Most of the other frequencies match extremely well within each suspension series (TNI with compound test masses vs. RefC with bulk mirrors). The cantilever design was changed during the suspension assembly phase (after modeling) which resulted in a slightly stiffer stage and thereby additional required mass. This causes a softer differential roll and vertical mode. The most reasonable explanation for differential yaw softness is the lateral compliance of the upper mass blades, although it is included in the state space model in principle.

1 Weakly damped means that the damping force is negligible against the restoring force

	model	TNI-A	TNI-B	RC1a	RC2a	RC2b
long	0.64	0.63	0.63	0.64	0.64	0.66
	1.39	1.37	1.38	1.38	1.38	1.37
	2.59	2.58	2.58	2.55	2.54	2.54
pitch	0.98	0.75	0.86	0.82	0.79	0.61
	1.88	1.80	1.68	1.76	1.76	1.79
	5.20	5.42	5.68	4.97	5.02	4.98
roll	2.26	1.54	1.58	1.06	1.08	1.05
	9.12	3.67	3.90	3.89	3.65	3.63
	26.54					
side	0.64	0.64	0.64	0.64	0.64	0.63
	1.39	1.37	1.38	1.41	1.44	1.43
	2.61	2.59	2.59	2.54	2.53	2.54
vert	1.24	0.99	1.02	0.99	1.01	0.98
	4.07	3.88	3.90	3.70	3.73	3.76
	18.62					
yaw	0.97	1.02	1.03	0.84	0.84	0.81
	2.30	1.86	1.85	1.61	1.60	1.59
	5.55	3.17	3.16	3.10	3.11	3.06

Table 4.2.: The resonance frequencies of all used triple suspensions are shown. They are in good agreement with each other, especially within the individual productions runs (RefC and TNI suspensions were assembled at different times). The table also shows the limits of suspension modeling by means of the non-fitted design parameters. Recent works went into system identification in order to adjust the model to actual suspension systems [66].

4.4 support structure: the cage

As a suspension is usually hung from above, it requires a support structure for the suspension point. This should be stiff in order to have its eigenmodes in a frequency range where the suspension's filtering is efficient. This was ensured by adding cross-braces and checking by measuring impulse responses at various points of each structure.

At the same time the cage needs to be light-weight with a small footprint. The RC2 cage is designed to host two suspensions under 45° angle of incidence. The RC1 cage is suited for two suspensions as well: The mirror RC1a under 0° and a potential reaction pendulum RC1b behind. The RC2 cage is slightly bulkier in comparison to benefit from common mode rejection despite of the rather large suspension distance.

In addition to simply supporting the suspensions, the structures also mount safety catchers, shown in figure 4.3 and 4.4. These hold the masses in case of wire failure and provide end stops in case of excess

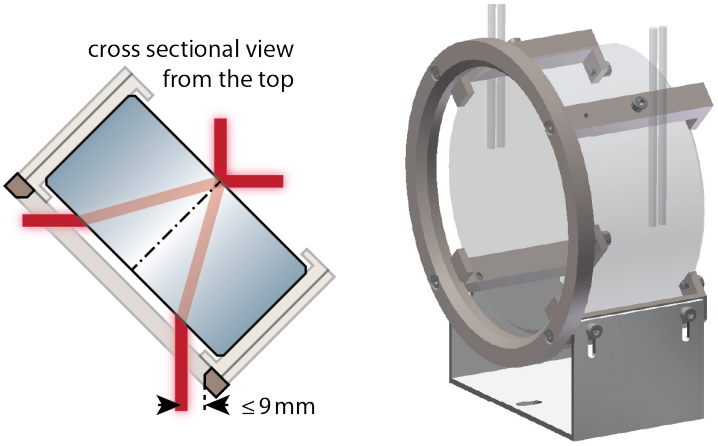

Figure 4.3.: Safety structures reduce the motion range of the suspended masses in case of excess table motion. They prevent the mirrors from falling down and breaking in the case of a suspension failure and Furthermore, serve as a locking structure for the suspension. On RC1a additional coils for test mass actuation are mounted onto the ring (not shown). On the 45°irrors RC2a and RC2b, they limit the clearance for sideways motion of the laser beam to a few mm.

excitation for example due to 'table quakes'[2]. The upper mass catcher is significantly more elaborate than the others. It also defines the positions of the shadow sensor assemblies described in the next section and therefore requires full 6D tunability.

4.5 LOCAL DAMPING & CONTROL

Any internal mode of a mirror suspension system couples to the longitudinal degree of freedom which is read out by the interferometer and thereby requires controllability. The term 'local' comes from the fact that only local information is processed in contrast to global approaches, such as global damping [66]. In this case, the more sensitive interferometric readout is used to replace the position signals of selected degrees of freedom, usually differential longitudinal motion of the suspension chain. For local damping there are two main schemes.

Passive damping introduces artificial, usually velocity proportional losses (compare figure 3.4). The geometry of the described suspension does not allow for efficient eddy current damping (see chapter 3.2.9). As it was designed rather thin to allow for a close-by reaction pendulum and the short TNI, the maximally feasible lever arm especially for pitch damping is too short. An extension in the vertical towards a cross-structure might have circumvented this.

2 Excess table motion due to strong external excitation or internal malfunction of feedback loops.

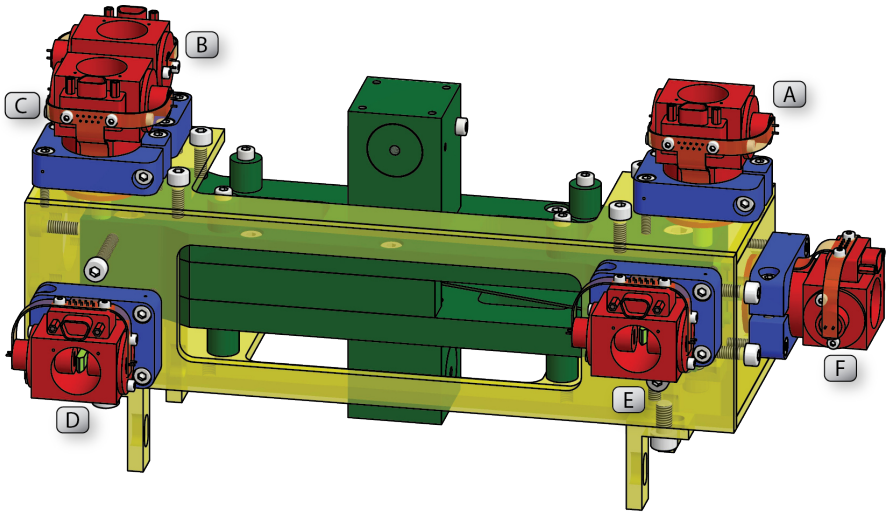

Figure 4.4.: The upper mass (dark green) with the shadow flags (light green) attached is freely movable. The catcher (transparent yellow) is attached to the frame and moves together with ground. It serves as end stop for suspension motion (screws as stoppers) and fixes the shadow sensor/actuator assemblies (BOSEM, red) named with Latin letters A..F in place. The catcher is coarse aligned to the required upper mass alignment (approx. mm precision). Axial fine tuning of the BOSEMs is accomplished by means of clamps (blue).

Active damping, in contrast, measures the suspension's position relative to local ground and feeds it back by means of an active servo. This method allows for less constraints in the choice of actuator positions and an almost arbitrary feedback shape, especially feedback noise suppression in the detection band (compare chapter 3.2.3). Furthermore, the sensors give valuable information about the suspension's orientation for cavity alignment.

For the local readout, shadow sensor units from a pre-production run for Advanced LIGO were obtained from the University of Birmingham. The readout scheme and electronics are described in the following sections. Space constraints (compare figure 4.4) require a custom support structure accompanying the readout unit, a compact actuation coil and the axial adjustment mechanism. This structure defines the work position of the flag and the distance to the coil as required by figure 4.20. See figure 4.5 for the reduction in size compared to the Advanced LIGO version. In the next sections the sensing mechanism and the readout are explained. Right after that, the actuation principle and the developed electronics are described.

3 Optimally it would be called differently (sOSEM?), but in most respects other than the mounting and the size is held compatible with its larger brother.

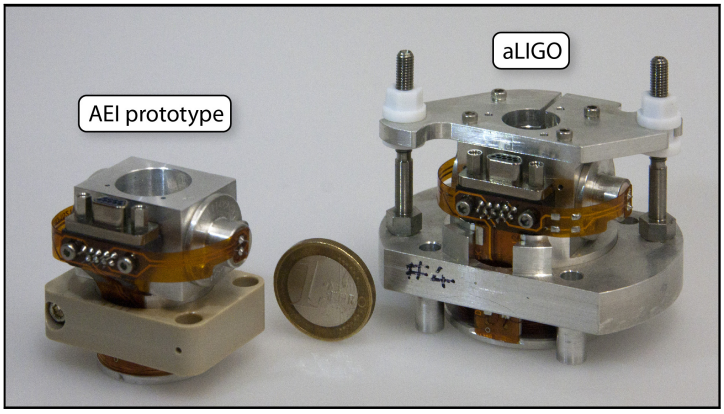

Figure 4.5.: Limited physical space around the 850 g triple suspensions and different actuation required a re-engineering of the shadow sensor assembly six of which are used for active damping of each suspension's resonances. The aLIGO BOSEM [31, 67] (right) uses the same readout unit (PD, LED, connector) as the reduced Small BOSEM on the left.[3]

4.5.1 *Shadow sensor – BOSEM sensing units*

Active damping and reproducible alignment of a complex suspension system require knowledge about its position and or state of motion. It was shown in the past that this information can be obtained by shadow sensors at the uppermost stage of a suspension chain [68, 69, 70]. A small, opaque object, the so-called flag, is mounted to the suspended mass. The active part of the sensing unit consists of an LED (sending unit) and a single element photodiode (receiving unit). It is usually mounted to the suspension's support structure, the cage. Dependent on the position of the suspension relative to the sensing unit, the flag pushes into or retracts from the beam path between LED and PD. Over a large fraction of the sensors range, a linear relation between position and current through the reverse-biased PD is obtained. A clear advantage of this readout method is that there is no connection between the suspended mass and the ground whatsoever[4]. Also the flag usually can be lightweight. The advantages of a shadow sensor come at the disadvantage of measuring only the position relative to ground (recall figure 3.5).

In the following, the sensing unit delivered by the University of Birmingham is described in more detail. The units are UHV compatible. Their emitter and sensors properties are summarized in table 4.3. A lens integral to the OPTEK IRLED (OP232) narrows the output. It is further collimated by a dedicated lens. A slit of 1.4x4.5 mm size serves as aperture to block the less homogeneous sections of the beam and cut away light, which could spoil the detection due to multiple reflec-

4 In comparison, cables running to accelerometers or LVDTs are mechanically lossy and therefore cause nonzero transmissibility and suffer from hysteresis

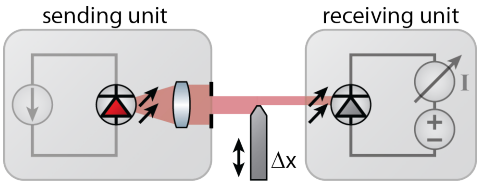

Figure 4.6.: An LED is driven by a constant current. The light is collimated by a lens. The non-homogeneous outer part of the beam is filtered out by an (rectangular) aperture to give a flat top beam. The light is sensed by a reverse biased photodiode. The native point of operation is in the half-light position, i.e. when the flag shades half of the light. Around this operation point the detected power is directly proportional to the obstruction due to an opaque object, the flag, mounted to a suspension and shading the light.

IRLED (OP232)
TO46 Kovar Package
Hermetically sealed
Peak emission = 890 nm
Maximum forward current = 100 mA
Operating forward current = 0.35 mA
Maximum radiant power = 8 mW (at 100 mA)

Photodiode (BPX65)
TO-18 Steel Package
Hermetically sealed
Peak sensitivity = 850 nm
Responsivity = 0.56 A/W (at 890 nm)
Responsivity 0.15 A/W (at 1064 nm)
Dark Current = 5 nA

Table 4.3.: The key specifications of the BOSEM sensing unit as taken from [31] and the [71, 72].

tions or scatter processes. The detection photodiode does not contain further optics but senses, how much of the light is shaded by the flag. Originally the flags were round rods and later had flats on their sides [73]. In the current design, the tip is angled as shown in figure 4.6 so that reflected light can not travel exactly the same way back which would increase the risk of multiple beam paths. The flag is made of aluminum and is sandblasted to reduce reflections. The power on the photodiode and therefore the current through it

$$I_{\mathrm{PD}}(\Delta x) = \Delta x \cdot \frac{I_{\max}}{\Delta x_{\max}} \tag{4.2}$$

is proportional to the flag position Δx. This equation is assumed to hold over a linear range $\Delta x_{\max}$ which is typically short of a millimeter (compare figure 4.7). The maximum current through the photodiode is on average 62.5µA. It is checked for every single BOSEM unit and together with the $\Delta x_{\max}$ used to calibrate the sensors in units of meters.

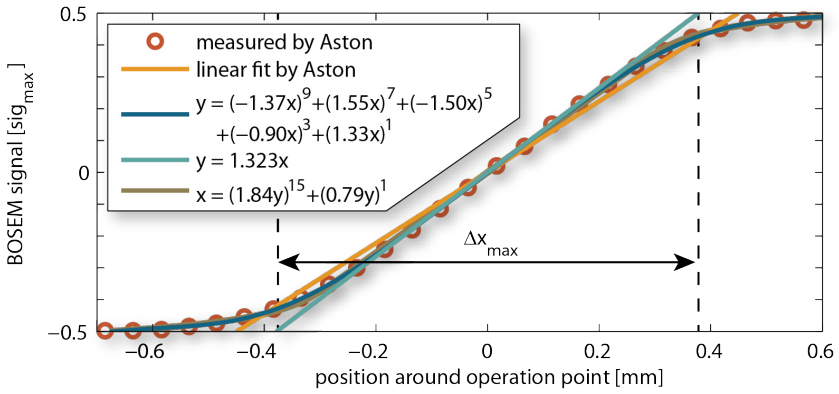

Figure 4.7.: The BOSEM photocurrent vs. flag position was characterized by Aston [31]. A ninth order fit with odd exponents is added, where $\tilde{x} = x - 0.735$ to symmetrize the problem around the working point. The linear approximation agrees very well in the central 0.5 mm. Under the assumption that a slope (gain in feedback) error of 2 is tolerable, the linear range is 0.75 mm wide. The signal could be linearized by applying the inverse function. However, this is difficult to calculate analytically. A fit yields e.g. $x = (1.184 \cdot \tilde{y})^{15} + (0.79 \cdot \tilde{y})^1$ where $\tilde{y} = y - 0.511$. Beyond the interval y=[0,1] the function must be set to the function value of the boundary values!

The linear range, however, was defined [31] in a way that the slope of the measured response must not be off by more than a factor of two. In degree of freedom damping mode (see chapter 4.5.15) this can already cause large cross couplings or even instabilities. An approach to circumvent this is to fit the inverse of the position response relation (brownish graph in figure 4.7). Applying the correction is relatively easy in a digital control system.

The linearization of the BOSEM response can provide stability of damping loops over a wider range. On the other hand it comes with drawbacks: As the slope of the BOSEM signal per flag displacement goes to zero asymptotically, the inverse function goes to infinity so that noise in the linearized signal increases dramatically in this region. This can be circumvented by holding the position value constant beyond some detected BOSEM signal (say ±0.45). As velocity damping is proportional to the slope, it would not be smooth at the transition. This could cause kicks by the damping loop so a better option might be to approximate the response by a linear function beyond the range, if necessary.

Furthermore, the linearization relies on a fixed open light signal. In reality the optoelectronics will degrade. In particular, the LED's efficiency changes with temperature and time (see figure 4.26). This will cause the described error signal linearization to be less trustful at the open light signal end of range.

4.5.2 *Shadow sensor – readout*

Shadow sensors are extremely sensitive and have a relatively high dynamic range. But the motion on top of the SAS tables is close to the ultimate (shot noise limited) sensitivity of the current generation OSEMs across a substantial frequency range. Also the control and data system has a limited dynamic range. The active damping loops provide feedback in the few Hertz region. In the closed loop, any kind of readout noise will inject energy into the suspension system. This makes it especially challenging to build low noise readout and actuation electronics. Therefore the most important noise sources were simulated in order to design a circuit fulfilling the requirements. The requirements for the individual building blocks were set to 1/10th of the 'fundamental' BOSEM sensitivity shown in table 4.4 and figure 4.8. Either the noise sources need to be projected into displacement sensitivity or the fundamental sensitivity is expressed relative to the maximal linear range.

As a simplified example, power output is proportional to the LED current which thereby linearly enters into the measured position. The thermal noise of the 56.2Ω current sensing resistor equals $\sqrt{S_{\mathrm{therm}}} = \sqrt{4k_{\mathrm{B}}T}\sqrt{R} = 0.96 \cdot 10^{-9}\,\mathrm{V}/\sqrt{\mathrm{Hz}}$. The DC current of 35 mA through it causes a DC voltage drop of 2 V. Then the relative thermal noise $\sqrt{S_{\mathrm{rel}}} = \sqrt{S_{\mathrm{therm}}}/U_{\mathrm{DC}} = 5 \cdot 10^{-10}/\sqrt{\mathrm{Hz}}$ can be projected into a displacement spectral density using

$$\sqrt{S_{\mathrm{disp}}} = \sqrt{S_{\mathrm{rel}}} \cdot \Delta x = 3.5 \cdot 10^{-12}\,\mathrm{m}/\sqrt{\mathrm{Hz}} \ .$$

4.5.3 *Shadow sensor – fundamental sensitivity*

The fundamental sensitivity limit of a shadow sensor is given by shot noise. This arises from the uncorrelated occurrence of photons which are converted into electrons inside the photodiode. The single sided linear spectral density

$$\sqrt{S_{P_{\mathrm{PD}}}} = \sqrt{2h\nu P_{\mathrm{PD}}} \ , \tag{4.3}$$

where h is Planck's constant and ν is the laser frequency. This can be converted to an equivalent photocurrent

$$\begin{aligned} I &= R \cdot P \\ &= \eta \frac{e}{h\nu} \cdot P \end{aligned} \tag{4.4}$$

by means of the PD responsivity R. The equivalent photocurrent noise

$$\begin{aligned} R\sqrt{S_{I_{\mathrm{PD}}}} &= \sqrt{2eRI_{\mathrm{PD}}} \\ \sqrt{S_{I_{\mathrm{PD}}}} &= \sqrt{\frac{2e}{R}I_{\mathrm{PD}}} \\ &= \sqrt{\frac{1}{\eta}2eI_{\mathrm{PD}}} \end{aligned} \tag{4.5}$$

is increased by the inverse of the square root of the quantum efficiency $\eta \approx 0.78$, so by about 13%, when compared to Schottky's formula for the photocurrent. In particular, the shot noise level is $\sqrt{S_{I_{\mathrm{PD}}}} \cdot 120\mathrm{k}\Omega \cdot 2/21000\,\mathrm{V/m} = 58\mathrm{pm}/\sqrt{\mathrm{Hz}}$, where 2 resembles the differential sender gain and 21000 V/m is assumed as average BOSEM responsivity. As verification, the relative noise $\sqrt{S_{I_{\mathrm{PD}}}}/I_{PD} = 5.1\mathrm{pA}/\sqrt{\mathrm{Hz}}/62.5\,\mu\mathrm{A} = 8.2 \cdot 10^{-8}$ can be calibrated as displacement noise. The total BOSEM range of 0.7 mm leads to a position noise of $57\mathrm{pm}/\sqrt{\mathrm{Hz}}$ which is in good agreement with the first result.

To improve the shot noise limited performance, higher power LEDs could be used. Yet this would come at the drawbacks of worse technical noise performance and heating. Illuminating the PD with more light might also be possible but would probably result in a less homogeneous power distribution and Hence, in a less linear readout. The actual sensitivity of a shadow sensor is strongly dependent on the supply and readout electronics. Figure 4.8 gives an example for BOSEM units produced in Birmingham in conjunction with original aLIGO electronics [74]. The measurements are summarized in a standard sensitivity given in table 4.4.

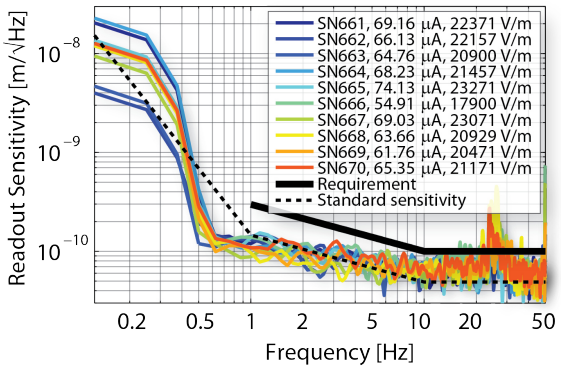

Figure 4.8.: A slightly modified version of the sensitivity plot of a variety of BOSEM units taken at the University of Birmingham [31] is shown. The legend shows the open light current and the corresponding calibration. Although the low frequency bump is probably an artifact, it was included into the deduced standard sensitivity shown as dashed curve, which is specified in table 4.4.

At high frequencies the readout is dominated by shot noise. In the mid frequency band below ≈ 10 Hz the noise has a $1/\sqrt{f}$ slope which

is probably dominated by the drive/readout electronics. Below 0.5 Hz the observed noise increases drastically. This could be a measurement artifact as not much effort was put into optimizing the performance at these frequencies [75] – the aLIGO requirement ends at 1 Hz.

frequency range	sensitivity @ 1 Hz	slope
$<0.5\,\mathrm{Hz}$	$1.5\cdot10^{-8}\,\mathrm{m}/\sqrt{\mathrm{Hz}}$	$\left(5\cdot10^{-2}\,\mathrm{Hz}\right)^2/f^2$
$<5\,\mathrm{Hz}$	$1.5\cdot10^{-10}\,\mathrm{m}/\sqrt{\mathrm{Hz}}$	$\sqrt{5\cdot10^{-1}\,\mathrm{Hz}}/\sqrt{f}$
$>5\,\mathrm{Hz}$	$5\cdot10^{-11}\,\mathrm{m}/\sqrt{\mathrm{Hz}}$	const.

Table 4.4.: From figure 4.8 a standard sensitivity for the BOSEM sensors was deduced. This serves as requirement for electronic noise in the BOSEM readout described in the next few sections.

4.5.4 *Shadow sensor – readout electronics*

As mentioned before, the sensed position is directly proportional to the optical power sensed by the PD. Each triple suspension built uses six shadow sensors. Since all the LEDs require the same current, it was decided to connect them all in series. This way only a single highly stable current source is required, while the increased voltage drop of $\approx 6\cdot1.2\,\mathrm{V}$ must be taken into account. As a drawback of this 'daisy chaining' the sensing of a whole suspension breaks down if one LED fails.

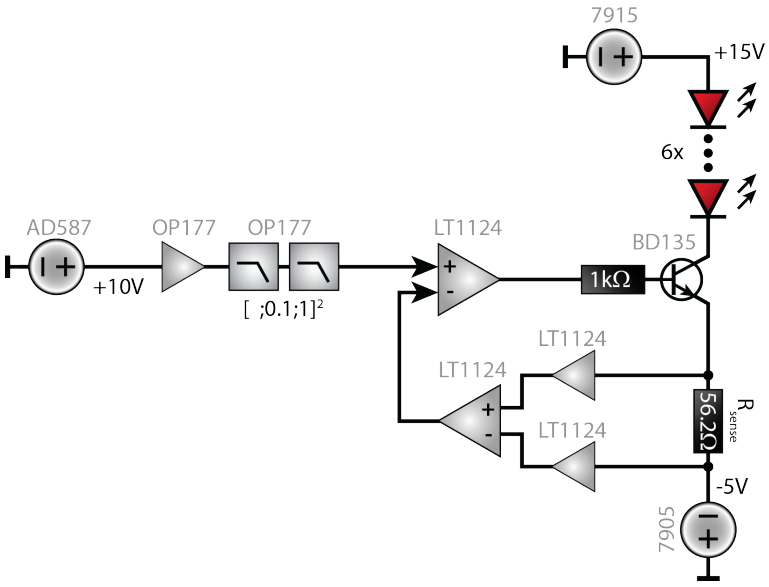

Figure 4.9.: The shadow sensor LEDs are supplied with a highly stable current by an active stabilization scheme. The voltage drop across the 56.2Ω resistor is matched to the noise-filtered 10 V voltage reference.

Inspired by the LIGO and GEO600 driving/readout scheme [76, 74] an active current stabilization scheme is used. The current through the LEDs (set current 35 mA) is regulated by an NPN transistor and measured by means of a shunt resistor. This resistor should have low flicker noise such as the Vishay Beyschlag MMA0204 0.1% [77] since standard of the shelf thick film resistors would limit the sensitivity. A differential amplifier made up from LT1124s measures the actual voltage drop across the 56.2Ω resistor. A comparator then matches it with a highly stable 2 V reference. The output serves as control signal for the transistor. The 2 V originates from an AD587 10 V reference. This is second order low pass filtered above 0.1 Hz for improved 'high frequency' stability and divided by a factor of five for even further improved noise characteristics using a low noise OP177. As a backup for malfunction, a 50 mA fuse is added in series to the LEDs which is not shown in figure 4.9.

The photodiode is biased and read out with a transimpedance amplifier. This readout mode provides large dynamic range and is less susceptible to noise coupling in the long cable than a photovoltage readout. The bias source can be chosen via a jumper: either -15 V from a 7915 voltage stabilizer or -10 V from the AD587 voltage reference originally used for the LED drive. No differences in terms of sensitivity could be observed so far. The transimpedance amplifier consists of an OP177 in conjunction with a 120kΩ low flicker noise resistor. The resistor was chosen in a way that with the worst expectable photocurrent of 80 µA (nominally 62.5 µA), the output voltage of 9.6 V (nominally 7.8 V) is still within the ADC range of CDS (equivalent to 10 V at this point of the readout). Furthermore, this first readout stage incorporates a low-pass filter at 6 kHz as there are no signals whatsoever expected at high frequencies in the shadow sensors (actually this frequency might be reduced if required from the rms point of view). After the transimpedance amplifier the signal is split into two paths: DC and whitened.

The DC path consists of a standard sending stage which is now being used in many other Prototype's electronics. It is built discrete and symmetric to fit the needs of low noise fully differential sending. The frequency response is white up to the low-pass corner at 10 kHz and has a gain of two to match the 10 V single sided signal to the CDS's ADC range of ±20 V differentially. With the 180Ω output impedance it is pretty much safe against output shorting (≈45 mA) while maintaining the exact gain of 2. Another sender output impedance could be added (e.g. to deal with signal reflections), which was not required yet. An additional feature is the input offset cancellation: resistors are chosen to match the voltage drop from parasitic opamp input currents in both inputs. The latter would cause thermally drifting offsets which causes low frequency noise. The cancellation scheme comes at the expense of a factor of $\sqrt{2}$ increased opamp current noise which is not limiting in any way.

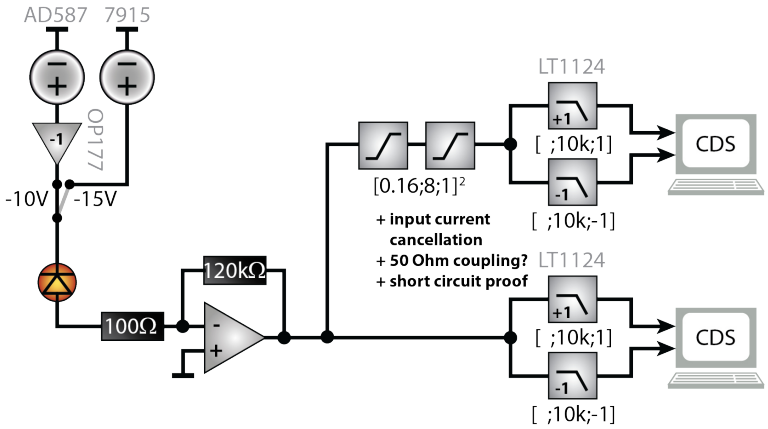

Figure 4.10.: A transimpedance amplifier converts the maximal 65 µA of photocurrent into a voltage. There are two readout paths. One with a white transfer function, one with a strongly frequency dependent response to whiten the signal (boost it above ADC noise). Both signal paths provide fully differential low noise signal sending.

In the whitened path, filters are employed to effectively increase the limited dynamic range of the ADCs/DACs. The shadow sensors are used to read suspension motion relative to the 'ground' (in this case the SAS surface). Almost all suspension motion is injected by ground motion passing through the SAS. As the SAS isolates beyond its resonance frequencies on the order of 0.1 Hz with a $1/f^2$ decay and seismic motion also goes down, less motion is expected above this frequency. A second order 0.16 Hz zero accounts for that. Above 8 Hz the sensor noise floor is well above the ADC noise, so a second order pole at 8 Hz levels the filter off. Another pole at high frequencies (1.06 kHz) attenuates the part of the spectrum, where no signals are expected. The output of the whitening stage is sent to CDS via another differential stage, identical to the one in the DC path.

One driver/readout combinations processes the information of six shadow sensors each.

4.5.5 *Shadow sensor – calibration: open light test*

In the aLIGO project every single BOSEM readout unit is characterized individually. The comparison in figure 4.13 shows, however, that the different readout units have very similar characteristics when normalized to the same open light voltage. This is the state, where the flag is removed completely.

From the legend in figure 4.8 it can be seen that the calibration divided by the open light current is almost the same for all BOSEMs tested (±0.5%). This lead to the following calibration method based on Aston's figure 3.23.

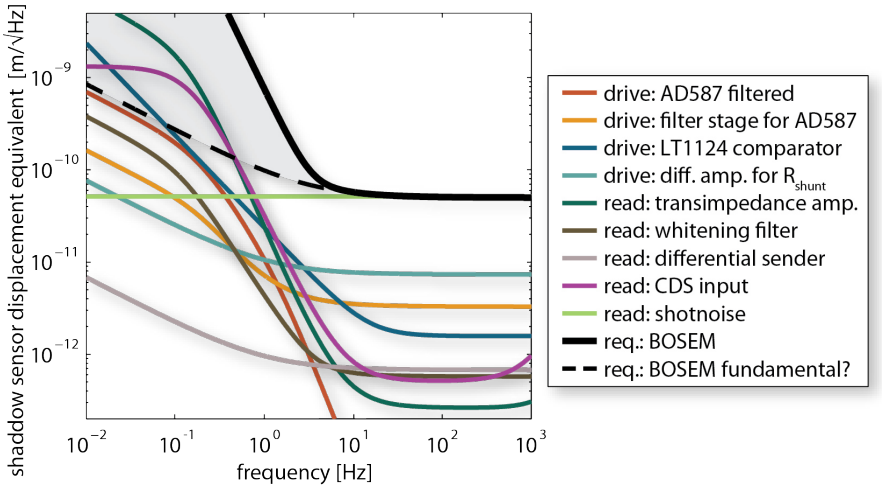

Figure 4.11.: The BOSEM sensitivity given in [31] is approximated by a standard sensitivity as shown in figure 4.8. The AEI readout electronics are based on a mixture of aLIGO (with less readback options but improved performance) and GEO600 electronics (with improved performance and CDS readout added). They are designed to stay well (10 times) below the requirement (given noise curve). All noise terms are simulated using the LISO [78] plug-in for Cadsoft EAGLE and projected into read out position noise via the whitened path. 'Drive' items refer to building blocks for the constant current LED driver, 'read' items to photodiode readout blocks. It follows that the low frequency noise in figure 4.8 is not necessarily caused by a too small measurement bandwidth but maybe caused by a lack of low frequency filtering capabilities.

The response is assumed to be linear across a range of 900 µm. With an open light voltage of 19.7 V this gives a calibration of 45.7 µm/V or 21900 V/m which is in excellent agreement with the mean value of 21400 V/m from the legend of the sensitivity plot. This calibration was applied to all BOSEM units: The flag is removed either physically or by pushing the upper mass out of the sensing unit. The sensed flag position is then calibrated to 900 µm by a digital calibration filter.

It was realized only later that the BOSEMs are required to be in the linear regime in order to obtain optimal degree of freedom sensing and Hence, damping, which is described in the following sections. Yet the calibration described above, takes an average slope across the 'almost linear' range. For optimal comparability with other sensors, it might be better to calibrate to the actual slope around half light. From the fit in figure 4.13 the slope of the normalized signal can be determined to be 1.21 /mm which is 23800 V/m in Aston's units. Then the open light voltage must be calibrated to a smaller value of 825 µm.

The open light voltage calibration will be carried out subsequently on one suspension at a time. The changes in the required damping strength are negligible. With the new calibration, better measures

for e.g. table tilt can be obtained. This comes at the drawback of new set positions for the upper mass positions in order to achieve an aligned cavity. It is advised to recalibrate regularly when possible as the BOSEM sensitivity was observed to degrade over time (see figure 4.26).

4.5.6 *Shadow sensor – sensing matrix*

The shadow sensors are distributed around the upper mass (compare figure 4.4) in a way that their signals can be separated into specific upper mass degrees of freedom. The scheme described in this section requires well calibrated sensors. The method is described in the last section.

Then linear combinations of the sensors give the upper mass motion in its degree of freedom (DOF) system.

$$\mathbf{x}_{\mathrm{dof}} = \boldsymbol{M}_{\mathrm{sense}} \cdot \mathbf{x}_{\mathrm{shadow}} \tag{4.6}$$

A method to find $\boldsymbol{M}_{\mathrm{sense}}$ is required: imagine a pure DOF motion, e.g. in *long* (or any other base vector of $\mathbf{x}_{\mathrm{dof}}$). Now find out in which sensors it causes a signal. The sign and the lever arm around the rotation axis are the important measures. Every single shadow sensor is sensitive to up to two rotational DOFs (the other one(s) appear(s) as sideways motion of the flag). Therefore one has to assume that the shadow sensors are only sensitive to motion along the flag axis and not to transverse motion. No sign of invalidity of this assumption has been found so far, unless light is passing by the side of a flag due to upper catcher misalignment.

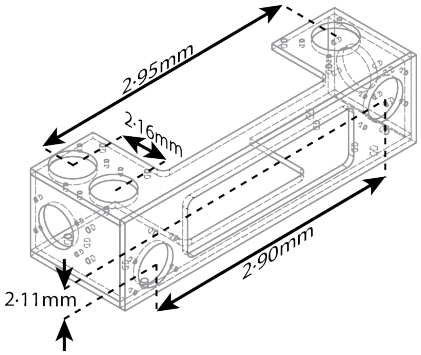

Figure 4.12: The flag positions are set by the upper mass. They are symmetric about the principle axes of rotation. The length of the lever arms determine the angular readout sensitivity and the exerted torque of the co-located coil magnet combination.

The geometry of flag placements was chosen in a way that the signals separate well into DOF signals. For rotational degrees of freedom one has to calculate the lever arms: project the flag position to a plane through the rotation axis and normal to the flag axis (in other words calculate the smallest distance of flag axis and rotation axis. There is always a set of two sensors equally far apart from the rotation axis but on opposite sides (see figure 4.12).

The sensor signal is divided by its according lever arm. Then the rotational as well as the translational signals are weighted according to the contributing sensors. The obtained sensing matrix

$$\boldsymbol{M}_{\text{sense}} = \begin{array}{c} \\ \textbf{long} \\ \textbf{pitch} \\ \textbf{side} \\ \textbf{roll} \\ \textbf{vert} \\ \textbf{yaw} \end{array} \begin{array}{c} \begin{array}{cccccc} \textbf{A} & \textbf{B} & \textbf{C} & \textbf{D} & \textbf{E} & \textbf{F} \end{array} \\ \begin{pmatrix} 0 & 0 & 0 & 0.5 & 0.5 & 0 \\ 0 & 31.25 & -31.25 & 0 & 0 & 0 \\ 0 & 0 & 0 & 0 & 0 & 1 \\ 5.264 & -2.632 & -2.632 & 0 & 0 & 0 \\ 0.5 & 0.25 & 0.25 & 0 & 0 & 0 \\ 0 & 3.819 & -3.819 & 5.556 & -5.556 & 0 \end{pmatrix} \end{array} \tag{4.7}$$

converts the units of $\mathbf{x}_{\text{shadow}}$ (when calibrated in meters) to $\mathbf{x}_{\text{DOF}}$ units which are meters and radians respectively[5]. Please note that large values in $\boldsymbol{M}_{\text{sense}}$ are bad as they enhance sensor noise. E.g. pitch is a noisy channel arising from the short lever arms of only 16 mm required due to space constraints around the upper mass. Please also note the more complex reconstruction of the yaw signal. The sensors D&E are not at the same height as there is the cut for the upper mass cantilevers in the way. Hence, they sense pitch motion as well. To correct the signal for this pitch motion, some of the real measured pitch signal is subtracted causing yaw to contain B&C contributions as well.

The described diagonalization scheme is slightly more prone to failure compared to simple local feedback to only the co-located actuator. As soon as one shadow sensor signal gets invalid (broken LED, cable, flag out of the sensors linear range or light passing by the side of a flag), several DOF channels are spoiled usually leading the suspension into chaotic motion. Only sensor F is sensitive to a single DOF channel, side motion, and vice versa, making the damping loop almost as robust as in local damping.

4.5.7 *Shadow sensor – extending the linear range*

A big drawback of DOF-damping is that it requires a linear shadow sensor response, i.e. with constant slope as in equation 4.2. Even with minor deviations of 20%, the feedback can lead to oscillations. Especially during alignment procedures the linear range is often exceeded. If the relation between flag position Δx and PD current I_{PD} was known

$$\begin{array}{ccc} & x \to f(x) & \\ \Delta x & \curvearrowright & I_{\text{PD}} \\ & f(x) \to f^{-1}\left(f(x)\right) = x & \end{array} ,$$

5 $\mathbf{x}_{\text{long}} = \frac{D+E}{2}$, $\mathbf{x}_{\text{pitch}} = \frac{1\text{rad}}{95\text{mm}} \frac{B-C}{2}$, ...

the inverse could be used to restore the position.

The response of six different BOSEMs (SN009..SN014) was characterized individually by [79] and [80].[6] Each unit's response is measured individually by displacing the flag deterministically by means of a micrometer table in steps of 0.1 mm. The responses are normalized to a maximum of one, i.e. divided by the open light value where the flag is completely removed. Since the absolute position of the flag is not determined, the central region of the data is fitted linearly. From the fit the half light voltage is deduced as zero-position. Normally this is rather meaningless, as shadow sensors are measuring only the relative position anyway. But in this case it is important for comparability of the different BOSEMs. After this data conditioning, all units show a rather similar response (compare figure 4.13). The deduced slopes are suffering mostly from position inaccuracies (accuracy of the micrometer screw). The slopes are constant across a range of approximately 600 µm. That is significantly less than the range, where they show similarities. This motivated the feasibility of proper error signal linearization.

For linearization of a sensor, the inverse of its input/output relation must be known. In this case, no sufficient analytical expression for the signal or its inverse was found. When looking at the slopes, however, a supergaussian

$$\frac{\partial \,\mathrm{sig}(\Delta x)}{\partial\, \Delta x} = b \cdot \exp\left\{ -\left(\frac{\Delta x}{a}\right)^{2n} \right\} \tag{4.8}$$

with adjusted scaling parameters a (which provides a measure for the width of the linear region) and b (the slope in the central region) of order $n = 2$ fits pretty well in a 1300 µm wide region. Further out, the supergaussian decays too quickly. There the response is only a few tenth of a percent and the slope is already extremely low. As the signal-to-noise ratio goes like 1/slope for most noise contributions, the artificially recovered signal would get 1000 times worse. Especially at the upper end close to full light, the signal is Furthermore, influenced relatively strong by power fluctuations induced for example by temperature changes. Therefore at the very wings (for extreme flag displacements) no clean signal (calibration) could be obtained anyway. Also in these extreme cases the individual BOSEM units start to differ from each other significantly. Hence, a linearization reaching further wouldn't be sensible.

From the supergaussian slope, the signal

$$\mathrm{sig}(\Delta x) = \int_{-\infty}^{\Delta x} \frac{\partial \mathrm{sig}(\Delta x)}{\partial \Delta x} dx \tag{4.9}$$

can be inferred only numerically. This is going to be the drawback in experimental implementation. The CDS will need to have a lookup

6 Three LEDs were exchanged after electrical failure. This measurement was carried out to verify that all units were working properly again.

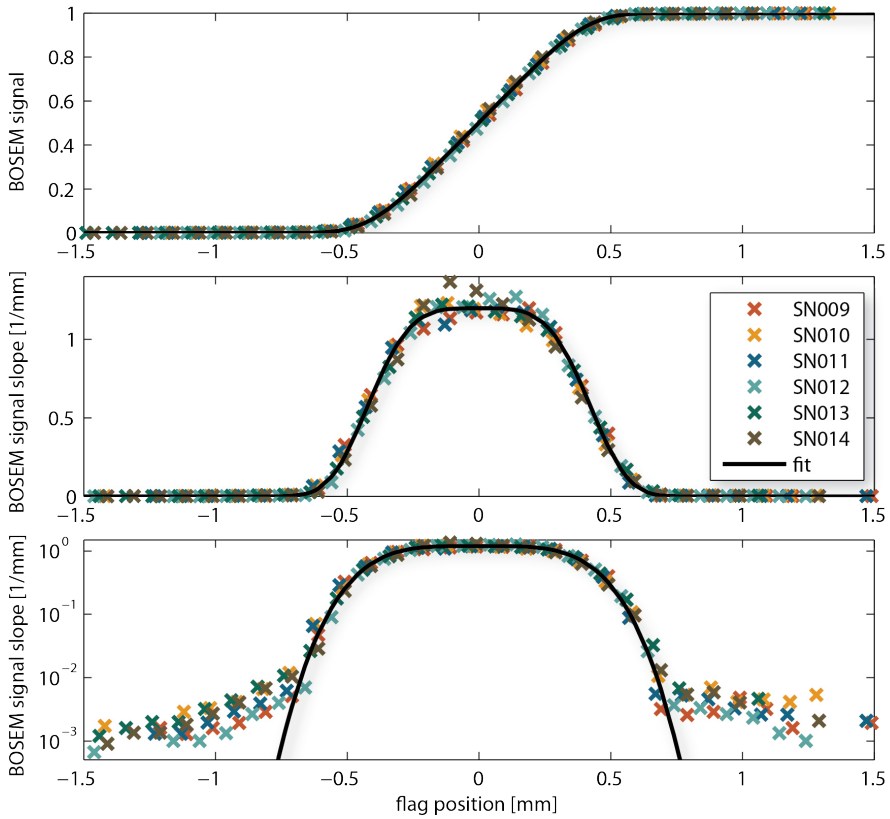

Figure 4.13.: The responses of six BOSEMs, measured by [79] and [80], are shown in the upper graph. They are normalized by the maximum value (open light calibration). The central regions are fitted linearly to define an absolute position for comparability. The slopes are shown in the middle graph on a linear axis and in the lower graph logarithmically. They are surprisingly similar to each other and constant ($\pm 20\%$) across a range of $\approx 600\,\mu$m. A supergaussian fit matches the data for about twice the range.

table. Possibly an even better approximation could be found and stored in this table. This, however, doesn't seem to help a lot due to the aforementioned power fluctuations (open light voltage), differences and noise far away from the optimal operation point. Also for the sake of a smooth signal, the supergaussian approximation was pursued.

After inverting the integral numerically – the last step in the whole procedure, which needs to be carried out only once – one can infer the flag position Δx by searching the corresponding position for the measured sig-value. Probably, the lookup table will be rather small and $\Delta x(\mathrm{sig})$ will be found by interpolation. From this reconstructed position a linear signal can be synthesized as

$$\mathrm{sig}_{\mathrm{lin}} = b\Delta x_{\mathrm{reconst}} + 0.5 \ , \tag{4.10}$$

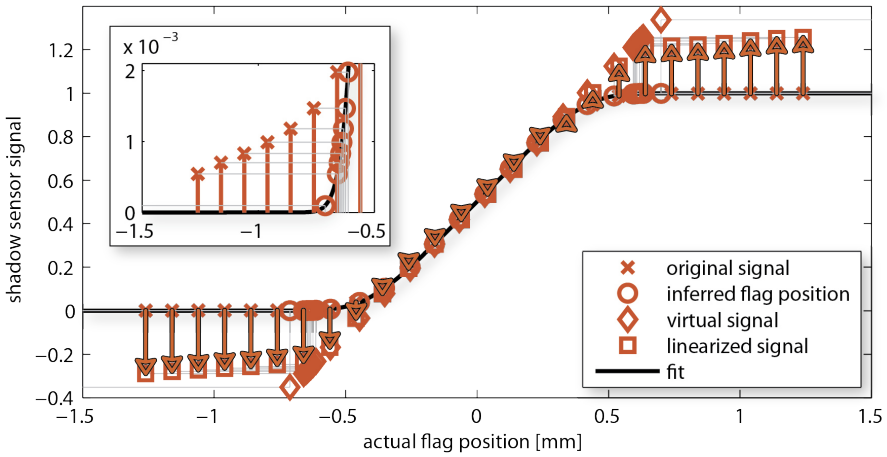

Figure 4.14.: The exemplary linearization of the BOSEM error signal is shown on SN009: The response of six BOSEMs was fitted using a supergaussian (black curve). From the actual BOSEM output the flag position is inferred by means of inverting the fit (circles). This is used to create a linear signal (diamonds) with the same slope in the central region. However, the synthetic signal is not all the way linear due to the aforementioned differences in the wings (shown in the inset).

which basically leaves the central region unaffected. This means that the new signal has got the same half light voltage $\mathrm{sig}(\Delta x = 0) = 0.5$ as well as the same slope

$$\left.\frac{\partial \mathrm{sig}(\Delta x)}{\partial \Delta x}\right|_{x=0} = b \tag{4.11}$$

as the original one. Not every individual BOSEM is characterized, so one supergaussian is fitted to all of the obtained slope data. The linearized signals are then deduced from only a single lookup table, reducing the complexity of future experimental implementation into CDS. Figure 4.14 shows the whole process and its limits exemplary on the dataset of SN009.

The results are shown in figure 4.15, where the original supergaussian fit is plotted for comparison. The width of the linear region (However, it may be defined exactly) is increased by more than a factor of two. The linearity in the central region is increased. This means there are less deviations from a constant slope paired with a sharper falloff at the edges. Also the slope doesn't approach zero but stays at the 10% level even in the wings.

4.5.8 *Shadow sensor – scattered light*

Recent experience showed that scattered light can pose a severe problem to shadow sensor readout. Despite being relatively far away from the light of the intra cavity enhanced 1064 nm main laser, the scattered

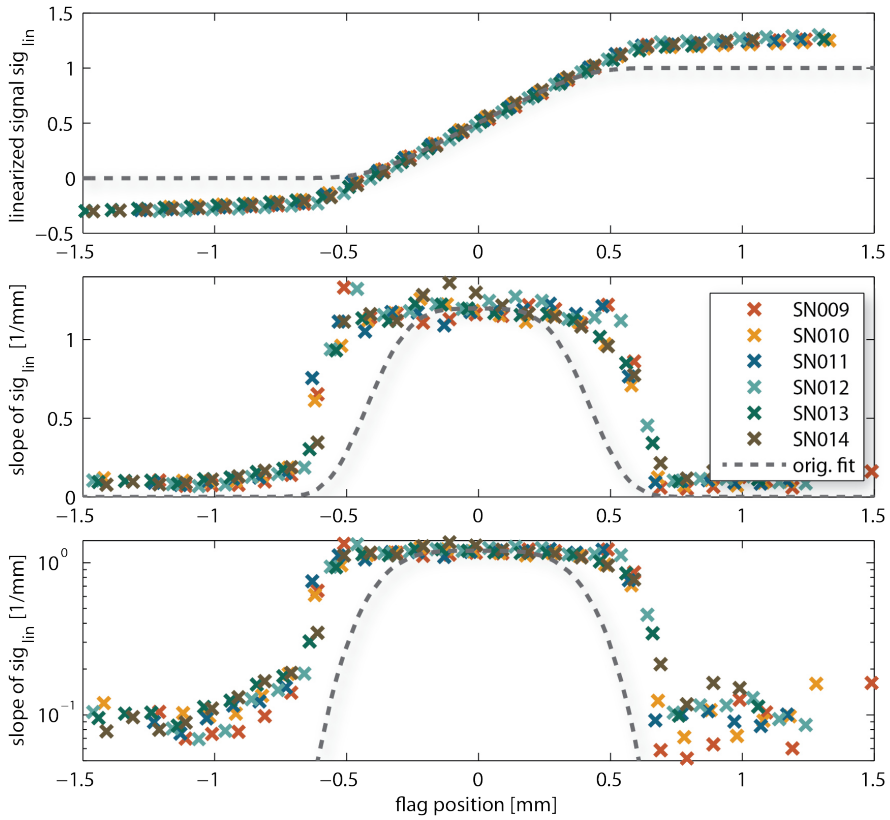

Figure 4.15.: After linearizing the BOSEM signals with a single supergaussian, the linear range is more than doubled. The linearization is limited by the slope of the original response, vanishing in its wings. This results in an extremely noisy signal in this range, even if a better matching fit was used.

light can spoil reference positions. However, even more dangerous is the possibility of introducing 'fake flag motion'. The countermeasures then taken by the damping system actually excite the suspended mirror. In the worst case this can cause a positive feedback via a power modulation inside the interferometer [81].

In GEO600 this is partly caused by the shadow sensor sensing unit being enclosed in transparent glass containers. As a workaround the LED current is modulated in the kHz range while the photodiode's current is demodulated at the same frequency where the test masses response is negligible and no signal is expected.

To avoid this complexity the coil holders were made from opaque aluminum. The large entrance hole opposing the flag can be closed by adding a cap (which is at hand). Additional optical cutoff filters were investigated but are not going to be installed until the taken measures turn out to be insufficient.

4.5.9 *Coil actuation – principles*

Optimally all alignment and damping is carried out at the upper mass, so that actuation noise is passively filtered by the lower suspension stages. It is beneficial, to place the sensors co-located to the actuators. This way creating stable servos is much easier and more robust. With shadow sensors this can be realized almost perfectly. A magnet can be used as or be implemented into the flag. Then a coil is wound 'around' the sensing unit to exert electromagnetic forces.

The required strength of an actuator (coil-magnet-geometry combination) is determined by the required actuation range and the stiffness of the suspension. As there are no requirements for the actuation range itself, the maximal range again given by the maximal sensing range of the shadow sensors was used as baseline. It is assumed that a poorly aligned shadow sensor may yield a total linear range of 0.7 mm in one direction. The original aLIGO BOSEMs incorporate 800 windings [31]. Due to the space constraints, 800 is the very maximum amount of turns on the BOSEMs. At the coils' sweet spot, 5 mmø, 5 mm thick neodymium magnets give a force of $\approx 10\,\mathrm{N/A}$.[7] Taking the number of coils per degree of freedom and the stiffnesses into account, this results in $\lesssim 10mA$ per coil for DC-positioning. In reality, however, it turns out that a tuning range of several shadow sensor ranges is required especially in the initial alignment phase: DC currents are applied to the coils and the shadow sensors are re-aligned (re-centered) multiple times in a row without realigning the suspension itself mechanically every time. To allow higher coil currents, smaller sensing resistors are being used for the start.

4.5.10 *Coil actuation – electronics*

The coil driver is supplied with a differential signal of maximally $\pm 10\,\mathrm{V}$ by the DACs. The low distortion, large slew rate, balanced line input receiver (SSM2141) yields 100 dB common mode rejection and converts the signal to single ended with an exact gain of one. A second order whitening filter (double pole at 0.16 Hz, double zero at 8 Hz) reduces the DAC noise below the requirement (see figure 4.18 and B.5). In a newer version this is switchable so that larger excitations can be exerted during the setup phase.

A low noise OP27 comparator matches the voltage drop across a sensing/shunt resistor and the set voltage (usually two resistors are used to increase the power that can be dissipated maximally, see figure 4.19).

7 Samarium cobalt magnets have a higher Curie temperature and suffer from less Barkhausen noise [82, 83]. They do not require a nickel plating for mechanical stability or vacuum compatibility. 5 mmø, 5 mm thick magnets compatible with the RefC suspensions and steerings are at hand and might be used in the future. When swapping, wider flags (>5 mm) should be installed as well to avoid light passing by their sides in case of poor alignment.

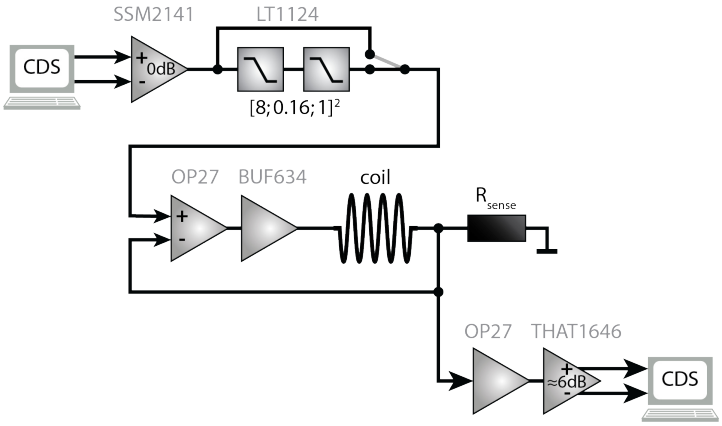

Figure 4.16.: The coil driver electronics receive the CDS signal differentially and apply de-whitening if chosen. The signal is applied to a current driver explained in figure 4.17. A copy of the measured coil current is put out differentially via a relatively noisy sender for diagnostic purposes.

Its output current (absolute maximum 25 mA) is amplified by a high speed unity gain buffer (BUF634, $I_{\max} = 250\,\mathrm{mA}$). This is used in high bandwidth mode to suppress its quiescent current as much as possible so it does not show up in the comparison. In this mode a 50Ω decoupling resistor should be placed in front according to the datasheet to provide stable operation.

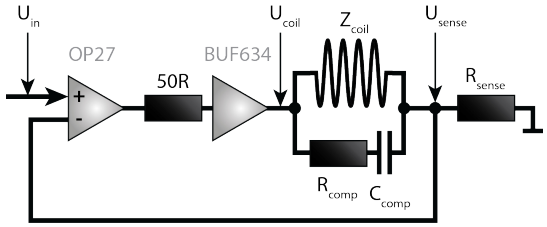

Figure 4.17.: Actuation coils are supplied by a current driver. This ensures that the exerted force is proportional to the CDS output (compare figure 4.16). The current is supplied by a BUF634 driver. It is measured via a sensing resistor and actively controlled to suppress noise. A high frequency bypass ($C_{comp} = 1\,\mu F$, $R_{comp} = 6.3\Omega$) is added parallel to the coil ($R_{\mathbf{coil}} = 50\Omega$ for triple suspension) to obtain a stable feedback loop.

As the coil being actuated is inside the high speed current driving loop, its inductance would drive the loop unstable. Therefore a compensation circuit is added in parallel to the coil, which allows the current to pass by at frequencies where no actuation would reach the test mass.

The voltage drop across the sensing resistor is buffered (gain = -1) and sent differentially with a balanced line driver of approximately gain 2 (5.2 to 6.2 dB dependent on the load). This current readback does not exhibit low noise performance (compare figure 4.18) but can be used to check the cancellation of whitening/de-whitening, the calibration

inside CDS using $I_{\text{coil}} = (U_{\text{out}+} - U_{\text{out}-})/2R_{\text{sense}}$ (to 1 dB accuracy) and the functionality: whether the driver saturates or the coil is even broken.

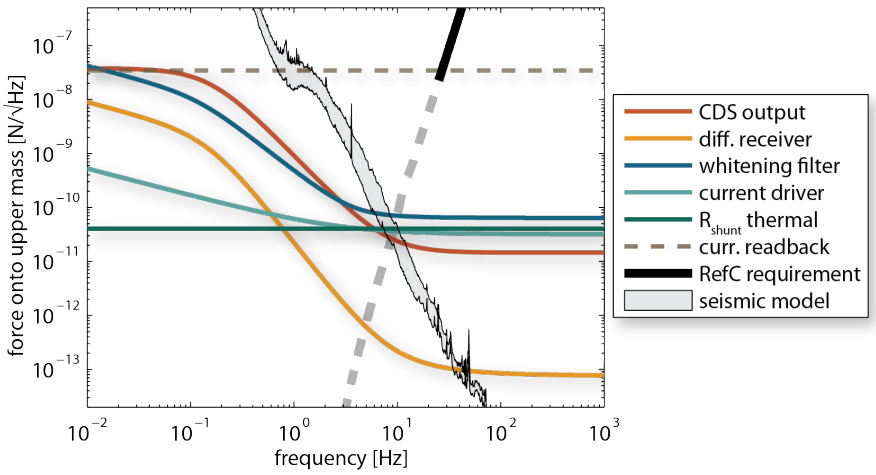

Figure 4.18.: Similar to the shadow sensor readout, all noise contributions of the actuation coil driving electronics were simulated using the LISO plug-in [78] for Cadsoft EAGLE and projected into forces applied to the upper mass assuming a (1kΩ) shunt resistor. The reference cavity test mass position requirement starts at 25 Hz. It is projected to a force allowed at the upper mass using the theoretical state space model [84] (the projection is continued towards lower frequencies as dashed curve). At low frequencies, the noise introduced by the coil drivers should be below the driving seismic if possible. The 90% confidence seismic in horizontal from figure 3.3 is projected using a simple SAS transfer function (resonance at 0.1 Hz, Q=3, no plateau). Noise occurring in the driving electronics is attenuated by large shunt resistors. For smaller values as used during the initial alignment procedure (10Ω), the coil driver noise starts to rise above seismic noise at 0.5 Hz (figure B.5).

4.5.11 *Coil actuation – current sensing resistor*

It turns out that with the used coil driving scheme, the choice for a sensing resistor is not trivial. On the one hand the output current (biggest possible actuation force) shall be maximized, on the other hand the driver's noise shall be minimized. The first point is achieved by maximizing the voltage drop across the coil and (due to the given maximal range of $\approx \pm 10\,\text{V}$) minimizing the sensing resistor. The latter is achieved by maximizing the voltage drop across the sensing resistor. A further limitation is the power dissipated in the sensing resistor

$$P_{\text{sense}} = U_{\text{coil}}^2 \frac{R_{\text{sense}}}{R_{\text{coil}} + R_{\text{sense}}} \tag{4.12}$$

which is illustrated in figure 4.19 and should not exceed the rating of the resistor. The dissipated power is maximal at the crossover, where

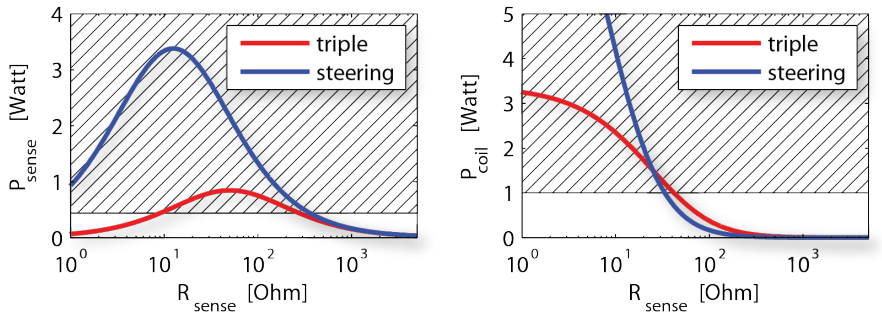

Figure 4.19.: The maximal power deposited in the sensing resistor depends on its value. It is shown in the left graph for $U_{\mathrm{coil}} = \pm 10\,\mathrm{V}$. For comparison the right graph shows the power dissipated in the coil. The shaded areas symbolize the region where ratings are exceeded. The steering mirror currents are sensed above the restricted area with 250 and 500 Ohm, the triples' below at only 10 Ohm to provide sufficient range.

the resistance of the coil equals that of the sensing resistor. However, with the used two SMD0805 resistors in parallel, no more than 0.5 W can be dissipated. This gives two possible regions of operation, above and below the crossover.

The coils themselves are located inside the vacuum system and electrically isolated from the suspension. Therefore their power dissipation capabilities are limited as well. A power of one Watt might be radiated at a large BOSEM temperature increase of about 100 °C (compare section 4.7.1). The current is not constant and its rms value is only a fraction of the peak value, especially for damping. Therefore the maximum of the temporarily deposited power in any coil

$$P_{\mathrm{coil}} = \frac{U_{\mathrm{coil}}^2}{R_{\mathrm{coil}} + R_{\mathrm{sense}}} \tag{4.13}$$

was set to 1 W.

In the case of the steering mirrors, a maximal current of 50 mA turns out to be sufficient for any sensible steering range, so a sensing resistor above 250 Ohm can be used. The triple suspensions are actively damped. Hence, higher coil currents are required for severe events during the commissioning phase. Maximum values up to 150 mA were observed in 'normal' operation. This requires the use of small (10 Ohm) sensing resistors. Once the whole system is fully commissioned, the required drive will be smaller so that larger resistors around 1 kΩ like Vishay Beyschlag 0204 with small flicker noise [77] can be used.

Keep in mind that, although restricted regions in figure 4.19 must be avoided, the according resistor values can be used nevertheless. In that case, U_{coil} must be limited as the dissipated power scales with it's square U_{coil}^2. In practice limiters can be set in CDS. For an optimal use of the DACs' dynamic range, the gain of the coil drivers input stage may be adjusted.

4.5.12 *Coil actuation – magnet sweet spot*

The force of a coil being exerted onto a magnet on its axis is proportional of the gradient of the electromagnetic potential and therefore strongly position dependent.

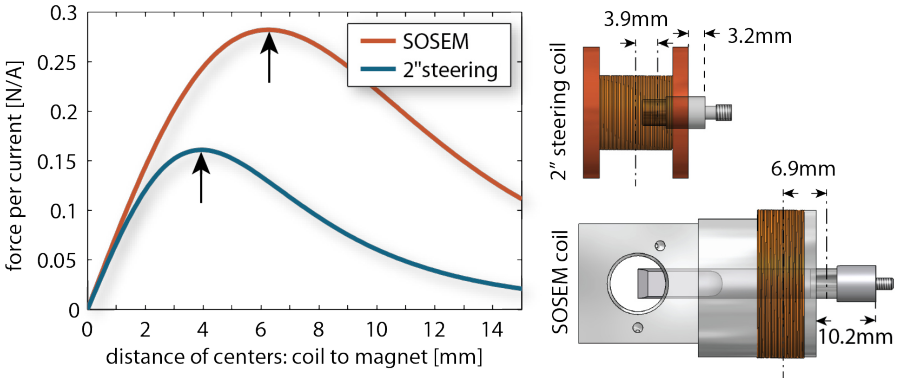

Figure 4.20.: A Mathematica script written by Mark Barton calculates the response of an electromagnetic actuator from the coil geometry and measured magnet parameters [85]. The sweet spot with maximal response and therefore the smallest position dependence are determined to be at 3.9 mm and 6.2 mm respectively. The picture on the right shows the required distance between the coil holder and the mass, where the magnet is attached to. For the steering it is important that the magnet sits well within the copper cup to obtain sufficient eddy current damping. For the BOSEM design, the flag length is chosen in a way that the flag's tip sits at the shadow sensors operation point when the magnet is in its optimal position.

However, when moving the magnet axially out of the coil, there is a maximum in the exerted force. Around this maximum, the force is position independent to first order. This sweet spot is the desired position for operation.

4.5.13 *Coil actuation – actuation matrix*

The actuators on the upper mass are co-located with the sensors. In fact the shadow sensor readout is fixed in place on the coil holders and the flags are glued onto the magnets on the upper mass. When actuating on a single coil, different DOFs are excited at the same time. Again the goal is, to find the linear combinations of coils

$$\mathbf{F}_{\text{coil}} = \boldsymbol{M}_{\text{act}} \cdot \mathbf{F}_{\text{DOF}} \tag{4.14}$$

to act on for driving each DOF at a time. In the case of co-aligned sensors and actuators, $\boldsymbol{M}_{\text{act}}$ is the transpose of $\boldsymbol{M}_{\text{sense}}$. To verify this, either virtually act on each coil at a time and invert the resulting actuation in the DOF system according to $\mathbf{F}_{\text{DOF}} = \boldsymbol{M}_{\text{act}}^{-1} \cdot \mathbf{F}_{\text{coil}}$ or follow

the same scheme as for the sensing matrix: Investigate how much of which coil to act on, to carry out a pure actuation in the DOF system (projection of DOF base vectors into the coils' coordinate system). The actuation matrix

$$\boldsymbol{M}_{\text{act}} = \begin{array}{c} \\ \mathbf{A} \\ \mathbf{B} \\ \mathbf{C} \\ \mathbf{D} \\ \mathbf{E} \\ \mathbf{F} \end{array} \begin{array}{c} \begin{array}{cccccc} \mathbf{long} & \mathbf{pitch} & \mathbf{side} & \mathbf{roll} & \mathbf{vert} & \mathbf{yaw} \end{array} \\ \begin{pmatrix} 0 & 0 & 0 & 5.264 & 0.5 & 0 \\ 0 & 31.25 & 0 & -2.632 & 0.25 & 3.819 \\ 0 & -31.25 & 0 & -2.632 & 0.25 & -3.819 \\ 0.5 & 0 & 0 & 0 & 0 & 5.556 \\ 0.5 & 0 & 0 & 0 & 0 & -5.556 \\ 0 & 0 & 1 & 0 & 0 & 0 \end{pmatrix} \end{array} \tag{4.15}$$

reverses from DOF coordinates (forces in newton and torques in newton-meter) to coil coordinates (all forces in newton). This time large entries attenuate noise introduced by the coil drivers but on the other hand amplify sensing noise which passes through the damping filters. In a student project, the correctness of the geometrically deduced sensing and actuation matrix was investigated [86]. DOF actuation to upper mass tilt was measured by means of optical levers. This project showed significant cross-coupling in the actuation. This might arise from the relatively small upper mass and Hence, the small distance between neighboring coils and magnets.

4.5.14 *Coil actuation – required strength*

The linear readout range of the shadow sensors is limited to about 0.7 mm. After an initial testing and commissioning period, it doesn't make sense to actuate more than the maximal readout range. This limits the maximally usable dynamic range to the values shown in table 4.5.

DOF	stiffness [N/m] or [mNm/rad]	coils [qty.]	dynamic range [mm] or [mrad]	I_{max} per coil (0.1 A/N) [mA]
long	120	2	0.7	4.2
side	120	1	0.7	8.5
vert	217	2 [8]	0.7	7.6
pitch	110	2	44	15
yaw	133	2 [8]	7.8	0.57
roll	60	2 [8]	7.4	0.23

Table 4.5.: From the stiffness of each degree of freedom, a maximal DC actuation which does not exceed the linear BOSEM range of 0.7 mm can be deduced.

8 The actual quantity of acting coils deviates, but this number accounts for the fact that some coils don't contribute their full strength for this specific degree of freedom.

The shown stiffnesses can be deduced from the suspensions state space model. In conjunction with the strength of the used actuators (10 N/A) this results in a maximally required current through the coil. This knowledge can be used to set the current sensing resistor. Although pitch formally requires the biggest current due to its short lever, the reader should bear in mind that using up the total pitch scanning range is not sensible. The same, short lever arm causes the pitch readout range to be significantly larger in terms of angle when compared to yaw. A current of 10 mA should suffice for all DC alignment demands.

4.5.15 *Different damping methods: local vs. degree of freedom*

In early times of suspension history, signals were fed back only very locally: Each sensor controlled only the co-located actuator. This scheme is called local damping. It is extremely robust, as a malfunction of one feedback loop is usually compensated by cross coupling to others, not in terms of optimal functionality but the suspension is not driven into instability until it crashes. The applied local damping makes best use of this robustness. The velocity proportional feedback guarantees almost unconditional stability at the drawback of noise injected in the detection band. The strength is chosen to the upper end, i.e. the suspension is slightly overdamped.

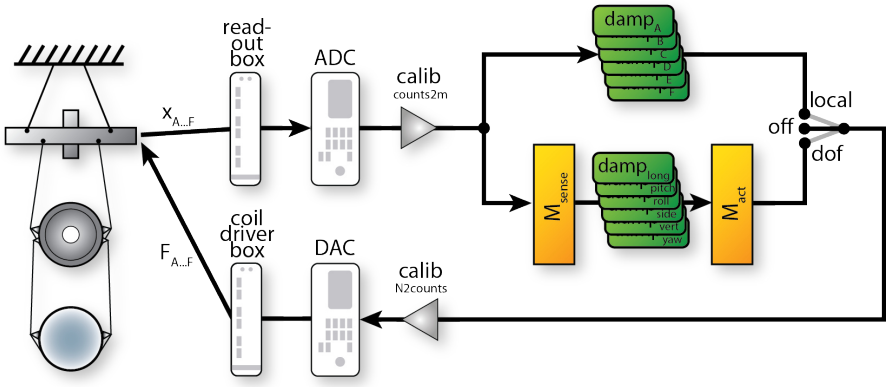

Figure 4.21.: The upper mass motion is read out by shadow sensors. Their signals are conditioned by readout electronics, digitized by ADCs and calibrated. The damping can be chosen between extremely robust local damping filters (sensor x to co-located coil x) and less noisy degree of freedom damping. Finally the actuation signals are reconverted to counts and to voltages by DACs and sent as coil currents by driver boxes .

When good detection band sensitivities are required, the feedback is switched to degree of freedom damping. The shadow sensor signals are decomposed into the upper mass degrees of freedom by means of $\boldsymbol{M}_{\text{sense}}$. The feedback signal is applied in the same system and is distributed to the individual actuators by means of $\boldsymbol{M}_{\text{act}}$. This way the damping

filters for the individual degree of freedom can be shaped to its needs. Versions of the filter which are not optimized to reduce interferometric rms noise yet are shown in figure 4.23.

Once the interferometric readout is commissioned, lower noise filters will be switched on, sacrificing robustness for detection band performance. These filters (see figure 4.24) roll off steeply towards the defined requirement starting at 25 Hz (compare figure 4.25). However, they are too delicate during the coarse alignment phase when flags occasionally leave the linear range or light is passing by their sides. A possible solution to the first point is presented in section 4.5.7.

In addition to the damping, alignment offsets are applied to the suspensions by the same actuation matrix in any damping mode. Attempts were made to use the shadow sensor signals as DC references as well. However, integrating the deviation from a set-point and feeding it back to the suspension does not work reliably. The differing stiffnesses of the individual degrees of freedom require differently strong actuations. Electromagnetic cross-coupling from coils for stiff degrees of freedom to soft suspension DOFs seems to be the limiting effect. Furthermore, glitches often drive the suspension into oscillations. This problem might be avoidable in future with an automatic state recognition that disables integration in the case of excess pendulum motion.

4.5.16 *Damping filter requirements*

Robust damping filters must fulfill more than the theoretical requirement of 1/f-unity gain crossing. The loop gain for example can change easily (see section 4.5.7 and 4.7.1). Therefore a gain margin of 3 dB is desired for all damping loops. Furthermore, a sufficient phase margin is required to ensure a stable system in the presence of variable non-steady state disturbances. It is chosen to be 20° at minimum.

To check the damping efficiency the suspension's impulse response from upper to lower mass was determined using the state space model. A ring-down of the lower mass to 1/e amplitude within 10 s is usually accepted as sufficient [87, 66]. If, however, the system consists of several coupled oscillators, some of the oscillations may decay quickly while others can be long-lived. This would cause a short 1/e ring-down time while a smaller amplitude oscillation could continue significantly less damped afterwards. Therefore the $1/e^4$ point is checked to be within 40 s instead. This measure ensures a reasonable calm-down time of all suspension modes. It is independent of the oscillation frequency while the Q-factor is not.

One special fact is not covered by this criterion: Assume there is a mechanical impedance mismatch between the upper mass and a mode which couples to the test mass. Then the impulse may not be transmitted to this mode in the first place, especially if the upper mass is strongly damped. Nevertheless feedback noise or other disturbances,

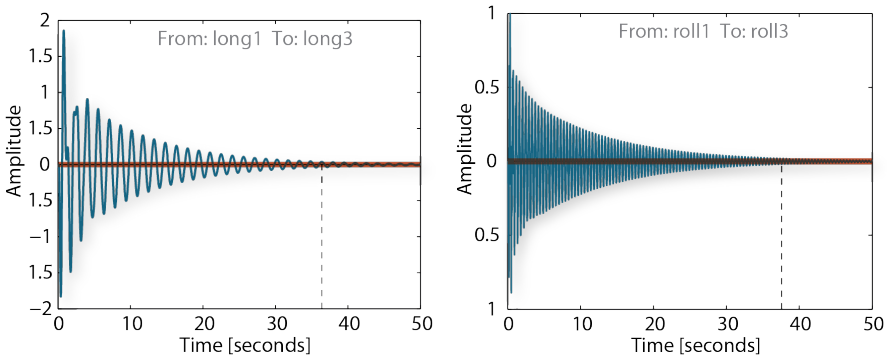

Figure 4.22.: The $1/e^4$ ring-down time, the duration after which the amplitude doesn't exceed the red region anymore, of all degrees of freedom is verified to be below 40 s. This ensures that even the most long lived excitations decrease by about 1/e within every 10 s.

which couple to the mirror directly, can slowly build up in this mode and remain almost undamped. This relates to the observability of this mode at the chosen readout location.

4.5.17 *General damping filter shape*

All thinkable damping filters (displacement to feedback force) have one point in common: their slope is f-like ($\widetilde{\propto} f$) in the feedback region, i.e. in the vicinity of the resonances to be damped. They are similar to velocity damping in order to extract kinetic energy. Actually higher frequency resonances are getting less excited as the driving noise (mostly seismic motion) usually also decays towards higher frequencies. Therefore a shallower damping filter slope ($\propto \sqrt{f}$) can be used. This minimized the noise injected beyond unity gain. Such a slope is sufficiently well approximated by one to two pole/zero pairs per decade. For the triple suspension this region is between 0.1 and 10 Hz.

Below the lowest resonance a high-pass filter is implemented for convenience. This reduces the DC-response which otherwise is disturbing when switching the damping on/off. The corner frequency is 10..100 mHz. If it was increased, too much phase would be lost for a clean unity gain crossing.

To the high frequency end, above the highest resonance, a low-pass filter needs to be implemented into the damping. The basic slopes of the $x_{\mathrm{GND}} \to x_{\mathrm{upper}}$ and $F_{\mathrm{upper}} \to x_{\mathrm{upper}}$ transfer functions are the same around resonance. But towards higher frequencies, the damping filters response $x_{\mathrm{GND}} \to F_{\mathrm{upper}}$ would bypass seismic noise to the upper mass if it kept rising like pure viscous damping. Actually it even has to decrease in order not to dominate the transmissibility (compare figure 3.8). A second order pole works well for this purpose. It also reduces the rms value of the coil actuation. However, when the requirements are

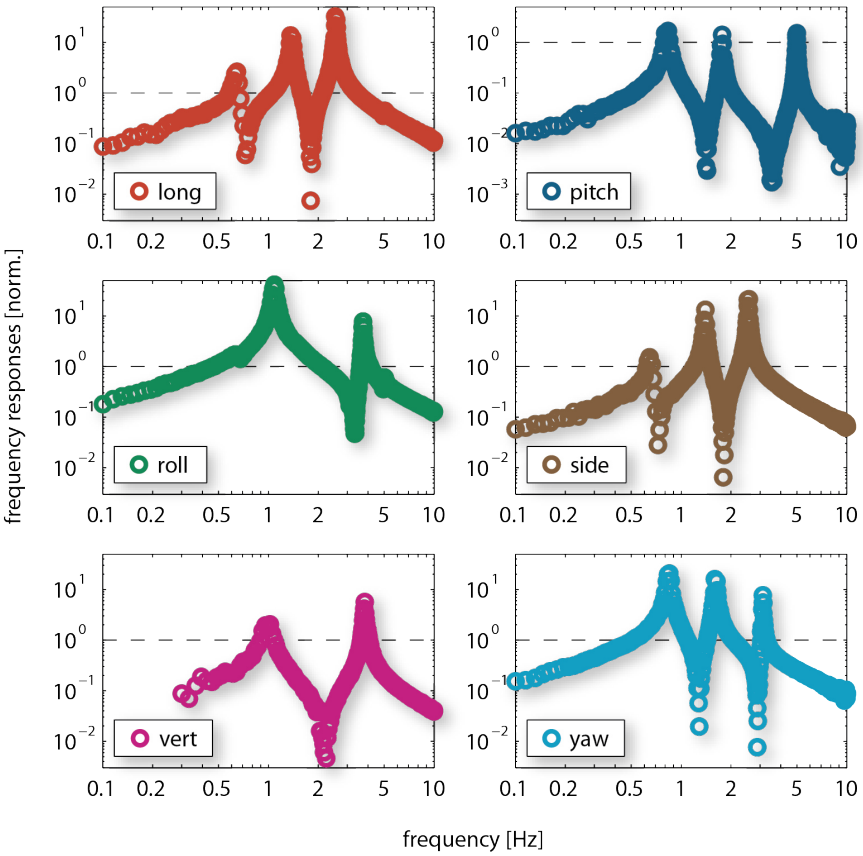

Figure 4.23.: Measurements of the open loop gain of all six DOF-damping loops are shown. A swept sine signal is injected digitally into each DOF-damping filters. Based on a combination of this measurement and a preliminary noise performance of the RefC, the individual gains were set as shown. Two modes (one in *roll* and one in *vert*) are not resolved due to weak coupling to the upper mass. The pitch mode got a factor of ten less gain than the others because of its lever arms. With more gain the injected shadow sensor noise would dominate the seismic noise, causing increased total noise without any benefits.

very stringent like in the RefC, further attenuation is required. Adding more poles is not an option, as the system would become unstable from excessive phase loss. An elliptic (Scultete) filter can produce a step at the drawback of increased response (servo bump) below the cutoff.

The more optimized the system is (by means of noise performance), the more susceptible it gets to malfunctions. For example, optimally, the complex multiple input multiple output system is well separated into single input single output systems, which can be easily controlled. In reality, the degrees of freedom are still coupled, which occasionally drives the system into instability, especially when couplings are changing. Additional notch filters might avoid resonant enhancement of the parasitically coupled degrees of freedom. Furthermore, each suspension

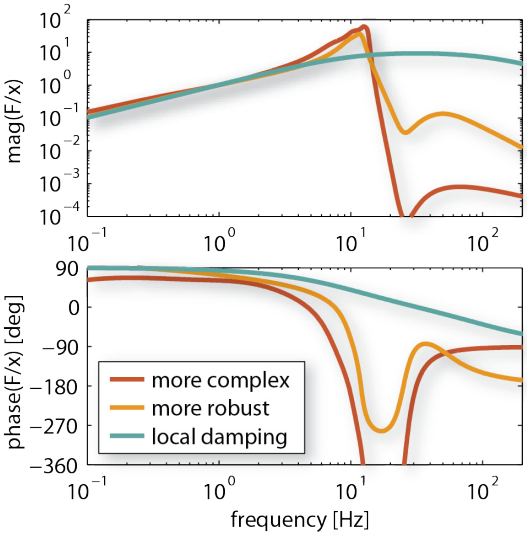

Figure 4.24.: Different damping filters were normalized to unity response at 1 Hz for comparison. The filter used in local damping is by far the most robust. The final reference cavity sensitivity However, requires reduced filter response above and especially at 25 Hz. An elliptical step filter (Scultete) is used to achieve this. When applied to the suspension, the more complex filter version aims for a gain margin as little as 3 dB all the way up to the step to allow a larger step and more detection band suppression. For the first phase of the experiment, a more robust version is implemented.

has the fallback option into the local damping mode using much more robust damping filters.

4.5.18 *Noise projection of the used damping system*

For convenience, the noise contributions of the shadow sensor driver and readout and the coil driver were given in 'native units' earlier, i.e. a force acting onto the upper mass and as position accuracy of the readout. In practice one is actually interested in the test mass displacement noise. Two effects play a role in the mitigation: The mechanical susceptibility of the test mass position to a force exerted onto the upper mass (this was taken into account earlier by projecting the requirement backwards into an equivalent force exerted onto the upper mass) and the feedback system shaping the injected sensor noise but also the actuation and seismic noise. Although the feedback system is only acting around the suspension resonances, the influence of velocity damping would decay slower than an non-damped suspension would allow. Active damping allows for a shallower damping filter ($\propto \sqrt{f}$) and a steep cutoff filter to fulfill the requirements at higher frequencies.

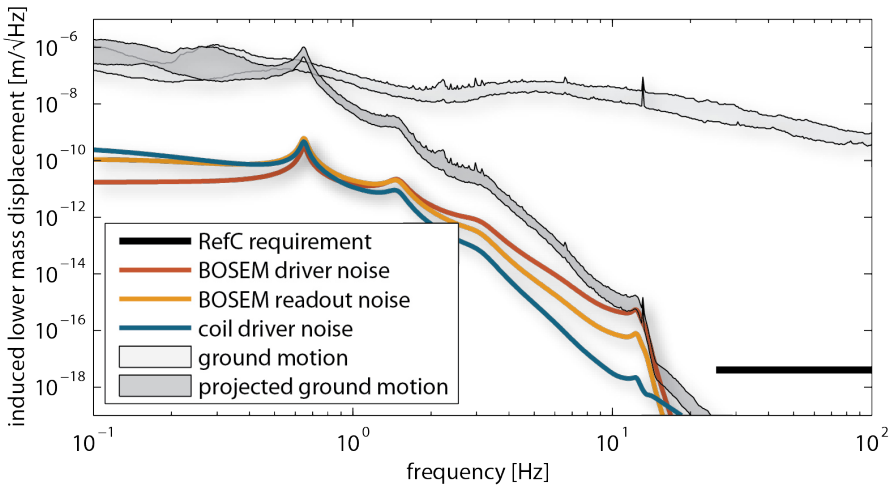

Figure 4.25.: The noise sources described earlier are summarized: The BOSEMs' inherent noise was measured with aLIGO electronics [31], BOSEM readout contains noise introduced between the shadow sensor's photocurrent and the CDS, BOSEM drive covers electronic noise introduced in front of the shadow sensors' LED and coil driver noise depicts everything injected between the CDS and the current driving the coil. All noise sources are projected to test mass displacement noise using the suspensions' state space model. The requirement relates to the sum of the simulated RefC noise contributions given in figure 5.20 in the detection band. A requirement for rms motion cannot be set but electronic noise is well below seismic noise.
All noise sources are well below the requirement. Furthermore, the electronic noise at low frequencies still leaves room for seismic improvement such as inertial SAS control.

4.6 TRIPLE SUSPENSION CABLING

For the communication to the CDS and for the signals from BOSEM drivers to the vacuum feedthrough (LED current, PD readout), Cat7 cables in conjunction with D-sub connectors are used. Cable bundles of four individually shielded twisted pairs and an additional shield around all pairs together carry all signals of a triple suspension. Each signal is sent via one twisted pair. This provides 90 dB of noise rejection [88]. The cabling is described in more detail in appendix C.3.

4.7 TEMPERATURE, PRESSURE AND TEMPORAL INFLUENCES

As the Prototype environment is meant to be cycled quite often between vacuum and air, some effort was put into understanding the changes in the upper mass readout. The major short-term influence is the temperature change from the semi-adiabatic expansion of the residual gas, which is analyzed in the following section. After that, the variability of cantilever stiffness and length with temperature are

investigated. These changes usually happen slow due to the heat capacity. The biggest permanent effect comes from the buoyancy which is then described in the last subsection. A settling of the artificially aged cantilevers could not be observed.

4.7.1 *BOSEM calibration changes*

This section covers changes in the calibration of BOSEM signal into actual flag position with special emphasis onto temperature dependence. The results are of special relevance for the linear range extension presented in section 4.5.7 and sensitive degrees of freedom such as pitch.

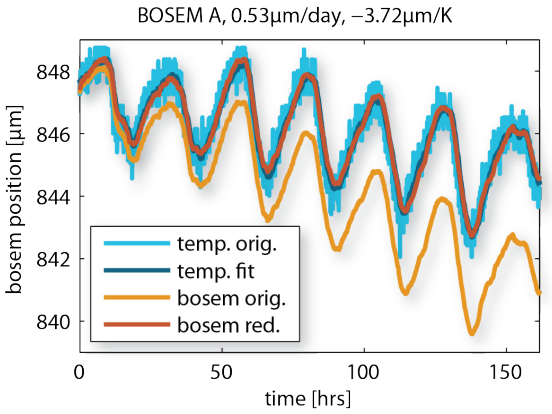

Figure 4.26.: Light blue shows the room temperature measured close to the exemplary chosen BOSEM F on the toy suspension. It is calibrated into flag displacement by means of a fitted conversion factor. In dark blue a 50 min single pole is added to account for delayed response due to heat capacities. Also some smoothing is applied. Compared, the orange original data show a drift. Fitting a continuous sensitivity degradation to it and subtracting the effect results in red graph which matches very well with the temperature.

The open light signal, where the flag is completely removed, shows a 24 hour cycle. Fitting the temperature, however, doesn't lead to good agreement. Another continuous degradation is required, to explain the change of BOSEM signal over time. This is surprising, as all units were undergoing an extended 50 h burn-in phase at 100 mA in Birmingham [31]. Also they were in use several months before the measurement was taken. The results of a fitting process for all six units of the toy suspension are shown in table 4.6.

The change with temperature can be explained by the dependence of LED efficiency from temperature. In the datasheet the temperature dependence between -60 and +100°C is given. Quadratic fitting results in an efficiency change of $(\partial P_{\max}/\partial T)\,/\,P_{\max}^{20°C} \overset{20°C}{=} -0.0073\,/\mathrm{K}$ around room temperature (see figure 4.27). During the open light test, the total BOSEM range was calibrated to $880 \pm 35\,\mu\mathrm{m}$. This leads to a

BOSEM unit #	$\partial x/\partial T$ [µm/K]	degrad. [µm/day]
A	-3.72	-0.53
B	-3.32	-0.19
C	-3.54	-0.33
D	-3.29	-0.16
E	-3.58	-0.28
F	-3.45	-0.17

Table 4.6.: Six readout units were monitored in an open light test (flag removed) over the course of about a week. The correlation of the signal with temperature and a continuous degradation are fitted according to figure 4.26.

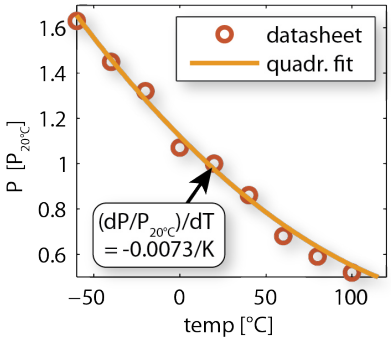

Figure 4.27: The efficiency of the BOSEM LEDs is temperature dependent. The measurement from the datasheet is fitted by means of a quadratic fit over a big temperature range. Around room temperature the efficiency is reduced by 0.0073/K.

change of 6.4µm/K, almost double as much compared to the observed value.

It should be noted that this investigation was actually carried out during an open light test. Whenever a flag shades a fraction of the light, the signal change induced by temperature is reduced by the same fraction. This means that tilt degrees of freedom, where two (ore more) flag positions are subtracted, might suffer from imbalanced calibration changes. Especially in pitch, where the lever arms are short, this can spoil reference positions.

4.7.2 *Cantilever stiffness changes*

The stiffness of most materials changes with temperature ($\partial E/\partial T \neq 0$). As the deflection of pre-stressed materials, such as the cantilevers of a suspension, depends on the stiffness, it changes with temperature as well. This can be seen well on the toy suspension in air, which shows a strong correlation between vertical position and temperature. Over the course of a few hours a temperature drop of 1 K raises the suspension by about 50µm, much more than the effect described in the last section. The temperature dependence of the Young's modulus in the cantilever material Marvel-18 is reported to be $(\partial E/\partial T)/E = 2.54 \cdot 10^{-4}$ /K [89], which would cause a lift of 56µm/K. This does not

yet take into account that the toy suspension cantilevers are extended by a relatively long, stiff clamp which doesn't flex. The latter would reduce the above mentioned change and probably would lead to even better agreement.

4.7.3 *Cantilever length changes*

Due to thermal expansion, the length of the cantilevers changes. As this defines the suspension point in horizontal, the suspension moves as well. With a top cantilever length of 207 mm and an average coefficient of thermal expansion of $10 \cdot 10^{-6}$ /K this results in only 2 µm/K. The suspension cage supporting the shadow sensors, however, is made from aluminum with a CTE of $24 \cdot 10^{-6}$ /K. This moves the shadow sensors by 5 µm/K, reversing the sensed longitudinal position by 3 µm/K. This is comparable to (twice as big) the calibration changes described earlier [90].

4.7.4 *Buoyancy change*

When being vented, the suspension is 'swimming' in air. In vacuum this support is missing. This is equivalent to the suspension getting heavier by the weight of the air, it displaces. The volume can be calculated from the effective suspension's density of $2.73\,\mathrm{g/cm^3}$ obtained from an Inventor model and its actual weight. Together with the density of the air ($1.2\,\mathrm{kg/m^3}$) it gives the buoyancy. The top vertical stage has to support this additional weight (see table 4.1 and therefore is expected to flex by 97 µm. Actual observations on different suspensions, however, showed a vertical change of only 64 µm. This measurement is better to obtain during venting, as the temperature change is much less significant in this case. The discrepancy might hint that the absolute BOSEM calibration is incorrect. Additionally, it might be due to some parameters, such as the cantilever stiffness, not being known accurately enough yet.

4.8 Horizontal vs. vertical suspension thermal noise

In a complex suspension system, equation 5.21 does not hold anymore. The susceptibility and its imaginary part, which determines the thermally driven motion, differ in shape. A major reason is that the Q-factors of the modes are all very different.

Longitudinal modes (same as sideways) benefit from the dilution factor which reduces their mechanical loss (compare chapter 5.7.5). This lowers the off-resonant thermal noise as well. Vertical modes, in contrast, do not experience loss dilution. This causes the vertical noise to be almost three orders of magnitude bigger than the horizontal noise in the 100 Hz-region. With the assumed 1:1000 coupling of other degrees

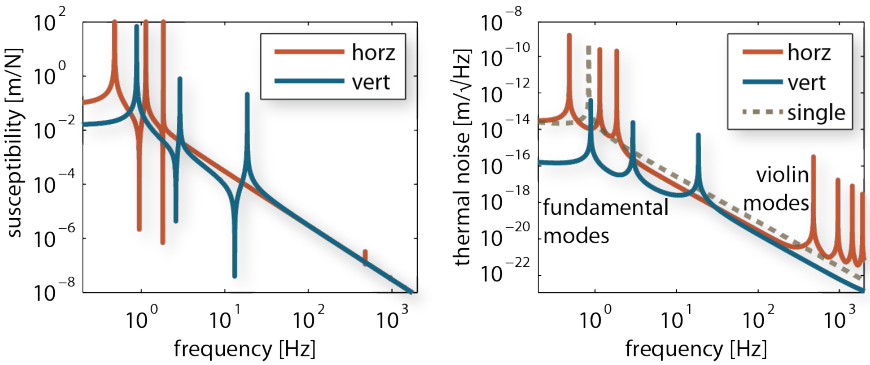

Figure 4.28.: The magnitude of the lower mass' susceptibility to excitation is shown on the left. The thermal noise in the interferometric readout consists of a direct longitudinal and a parasitic vertical contribution. Thermally driven vertical motion is assumed to be suppressed by a factor 1:1000. Both contributions depend only on the imaginary part of the susceptibility. For comparison to the full simulation results, the adopted model from [91] is shown as dashed curve. At 30 Hz it overestimates the noise by a factor of three.

of freedom into longitudinal, the associated interferometric readout signal from vertical and horizontal thermal noise has a similar level in the detection band.

5

FREQUENCY REFERENCE CAVITY

Interferometry relies on the measurement of path lengths by means of optical phase. Hence, precise measurements require a highly stable laser frequency. In a two path interferometer (such as a Michelson interferometer) one can think of one arm serving as reference for the other arm. If both arms were perfectly equal, frequency noise would be rejected completely. However, control schemes often require length asymmetries (e.g. Schnupp asymmetry) and tolerances add more imbalance (especially if arm cavities are being used). Therefore different stabilization schemes for the laser frequency were developed. The monolithic Non-Planar Ring Oscillator (NPRO) laser is inherently stable against vibrations and acoustics, thermal effects etc.. It is amplified to 35 W, which conserves almost all stability [92, 26][1]. Nevertheless, a much better frequency reference is required to achieve the roughly seven orders of magnitude of active frequency noise reduction in the frequency band of the SQL interferometer operation band (see figure 5.20. There are two major types of references:

- Atomic and molecular electronic transition energies are determined by fundamental constants and thereby well suited as low frequency reference (sub-Hertz). Molecular iodine has a set of transitions at 532 nm and can be used to stabilize a frequency doubled Nd:YAG laser.

- An optical cavity's resonance condition is determined by its length. It can either be fixed by a low thermal expansion spacer like in the PMC described in chapter 2 to have a good performance in the mid frequency region (hundreds of mHz to tens of Hz) while suffering from seismic motion. Or the mirrors are suspended, in which case they behave like free masses above some transition frequency making this the method of choice for higher frequencies (above a few Hz).

Naively one might expect, that frequency noise suppression is required only in the measurement band of the SQL interferometer. In practice, nonlinear effects can also convert noise to higher frequencies, so that

1 [92] shows in figure 4.7 that the amplifier (40 W Verstärker) doesn't introduce significant frequency noise to the NPRO (Miser). In [26] it is shown, that most other properties of the NPRO are well-conserved under the amplification

frequency stability is also required below the band. Therefore in the 10 m Prototype facility both active methods will be applied.

To fulfill the stringent requirements in the SQL interferometer's measurement band of 20 Hz to ≈ 1 kHz explained in section 5.1, a suspended 21.2 m round trip free space three mirror cavity, the Frequency Reference Cavity (RefC), was designed.

The InnoLight Prometheus laser used in the SPI setup is stabilized internally to an iodine reference. It is used to measure and control the inter table motion and thereby the cavity length indirectly. Around the fundamental RefC suspension resonances, table top motion is resonantly enhanced making the RefC no good reference. Hence, it might be required to stabilize the 35 W laser to the SPI laser directly by means of a phase lock loop.

In the RefC, two flat mirrors, the in- and outcoupler are located on the central SAS, a curved high reflective mirror is placed on the south SAS (see figure 5.3). The g-factor (radius of curvature) was chosen to provide a good rejection of higher order modes (see section 5.2) and reasonable spot sizes (> 2 mm) for low coating thermal noise. The design transmissivities of the mirrors were chosen to result in a high finesse impedance matched cavity for s-polarized light.

This enables a low shot noise limit of the Pound-Drever-Hall length readout. A triple suspension described in chapter 4 isolates the cavity mirrors from ground motion. The alignment of the cavity mode (especially during the alignment/lock acquisition mode) is achieved by means of DC spot position sensors described in chapter C.6. Once lock is established, spatially resolved PDH signals, so-called differential wavefront sensor (DWS) signals, can be used to accurately co-align the ingoing beam with the cavity mode by means of remotely controllable suspended steering mirrors explained in section 5.6.

In order to fulfill the requirements given in figure 5.20, the contributions of individual noise terms had to be simulated. They are deduced in section 5.7. This simulation finally led to a feasibility study for the Coating Thermal Noise Interferometer chapter 6.

5.1 REQUIREMENTS

The ultimate displacement sensitivity requirements for the Frequency Reference Cavity are driven by the susceptibility of the SQL interferometer to laser frequency noise. All subsystems should only contribute noise well below (factor of 10) the total classical noise of the SQL interferometer.

A Michelson interferometer with equal arms would not suffer from laser frequency noise. The effective arm length, however, is determined by the optical recycling factor expressed by the finesse. It is prone to imbalance between the arms. The absorption losses per reflection are extremely low (< 1 ppm) due to recent progress in coating technology.

The clipping losses on the mirrors (≤ 4ppm [93]) should be well balanced when the spots are centered on the mirrors. The cavity loss due to transmission through the ITMs ($T_{ITM} = 8500$ ppm) will be matched in the arms as well.[2] In the past, particle deposition on the coatings have shown to be unavoidable in a walk-in vacuum tank. These are a potential hazard in high power CW applications [95]. The issue is augmented by static charge buildup on the mirrors during the frequent pump cycles, which attracts e.g. dust, and the non-trivial clean-ability of suspended mirrors. It causes unpredictable scattering losses and absorption. Experience tells, these might be up to 30 ppm per mirror [96] and could add up to 60 ppm imbalance in the arm cavities, approximately 1% of the total losses. The finesse mismatch would cause the SQL interferometer to be a factor 1:100 as sensitive to laser frequency noise when compared to a similarly long single cavity like the RefC.

As no subsystem should contribute more than a tenth of the SQL interferometer's classical noise, it follows, that the total noise of the reference cavity calibrated in displacement can only be a factor of 10 times that of the SQL interferometer.

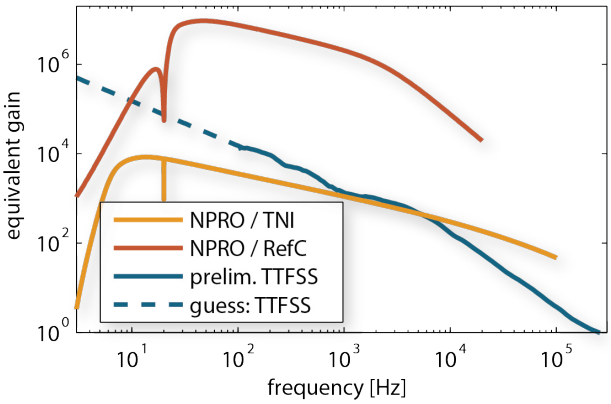

Figure 5.1.: The goal of laser frequency stabilization servo (TTFSS) [97] is to suppress laser frequency noise below the total RefC noise floor (see figure 5.20) in the relevant measurement band. As the TNI is shorter, it is less susceptible to frequency noise as seen in figure 6.27. The required gain for a 60µm spot size TNI is in reach with an early version of the TTFSS servo.

A short term requirement is emerging from the TNI described in chapter 6. Since it is designed as a single cavity without any frequency noise rejection, it fully relies on the reference cavity. As it is approximately a factor 100 shorter, the TNI is less sensitive to frequency noise by a similar factor. Desiring the same safety factor, the Reference cavity displacement noise may be a factor 10 higher than the TNI displacement sensitivity in order to achieve the full TNI sensitivity.

2 According to CMS [94], the coatings for each set of mirrors are grown in the same process providing extremely matched reflectivities

Furthermore, it is desired to provide a good low frequency stability of the laser, that is needed for many space applications and related experiments [98].The noise projections for the RefC and TNI calibrated in frequency are compared to the frequency noise of a free running laser. Here an NPRO [99] serves as reference, as the 35 W amplifier does not contribute a significant amount of noise [92, 26]. In order to not be gain limited in the frequency stabilization, the T*able* T*op* F*requency* S*tabilization* S*ervo* (TTFSS) [97]) gain should be higher across the measurement, than the ratio of NPRO noise and RefC noise. This is shown in figure 5.1. The gain, that is required to suppress frequency noise below the TNI noise floor is smaller and in reach with an early version of the feedback system. Additional tweaks [100] will have to be implemented in order to achieve the full frequency stability for the SQL interferometer around 100 Hz.

5.2 OPTICAL DESIGN

Simulations show, that a suspended mode cleaner would not suffice as frequency reference. Passing through all light (more than 10 W) would drive the mirrors by means of classical radiation pressure noise. Hence, only a small fraction ($\approx$ 250 mW) of the in-vacuum light is tapped of. As a positive side effect this minimizes thermal effects as well.

In contrast to a linear cavity, the light being reflected off a ring cavity is automatically separated from the incident light. Furthermore, a three mirror cavity is non-degenerate regarding polarizations due to the additional geometric phase flip in horizontal.

The maximal cavity length is limited by the facility to about 10 m. A reasonably high finesse (6200, later reduced to 3500, compare table 5.1 and 5.2) was chosen to reduce equivalent shot noise while not amplifying classical radiation pressure noise too much. The latter reason also motivates the choice of the relatively high mirror mass (when compared to the 100 g mirrors of the SQL interferometer). A g-factor of about 0.7 provides a stable cavity with a good higher order mode suppression (clean TEM_{00} mode) as described in chapter 2 and shown in figure 5.2. It also allows for spots on the mirrors that are sufficiently large to not be coating thermal noise limited.

The laser is controlled to follow the cavity length by means of three actuators, each covering a different frequency band and allowing for a unity gain frequency of $\approx$ 300 kHz. The error signal is provided by a Pound-Drever-Hall readout scheme in reflection. In the impedance matched case, which was the initial design as shown in table 5.1 no carrier light is reflected and only the 8 MHz sidebands contribute shot noise on the locking photodiode.

On the inquiry of the mirrors, the polarization was not specified. This lead the coater to match the reflectivity parameters given for unpolarized light. Since dielectric coatings used under 45° typically have

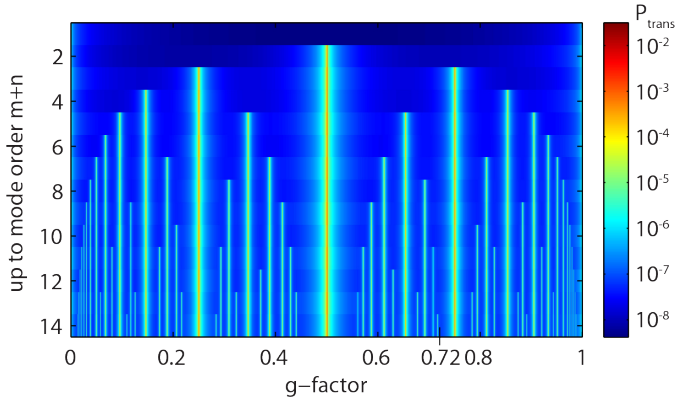

Figure 5.2.: The power cumulative transmissivity of higher order HG_{mn} modes up to order $m+n$ versus cavity g-factor is shown for the parameters given in table 5.2. The power content of each mode order is weighted as $P_{mn}=\exp(0.075(m+n)-2)$ according to the fit to a laser in [41]. The power distribution within each order is equal between the individual modes. For comparison, 0.73 of the fundamental mode is transmitted. The g-factor of 0.72 allows for a good higher order mode and s-pol suppression (compare figure 2.7 for the lower finesse equivalent) in conjunction with similar spot sizes on both mirrors (g close to 1).

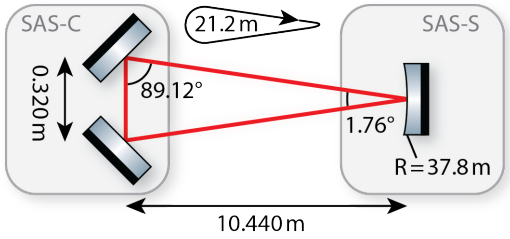

Figure 5.3.: The measured radius of curvature of the end mirror in conjunction with the desired g-factor determines the required optical round trip length (actually the radius of curvature was specified the other way around after knowing the available space). The distance between in- and outcoupler and thereby the opening angle of the mode is given by the suspension frame. A smaller opening angle results in less astigmatism (the effective radius of curvature in the given design is 4.5 mm bigger in vertical and 4.5 mm smaller in horizontal) but also leads to increased scattering into the reverse-traveling mode.

a ten to hundred times higher reflectivity in s-polarization(compare figure D.17), the actual p-reflectivity is half of the design value. It became clear quickly, that s-pol was no option anymore as the intra cavity losses would dominate which would reduce the overall sensitivity. Choosing p-pol also implies several drawbacks: The additional number of layers increases coating thermal noise, the reduced impedance matching requires more PDH modulation depth to dominate the additional re-

design parameter	RefC
T_{RC2a} (input)	500 ppm
T_{RC2b} (output)	300 ppm
T_{RC1a} (HR)	10 ppm
add. loss	guess: 200 ppm per round trip
Finesse	6218
$P_{trans,DC}$	59%
$P_{refl,DC}$	0%

Table 5.1.: The RefC design reflectivities in s-polarization are different to what was obtained in terms of actual coatings (see table 5.2).

parameter	RefC
T_{RC2a} (input)	1000 ppm
T_{RC2b} (output)	600 ppm
T_{RC1a} (HR)	10 ppm
add. loss	guess: 200 ppm per round trip
$P_{trans,DC}$	73%
$P_{refl,DC}$	1.1% (5.9% for 0 ppm loss)
$P_{refl,RF}$	2·1.3% (2·0.6% for $\beta = 0.15$)
Finesse	3468
FSR	14.14 MHz
FWHM	4.05 kHz
P_{in}	266 mW
w_0	2.40 mm
w_{RC2}	2.40 mm
w_{RC1}	2.83 mm
g-factor	0.720
$l_{round\ trip}$	2·10.6 m
f_{mod}	8.047260 MHz
β_{mod}	0.15..0.23 rad

Table 5.2.: The obtained RefC coatings deviate from the design by about a factor of two and in polarization (p instead of s). Based on the actual reflectivities the RefC parameters of the realizable cavity were deduced.

flected carrier by sidebands and the reduced finesse compromises shot noise limited sensitivity.

5.3 CAVITY ALIGNMENT

Suspended mirrors have the tendency to drift in terms of alignment. Therefore spot references are required. While the reference cavity is locked, these will provide a slow feedback signal for the cavity mirror

alignment actuation. The fast alignment compensation is covered by another active feedback system described in the AC alignment section.

5.3.1 *Alignment acquisition and DC control*

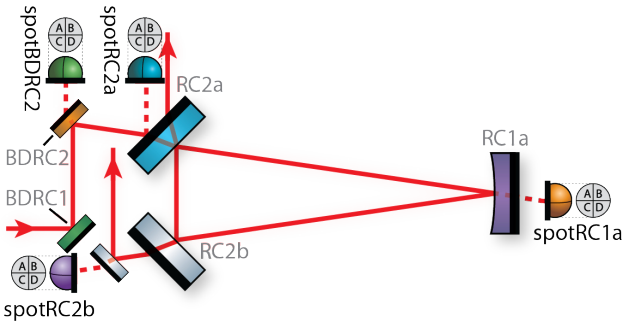

Figure 5.4.: Spot position sensors serve as references for most suspensions' alignment. These sensors are rigidly connected to the SAS surface to provide local beam positions free of SAS motion relative to ground. The colors symbolize the mirror whose alignment is read out. This information can be used to reach a known optical state of the cavity during lock acquisition and for slow feedback during lock.

It is crucial to provide alignment references for lock acquisition. During air/vacuum cycling, the suspensions are getting heavily disturbed. The shadow sensors cannot provide information about the actual test mass alignment (those are only sensing the upper mass). The spot position sensors, in contrast, monitor the angular test mass alignment. The alignment procedure using these sensors is described in chapter 5.3. There are sensors for all but RC2b alignment. But this single mirror has only two unknown alignment degrees of freedom and flashing of the non-locked cavity gives information about the residual cavity misalignment. During lock, the auto alignment system will keep the ingoing and the cavity mode overlapped. Thus the transverse beam (between the RC2 mirrors) is matched to the beam coming from BDRC2 and spotBDRC2 provides some reference for it as well.

All QPD signals are normalized to get rid of power fluctuation and gap influences as described in chapter 6.7.4. Hence, the set position doesn't have to be centered exactly on the QPD and no fine tuning for the alignment (like a steering mirror) is foreseen. The readout scheme of the sensors is described in more detail in chapter D.2. Based on this, there is also a readout scheme for extremely low power such as spotRC1a, for when the cavity isn't locked yet. Furthermore, as some of those signals vary strongly between locked and unlocked cavity state, i.e. by finesse squared, the sensitivity of spotRC1a and spotRC2b are switchable as shown in the next section.

5.3.2 *Spot positioning at the pW level: QPD readout box switchable*

In cases, where the in-vacuum QPDs are used to sense the alignment of a cavity mode, the detected amount of light decreases hugely if the cavity is not resonant. The difference can be as big as six orders of magnitude for high finesse cavities like the reference cavity ($\mathcal{F} \approx 3500$). Yet, especially in the non-resonant case a method is required to get the suspended mirrors aligned before locking the length degree of freedom. Investigations showed, that commercially available, continuously tunable amplifiers could bridge the different power levels but do not reach the required noise performance.

The spot position detector behind RC1a poses the most stringent requirements: The mirror's transmissivity is only approximately 4 ppm [101]. With a power buildup factor of about 1000, the intra cavity power out of lock is only 10^{-3} of the input power, so the fractional RC1a transmitted power is below the $4 \cdot 10^{-9}$ level or 1 nW in absolute units.

As there are only two states to be distinguished, resonant and not resonant, i.e. high power and low power, a continuous tuning of the sensitivity is not required. Hence, the amplifier can be built discrete with only two states as well: low gain and high gain. Now an amplifier after the photo current to voltage conversion would amplify the transimpedance amplifier's noise as well. It turns out that the signal-to-noise ratio can be increased by changing the actual transimpedance resistor instead. Then, the noise only increases by the square root of the resistance while the signal amplification goes linearly with the resistance. In practice, a DG419 analog switch was used to choose between a 20kΩ and a 303kΩ transimpedance resistor. A higher value was not possible using the original design of chapter B.8 due to the input impedance of the OP27 which is only 4MΩ.

Therefore, as a next iteration step, the transimpedance amplifier was changed from an OP27 to a pin compatible AD711 low noise FET opamp with much higher input impedance. It is crucial to use the DIP version as the SMD Package suffers from a factor of three increased noise. This allows to implement a transimpedance resistor as large as 100MΩ. In this extreme case, a 1 nF capacitor has to be stacked in parallel resulting in a 1.6 Hz low-pass. The 20kΩ path is limited to 8 kHz by a parallel 1 nF capacitor.

Being able to detect extremely low photo currents with the new layout, the dark current of the biased photo diode, and especially its variability e.g. with temperature, turned out to be the limiting factor. This can only be overcome practically, by reducing the bias,

$$I_{\text{dark}} = \left(e^{\frac{qU_{\text{bias}}}{k_{\text{B}}T}} - 1 \right) \tag{5.1}$$

which sacrifices detector speed and power handling capabilities. Therefore, the bias voltage is switched together with the gain between the

(for safety reasons current limited) 15 V of the standard QPD readout box (check figure B.6) for high gain mode and a reduced bias as small as 10 mV for the low gain mode.

Finally, the offset of the LT1124-stage for differentially sending the signal becomes the bottleneck. This can be improved by using an offset/drift compensated LTC1151 opamp. Yet, it was not robust enough for an experimental lab environment. Not only is it quite expensive in comparison to the LT1124, but also it broke extremely easily, so this change was not implemented into the final design.

To confirm the potential performance, a QD50-3T QPD is attached to the switchable readout box via a long (10 m) Cat7 cable to simulate 10 m Prototype conditions. The photodiode is shielded from as much ambient light as possible. The dark currents of all four quadrants are measured by means of differential output signal and converted to photo currents and finally to equivalent detected power assuming an efficiency of 0.1 A/W (taken from the datasheet). The result is shown in table 5.3

quadrant	U_{out}	I_{PD}	equiv. power
A	0.74 mV	3.7 pA	37 pW
B	0.24 mV	1.2 pA	12 pW
C	0.14 mV	0.7 pA	7 pW
D	0.54 mV	2.7 pA	27 pW

Table 5.3.: Performance of the switchable QPD in high gain mode (100MΩ).

quadrant	U_{out}	I_{PD}	equiv. power
A	0.72 mV	109 nA	1091 nW
B	0.24 mV	36 nA	364 nW
C	0.14 mV	21 nA	212 nW
D	0.54 mV	82 nA	818 nW

Table 5.4.: Performance of the switchable QPD in low gain mode (3.3kΩ).

and 5.4. From the comparison of the output voltages of low and high gain mode it can be seen, that the output offset stays almost constant, a hint that it arises from the common readout electronic path and not the QPD itself. Furthermore, it can be seen that the average DC offset of 415 µV is well above the CDS input noise of approximately 20 µV rms (equivalent to 1 pW rms). Hence, optical beams brighter than the equivalent power levels should be detectable. A further improvement appears achievable by using a better differential sender stage in future, for example the input offset cancellation scheme of the BOSEM readout

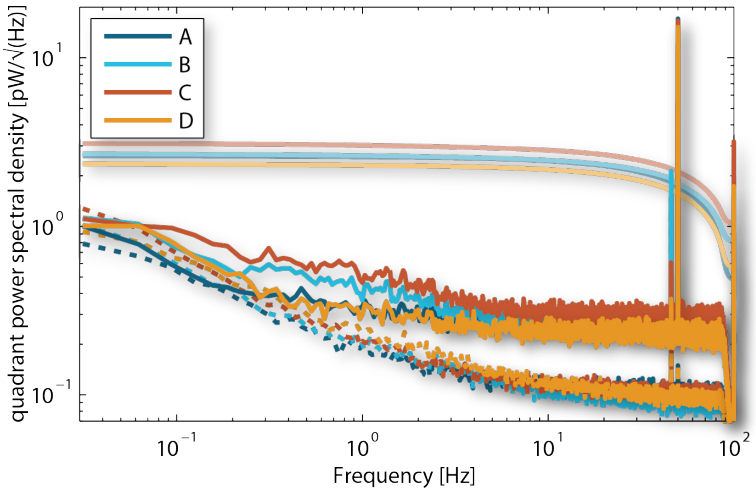

Figure 5.5.: Shown is the total noise spectral density of the readout electronics (dashed) and of the full QPD readout (straight lines) of all four quadrants of the switchable QPD in high gain mode. The electronic dark noise barely contains any 50 Hz signal. The QPD readout shows 50 Hz incoupling into the long cables, which is canceled completely in the pitch and yaw signals while 100 Hz originates from faint ambient light coupling which is not subtracted. The 46 Hz signal (shows up mostly in yaw) is unexplained yet. Light colors depict each channels rms, neglecting the 50 Hz signal.

box or a more reliable version of the LTC1151. Nevertheless, with the current readout scheme a detection and location of the beam behind RC1 is possible when using digital DC offset subtraction, as described in the following paragraphs.

In practice, the reliable detection of such light levels requires further work like the elimination of stray light and ambient light. For this purpose, a blocking tube with a baffle and an RG850 filter is attached in front of the spot position sensor behind RC1. Nevertheless, other experiments were found to introduce stray light at the several nW level while the RC1 transmitted beam only shows about 30 pW. Further stray light elimination might be possible by implementing polarizing filters. The RefC uses p-polarized light while almost all other experiments utilize s-pol. Hence, the stray light is probably mostly s-polarized and can be filtered away which remains to be checked.

To demonstrate that the QPD is working as supposed, the other experiments were shut down. In normal use longer averaging times must be used while in future more care will be taken to terminate potential stray beams (see chapter D.1). To demonstrate the alignment procedure, the cavity was strongly misaligned intentionally to simulate a real alignment procedure under vacuum. This is important, since flashing of higher order modes produces multiple spots even far apart from the optical axis of the ingoing beam. Then, the cavity input

beam is steered by means of BDRC2 while the cavity is misaligned to avoid flashes (compare chapter 5.3.4). The sum channel of the QPD is monitored (see figure 5.6). A strong signal can be observed whenever

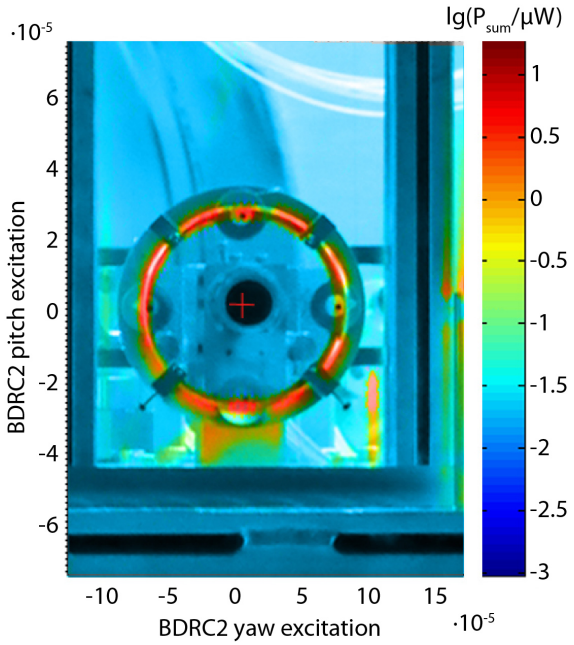

Figure 5.6.: The intra cavity beam can be located with respect to the table surface by scanning in vertical and horizontal by means of BDRC2 excitation. Observing the spotRC1a sum channel shown in units of $\ln(P_{\mathrm{sum}}/1\mathrm{nW})$, many suspension features, which can be seen on the overlaid photo as well, can be identified. Please note that this is almost all multi path stray light! The uncoated bevel of the mirror diffracts light into the PD. This gives a nice reference to find the center of the mirror (the actual QPD position). Hitting the QPD center itself produces a much weaker signal. Hence, it is marked with the red cross (the stray light barrel is not optimally aligned).

the beam is hitting the uncoated mirror's bevel. Then it is diffracted into the scatter tube which cannot shield against the relatively strong beam. The circular shape of the signal makes it is rather easy to pinpoint the mirror's center. The large signal-to-noise ratio speeds up the process. It is basically limited by the fact, that an instant response of the steering mirror is required (scanning well below the resonance frequency).

Once the center of the mirror is located, the beam can be steered onto it. Figure figure 5.7 shows, that despite of the pW light levels the pitch and yaw channels can be used well for further aligning the beam to the QPD's very center. The error signals are in good agreement with the theoretical model shown in figure 5.8. It can be used for automatic spot centering. After steering the cavity input beam to the correct position care must be taken, that the automatic alignment loop is switched off

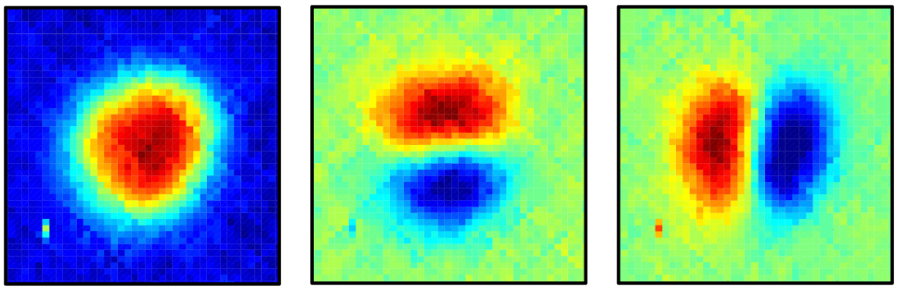

Figure 5.7.: The figure shows the intra cavity beam measured behind RC1 at the pW level. The beam is scanned in vertical and horizontal while the RefC is misaligned intentionally to avoid flashing. Three channels are observed: sum, pitch and yaw (from left to right). The sum signal can be used to find the beam initially. Pitch and yaw in turn serve as error signals to align the beam to the QPD's very center. The whole measurement took only a few minutes.

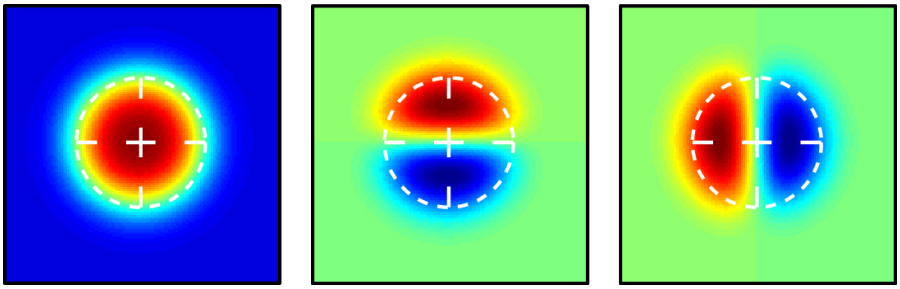

Figure 5.8.: The simulation for the signals in figure 5.7 are shown. Even without any fitting they match the measurement extremely well. For a better understanding, the 8 mm photodiode with its four quadrants is depicted. The beam is assumed to have a size of 2.7 mm.

to prevent confusion from flashing. Once the cavity can be locked, the very same QPD can be used again, this time on low gain mode, for spot positioning.

5.3.3 *AC alignment control*

Differential wavefront sensors are keeping track of misalignments between the cavity- and the ingoing mode [78, 102]. Only the steering mirrors are acted by a feedback loop in order to compensate for the misalignment. This approach assumes the cavity mirrors to be the most quiet reference in the whole system, which is only true above a certain frequency. Together with slow drifts of the triples, the cavity mode moves as well. Therefore at low frequencies an additional loop is required to center the spots on the individual mirrors.

5.3.4 *'Initial' RefC alignment*

The scope of this section is to give a checklist how to obtain reference cavity lock from a completely misaligned cavity by means of a reference position which is defined in the following section. Sometimes BOSEM positions serve as good reference but they can change very strongly, especially during/after pump down Furthermore, they only resemble upper mass alignment. Therefore, spot position sensors were installed, reading the alignment of the actual cavity mode.

- Align the two SAS platforms. The RC mirror actuators may exceed range otherwise.
- Use BDRC1 actuation to reach the set position of the normalized spotBDRC2 sensor. Verify that the beam is hitting by checking the sum power level on the QPD.
- Steer the AR reflex from RC2a onto spotRC2a by RC2a upper mass' angular actuation.
- Misalign RC2b to avoid flashes.
- Switch spotRC1a to high gain mode.
- Center the beam on spotRC1a by BDRC2 actuation. If the beam cannot be found on the sensor at all, search for the RC1a chamfer by increasing the scanning range. The QPD is close to the center (see figure 5.6).
- Ensure that there is not clipping on RC2a. There is little margin for in-going and reflected beam on the AR side as seen in figure 4.3.
- Actuate on RC1a to hit spotRC2b being set to high gain mode. Again, sweeping across the chamfer might help to find the correct spot.
- Re-align RC2b and search for flashes. There is no reference QPD for this mirror.

A reference position is a fully defined state, in which the fundamental mode of the reference cavity flashes significantly or at best lock is obtainable. This state should be restorable under varying conditions like an evacuated system or small changes in the suspensions such as wire slippage or thermal drifts. 'Fully defined' requires all sensors to read sensible signals. For this, the following checklist must be enforced.

- Of course the cavity must flash, i.e. be lockable.
- None of the spotPD may be saturated or more than 0.8 off from the center in terms of normalized pitch/yaw channel.

- The offset cancellation for the sensitive spot sensors must not be calibrated too long ago.[3]
- Shadow sensors must be well within their linear range.
- Light should be sensed on the RefC reflected and transmitted photodiode. This requires SAS-C to be in a restorable position. Then all QPDs should be reachable as well.
- All suspensions must be free. The spot sensors are a good tool to ensure this.

5.4 NOISE CORRELATION IN A TRIANGULAR CAVITY

In the Reference Cavity, two mirrors are sensed under an angle of incidence close to 45°. These can move longitudinally in common, i.e. towards a common center, or differentially which is illustrated in figure 5.12 and 5.13. The differential mode does not change the round trip length in first order but is equivalent to sideways motion of the curved mirror. The common mode, in turn, has impact onto the round trip length. Therefore the effect of a single mirror's longitudinal motion is halved. Both 45° mirrors contribute the same as if they were replaced by a single mirror under normal incidence. Another way to look at the problem is to neglect the geometry change of the mode for simplicity. The given longitudinal displacement of a mirror hit under normal incidence, such as RC1a, causes twice the amount in optical path length change per round trip. In the case of non-normal incidence under an angle of β, as with the RC2-mirrors, it contributes only $1/\cos\beta$ as much to path length change, i.e. for $\beta \approx 45°$ this is $\approx 1/\sqrt{2}$ of the normal incidence effect.

If the longitudinal displacement spectrum $\sqrt{S_\mathrm{L}}$ of all three cavity mirrors is similar but uncorrelated (as in the case of thermal noise), their incoherent sum

$$\begin{aligned} S_\mathrm{round} &= \left(2\sqrt{S_\mathrm{1a}}\right)^2 + \left(\frac{2\sqrt{S_\mathrm{2a}}}{\sqrt{2}}\right)^2 + \left(\frac{2\sqrt{S_\mathrm{2b}}}{\sqrt{2}}\right)^2 \\ &\approx 8S_\mathrm{L} \end{aligned} \tag{5.2}$$

gives the round trip length change. Imagine a two mirror cavity consisting of the mirrors TNI-A and TNI-B, then the round trip length change caused by uncorrelated motion

$$\begin{aligned} S_\mathrm{round}^\mathrm{TNI} &= \left(2\sqrt{S_\mathrm{A}^\mathrm{TNI}}\right)^2 + \left(2\sqrt{S_\mathrm{B}^\mathrm{TNI}}\right)^2 \\ &\approx 8S_\mathrm{L} \end{aligned} \tag{5.3}$$

3 It was observed, that the offset is quite constant on short timescales but prone to comparably large drifts, especially dependent on operational status of other subsystems.

is the same!

If the noise occurring at the cavity mirrors is correlated however, like it is the case for radiation pressure noise, the coherent sum

$$\sqrt{S_{\text{round}}} = 2\sqrt{S_{1\text{a}}} + 2\frac{\sqrt{S_{2\text{a}}}}{\sqrt{2}} + 2\frac{\sqrt{S_{2\text{b}}}}{\sqrt{2}} \tag{5.4}$$

must be taken. It is important to note, that the radiation pressure onto RC2a & RC2b is also reduced by the angle of incidence ($S_{2\text{x}} \approx S_{1\text{a}}/2$). Then the total noise

$$\begin{aligned} \sqrt{S_{\text{round}}} &= 2\sqrt{S_{1\text{a}}} + \sqrt{2}\sqrt{S_{1\text{a}}/2} + \sqrt{2}\sqrt{S_{1\text{a}}/2} \\ &\approx 4\sqrt{S_{1\text{a}}} \\ S_{\text{round}} &\approx 16 S_{1\text{a}} \end{aligned} \tag{5.5}$$

is again the same as that in the two mirror cavity

$$\begin{aligned} \sqrt{S^{\text{TNI}}_{\text{round}}} &= 2\sqrt{S^{\text{TNI}}_{\text{A}}} + 2\sqrt{S^{\text{TNI}}_{\text{B}}} \\ &\approx 4\sqrt{S_{\text{L}}} \\ S_{\text{round}} &\approx 16 S_{\text{L}} \ . \end{aligned} \tag{5.6}$$

5.5 COMMON MODE REJECTION

A linear optical cavity like the TNI described in chapter 6 provides common mode rejection. If the ground moves along the beam axis, approximately the same force is exerted onto both mirrors. Usually the mirror mounts are similar in a sense, that their transmissibility of ground motion is the same. Then they move mostly in common. This will not produce a first order interferometric length signal. If the ground moves transverse to the beam axis, the force onto the mirrors will be sideways which does not couple to the length signal either.

In the case of the reference cavity, the symmetry is broken. First of all the suspensions are more than 10 m apart. For frequencies well below the inverse travel time of sound $3\text{km/s}/10\text{m} = 300\text{Hz}$ the two 'sites' move mostly in common. But then the suspensions are placed on elaborate seismic attenuation systems (SAS-tables). Due to their complexity, the transfer functions don't match perfectly. Finally, two of the three mirrors making up the reference cavity are used under an angle of $\approx 45°$. The rest of this section is dedicated to calculating the influence of the latter.

Due to the different orientations of the mirrors, several coordinate systems are involved. The Prototype-coordinate system (x, y) is aligned along the arms (west, south). The suspensions have their own, local coordinate system (longitudinal, side). For simplicity, the angle of incidence onto RC1a is assumed to be 0°, the angles of incidence onto RC2a and RC2b optimally are equal and therefore 45°. A more detailed study without these restrictions can be found in chapter D.5. With

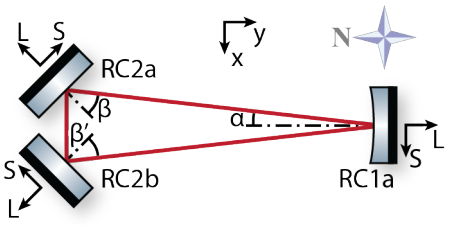

Figure 5.9.: Due to the triangular reference cavity geometry the suspensions show eigenmodes in different coordinate systems. Furthermore, there is the Prototype's reference system (x,y).

these assumptions it is easy, to decompose the motion of the ground (top of SAS) in the Prototype's (x,y)-system into the local coordinate system $(L,S^{\mathrm{gnd}}_{\mathrm{susp}})$ oriented along the mode directions **L**ongitudinal and **S**ideways of any suspension. In this local coordinate system the mechanical modes of the corresponding suspension decouple well. Then the mirror motion $L,S^{\mathrm{mirr}}_{\mathrm{susp}}$ can be expressed in terms of the transmissibility $H^{\mathrm{DOF}}_{\mathrm{susp}}$ along the degree of freedom DOF and the ground motion.

$$
\begin{aligned}
L^{\mathrm{gnd}}_{\mathrm{1a}} &= y & L^{\mathrm{mirr}}_{\mathrm{1a}} &= H^{l}_{\mathrm{1a}} L^{\mathrm{gnd}}_{\mathrm{1a}} & \partial_{L^{\mathrm{mirr}}_{\mathrm{1a}}} \Delta_{\mathrm{rt}} &= 2 \\
S^{\mathrm{gnd}}_{\mathrm{1a}} &= x & S^{\mathrm{mirr}}_{\mathrm{1a}} &= H^{s}_{\mathrm{1a}} L^{\mathrm{gnd}}_{\mathrm{1a}} & \partial_{S^{\mathrm{mirr}}_{\mathrm{1a}}} \Delta_{\mathrm{rt}} &= 0 \\
L^{\mathrm{gnd}}_{\mathrm{2a}} &= \frac{-x-y}{\sqrt{2}} & L^{\mathrm{mirr}}_{\mathrm{2a}} &= H^{l}_{\mathrm{2a}} L^{\mathrm{gnd}}_{\mathrm{2a}} & \partial_{L^{\mathrm{mirr}}_{\mathrm{2a}}} \Delta_{\mathrm{rt}} &= \sqrt{2} \\
S^{\mathrm{gnd}}_{\mathrm{2a}} &= \frac{-x+y}{\sqrt{2}} & S^{\mathrm{mirr}}_{\mathrm{2a}} &= H^{s}_{\mathrm{2a}} L^{\mathrm{gnd}}_{\mathrm{2a}} & \partial_{S^{\mathrm{mirr}}_{\mathrm{2a}}} \Delta_{\mathrm{rt}} &= 0 \\
L^{\mathrm{gnd}}_{\mathrm{2b}} &= \frac{+x-y}{\sqrt{2}} & L^{\mathrm{mirr}}_{\mathrm{2b}} &= H^{l}_{\mathrm{2b}} L^{\mathrm{gnd}}_{\mathrm{2b}} & \partial_{L^{\mathrm{mirr}}_{\mathrm{2b}}} \Delta_{\mathrm{rt}} &= \sqrt{2} \\
S^{\mathrm{gnd}}_{\mathrm{2b}} &= \frac{-x-y}{\sqrt{2}} & S^{\mathrm{mirr}}_{\mathrm{2b}} &= H^{s}_{\mathrm{2b}} L^{\mathrm{gnd}}_{\mathrm{2b}} & \partial_{S^{\mathrm{mirr}}_{\mathrm{2b}}} \Delta_{\mathrm{rt}} &= 0
\end{aligned}
\tag{5.7}
$$

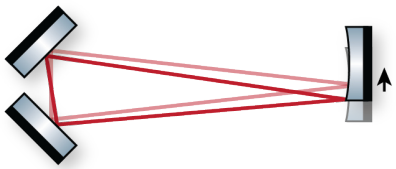

Figure 5.10.: Shifting the curved mirror sideways and leaving the other mirrors where they are, deforms the cavity mode with respect to the initial mode shown for reference as well. From pure symmetry the round trip length cannot change to first order (it is maximal with respect to the curved mirror). It was verified in geometric optics using Autodesk Inventor, that the second order length change is small as well.

In the proximity of optical resonance, the change of round trip length Δ_{rt} can be deduced to first order by means of each mirror's contribution $\partial\Delta_{\mathrm{rt}}/\partial X^{\mathrm{mirr}}_{\mathrm{susp}} := \partial_{X^{\mathrm{mirr}}_{\mathrm{susp}}}\Delta_{\mathrm{rt}}$ along the X-degree of freedom (replace by

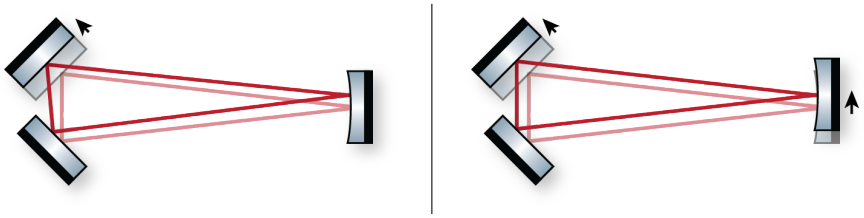

Figure 5.11.: The left figure shows the cavity eigenmode deformation when shifting the in- or outcoupler. Reducing the situation by the effect from shifting the beam on the curved mirror, which doesn't change the cavity length (see figure 5.10) makes the round trip length change obvious.

either L or S) which are shown graphically in figure 5.10 and 5.11. The sum of all contributions

$$\begin{aligned}\Delta_{\mathrm{rt}} &= 2L_{1\mathrm{a}}^{\mathrm{mirr}} + \sqrt{2}L_{2\mathrm{a}}^{\mathrm{mirr}} + \sqrt{2}L_{2\mathrm{b}}^{\mathrm{mirr}} \\ &= H_{1\mathrm{a}}^{l}\,(2y) + H_{2\mathrm{a}}^{l}\,(-x-y) + H_{2\mathrm{b}}^{l}\,(x-y)\end{aligned} \tag{5.8}$$

again can be decomposed into round trip length change induced by ground's x-motion

$$\left.\frac{\partial \Delta_{\mathrm{rt}}}{\partial x_{\mathrm{gnd}}}\right|_{y=0} = H_{2\mathrm{b}}^{l} - H_{2\mathrm{a}}^{l} \tag{5.9}$$

and ground motion in the y-direction

$$\left.\frac{\partial \Delta_{\mathrm{rt}}}{\partial y_{\mathrm{gnd}}}\right|_{x=0} = 2H_{1\mathrm{a}}^{l} - H_{2\mathrm{a}}^{l} - H_{2\mathrm{b}}^{l}\ . \tag{5.10}$$

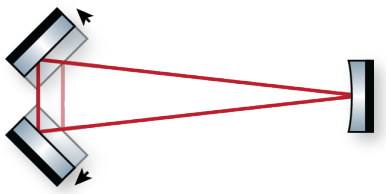

Figure 5.12.: The RC2-shift to round trip length coupling becomes more intuitive when separating it into common and differential mode. The common mode shifts the traversing beam. For small opening angles this increases the round trip length by twice the sideways shift.

It is astounding, that the rejection of ground's x-motion only depends on the matching of the 45°-mirrors' transfer functions. This should be extremely good in the higher frequency range above the resonances, where the response is governed by inertia and moments of inertia. The susceptibility to y-motion is reduced by the matching of all three transfer functions. In reality RC1a might see a different ground motion due

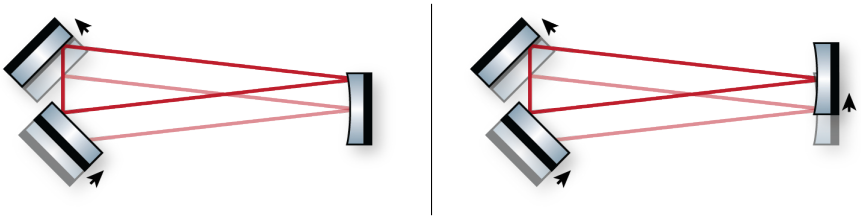

Figure 5.13.: A differential shift of the RC2 mirrors causes an almost pure sideways shift of the mode. Due to the curvature of RC1 this induces a mode tilt as well which, however, can be canceled by shifting RC1. According to figure 5.10 this doesn't produce any length change and shows that the differential shift barely affects the round trip as well.

to unmatched SAS transfer functions. Also in the real Reference Cavity geometry with an angle of incidence of $\approx 1°$ onto RC1a and 44.5° onto the other mirrors (see figure 5.3) the common mode rejection in x-direction is determined by the matching of the suspensions if the beam between in- and out-coupler is aligned along the x-arm. In the y-direction, however, it cannot get better than 96.5% (as calculated in chapter D.5).

It is a surprising result, that the three mirror geometry yields almost the same insensitivity for seismic noise transverse to the long axis as a two mirror cavity would. Also the rejection of common noise along the long axis is of the order of (or even better than) the expected correlation of ground noise on top of the SAS platforms.

5.5.1 *alignment to length coupling*

A way to come up with angular stability requirements for the RefC might be to calculate the alignment to round trip length coupling. Then the stringent length requirements can be projected backwards into angular requirements.

There are two such couplings due to a deformation of the mode when tilting a mirror: the first one is moving the spot on the tilted mirror. Due to the tilt, the path length may change at this new spot position. The second one is a mode deformation directly leading to a round trip change. It will become obvious, that the first effect is only of second order as assumed in the last section, so that just the second effect can induce significant angular to length coupling. In the following section such a coupling is searched for in the case of a well aligned reference cavity (as in figure 5.3 with horizontal beams).

From geometry considerations, it is clear that a pitch change of RC1 walks the mode up and down. Depending on the exact rotation point of the mirror this may or may not cause a second order length coupling. This is also true for a differential pitch misalignment of RC2a and RC2b as shown in figure 5.14. It simply tilts the beam between the

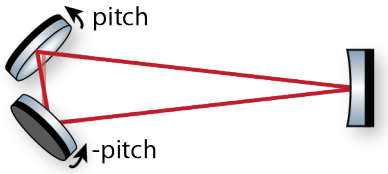

Figure 5.14.: A differential tilt of the RC2 mirrors results in a tilting of the transverse-propagating beam.

mirrors increasing the round trip in second order to both directions. The effect onto the resonating polarization is negligible. It is slightly rotated inside the cavity but light with the incorrect polarization is suppressed by the triangular geometry. A common pitch misalignment is easiest to understand when looking at the two mirror equivalent of the cavity as shown in figure 5.15. Then the round trip length change can be calculated by means of

$$\begin{aligned}\Delta_{\mathrm{rt}} &= (1-\cos(\mathrm{pitch}_{\mathrm{eff}}))[R_{\mathrm{RC1}} - L_{\mathrm{eff}}] \\ &\approx \frac{(\sqrt{2}\,\mathrm{pitch})^2}{(\sqrt{2}\,\mathrm{rad})^2}[37.5\,\mathrm{m} - 10.44\,\mathrm{m}] \\ &\approx 27\,\mathrm{m}\cdot\frac{\mathrm{pitch}^2}{(1\mathrm{rad})^2}\end{aligned} \tag{5.11}$$

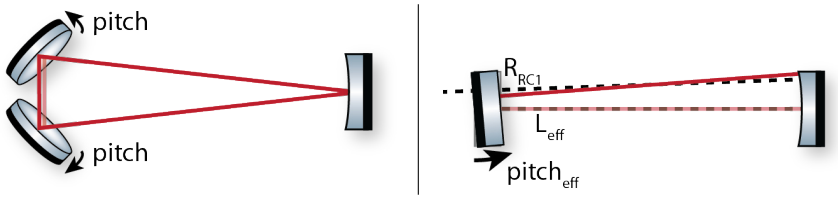

Figure 5.15.: A common pitch misalignment of the RC2 mirrors by an angle 'pitch' on both mirrors as shown on the left is easier understood in the linear equivalent of the cavity depicted on the right. Here the flat effective mirror must be tilted by $\mathrm{pitch}_{\mathrm{eff}} \approx \sqrt{2}\cdot\mathrm{pitch}$.

For a yaw misalignment of the mirrors the situation is slightly more complicated. A geometric beam propagation model written in Autodesk Inventor reveals the couplings shown in figure 5.16. The fits

$$\begin{aligned}\Delta_{\mathrm{rt}}^{\mathrm{RC1\,yaw}} &\propto 2.5\,\mu\mathrm{m}\cdot\frac{\mathrm{yaw}^2}{(1\mathrm{rad})^2} \\ \Delta_{\mathrm{rt}}^{\mathrm{RC2\,yaw}} &\propto 1.0\,\mu\mathrm{m}\cdot\frac{\mathrm{yaw}^2}{(1\mathrm{rad})^2} \quad + 0.10\,\mu\mathrm{m}\cdot\frac{\mathrm{yaw}}{1\mathrm{rad}}\end{aligned} \tag{5.12}$$

for deviations 'yaw' from optimal alignment emphasize further, how small the couplings are.

In summary there is only significant alignment to length coupling in the common RC2 pitch degree of freedom.

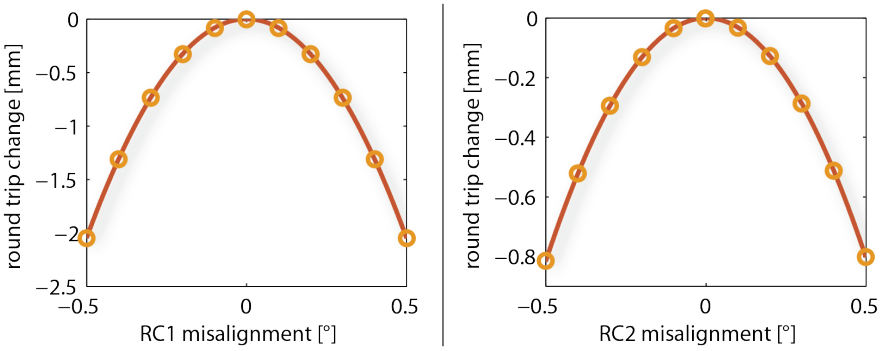

Figure 5.16.: The optical round trip length change with yaw misalignment of each mirror in the case of an otherwise well aligned RefC is shown. Only changes in second order are relevant. (There is a very minor linear coupling of 6µm/° observed in the RC2 fit since RC2 is not a perfect 90° corner cube. The exact value could also be spoiled by numerical inaccuracies.) Due to symmetry, RC2a and RC2b show the same response.

5.6 ALIGNMENT: 2" SUSPENDED STEERING MIRRORS

In suspended interferometers, the optical eigenmode always moves with respect to the environment. This motion is strongest on eigenmodes of the suspensions, which may not all be strongly dampable.

Maintaining optimal overlap with the ingoing beam requires some sort of alignment method. In general there are two widely used schemes: fast actuation onto small mirrors e.g. by means of piezo electric drives [41, 103], or slow alignment onto larger mirrors by means of suspended optics [102]. For the application in the RefC as well as the TNI, the second approach was chosen. It allows for larger optics, a bigger steering range and introduces less jitter noise at higher frequencies, especially in the detection band.

A good suspension provides low noise pivot points (compared to e.g. bearings). A wire support results in a weak restoring force and a low eigenfrequency. Above the resonance frequency, its behavior is governed by the inertia of the suspended mass, reducing coupling of ground motion and unavoidable actuation noise.

A 2"ø by 1 cm thick substrate is held inside an aluminum 'ring' using a three point Peek clamping. This compound structure increases the inertia compared to the bare mirror and gives mechanical mounting possibilities for push rods used for mechanical alignment, wire clamps for the suspension, magnets for actuation and robust surfaces for end stops. The overall mass distribution is relatively symmetric to have similar inertia and therefore the same high frequency behavior in pitch and yaw (see figure 5.19).

The compound mirror is hung from a single wire loop, whose ends are clamped using a length defining jig. The clamps are then bolted to the sides of the compound mass. The height of the break-off point was

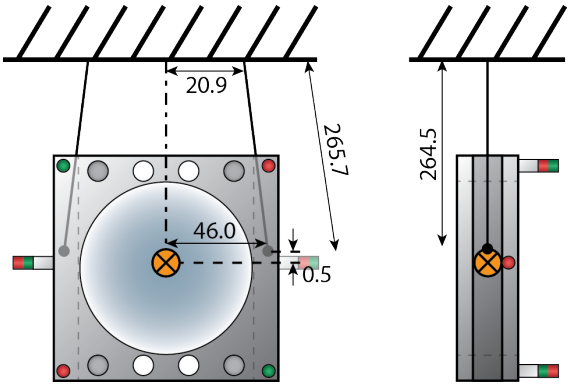

Figure 5.17.: In the 2" steering suspensions displayed (not to scale!), the uncertainties are very small due to the simpler construction compared to the triple suspensions described earlier. There are no cantilevers involved as in the triples. The top wire separation defining the side/roll modes and the yaw modes, is set by the clamping mechanism. This manifests in almost identical suspensions (compare figure 5.19 and 6.18)

chosen small to obtain the same pitch rotation point at all frequencies. At the top, the wire is wound around dowel pins defining the separation. Angling the wires inwards (closer together at the top) brings the yaw frequency down towards the pitch frequency. Once the suspension is leveled in roll, the wire is clamped at the top using a big brace.

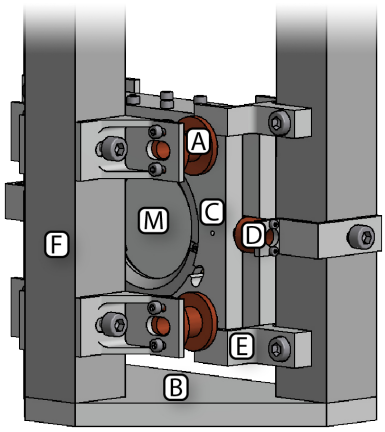

Figure 5.18.: The steering mirror's **B**aseplate holds a **F**rame reaching up to the suspension point (not shown). The **C**ompound mass hosts a 2"ø, 1 cm thick fused silica **M**irror. There are four **A**ctuation coils which also provide eddy current damping and two additional side-**D**ampers. **E**ndstops serve as safety guards in case of excess table motion.

The suspension is actuated electromagnetically. Four cylindrical 5 mm ø, 5 mm thick NdFeB magnets are glued to the back corners of the compound mass, two are attached to the sides. Their orientation is chosen to minimize coupling from ambient magnetic fields into pitch and yaw (compare figure 5.17). The actuation coils (see figure 4.20)

are mounted to the support frame. They have 200 windings each. The cores are made from copper to provide sufficient eddy current damping.

Every coil is actuated individually by means of its own CDS controlled current drivers (see chapter B.6). Inside CDS there are four actuation degrees of freedom synthesized. Pitch and yaw are used for alignment purposes. Longitudinal can sometimes be used to avoid hitting end stops in case of extreme alignment settings. Butterfly should not be used as it does not result in any motion and only produces heat. It can, however, inform about minor magnetization imbalances and was used e.g. in LIGO to investigate Barkhausen noise coupling [82, 104]. The pitch and yaw transfer functions of the RefC and TNI steering mirrors are shown in figure 5.19 and 6.18 respectively.

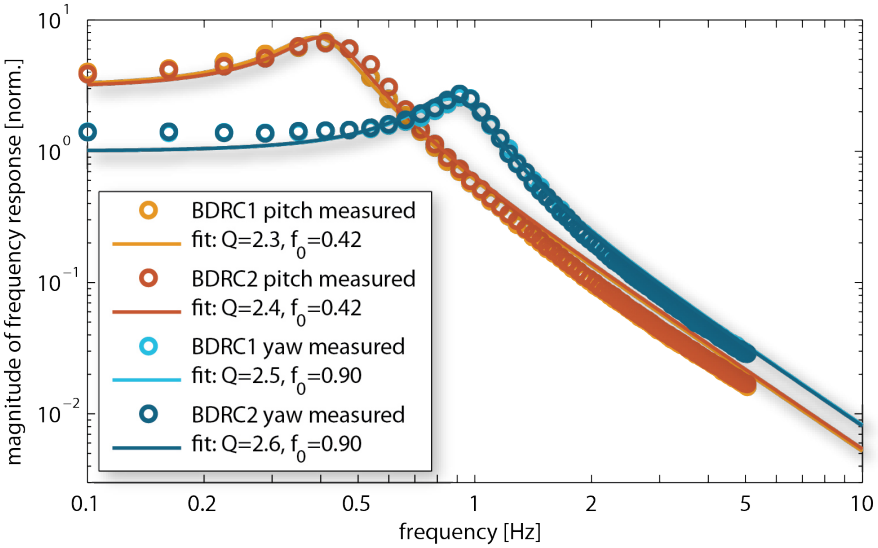

Figure 5.19.: This graphs show essentially the same as figure 6.18, the suspensions are identical in construction (but from a different assembly run). An important difference is, that this time the beam motion was measured outside vacuum on a table moving relative to the SAS-table with the suspensions. The bigger necessary excitation amplitudes caused the signal to run into nonlinearities (a considerable fraction of the beam moved across the photodiode's gap), which is probably the cause for a worse fit and differences in the obtained Q-values.

The support structure is fairly simply. Three 30 mm by 30 mm item posts (profile 6) support the top plate which is giving the suspension point. A higher cage would allow for longer suspension wires and thereby a better mid frequency isolation. However, due to the compact design, the torsional stiffness would suffer a lot by means of strongly reduced cage resonance frequencies. The three-legged design provides full access to transmitted beams when used under 45° angle of incidence even with the actuation coils mounted onto the frame. For a special use in the SQL interferometer which is under normal incidence, the design had to be adopted slightly to four posts. Mechanical yaw

adjustment is performed by rotating the base of the suspension with respect to the table. Pitch can be changed by shifting the center of mass with respect to the wire break-off by means of stainless steel push rods.

For the application of feedback signals refer to section 5.3.

5.7 REFC DESIGN SENSITIVITY

The SQL interferometer imposes a requirement on the frequency (length) stability of the Reference Cavity. In order to find a feasible cavity design, all potentially limiting noise contributions needed to be simulated. The result is shown in figure 5.20.[4] More background information for the individual contributions is given in the following sections.

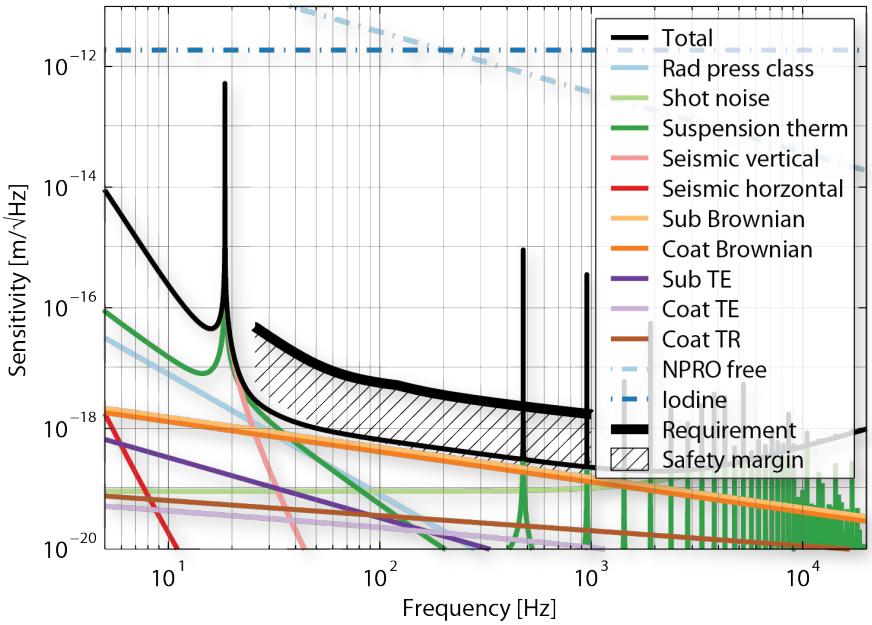

Figure 5.20.: Several noise terms are simulated for the reference cavity. The used parameters are summarized in table 5.2. Seismic and control noise (latter is partly predicted in figure 4.25) limit the low frequency range. Towards high frequencies, where the displacement response of the cavity goes down and shot noise takes over. In the intermediate range, the Brownian noise of the substrates and the coatings are dominating. Also some suspension thermal noise may show up. All noise sources are designed to be at least a factor of 10 below the equivalent classical noise of the SQL interferometer calibrated in laser frequency. The incoherent sum, however, is exceeding this safety factor slightly ($< \sqrt{2}$) when using the less optimistic substrate Brownian noise estimate.

4 This simulation is an extension of initial work carried out by F. Kawazoe during the planning phase of the RefC.

5 beam radius, where the power dropped to $1/e^2$

parameter	symbol	value
room temperature	T	293 K
laser wavelength	λ	1.064 µm
spot size HR-mirror[5]	w_{RC1a}	2.8 mm
spot size in-/outcoupler[5]	$w_{\mathrm{RC2a}} = w_{\mathrm{RC2b}}$	2.4 mm
coating layers HR-mirror	N_{RC1a}	≥ 36
coating layers incoupler	N_{RC2a}	≥ 28
coating layers outcoupler	N_{RC2b}	≥ 30
thermal expansion SiO_2	α_S	$0.51 \cdot 10^{-6}$ /K
temp. dependence of n for SiO_2	$\partial n_S / \partial T$	$8 \cdot 10^{-6}$ /K
thermal conductivity SiO_2	κ_S	1.38 W/Km
specific heat capacity SiO_2	C_S	746 J/kgK
density SiO_2	ρ_S	2200 kg/m^3
heat capacity per volume SiO_2	$C_S \rho_S$	1.64 GJ/Km^3
Young's modulus SiO_2	Y_S	72 GPA
Poisson's ratio SiO_2	σ_S	0.17
refractive index SiO_2	n_S	1.45
thermal expansion Ta_2O_5	α_T	$3.6 \cdot 10^{-6}$ /K
temp. dependence of n for Ta_2O_5	$\partial n_T / \partial T$	$14 \cdot 10^{-6}$ /K
thermal conductivity Ta_2O_5	κ_T	33 W/Km
specific heat capacity Ta_2O_5	C_T	306 J/kgK
density Ta_2O_5	ρ_T	6850 kg/m^3
heat capacity per volume Ta_2O_5	$C_T \rho_T$	2.1 GJ/Km^3
Young's modulus Ta_2O_5	Y_T	140 GPa
Poisson's ratio Ta_2O_5	σ_T	0.23
refractive index Ta_2O_5	n_T	2.06

Table 5.5.: Material parameters for noise simulations are mostly taken from [105] and double-checked with their original source [106]

Now, that a realistic RefC sensitivity which fulfills the posed frequency stability requirements was deduced, it can be used throughout the remainder of the thesis as new requirement. Technically it is not required, to bring the performance of the system down to this level over a broad frequency range. However, it would be a waste to not stabilize the laser noise to this incredible reference but being gain limited above a few hundred Hertz.

Hence, the full design sensitivity is used as requirement e.g. for local control as presented in figure 4.25, TTFSS as shown in figure 5.1 and many others.

5.7.1 *Laser frequency noise*

The measurement principle of the Frequency Reference Cavity relies on the fact that relative frequency noise

$$\frac{\Delta\nu}{\nu} = \frac{\Delta L}{L} \tag{5.13}$$

is measured by means of fractional length stability[6]. The non planar ring oscillator (NPRO) design provides already a high inherent frequency stability due to its monolithic nature. The free running frequency noise

$$\sqrt{S_{\text{freq}}^{\text{NPRO}}} = 100\,\frac{\text{Hz}}{\sqrt{\text{Hz}}} \cdot \frac{f}{100\,\text{Hz}} \tag{5.14}$$

is pretty common to any NPRO unit [99]. Even if the NPRO was locked to the molecular iodine reference of the SPI, this could only provide an improvement to $50\text{Hz}/\sqrt{\text{Hz}}$ at frequencies down to 10 mHz ([22] figure 4.7). This is still far from the requirement in the detection band but in the range of suspension resonances, where no requirement exists so far, better than the projected RefC noise (the extrapolation of the RefC noise would rise above the iodine reference at low frequencies in figure 5.20).

The difference between free running laser noise and the requirement sets the minimum required loop gain of the table top frequency stabilization servo (TTFSS) as used in section 5.1. Its error signals are fed back to the actuators built into the seed laser (temperature via a slow Peltier element and stress induced birefringence via a faster piezo electric actuator). In order to achieve the extremely high required gain (7 order of magnitude at 100 Hz), an even faster actuator is necessary to push the unity gain frequency to $\approx$300 kHz. This is done by a low range but high speed phase correcting EOM which is implemented between seed laser and amplifier.

In the desired mode of operation, the RefC sits on the isolating SAS tables and is used under vacuum. Then the laser frequency is locked to the Reference Cavity length. However, this scheme poses problems in air and especially with clamped SAS tables. Then the laser tries to follow the non-constant length of the Reference Cavity faster than the slew rate limit of the mode cleaner lock allows (unity gain frequency $\approx$5 kHz with a well behaved frequency response). This modulates the power incident on the RefC which occasionally causes positive feedback, so that the whole system becomes non-lockable.

5.7.2 *Laser intensity noise – radiation pressure effect*

The direct coupling of laser intensity fluctuations to the length detection is difficult to predict as it depends on too many yet to be deter-

6 It is important to note, that L refers to round trip length if ΔL refers to round trip changes which are equivalent to twice of a mirror displacement.

mined quantities. However, one major coupling mechanism is indirect: radiation pressure. As every photon carries momentum ($p = \mathrm{h}/\lambda$), a force

$$F = 2\,\cos(\alpha)\frac{P}{c} \tag{5.15}$$

proportional to the incident power P is exerted at reflection under an angle of incidence α. This force is called radiation pressure (RP) effect. Now the force is not constant as the reflected power may change. There are two contributions: classical RP due to technical power fluctuations and quantum RP arising from the quantization of light. Since the mirrors are suspended, they can be treated as free above their resonance frequencies. Then their longitudinal displacement fluctuation

$$\tilde{x} \propto \tilde{F}/m. \tag{5.16}$$

is proportional to the radiation pressure and the inverse mirror mass m. Lighter mirrors are more susceptible than heavier ones. The SQL interferometer with its 100 g test masses set the requirement for relative intensity noise down to the best demonstrated (from the point of the RefC quite comfortable) value of $2{\cdot}10^{-9}$ [107, 29].[7] The Reference Cavity mirror mass of 850 g limit the maximally tolerable power buildup (i.e. the finesse). The finesse reduction (compare table 5.1 and 5.2) also lead to a radiation pressure noise reduced by a factor of 2.

5.7.3 *Thermal noise prediction – the Fluctuation Dissipation Theorem*

The Fluctuation Dissipation Theorem proven by [108] allows to predict thermally driven motion of a linear system in thermal equilibrium in the direction of a generalized coordinate[8]

$$S_x = -\frac{4k_\mathrm{B}T}{\omega}\,\mathrm{Im}\{\chi(\omega)\} \tag{5.17}$$

by means of its dissipation[9] [58]. The dissipation can be calculated by the amount of dissipated energy per energy stored when driving the system in the questioned degree of freedom (see next section).

Mathematically it is expressed by the imaginary part of the susceptibility

$$\chi(\omega) = \frac{x(\omega)}{F(\omega)} \tag{5.18}$$

also referred to as the frequency response of the system in displacement per applied force. A similar formula

$$S_x = \frac{4k_\mathrm{B}T}{\omega^2}\,\mathrm{Re}\{Y(\omega)\} \tag{5.19}$$

7 This is achieved using a high gain intensity stabilization loop (ISS) with high power in-vacuum detection on a photodiode array.

8 This doesn't necessarily have to be a displacement [109].

9 Eq. 5.17 gives the single sided power spectral density, while other sources prefer a double sided PSD (half the value) [110]

can be given for the admittance

$$Y(\omega) = \frac{v(\omega)}{F(\omega)} = \frac{i\omega x(\omega)}{F(\omega)} = i\omega\chi(\omega) \tag{5.20}$$

or its inverse, the impedance $Z(\omega) = 1/Y(\omega)$.[10]

Modal approach

Predicting the imaginary part of the susceptibility is not trivial. Loss factors can be determined experimentally for resonances [111, 112], which leads to the modal approach. Every mode is assigned its own measured loss factor, or loss factors are predicted. The shape of each mode is calculated numerically which gives its eigenfrequency. From these parameters, the thermal motion of each mode is determined by means of equation 5.17. Finally the overlap of each mode with the interferometric readout gives a weighting factor resulting in an effective thermal noise for the readout.

The drawback of this approach is, that it assumes homogeneous losses across each mode. A classical example which breaks the assumption is when magnets are attached to the back side of a mirror. The introduced loss reduces the Q of substrate modes and couples to the interferometric readout directly due to symmetry of the modes. Hence, it usually leads to overestimation of thermal noise. This can be circumvented by Levin's direct approach.

5.7.4 *Levin pressure formalism*

In 1998, when the sensitivities of interferometric gravitational wave detectors were strongly pushing towards thermal noise limits in their most sensitive range, Levin revolutionized the theoretical simulation of thermal noise couplings.

The underlying principle of the idea is very simple. The fact, that a lasers senses the thermal noise unevenly had been accounted for by decomposing mirror fluctuations into eigenmodes. This approach assumed equal losses all over the substrate (uncoupled rigid body modes). Levin suggested a new technique [113] which calculates the effect of thermal noise onto the readout variable of longitudinal phase of the reflected light directly. For the first time it included the effects of non-homogeneous dissipation and large spot sizes (not negligible compared to the mirror diameter) correctly. The Levin Pressure Formalism is inspired by the idea of the Fluctuation Dissipation Theorem [108]: deducing the thermal noise from the mechanical admittance. The formalism makes use of this by virtually measuring the mechanical admittance by injecting elastic energy to locate dissipation channels.

10 Please note the concept of *mobility analogy* and *impedance analogy* for a more intuitive understanding of these mechanical quantities, especially for complex systems.

The novelty of Levin's approach is to assume the injected energy to have the same distribution as the profile of the interferometric readout beam. In the case of elastic processes, this can be realized by means of exerting a force. The loss angle (imaginary part of the restoring force, compare equation 3.6) then determines the amount of dissipation. Thermo-refractive processes, in contrast, are estimated by introducing an entropy [109]. The Fluctuation Dissipation Theorem then links the energy loss with the thermally driven motion.

The theory automatically covers the effects of non-homogeneous dissipation and large spot sizes (not negligible compared to the mirror diameter) correctly. It therefore leads to the result, that, in the domain of small beams, surface losses ($\propto 1/r^2$) become dominant over bulk losses ($\propto 1/r$), which is especially important for the TNI.

Example: the harmonic oscillator

In order to calculate the thermal noise of an arbitrary system, the imaginary part of the susceptibility $\chi = x/F_{\text{ext}}$ must be known according to equation 5.17. For a harmonic oscillator with mass m, spring constant κ and loss angle ϕ, it is given implicitly in equation 3.7 to be

$$\begin{aligned} \mathrm{Im}\{\chi(\omega)\} &= \mathrm{Im}\left\{\frac{1}{(-m\omega^2+\kappa)+\kappa\phi\, i}\right\} \\ &= -\kappa\phi\cdot|\chi(\omega)|^2 \ . \end{aligned} \tag{5.21}$$

Hence, according to equation 5.17, the thermal noise PSD

$$S_x = 4k_{\mathrm{B}}Tm\omega_0^2\frac{\phi}{\omega}\cdot|\chi(\omega)|^2 \tag{5.22}$$

stands in close relationship with the susceptibility. The ASD has the same shape as the susceptibility aside from a factor $\sqrt{\phi(\omega)/\omega}$. For viscous damping this is a constant, while for structural damping it is proportional to $1/\sqrt{\omega}$.

5.7.5 *Suspension thermal noise*

Losses in the suspension system couple the pendulum/mirror motion to the thermal heat bath. Noise being injected into the upper stages is filtered by the lower pendulum stages. Therefore the mirror motion is dominated by the lowest stage's thermal noise. In the frequency range above the suspension resonances, the suspension's degrees of freedom are well decoupled. In this region according to [114], the thermal noise can be approximated by

$$S_{\text{therm}}^{\text{sus}} = \frac{4k_{\mathrm{B}}T\omega_0^2(K_e/K_g)\phi_e}{M\omega^5} \tag{5.23}$$

for big dilution factors K_e/K_g (compare [58] eq.(22)). $K_e = T\Delta/L^2$ and $K_g = T/L$ are the pendulum spring constants due to elasticity, (bending of the wire) and gravitational potential respectively. The gravitational restoring force is considered as lossless, while bending losses are 'diluted' by the ratio of the spring constants. This is approximated well by the ratio $K_e/K_g = \Delta/L$ of the characteristic elastic length $\Delta = \sqrt{EI/T}$ [115], over which the wire bends and the suspension length[11]. The eigenfrequency of the stage $\omega_0^2 = K_g/M$ is hugely dominated by the gravitational restoring force and the mirror mass M. Concerning the choice of the parameters, a high effective Q-value $Q_{\text{eff}} = 1/[(K_e/K_g)\phi_e]$ is desired to lower suspension thermal noise. Values up to 10^6 have been shown for steel wires in GEO600 [116]. This can be achieved by means of high dilution factors which is equivalent to loading the suspension close to its breaking limit. Usually, suspensions are not loaded more than 30% of their maximum yield strength. In the RefC case the loading was increased to 40% to keep the frequency of bounce modes low and violin modes high. After several failures, the suspension was converted to specially hardened 3 GPa wires. This gives a much safer <30% loading after which no wire failure was observed anymore.

Since the intermediate mass is in a stiffer potential, the recoil should be low. Figure 4.28, however, shows that the simplified model overestimates the suspension thermal noise by a factor 3. For more accurate results, especially in the lower detection band around 20 Hz, the state space model of the suspension had to be solved and inserted in equation 5.17.

Other degrees of freedom usually couple weakly into the interferometric readout. [114] claims for LIGO, that '*When added in quadrature, the total thermal noise is 23% higher than the contribution of just the horizontal thermal noise.*'. In the RefC this is about 33% in the off-resonant case. At the lower end of the detection band, which is actually limited by the lowest stage vertical bounce mode, vertical suspension thermal noise becomes even dominant over longitudinal (compare chapter 4.8).

According to section 5.5, the total effect of all three suspensions onto the interferometric readout is the incoherent sum of that of the three individual contributions.

5.7.6 *Coating thermal noise*

The thermally driven path length noise induced by the reflective coating of a mirror is called coating thermal noise [117, 118, 105]. There are various manifestations of thermal fluctuations: The uncorrelated motion of the molecules causes Brownian noise, thermally induced stresses cause thermo elastic noise and the change of the index of refraction in-

11 The steel wire suspension with the highest Q measured until today, is the GEO600 mode cleaner suspension with a dilution factor of $1.5 \cdot 10^{-3}$ [116]. The RefC suspension might break this record, providing a factor 2 more dilution($5.9 \cdot 10^{-4}$)

side the coating causes thermo refractive noise. The latter two are not necessarily uncorrelated, even cancellation is possible [11] and may be summarized as thermo-optic noise.

Coating Brownian noise

Coating Brownian noise has the same origin as substrate Brownian noise, i.e. mechanical loss of the material. However, it is usually treated separately, as the thin films of the coating stack have much higher losses than the bulk substrate. A mathematical derivation of Brownian noise can be found in [119]. There are assumptions made, which shall be checked: The measurement band of the RefC, i.e. the frequency region in which a sufficiently high TTFSS gain appears achievable, reaches up to a few kHz (compare figure 5.1). This is definitely well below any mirror resonances in the several tens of kHz range. The calculation is simplified a lot with very minor changes when the readout beam is small compared to the mirror dimensions. Then the substrate can be approximated as being infinite (filling the semi-infinite half plane behind the mirror surface). This method neglects boundary effects from the circumference and the back of the mirror. For larger beams, a different theory must be used [120]. According to [119] equation 22, the Brownian coating noise of an infinite half plane can be calculated by

$$\begin{aligned} S_{\mathrm{Brown}}^{\mathrm{coat}} =& \frac{2k_{\mathrm{B}}T}{\pi^2 f}\frac{1-\sigma_{\mathrm{s}}^2}{wY_{\mathrm{s}}}\frac{d}{w}\frac{1}{Y_{\mathrm{s}}Y_c(1-\sigma_c^2)(1-\sigma_{\mathrm{s}}^2)} \\ &\times[Y_c^2(1+\sigma_{\mathrm{s}})^2(1-2\sigma_{\mathrm{s}})^2\phi_{\parallel} \\ &+ Y_cY_s\sigma_c(1+\sigma_c)(1+\sigma_s)(1-2\sigma_s)(\phi_{\parallel}-\phi_{\perp}) \\ &+ Y_{\mathrm{s}}^2(1+\sigma_c)^2(1-2\sigma_c)\phi_{\perp}] \end{aligned} \tag{5.24}$$

with the Young's modulus Y_s and Poisson's ratio σ_s of the substrate, the beams 1/e-radius of the electric field w and the optical thickness of the coating d. The formula for the volume averaged effective values

$$(X)_c = \frac{d_{\mathrm{SiO_2}}}{d_{\mathrm{SiO_2}}+d_{\mathrm{Ta_2O_5}}}X_{\mathrm{SiO_2}} + \frac{d_{\mathrm{Ta_2O_5}}}{d_{\mathrm{SiO_2}}+d_{\mathrm{Ta_2O_5}}}X_{\mathrm{Ta_2O_5}} \tag{5.25}$$

Young's modulus Y_c and Poisson's ratio σ_c of the coating are taken from the Appendix D2 of [106].

The '*loss angles associated with energy stored in strains parallel to the plane of the coating are*' assumed to be '*all equal*' and are summarized by $\phi_{\parallel}$ [119]. This is not entirely clear, but '*many isotropic amorphous materials, like fused silica, do not show significantly different quality factors for many modes even though the relative magnitude of the various terms in the elastic energy varies significantly between the modes*'. The in-plane loss angle $\phi_{\parallel}$ can be measured by monitoring ring-downs of thin cantilever blades [119]. The main problem is, that the perpendicular loss angle $\phi_{\perp}$ remains unknown. In the literature it is often guessed, that it equals the parallel one $\phi_{\parallel} = \phi_{\perp}$.

For rough estimates within a factor 2, it is Furthermore, sufficient to assume the parameters $Y_c = Y_s$, $\sigma_c = \sigma_s$, and $\phi_c = \phi_s$ of coating and substrate to match each other. Then equation 5.24 simplifies to

$$S_{\text{Brown}}^{\text{coat}} \approx \frac{8k_{\text{B}}T}{\pi\omega}\frac{(1+\sigma)(1-2\sigma)}{w^2 Y}\cdot\phi d \tag{5.26}$$

which is used for figure 5.20. Here an effective loss angle of $\phi = 4.2{\cdot}10^{-4}$ is chosen[12] [119]. The exact design of the coating is usually not provided by the coater. A lower bound for the number of coating layers N can be calculated from the reflectivity (compare figure D.17). A normal stack consists of N/2 layers of high and N/2 layers of low refractive index material, each having an optical quarter wave thickness. Then the total thickness can be calculated by means of

$$d_c = \frac{\lambda/4}{n_{\text{SiO}_2}}(N/2+1) + \frac{\lambda/4}{n_{\text{Ta}_2\text{O}_5}}N/2 \ . \tag{5.27}$$

The fact that the very first layer is made of low refractive index material (silica) means, that it must have half wavelength thickness. With highly reflective coatings this is usually negligible.

Coating thermo elastic noise

In addition to mechanical losses happening on the microscopic scale, energy can also be dissipated by heat flow on a larger scale (on the order of the thermal diffusion length $r_T = \sqrt{\kappa/2\pi\rho C_v f}$, where $r_T(_{\text{SiO}_2,\ 100\,\text{Hz}}) =$ 3.9mm, and beyond). Following the Fluctuation Dissipation Theorem, there are temperature fluctuations on these larger scales. One effect, how they can influence the interferometric phase readout is by simple thermal expansion: the surface of a coating locally moves with respect to the back side. But thickness variations of the stack layers e.g. also change the phase accumulated by the parts of the light field which enter the layers.

The total apparent position fluctuation is given by [106]

$$S_{\text{TE}}^{\text{coat}} = \frac{8k_{\text{B}}T^2}{\pi^2 f}\frac{d}{w^2}\frac{\alpha_s^2 C_c}{C_s^2}(1+\sigma_{\text{sub}})^2\tilde{\Delta}^2 g(\omega) \tag{5.28}$$

where $\tilde{\Delta}^2$ accounts for the averaged thermal properties across the coating stack and $g(\omega)$ containing the frequency dependence of the thermoelastic losses. It peaks up at a frequency, where the stack layers cannot be approximated by it's averaged properties anymore since thermoelastic dissipation between the layers becomes 'optimal'.

12 Amorphous materials seem to be limited by 'rubbing on the molecular scale'. Crystalline materials such as AlGaAs have a higher degree of order and can provide much better performance [11].

Coating thermo refractive noise

The temperature dependence of the refractive index of the coating material poses another coupling of the read out phase and the temperature inside the coating material. The Levin pressure formalism turns slightly awkward in this case. It is not a pressure which is injected into the material anymore but an entropy. It is dissipated in the material similar to the thermoelastic case.

Given statistical fluctuations of the temperature, the read out thermo refractive noise is then [121]

$$S_{\mathrm{TR}}^{\mathrm{coat}} = \frac{\sqrt{2}\beta^2\lambda^2 k_{\mathrm{B}}T^2}{\pi w^2\sqrt{\rho C\kappa\omega}} \ . \tag{5.29}$$

Coating thermo optic noise

Thermo optic noise consists of two contributions: thermo elastic and thermo refractive. Their temperature to phase couplings have opposite signs. As both occur inside the coating, the temperature fluctuations may be sufficiently correlated and Hence, may cancel out each other [11]. [118] claims, that '*The effective volumes of thermo-refractive and thermoelastic layers are significantly different as the wave is mostly reflected from a few outermost layers where the optical power decays exponentially and the thermal expansion is provided by the whole structure of the coating.*' In contrast, [122] claim to '*have demonstrated cancellation of photothermal noise in high-reflectivity substrate-transferred AlGaAs coatings.*' This, however, couldn't be shown in a direct thermal noise measurement yet. Instead, temperature fluctuations were injected artificially by means of laser intensity modulations, so '*measuring the photothermal transfer function*',[13] which gives '*evidence that this optimization has been successful*' for thermo optic noise as well.

For figure 5.20 no correlation was assumed, as the theory was rather new at the time of the simulation which is setting the foundation for several other subsystems described in this work. A coherent treatment cannot spoil the requirement anyway but only improve the RefC sensitivity.

5.7.7 *Substrate thermal noise*

Above its suspension's resonances, a suspended mirror can be treated as a free test mass. Therefore the momentum of its center of mass is a conserved quantity. Interferometry, however, measures the position of the reflective surface which is driven by thermal fluctuations of the substrate.

13 The local temperature is modulated with a cross-section of the readout variable by means of absorbed (amplitude modulated) laser power similar to [109]. The induced phase change of the reflected light gives rise to the photothermal transfer function

Substrate Brownian noise

For a free body, the center of mass momentum is conserved. The individual particles, however, are subject to an uncorrelated force. This may move the substrate's surface, where the laser is reflected, with respect to the center of mass. Interestingly, according to Levin the influence of losses introduced at the back and the sides of a mirror onto the interferometric readout are reduced with respect to the homogeneous loss approach. Hence, magnets glued to the back (as in RC1a) and prisms attached to the sides of a mirror (as all RefC mirrors) contribute only little additional noise although they can reduce mechanical substrate modes significantly.

For the simulation in figure 5.20, the first model (equation 17 in [118][14])

$$S_{\mathrm{Brown}}^{\mathrm{sub}} = \frac{4k_{\mathrm{B}}T(1-\sigma_{\mathrm{sub}}^2)}{\sqrt{\pi}wY_{\mathrm{sub}}Q_{\mathrm{sub}}\omega} \tag{5.30}$$

is used for simplicity.

Like in any other thermal noise process, a low loss (and thereby a high Q) substrate is beneficial. It concentrates thermal energy in narrow resonances in the tens of kHz range [124] and reduces the broadband noise which otherwise could spoil the detection window. Here, the substrate loss is assumed to be independent of the frequency [125].

For the RefC mirrors, fused silica of type Suprasil2 is used. It combines extremely low losses in conjunction with superb optical quality. Mechanical Q-values up to $2 \cdot 10^7$ have been shown [125, 126].

However, break-off bars and magnets glued to the mirrors introduce additional losses and degrade the Q-value. The GEO600 mode cleaner mirrors are very similar in construction. A coarse investigation of their drum modes suggests a Q of $5 \cdot 10^6$. For the simulation a rather pessimistic Q-value of 10^6 is assumed.

Substrate thermo elastic noise

In addition to structural losses causing Brownian noise, the other major loss channel of the substrate is caused by thermodynamic heat flow. Deformation locally changes the temperature by means of induced stress (temperature dependence of the Young's modulus). Due to heat flow, the local temperature variations can average out and dissipate a part of the elastic energy this way. In turn, statistical local temperature fluctuations can induce stress. The arising force is the origin of thermoelastic noise. It deforms the test mass via elasticity. The sensed displacement is given by [118] equation 4 to be

$$S_{\mathrm{TE}}^{\mathrm{sub}} = \frac{4k_{\mathrm{B}}T^2\alpha_S^2\left(1+\sigma_S\right)^2\kappa_S}{\pi^{5/2}\left(C_S\rho_S\right)^2 w^3 f^2} \tag{5.31}$$

14 Other authors give twice the value [123]

with the coefficient of thermal expansion α_S, the Poisson's ratio σ_S, the thermal conductivity κ_S, the specific heat capacity C_S, the density ρ_S and the spot size on the mirror w.

Substrate thermo refractive noise

As the name tells, substrate thermo refractive noise arises from the dependence of the refractive index of the substrate on temperature (fluctuations). In a Michelson interferometer, the light of one arm passes a substrate which is not sensed by the other arm, e.g. the beam splitter. In a single cavity, however, the measurement path (intra cavity light) and the reference path (sidebands being reflected by the cavity), travel the same path through the substrate. Hence, they see the same path length fluctuations induced by a refractive index change.

There is one more noise contribution, which is somewhere between substrate and coating thermo refractive noise. The carrier is transmitted through the coating and Hence, sensing refractive index fluctuations. It is then circulated inside the cavity. During its round trips it is reflected on the cavity side of the coating and finally transmitted through the coating once more when leaving the cavity. The sidebands, in contrast, are reflected on the substrate side of the coating. Hence, the double-pass of the carrier through the coating can contribute additional noise. As it doesn't occur within the cavity, its effect is not amplified. Now the finesse rises exponentially with the number of coating layers, while the described effect only scales linear in the worst case, i.e. when the temperature fluctuations are all correlated within the coating. It can be neglected for sufficiently high finesse cavities.

5.7.8 *Seismic noise*

Seismic ground motion is easily measurable using a seismometers like the Streckeisen STS2 (compare figure 3.3). However, the effect onto objects separated some distance away from each other (like the reference cavity mirrors) is more complex to predict. This is an attempt to determine the expected amount of common mode rejection.

On a 2 dimensionally homogeneous boundary such as the earth's surface (without obstacles), seismic disturbances can propagate as surface waves. Especially the speed of the fundamental Rayleigh waves is significantly lower ($c_{\mathrm{surf}} \approx 205\,\mathrm{m/s}$ [127]), than that of body waves ($c_{\mathrm{body}} \approx 2\,\mathrm{km/s}$ [127]). Hence, the associated wavelength are relatively small. The simplest model for seismic ground noise is that of an isotropic background of Rayleigh waves. In this case the correlation between two test objects such as the SAS platforms is given by

$$\rho\left(x_{\mathrm{SAS_C}}, x_{\mathrm{SAS_S}}\right) = S_{\mathrm{gnd}}(\omega) J_0(kr) \tag{5.32}$$

where $k = \omega / c_{\mathrm{surf}}$ is the magnitude of the wave vector, $r = 11.65\,\mathrm{m}$ is the distance between the test objects and S_{gnd} is a measured ground

spectrum (PSD). The J_0 is the zeroth order Bessel function J_0 has a zero crossing around 7 Hz where the correlation should vanish in this noise model. Moreover that it is getting negative and reaches -0.4 (in power) at $\approx$20 Hz, meaning that the tables move anti-correlated,

Other, more detailed noise models take local sources into account, such as fans or structural resonances of the building driven by seismic or acoustics. It is important to include these accurately for noise subtraction in gravitational wave detectors, especially when fighting gravity gradient noise. In this noise budget they are neglected for simplicity.

The in- and out-coupler are placed on the same optical bench. Therefore it is safe to assume that they move well in common. For direct coupling to optical round trip noise the lack of ground motion correlation between $\mathrm{SAS_C}$ and $\mathrm{SAS_S}$ and the imbalance between the transfer functions probably dominates. At low frequencies the ground moves better in common due to the longer associated wavelength: $\sqrt{J_0(\omega c_{\mathrm{surf}})} \approx 98\%$ at 1 Hz (where most pendulum resonances are) and even more than 99.9% at 0.2 Hz (where the microseismic peak is). Here However, the SAS construction comes into play. Due to its softness, the two isolation platforms perform differently. In several low frequency bands only 30% of the motion is coherent between the top of both platforms [49].

In summary it is quite realistic to assume two optics being driven uncorrelated along the long cavity axis (y-arm) by seismic in this case. If being more pessimistic, two mirrors being driven anti-correlated can be assumed. Transverse motion barely has any additional effect (see chapter 5.5). Vertical seismic activity is taken into account by assuming 0.1% amplitude coupling into longitudinal (compare chapter 4 or [63]). The coupling channel is probably different in all mirrors, so no common mode rejection can be expected. The associated round trip change is then $\Delta_{\mathrm{rt}} = 3 \cdot (0.1\%)^2 S_{\mathrm{vert}}$, with a rather large uncertainty. The other degrees of freedom couple into round trip length as well.[15] Their influence, however, can only be quantized when the excitation in these degrees of freedom is well know in the first place. As an example, the SAS platforms show poor tilt-attenuation which causes effective vertical motion 1 m away from the center of the table, where the RefC suspensions are placed. This was observed to be much stronger than residual vertical SAS motion. In the suspension, however, side-excitation has a very similar shape to long motion which couples 1000 times stronger. Tilt excitations cannot be quantized and Hence, are not considered.

5.7.9 *Control noise*

Alignment control noise is difficult to assess. The design and optimization of the involved servo transfer functions will only be carried out

15 Usually 0.1% coupling to *long* is assumed for rotational degrees of freedom *pitch* and *yaw* as well as translations *side* [53].

during the commissioning phase. Local damping readout and actuation noise However, are easier to predict. A detailed noise projection carried out during the design phase of the local control loops is described in chapter 4.5. Finally there are two damping modes: classical *local damping* with extremely strong and robust feedback to quickly bring an excited suspension to rest e.g. during lock acquisition and *degree of freedom damping* with weaker, only conditionally stable feedback (compare figure 4.24). The latter is optimized to fulfill the stringent requirements in the detection band while maintaining a reasonable eigenmode damping. On the downside it can easily fail and even start to excite the suspension during strong seismic events due to the limited shadow sensor detection range (and the nonlinearities connected with saturating signals).

5.7.10 *Shot noise*

The quantization of the light detected in the length readout photodiode causes statistical fluctuations of the detected power. These are indistinguishable from any length signal. Assuming a rather stationary detected power, the Pound-Drever-Hall length readout in the vicinity of resonance is limited to [128]

$$S_{\text{shot}} = \frac{\sqrt{hc}}{8}\frac{\sqrt{\lambda}}{\sqrt{\mathcal{F}P_c}} \cdot \chi \tag{5.33}$$

where P_c is the carrier power which is well approximated by the input power (compare chapter D.10). The factor $\chi = \sqrt{1+f^2/f_{\text{pole}}^2}$, which is not given in the source, takes the decrease of the response above the cavity pole into account. When keeping the input power constant, a higher finesse leads to a better displacement calibrated sensitivity. However, the finesse is limited by practicability and radiation pressure noise. The optimal shot noise limited readout assumed in equation 5.33 can be performed only in the absence of other junk-light. In practice this requires the alignment of the ingoing beam to be perfect. This is realized quite well by means of the auto alignment system. Also the mode matching (waist size and position) must be good. In theory the eigenmodes of mode cleaner and RefC are almost perfectly matched aside from tiny astigmatism. In reality a few percent might be reflected due to mode mismatch. Furthermore, the mirror reflectivities were originally designed to achieve impedance matching at a finesse of 7300. Due to a mistake in specifications the polarization needed to be changed (compare table 5.1 and table 5.2). This reduces the achievable finesse to 3500. Also it results in an impedance mismatch. According to equation 6.31, around 1%..6% of the incident DC power is always reflected. The exact value depends on the actual intra cavity losses.

With the achieved modulation index of 0.23 rad, a sideband power of 2.7%[16] is off-resonant and therefore reflected. Ideally this is the only contribution for shotnoise. In practice, mode and polarization mismatched light contribute shotnoise as well. Comparison shows, that the actual shot noise level lies up to a factor of $\sqrt{2}$ to $\sqrt{3}$ higher than the optimally achievable one.

16 single sideband power $J_1(0.23)^2 = 1{,}3\%$, carrier power $J_0(0.23)^2 = 97{,}3\%$, see chapter D.10

6

THERMAL NOISE INTERFEROMETER

Coating thermal noise (CTN) is amongst the most important noise sources in optical metrology [119]. The highly reflective surface of modern mirrors are constructed of dielectric multi-layer thin film structures. Compared to the substrate, these thin layers exhibit much higher losses. Recently, a lot of effort has been put into the reduction of the losses. Annealing and doping techniques are being developed for the most widely used amorphous layer structures made from Ta_2O_5 and SiO_2. Radically different approaches try to separate the losses mechanically from the interferometric readout [129] or aim for avoiding the lossy reflective coating completely. Recently a major breakthrough has been achieved by the invention of a production technique for crystalline coatings made from GaAs/AlGaAs and the corresponding transfer technique to fused silica substrates [11, 130, 131, 132].

These coatings provide reduced Brownian noise at room temperature which improves even more in cryogenic environments. This comes at the drawback of significantly increased thermo elastic and thermo refractive noise. However, it is predicted that '*various manifestations of thermal noise can be coherent one with another*' [117]. In particular, coating thermo elastic and coating thermo refractive noise might occur coherently, resulting in coating thermo optic noise [105]. First measurements hint a confirmation by showing photo thermo optic cancellation [122], while thermo optic cancellation remains experimentally unproven.

6.1 FEATURES OF THE TNI

The main goal of the TNI is to investigate coating thermal noise over a wide frequency range interesting for gravitational wave detectors. Special emphasis is put onto the low end of the gravitational wave band, i.e. between 10 and 100 Hz. This region was barely investigated earlier [133, 134]. Fixed spacer cavities, like those used in optical clocks for example, usually suffer from seismic noise exciting internal resonances at their upper sensitivity end. In a suspended cavity this region requires extremely good low frequency noise management, e.g. properly designed suspensions and low noise feedback.

The TNI was designed to be able to easily exchange the test mirror(s). Recently, AlGaAs coatings became feasible for interferometric applications. However, since it is still a relatively new coating material, their optical properties have not been widely investigated. Hence, the TNI is designed as a free space cavity, which allows tuning of the spot size and beam position on any single mirror to map its properties.

Furthermore, the optical design of the TNI is chosen to be able to accommodate 'irregular' prototype mirrors. The test mirror is flat, which simplifies the early production of new mirror designs such as waveguide gratings [37]. The test mirror's transmission is not required, so that opaque substrates and ultrahigh reflectivity designs can be investigated as well.

6.2 EXPERIMENTAL LAYOUT

Any mirror displacement to light phase coupling can be amplified resonantly using a cavity with a reasonable finesse. The easiest layout is a linear design involving only two mirrors. The idea in the TNI is, to have one test mirror and one reference mirror. This is facilitated by an asymmetrical design: the test mirror is flat, so that the spot size on its surface is minimal. The reference mirror is concave. As the cavity length approaches the mirror's radius of curvature, the two spot sizes become more and more different (compare figure 6.10). Since coating thermal noise depends on the spot size, for most length choices the test mirror's noise is dominating the signal.

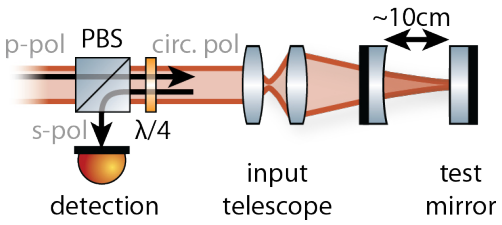

Figure 6.1.: The spot size on the TNI test mirror is small to enhance coating thermal noise. The CTN signal is amplified by a ≈10cm long optical cavity. The reflected light is split off by a $\lambda/2$-waveplate/PBS combination and detected by means of a Pound-Drever-Hall readout scheme.

Seismic isolation: suspended spacer or individual mirrors

The aspired low frequency sensitivity of the TNI (about $2{\cdot}10^{-17}\,\mathrm{m}/\sqrt{\mathrm{Hz}}$ at 20 Hz) requires seismic isolation. The SAS-tables contribute low frequency isolation, but in the most interesting detection band they suffer from multiple internal resonances. The 850 g suspensions described in chapter 4 are a good complement with sufficient isolation at the SAS's internal modes. The feasibility of a suspended 850 g spacer was inves-

tigated as well. This reduces the number of required suspension chains (from two to one) and, much more important, fixes the inter mirror degrees of freedom. More specifically it provides good internal alignment stability and extremely high common displacement mode (cavity length) rejection. Yet the spacer's motion would still require some sort of auto alignment. The rigidity would also be its biggest drawback: a new beam geometry (different spot size, different spot position) requires a whole new spacer and thereby a different mirror which is bad for the comparability of results.

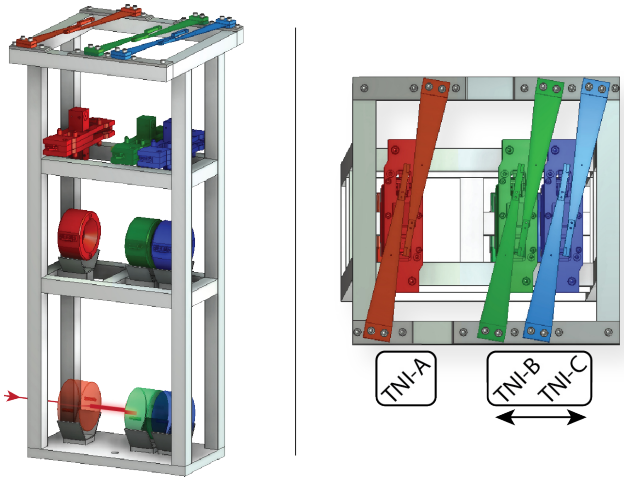

Figure 6.2.: The TNI contains two mirror suspensions: the one for the incoupler TNI-A shown in red and the other for the test-optic TNI-B shown in green. The additional suspended mass TNI-C shown in blue can be used as reaction pendulum. Suspensions B and C can be moved in common to tune the cavity length.

Hence, two individual suspensions are accommodated inside one common frame structure instead. The option for a third suspension (TNI-C), which could serve as an isolated actuation platform behind the end mirror, was included in the design. The suspension design had to be changed slightly: the uppermost vertical isolation stage has 'crossing' cantilevers, similar to the blades inside the upper mass (compare figure 6.2).

Cavity length

The question for the length is quickly answered: For laser frequency noise sensitivity, the shorter, the better. Fixed spacer thermal noise experiments are usually operated in the mm to cm length scale. The sensing/actuation around the upper mass of the 850 g suspensions requires 10 cm distance to be safe from touching each other. If one sacrifices the possibility to fit a reaction pendulum, one suspension could be turned around to result in a shorter cavity down to a few mm. However, the SQL interferometer and even the single arm test will require the Reference Cavity to perform much better (compare figure 5.1). Due

to their length, they are 100 times more sensitive to laser frequency noise than the TNI. In a cavity shorter than 10 cm, it is much more difficult to achieve significantly different spot sizes on the two mirrors. Then the experiment would be sensitive to thermal noise of both coatings and both mirrors would have to be exchanged to investigate new coating technologies. This might become problematic for experimental coatings, where a partially translucent incoupler might not be feasible.

Full size vs. small mirror

The fact that the suspensions require 850 g of load in the lowest stage is actually a drawback. A typical mirror with aspect ratio of 2:1 (10 cm diameter, 5 cm thickness) for every new coating coating to be tested is first of all expensive, but secondly also difficult to polish.

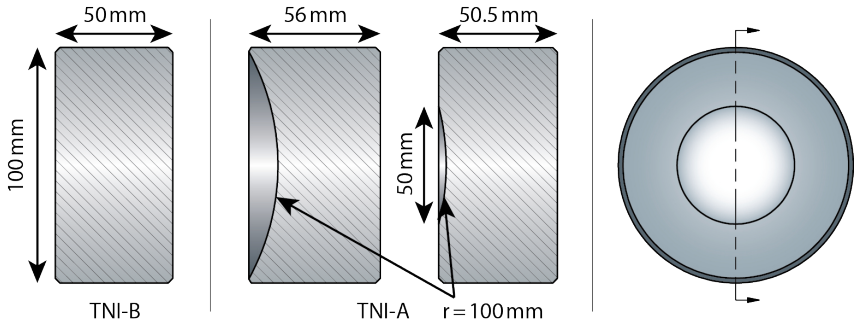

Figure 6.3.: Cross-sections through possible mirrors are shown. A 100 mmø, 50 mm thick flat-flat TNI-B mirror weights 850 g as required by the triple suspension system. The strong curvature (100 mm) of TNI-A requires a more special design. According to manufacturers it is still easier to produce mirrors, that's curvature reaches across the full front face, than just carving out the middle section.

Experiments have been carried out, to bond a small mirror (e.g. 1"ø, 1/4" thick) onto a bigger substrate (optimally keeping the overall optical properties and achieving a very thin bond for low losses: Adhesion from water and isopropanol is very good. The thickness of the film can be reduced well below 1 µm. Surprisingly, over a course of a few days the film starts to dry off, either by evaporation through the microscopic gap or by diffusion of the liquid into the material.

In another experiment, two mirrors were bonded together using UV-curing glue. High pressure (several hundred Newtons) has to be exerted during curing to reduce the film thickness. This might cause tension/surface figure deformations. From the Airy fringes it could be verified that the film size reduced to a few µm. The fringes are not circular but follow the points where the pressure was applied (compare chapter D.6). Yet this method seems most promising when using proper tools.

Optical layout

Since the central SAS is by far the most crowded one, it was decided to place the TNI onto the south SAS. A part (100 mW) of the Reference Cavity light is split off after being phase modulated. The beam is collimated and sent to the south table. It is received with a 2" lens and focused down onto a suspended steering mirror. A second suspended steering mirror is placed in the far field. This way, both steering mirrors are separated by almost 90° in Gouy phase and two independent quadratures can be actuated separately (compare figure 6.9). The power coupled into the TNI can be tuned by means of a zeroth order $\lambda/2$-waveplate and polarizing beamsplitter combination. This is especially important for very small spot sizes, so that the destruction threshold of the coatings is not exceeded.

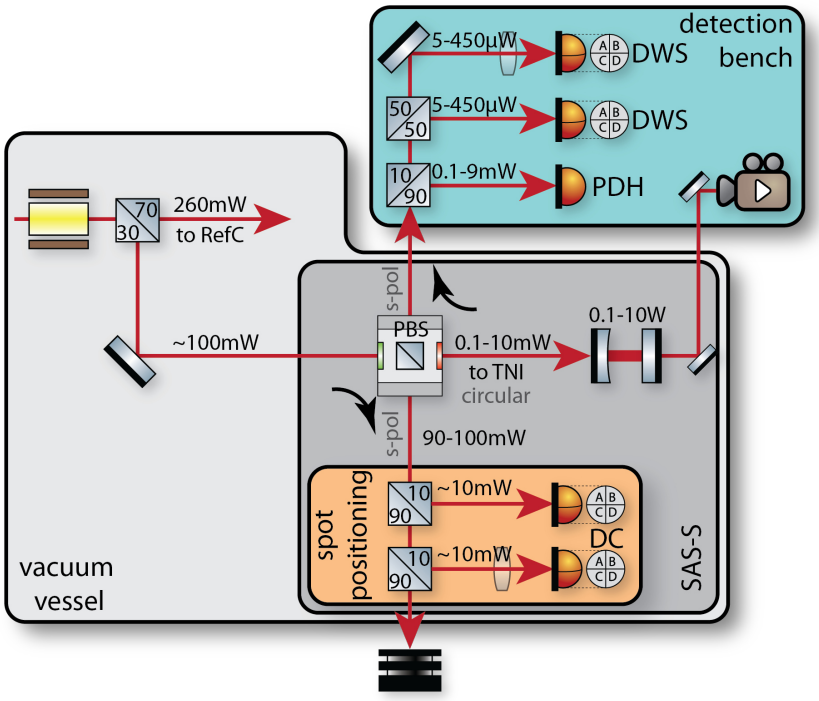

Figure 6.4.: About 100 mW of power is sent towards the south table. Via an attenuation unit ($\lambda/2$-waveplate & PBS) the amount of circularly polarized light entering the TNI can be chosen. The unused light is detected on QPDs to stabilize the beam with respect to the south table (SAS-S). The light transmitted by the TNI is monitored on a camera to inform on the shape of the resonating mode and eventually on the spot size. The reflected light is measured on the non-suspended detection bench outside vacuum. Most of its light is attributed to the length stabilization. Only 10% is used for differential wavefront sensing.

Ten percent of the power not being sent into the TNI are sensed on in-vacuum quadrant photodiodes of type QD50-3T, the rest is dumped outside of vacuum. The photodiodes (compare section 6.7.1) are used

as position references on top of SAS-S for feedback at low frequencies (compare section 6.7). It might appear counterintuitive that the beam position is stabilized to the SAS surface while the TNI is suspended and hence is isolated from the table. Yet this isolation happens only at high frequencies. Below about 1 Hz it moves in common with the tables. Furthermore, the beam originates from the PMC which is fixed on the central table. The residual inter table motion is canceled by the stabilization.

A $\lambda/4$-waveplate circularizes the light going into the TNI. Lenses then match the mode to the eigenmode of the cavity. The concave incoupler serves as an additional lens, so the input needs to be focused even tighter which is a real challenge in the constricted space (compare section 6.5). The reflected light is linearly polarized by passing the $\lambda/4$-waveplate backwards. This time it is reflected off the PBS and thereby split off from the incoupling light (this scheme cannot be applied for a polarization rotating cavity, e.g. using birefringent AlGaAs coatings where a Faraday isolator might be used). Finally it is sensed outside of vacuum on the detection bench.

There are three photodiodes for the reflected beam: one single element PD for a Pound-Drever-Hall type stabilization scheme of the length and two quadrant RF-photodiodes. Since the length stabilization is the most critical of the feedback loops, it is assigned about 90% of the reflected light, to keep the signal-to-noise ratio high. The quadrant RF-photodiodes are utilized as differential wavefront sensors (DWS). They measure the misalignment of the mode going into the TNI with respect to its eigenmode. Both QPDs are separated nominally by 90° of Gouy phase. The two quadratures are used to correct the input beam misalignment at high frequencies by means of the two steering mirrors in front of the TNI.

If the end mirror of the TNI allows, the transmitted beam is directed to the detection bench as well. A camera monitors which mode is resonating inside the cavity. Furthermore, it can be used to easily estimate the spot size on the test mirror. During the alignment procedure, the length is not locked and the cavity is usually swinging multiple free spectral ranges. Dependent on the misalignment, higher order modes are being excited and transmitted to the camera. They give information about the required corrections whereas the DWS don't give sensible signals.

Mirror reflectivities

The design values for the mirror reflectivities had to be decided. A cavity with a lower finesse has less off-resonant suppression and a wider bandwidth. This makes it easier to handle in practice. Light is leaking into the cavity even if it is not resonant or strongly misaligned. Both eases the initial alignment significantly which is important for a testing environment like the TNI. Lock acquisition is simpler as the resonance

is broader. However, the cavity pole might approach the PDH modulation frequency (compare figure 6.22 and 6.23).

A higher finesse results in more round trips. The light may accumulate more phase shift from the same test mass displacement. Hence, more signal is created while the shot noise stays constant. So the signal normalized shot noise is inversely proportional to the finesse (compare equation 6.37).

But the finesse must not be too high. With a large power buildup and a small spot, the destruction threshold of the coatings might be exceeded. At very small spot sizes this can be avoided by decreasing the input power. The power reduction increases the shot noise, but the 'signal', i.e. coating thermal noise, increases with reduced spot size as well (compare figure 6.11).

For a given finesse, the intra cavity buildup and thereby the signal amplification is the biggest in a strongly overcoupled cavity (compare figure 6.7). Yet an impedance matched cavity performs better in terms of shot noise on resonance, as the carrier light is transmitted through the cavity and does not contribute shot noise on the PDH photodiode in reflection.

None of the considerations leads to an exact requirement for mirror reflectivities. Experience tells that a suspended cavity with a finesse of 3000 is reasonable to control and yet good enough in terms of noise performance (compare figure 6.27). The aspired power reflectivity is the same for both mirrors, 99.9%, to obtain approximately impedance matching. The round trip losses may be small compared to the 2000 ppm transmission loss per round trip. See table 6.2 for the resulting cavity parameters.

6.3 JUGGLING REFLECTIVITIES

The intra cavity power of a linear cavity strongly depends on its length tuning described by the so-called Airy function. To calculate the on resonance power amplification, the mirrors' transmissivities are weighted against other loss channels of the cavity.

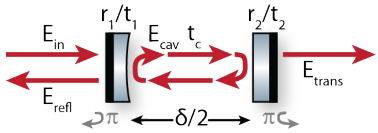

Figure 6.5.: The field inside a linear cavity can be calculated for the static case when changes happen slower than the decay time of the field inside, by means of the mirror parameters, the cavity losses and the microscopic length. A phase flip is attributed to the outside reflection to obtain real amplitude reflectivities and transmissivities inside the cavity.

Assume, the amplitude reflectivities and transmissivities r_x and t_x of the involved mirrors do not have an imaginary part, i.e. they do not contribute a phase shift. The 'required' phase flip is attributed to the reflection on the outside for simplicity. After each round trip a fraction a of the field is lost in addition to the transmission losses. For the required accuracy it doesn't matter whether this happens in 'free space' due to residual absorption or at the mirrors due to scattering or clipping. This can also be described by a round trip cavity propagation transmissivity t_c, so that $a^2+t_c^2=1$. In this discussion, the losses are assumed to be distributed evenly amongst the reflections, so that a power of $a^2/2$ is lost at each reflection. The phase, that is accumulated over one round trip of length L_{rt}, is denoted by $\delta=2\pi L_{\mathrm{rt}}/\lambda$. There is an elegant way of calculating the intra cavity field E_{cav} behind the incoupler: in the static on-resonance-case, the field may replicate itself after one round trip

$$E_{\mathrm{cav}} = E_{\mathrm{cav}} e^{i\delta/2}\sqrt{t_c} r_2 e^{i\delta/2}\sqrt{t_c} r_1 \; + \; E_{\mathrm{in}} t_1 \tag{6.1}$$

when being interfered with the ingoing field E_{in}, which is partly transmitted through the incoupler. This can be rearranged

$$\frac{E_{\mathrm{cav}}}{E_{\mathrm{in}}} = \frac{t_1}{1 - r_1 r_2 t_c e^{i\delta}} = \frac{t_1}{1-\rho e^{i\delta}} \tag{6.2}$$

to obtain the fractional intra cavity field. Here the amplitude $\rho = r_1 r_2 t_c$ remaining after one round trip is introduced.

The field being reflected and transmitted by the cavity

$$\begin{aligned} \frac{E_{\mathrm{refl}}}{E_{\mathrm{in}}} &= \frac{E_{\mathrm{cav}}}{E_{\mathrm{in}}} t_1 r_2 t_c e^{i\delta} \; - r_1 \\ \frac{E_{\mathrm{trans}}}{E_{\mathrm{in}}} &= \frac{E_{\mathrm{cav}}}{E_{\mathrm{in}}} t_2 \sqrt{t_c} e^{i\delta/2} \end{aligned} \tag{6.3}$$

can be deduced from the intra cavity field easily. The transmitted power is shown in figure 6.6 exemplary for two different finesse values being in the interesting range for the TNI. For most applications the loss $t_c \approx \sqrt{t_c} \approx 1$ can be neglected. However, they gain importance in high finesse cavities.

The fractional intra cavity power $P = E \cdot E^*$ is

$$\begin{aligned} \frac{P_{\mathrm{cav}}}{P_{\mathrm{in}}} &= \frac{t_1^2}{1+\rho^2-2\rho\cos(\delta)} \\ &= \frac{t_1^2}{(1-\rho)^2 + 4\rho\sin^2(\delta/2)} \end{aligned} \tag{6.4}$$

which is visualized in figure 6.7. It is interesting to remark that close to the resonance (where $\sin^2(\varepsilon) \approx \varepsilon^2$) this so-called Airy functions has a Lorentzian profile. The equation can be simplified further

$$\frac{P_{\mathrm{cav}}}{P_{\mathrm{in}}} = \frac{\mathrm{pbf}}{1 + F\sin^2(\delta/2)} \tag{6.5}$$

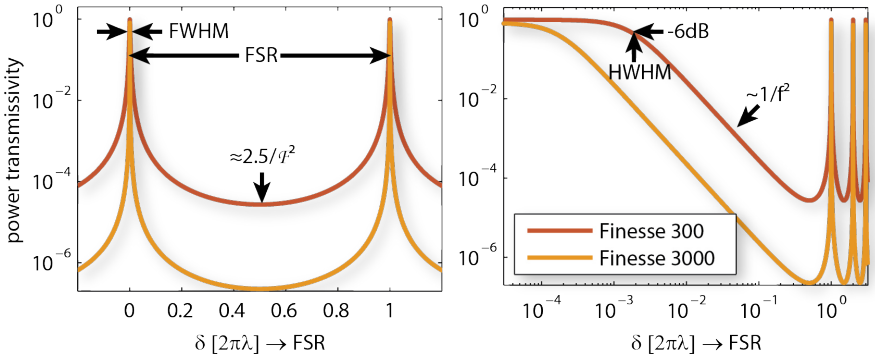

Figure 6.6.: The power transmissivity of a linear impedance matched cavity is shown for two different finesse values (ratio of free spectral range (FSR) and full width at half maximum (FWHM)). For low losses, the maximal power buildup inside is proportional to the finesse ($\mathcal{F}/4\pi$) and the minimal is inversely proportional to the finesse ($\pi/(4\mathcal{F})$. At a very high finesse, the losses (100 ppm per round trip) are not negligible anymore and reduce the maximal throughput. In particular, the resonance peaks decrease. For transfer functions, often a logarithmic detuning scale is used for the otherwise same diagram, shown on the right. The pole frequency of the amplitude transfer (-3 dB) matches the half width at half maximum of the power transfer.

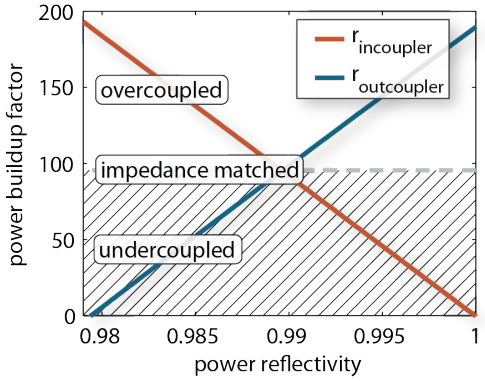

Figure 6.7.: Given a moderate finesse of $\mathcal{F}=300$ and negligible losses $t_c=1$. For any combination of the reflectivities r_1^2 and r_2^2 the buildup factor can be deduced. At impedance matching ($r_1 \approx r_2$), the power buildup is $\mathcal{F}/\pi$. In the strongly overcoupled regime ($r_1 \ll r_2$) it is twice as big. When being undercoupled, most of the incident light doesn't enter the cavity and hence doesn't sense its length.

by means of the finesse factor

$$\begin{aligned} F &= \frac{4\rho}{(1-\rho)^2} \\ &\overset{\rho\approx 1}{\approx} \frac{4}{(1-\rho)^2} \end{aligned} \tag{6.6}$$

and the maximal power buildup factor

$$\mathrm{pbf} := \max\left(\frac{P_{\mathrm{cav}}}{P_{\mathrm{in}}}\right) = \frac{t_1^2}{(1-\rho)^2} \ . \tag{6.7}$$

This maximal power buildup is achieved for the resonance condition $\delta = 2n\pi$. Due to the periodic nature of the phase, the same results are obtained when replacing the round trip phase δ by $\delta' = \mathrm{mod}_{2\pi}\delta$. The length tuning between two resonances, where $\delta' = \pi$, is called antiresonance. Here, the power inside the cavity

$$\begin{aligned} \mathrm{psf} := \min\left(\frac{P_{\mathrm{cav}}}{P_{\mathrm{in}}}\right) &= \frac{t_1^2}{(1+\rho)^2} \qquad \overset{\rho\approx 1}{\approx} \frac{t_1^2}{4} \\ &= \frac{\mathrm{pbf}}{1+F} \qquad \overset{F\gg 1}{\approx} \frac{\mathrm{pbf}}{F} \end{aligned} \tag{6.8}$$

is suppressed maximally. The antiresonances are significantly broader than the resonances (compare figure 6.6)

The frequency spacing between two resonances

$$\mathrm{FSR} = \frac{c}{L_{\mathrm{rt}}} \tag{6.9}$$

is called the free spectral range. It is equivalent to a phase tuning difference of $\delta_{\mathrm{FSR}} = 2\pi$. The detuning, at which the cavity power drops to half its maximum

$$\frac{P_{\mathrm{cav}}}{P_{\mathrm{in}}}(\pm\delta_{\mathrm{HWHM}}) = \frac{\mathrm{pbf}}{2} \ , \tag{6.10}$$

is defined as half bandwidth. Twice the value

$$\begin{aligned} \delta_{\mathrm{FWHM}} &\overset{6.5}{=} 2 \cdot 2\arcsin\left(\sqrt{\frac{1}{F}}\right) \\ &\overset{6.6}{=} 2 \cdot 2\arcsin\left(\frac{1-\rho}{2\sqrt{\rho}}\right) \\ &\overset{\rho\approx 1}{\approx} 2(1-\rho) \end{aligned} \tag{6.11}$$

gives the full bandwidth of the resonance. The ratio of free spectral range and bandwidth

$$\begin{aligned} \mathcal{F} &= \frac{\pi}{2\arcsin\left(\frac{1-\rho}{2\sqrt{\rho}}\right)} \\ &\approx \frac{\pi\sqrt{\rho}}{1-\rho} \\ &\overset{\rho\approx 1}{\approx} \frac{\pi}{1-\rho} \\ &\approx \frac{2\pi}{1-\rho^2} = \frac{2\pi}{\text{round trip power loss}} \end{aligned} \tag{6.12}$$

is called finesse. It is related to the finesse factor by $2\mathcal{F}/\pi \approx \sqrt{F}$. With this new measure, the power buildup factor can be rewritten as

$$\mathrm{pbf} \approx \frac{\mathcal{F}}{\pi} \cdot \frac{t_1^2}{1-\rho} = \begin{cases} \frac{\mathcal{F}}{\pi} & \text{(imp. matched)} \\ \frac{2\mathcal{F}}{\pi} & \text{(overcoupled)} \end{cases} \tag{6.13}$$

with the two cases explained in the following section. The power suppression factor

$$\mathrm{psf} \approx \frac{\pi}{4\mathcal{F}} \ , \tag{6.14}$$

in contrast, is independent on the impedance matching condition. Hence, the suppression of an off-resonant mode with respect to a resonant one pbf/psf is $(2\mathcal{F}/\pi)^2$ for an overcoupled and $2(2\mathcal{F}/\pi)^2$ for an impedance matched cavity.

6.3.1 *Impedance matching condition*

Three distinct regimes based on reflectivity distribution and on resonance performance are discussed in the following.

- The undercoupled case, when $t_1^2 \ll t_2^2 + a^2$, is the least interesting one for experiments. Most of the signal leaves through the outcoupler but due to the incoupler's high reflectivity, barely any light enters the cavity in the first place to cause any signal initially.
- In the impedance matched case $t_1^2 \approx t_2^2 + a^2$ no light is reflected on resonance. This gives the cleanest Pound Drever Hall signal as the carrier light is stripped off from the locking signal in reflection.
- An overcoupled cavity $t_1^2 \gg t_2^2 + a^2$ has the highest power buildup for a given finesse. This regime is used in arm cavities of gravitational wave detectors for example.

For any given finesse of a cavity, it is possible to minimize the amount of reflected light. Exact impedance matching is achieved if the reflected light vanishes

$$\frac{E_{\mathrm{refl}}}{E_{\mathrm{in}}} \stackrel{!}{=} 0 \ . \tag{6.15}$$

The phase relations of the individual field contributions actually require the cavity to be on resonance ($\delta' = 0$) for this. Then it can be shown that equation 6.3 leads to

$$r_1 \stackrel{!}{=} r_2 t_c \tag{6.16}$$

the impedance matching condition. Assuming that the losses of the mirrors are negligible ($r_x^2 + t_x^2 = 1$) this translates into $r_1^2 \stackrel{!}{=} r_2^2 t_c^2$ and hence leads to

$$t_1^2 \stackrel{!}{=} t_2^2 + a^2 \ \cancel{-t_2^2 a^2} \tag{6.17}$$

where the last term can be neglected for reasonably high finesse cavities.

6.4 OPTICS

6.4.1 *Commissioning optics*

For initial commissioning of the TNI, a low finesse and a compound test mass design were chosen. Standard 1"ø, 6.25 mm thick optics are mounted as compound test masses. They are clamped from the side. Gluing might be more robust at the cost of interchangeability. The aluminum ring of the intermediate mass was designed to house such optics resulting in a mass with properties similar to those of the final test mass design, e.g. mass, inertias, used wire length, break-off points. The only significant difference is that the surface of the relatively thin mirror is mounted in the very center of the 'ring' so that the reflecting surface is recessed from the front. Hence, the radius of curvature was increased slightly from 10 to 15 cm to result in similar suspension positions to the final ones.

parameter	$TNI_{commissioning}$
$T_{TNI\text{-}A}$ (input)	2 %
$T_{TNI\text{-}B}$ (output)	2 %
add. loss	guess: 100 ppm per round trip
Finesse	155
FSR	1 GHz
FWHM	6.5 MHz
P_{in}	$\leq$100 mW
w_0	120 µm $\rightarrow$ 0 µm
$l_{round\ trip}$	2·0.15 m
f_{mod}	8.047260 MHz
β_{mod}	0.15..0.23 rad

Table 6.1.: The most important parameters of the TNI during its commissioning phase are summarized. The lower reflectivity of the optics results in a reduced finesse and hence easier alignment and locking. The sensitivity given in figure 6.34 resulted from this TNI version.

The low reflectivity of 98 % results in a finesse of only 160. The bandwidth of the cavity is drastically increased easing the locking and lock acquisition[1]. While working out alignment procedures the low reflectivity helps vastly, as the beam can be detected inside the cavity. Also the off-resonant suppression is reduced. The increased bandwidth of 6.5 MHz comes at the slight drawback of less odd order higher order mode suppression.

1 It should be noted that the sensitivity against misalignment remains unchanged, as this is determined by the spatial overlap integral of input beam and cavity mode

6.4.2 *IBS silica-tantala test optics*

The final design testing tantala-silica coatings aims for a finesse of 3000. This value is not a tight requirement, but it approximately balances some counteracting effects. A high finesse increases the shot noise and readout noise clearance. It suppresses non-resonant higher order modes more effectively, but in turn it makes lock acquisition and alignment a lot harder.

The finesse is achieved with 99.9% power reflectivity of both mirrors. This value is reached for 11 double layers (compare figure 6.8). Although it does not provide additional reflectivity, a half-wave silica cap must be applied to make the coating chemically inert. The resulting bandwidth of the cavity at 10 cm length is 0.5 MHz and a free spectral range is 1.5 GHz.

parameter	TNI
$T_{\text{TNI-A}}$ (input)	1000 ppm
$T_{\text{TNI-B}}$ (output)	1000 ppm
add. loss	guess: 100 ppm per round trip
Finesse	3000
FSR	1.5 GHz
FWHM	0.5 MHz
P_{in}	$\leq$100 mW
w_0	120 µm $\rightarrow$ 0 µm
$l_{\text{round trip}}$	2·0.1 m
f_{mod}	8.047260 MHz
β_{mod}	0.15..0.23 rad

Table 6.2.: The key parameters of the proposed TNI are shown. They were used for the sensitivity plots in figure 6.27 and 6.28.

For substrate thermal noise reasons the Aluminum/mirror compound test mass should be exchanged for a (quasi-) monolithic mirror. According to discussions with polishers, it is extremely difficult, to produce a 10 cm diameter substrate with a radius of curvature of 10 cm for the incoupler (compare figure 6.3). Therefore, the path of another, quasi-monolithic test mass was pursued. A small (e.g. 1"ø) plane-concave optic can be bonded onto a plane-plane full scale substrate. Tests showed that the viscosity of UV-curable glue (Optocast) is rather big. Even with large amounts of pressure, the thickness and especially the homogeneity of the thickness could not be decreased to sub-wavelength level. This is not yet satisfying for the incoupler, where the input beam has to pass the bond. Another face-bonding technique is optical contacting, but this requires further investigation with respect to the optical quality. Inspired by rigid spacer cavities is the idea of 'drilling' the substrate with a diameter close to that of the small optic and bonding it only at the rim. Then the beam would not have to pass the bond

itself. The thermal noise performance of such construction remains to be investigated.

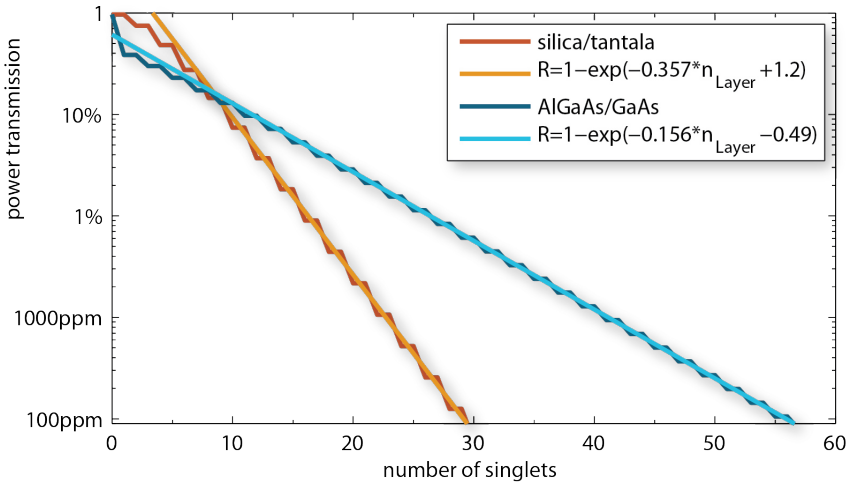

Figure 6.8.: The reflectivities of amorphous silica/tantala and crystalline AlGaAs/GaAs stacks are simulated and fitted for a reasonable number of layers. Tantala coatings are capped with a half-wave silica cap, AlGaAs is capped with a quarter or three quarter wave cap of GaAs to provide chemical stability. Due to the smaller differences in the index of refraction, the individual reflections in AlGaAs stacks are weaker than in tantala structures resulting in a shallower slope. Yet due to the higher averaged index of refraction (3.2 instead of 1.8), crystalline coatings provide a similar reflectivity for the same physical stack thickness.

6.4.3 *Crystalline AlGaAs test optics*

AlGaAs coatings are of special interest. They appear to be the most promising low coating thermal noise technology for room temperature detectors. Their crystalline structure yields up to a tenfold reduction of noise (in PSD) [11]. Their mechanical loss and thereby the coating thermal noise is decreased as AlGaAs has a crystalline structure in contrast to the amorphous silica/tantala layers. The index of refraction variations are achieved by a different content of Aluminum (replacing 92 percent of the gallium with aluminum). The index of refraction difference is smaller compared to silica/tantala structures leading to weaker reflections on the individual layers. Yet, the total thickness of a structure with similar reflectivity is very similar to silica/tantala coatings, as the index of refraction itself is higher, making the individual AlGaAs quarter-wave layers thinner.

For these coatings, the same arguments as listed in the last chapter count as well. Hence, the baseline design still foresees a finesse of 3000 resulting in the same cavity parameters. While coating a full scale test mass is possible in principle there are no machines to bond the AlGaAs

coating onto a ≈5 cm thick substrate available. Therefore, a compound test mass must be used in any case with the crystalline coating bonded onto a small optic. This in turn must be bonded to a larger substrate in order to gain mass and inertia to serve as lowest mass in the triple suspension.

According to figure 6.8, a reflectivity of 99.9% requires about 20 double layers. Gallium arsenide (n_{low}) is chemically more stable and therefore applied as top layer. An additional half wavelength thick cap on top, i.e. a $3/4\lambda$ GaAs cap layer may compensate thermo-optic noise optimally, well below Brownian thermal noise [135].

6.5 MODE MATCHING

As described in section 6.2, the input beam to the TNI is collimated and sent to the south SAS. Here it is being focused right after the first steering mirror. The second one is placed 45 cm away, i.e. well in the far field, to achieve 84° Gouy phase difference. Directly after follows a combination of waveplate and polarizing beamsplitter. It provides the beam for input spot position control and separates the TNI's reflected light from the ingoing one. Optimally the experiment is never changed up to this point.

The TNI with its suspension cage is also regarded as fixed on the table. There is no space to move it further back and the space in front is required for mode matching. Hence, the position of the TNI waist on TNI-B is fixed as well. The waist size and thereby the divergence angle, in contrast, is subject to significant changes when investigating the spot size dependence of coating thermal noise. Tracing it back, the mode must unavoidably pass the incoupler. It serves as an additional 'strong' concave lens. This increases the large divergence angle of the TNI mode even further. Also the resulting virtual waist position is not fixed in place anymore when changing the waist size.

In general, it is possible to match two optical modes to each other using a set of two lenses with a given focal length. The challenge is to fit the mode conversion optics required for the strongly converging TNI mode into the tightly constrained space as well as the availability of good quality short lenses. The situation is depicted in figure 6.9, where the shaded areas show unaccessible space containing fixed components. One example solution resulting in a 110 µm waist at the surface of the outcoupler is shown as well. Generally speaking, the mode matching works best when using a convex lens with a short focal length to form a very narrow waist (30 µm small in figure 6.9). After the small waist, the beam expands quickly. This large beam is required to be focused down to the cavity waist sufficiently strong. For a 110 µm waist on the test mirror's surface, the ≈82 µm virtual waist is 32 mm in front of the real one.

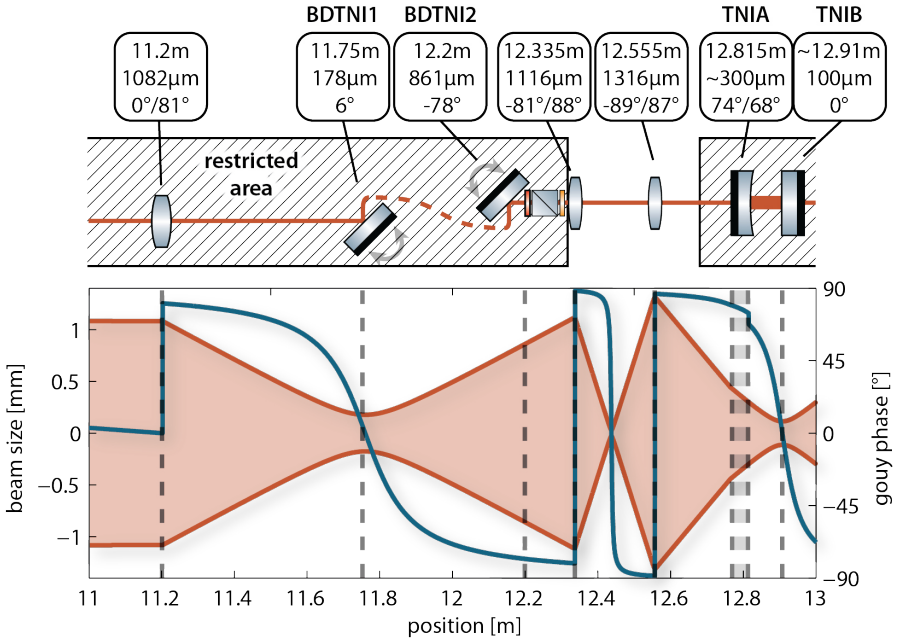

Figure 6.9.: The mode matching for a 110µm beam is shown exemplary. The PMC's waist (at 0 m) is collimated on the central bench and sent to the south table. It reaches the first lens with 1 mm radius. The steering mirrors are separated by 84° Gouy phase, the TNI mirrors by 68°. When investigating the spot size dependence of coating thermal noise, the cavity mode changes significantly and the mode matching should be adjusted. This proves difficult as there are tight space constraints, since the components in the shaded areas are basically fixed, and the incoupler serves as an additional concave lens.

6.5.1 *Changing the cavity mode*

A small spot size enhances coating thermal noise. The smallest possible size of any beam is at its waist. There the wavefronts are flat. Therefore, the test mirror must be flat as well. Its position defines the position of the waist inside the cavity. The second, concave mirror's radius of curvature R must be longer than the intended cavity length L for optical stability reasons ($|g|<1$, where $g=1-L/R$). When the length approaches the radius of curvature, the waist size decreases significantly. In contrast, the spot on the concave mirror increases which reduces its thermal noise contribution.

This hemispherical regime of dissimilar spot sizes is the intended mode of operation for the TNI. It allows to change the spot size with little experimental modifications. Across the range of approximately 1 mm the test mass can be shifted electromagnetically without any changes at all while keeping the full shadow sensor position information (the value assumes an integration of chapter 4.5.7). This allows the spot size to be reduced from 60µm down until the cavity gets unstable.

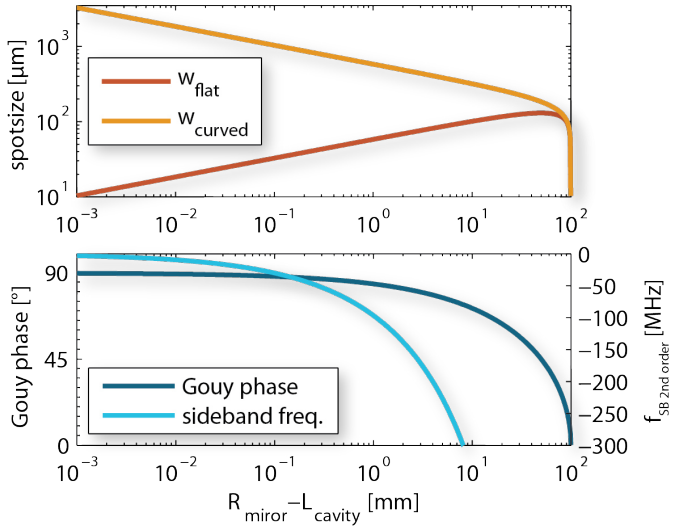

Figure 6.10.: The top graph shows the spot sizes on the mirrors of a plane-concave cavity with 0.1 m radius of curvature. The $R-L=R\cdot(1-L/R)=R\cdot g$ on the abscissa is another, rescaled measure for the cavity g-factor. The maximal spot size on the flat mirror is 130 µm. Close to the optical instability ($L=0$ or $L=0.1$ m) the spot is getting small which enhances coating thermal noise. The according Gouy phase is shown on the bottom left axis. It approaches 90° for the 'long' unstable case which is used in the TNI. Hence, the first order modes are suppressed for geometry reasons. The second order sideband frequency is shown on the bottom right axis.

The smallest achievable waist will probably be limited by large scale surface deviations such as astigmatism. Very little experience with nearly unstable suspended cavities is existent. The single arm test (single arm version of the SQL interferometer) will investigate the regime close to 180° Gouy phase, where all modes become degenerate. A nice feature of the TNI is that due to the Gouy phase of almost 90° between the mirrors the higher order modes of odd order, especially the misalignment modes resembled by the first order, are optimally suppressed. The according resonance frequency of the second order modes is shown on a second axis in figure 6.10. It crosses 15 MHz at about 30 µm spot size and 5 MHz at about 3 µm. This is both well beyond the linewidth of 0.5 MHz ($\mathcal{F}=3000$) while it might not be sufficiently suppressed with a low finesse of e.g. 300.[2] The effects of being close to the PDH modulation frequency have not yet been studied.

2 The commissioning optics have twice the transmission which results in a finesse of only 155.

6.5.2 *Mode matching to a changed cavity mode*

As seen in the last chapter, changing the spot size on the TNI's test mirror can be accomplished by tuning the length close to instability. This of course results in a variation of the cavity mode which in turn leads to a mode mismatch of the incident light. There are two ways to deal with this:

First the input mode can be re-matched using the input lenses as shown in figure 6.9. Very close to instability ($<60\,\mu$m spot size), the length tuning can be accomplished remotely by means of coil magnet actuators while staying in the linear BOSEM range. However, there is no realistic UHV compatible way of mode matching other than venting the system an adjusting lens positions manually.

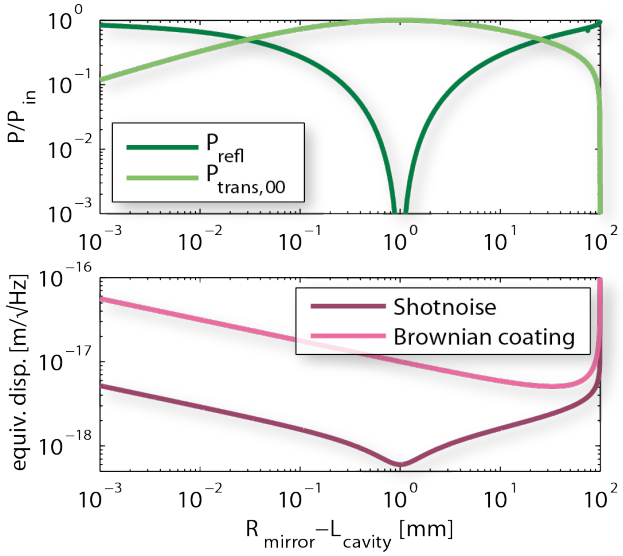

Figure 6.11.: The mode overlap of an unchanged input mode optimized for 60 µm spot size inside the cavity and the varying TNI mode was determined numerically using Finesse [136]. The transmitted TEM_{00} mode is a good estimation for μ in figure 6.24. The second plot shows the change of coating Brownian noise at 100 Hz with spot size according to equation 5.24. Despite of unchanged mode matching, it is well above the shot noise according to equation 6.37 using the measured modulation index $\beta_{\mathrm{mod}} = 0.15$.

Therefore, a second option was investigated: not adjusting the lenses at all. This causes excess power reflection of light without any length information. The additional light reaches the PDH readout diode with all its noise contributions. Technical noise terms are suppressed far beyond the requirements of the TNI by other prototype subsystems. As such, it is possible that they won't limit the sensitivity too much. But mismatch unavoidably causes an increased shot noise level. The important point is that the predicted signal, in this case coating thermal noise, rises faster than shot noise. The effect of 'junk' signals onto feedback loops must be tested experimentally.

A big drawback of spot size changes with a fixed input mode is that the mode matching into the TNI also acts as mode conversion of the output mode. If the input and the cavity mode are matched perfectly, this means that the signal mode has the same shape as the input. In that case the whole detection path is fed by a beam with constant parameters, regardless of what the cavity mode looks like. With a fixed input mode, in contrast, the signal mode being sent out of vacuum changes. It might need adjustments in terms of spot sizes or at least re-calibrations of the auto alignment system as Gouy phases change. The advantage is that the detection components are outside of vacuum and hence easily accessible. An adjustable Gouy phase telescope in the common path could even supply the whole detection bench with an unchanged mode so that no further changes are required.

6.5.3 *Intensity limits: LIDT*

Optical cavities enhance the laser power circulating inside. The non-negligible absorption of the HR-coatings of cavity mirrors introduces heat. This causes a temperature rise and hence conductive energy transport. Its efficiency is determined by the steepness of the temperature gradient ∇T which is inversely proportional to the cross section A where the energy has to pass through.

The simple model in [137] assumes a beam radius much smaller than the dimension, i.e. the thickness, of the mirror. Then the heat distribution can be approximated to have a hemispherical profile. The steepest gradient is assumed to occur across the hemisphere with the same radius as the beam, i.e. $A = 4\pi w^2/2$. According to the source, the temperature gradient is well approximated by a temperature increase ΔT happening across the beam radius, so $\nabla T = \Delta T/w$. Then the temperature increase can be quantified

$$\Delta T = \frac{P_A}{2\pi\kappa w} \tag{6.18}$$

according to their equation 4, where $\kappa_{SiO_2} = 0.014\,\mathrm{W/cm\cdot K}$ is the thermal conductivity of the fused silica substrate and P_A is the absorbed power. This is a surprising result, as the temperature depends linearly on the inverse beam size and not on the intensity, i.e. $1/\text{beam size}^2$.

[138] sets the temperature threshold before the onset of laser induced damage (LIDT) to the softening point of fused silica at 1610°C. This gives a maximally absorbed power of $140\,\mathrm{W/cm\cdot}w$ which is 14 mW for a 10 µm beam. This should be very well within the limits of current coatings.

However, there are a few facts which show that this is only a very optimistic upper limit: the peak intensity and hence the peak temperature is twice as high as in the flat-top beam used in this theory. Either the substrate or the coating will suffer before reaching the softening point. For example micro crystals will form at 600..700°C [96]. And

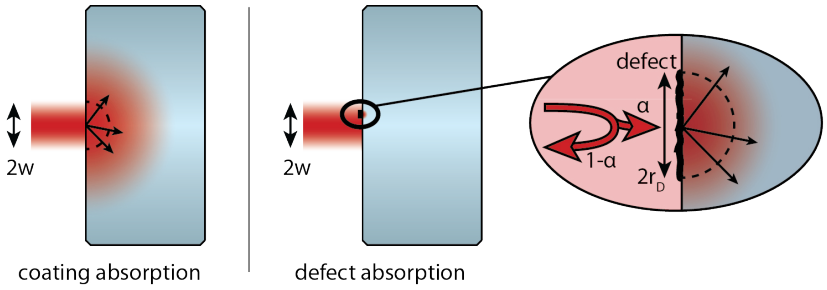

Figure 6.12.: A laser beam can transfer heat into a substrate by means of absorption in the coating. The absorption of modern coatings is limited by defects. These are much smaller than a typical beam ($r_D \ll w$), which can increase the induced peak temperature drastically.

the absorption of modern day coatings is limited by inhomogeneities and impurities [139, 138] instead of bulk absorption.

If defects are much smaller than the beam profile, $r_D \ll w$, then the absorbed power

$$P_A = \alpha I \cdot \tilde{A}_D \tag{6.19}$$

depends on the local intensity $I \leq 2P/\pi w^2$ of the Gaussian beam, the radius of the defective area $\tilde{A}_D = \pi r_D^2$ and the absorption coefficient of the defect α. Replacing the beam radius in equation 6.18 with the defect radius ($w \to r_D$) yields

$$\Delta T \leq \alpha P \frac{r_D}{w} \frac{1}{\pi w^2 \kappa} \quad . \tag{6.20}$$

This gives the same results as equation 6.18 for $r_D = w$, aside from a factor 2 which arises from the increased peak intensity of the Gaussian beam with respect to a flat-top beam. Inserting reasonable values such as a 1 µm absorbing defect ($\alpha = 1$) illuminated by a 10 µm small 1 W beam as used in the TNI already exceeds the melting point of fused silica ($\Delta T = 2300$K).

For orientation compare the power density on the PMC mirrors. The input power was increased to about 12 W in [39, 28] which gives 3 kW circulating power at a spot size of close to 400 µm. The corresponding power densities are 8 W/µm and 20 W/µm^2. The latter would be exceeded with a TNI circulating power of 1 W and spot sizes significantly smaller than 10 µm.

For GaAs the situation might be much more problematic. [140] reports surface destructions on a 350 µm thick GaAs waver at 10 W concentrated in a 270 µm beam which matches a power density of 40 mW/µm or 140 µW/µm. However, the absorption of AlGaAs coatings was strongly reduced since the publication [135].

6.5.4 *Measuring the cavity geometry*

It is not trivial to measure the mode shape inside the TNI with special emphasis on the spot size on the test mirror. With the commissioning optics in place, the divergence of the transmitted mode could be measured. This, however, requires a well characterized transmission path.

In practice, two other approaches were followed: The non-aligned cavity shows a Herriott cell pattern in transmission. Its shape is characteristic for the cavity geometry. The aligned cavity can be scanned to observe the higher order mode spacing which gives the cavity g-factor with high accuracy.

Herriott cell pattern

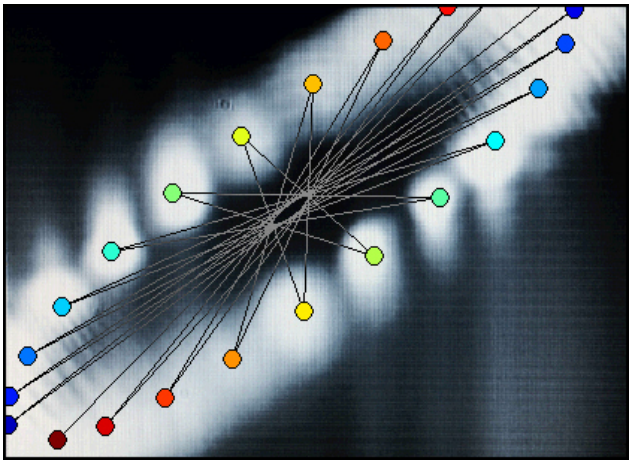

Figure 6.13.: A strongly misaligned linear cavity behaves equivalent to a Herriott cell. In the nearly hemispherical case the transmitted spots are on opposing sides of an ellipse pattern. Their angular separation of the transmitted beams is determined by the exact cavity geometry. Overlaid to a CCD image is the color coded sequence of spots. Next order round trips are connected by lines.

Initial gravitational wave detectors were originally planned to employ Herriott delay lines in the arms [141]. The beam pattern on the mirrors actually doesn't differ so much from nowadays used Fabry Perot cavities used nowadays if illuminated off-center, e.g. by misaligning the input beam.

In order to describe the pattern by means of Herriott cell theory, interference of the individual spots must be avoided. This is why this method only works for rather stable and reasonably low finesse cavities. [142] predicts that all spots are evenly separated by the same azimuthal angle θ on the same circle.

In order to adopt the theory for a symmetric delay line described in the source to the TNI, the delay line length $d \rightarrow L_{\mathrm{rt}} = 2L$ is replaced

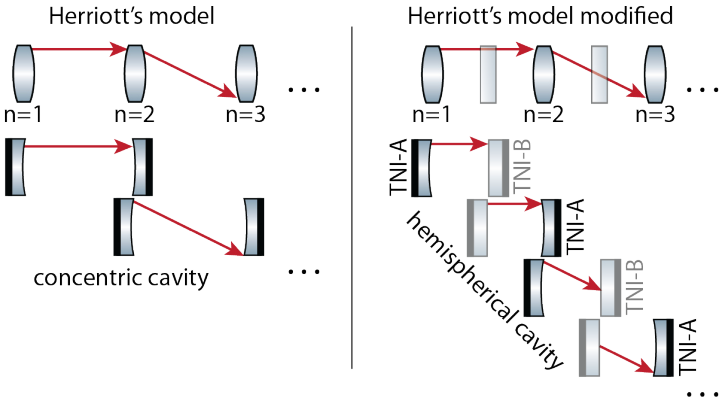

Figure 6.14.: In Herriott's model of a concentric geometry the beam hits the same mirror every second n. In the nearly hemispherical TNI the beam is hitting the same mirror every n. Hence, their equations 4 and 7 give the spot positions on one and the same mirror. They are separated by θ.

by the TNI round trip length and the focal length $f \to R/2$ by half the input coupler's curvature. Then Herriott's equation 2 in [142]

$$\cos\theta = 1 - \frac{d}{2f} \tag{6.21}$$

can be reformulated to give the length

$$\frac{L}{R} = \frac{1-\cos\theta}{2} \tag{6.22}$$

relative to the radius of curvature and hence the cavity g-factor.

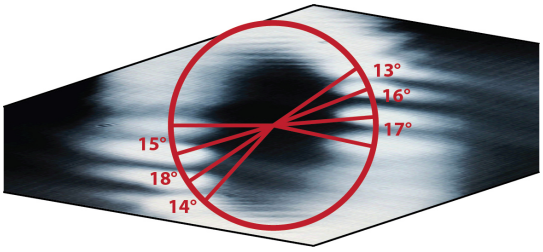

Figure 6.15.: Projecting the picture in figure 6.16 to a circular spot-pattern according to figure 2 in [142] allows to measure the angular separation. On average neighboring spots are separated by 15.5°.

For the $\theta = 180° + 15.5°/2$ deduced from figure 6.15 this gives $L/R = 0.995$. However, it is difficult to determine θ, as patterns with e.g. three times the azimuthal separation may look very similar.

The presented method is limited to low finesse cavities since interference between the spots spoils the accuracy. However, it allows investigation of accidentally unstable cavities as well. Furthermore, a good understanding of the pattern by means of Herriott's equations 4 and 7 in [142] eases initial alignment significantly.

Higher order mode spacing

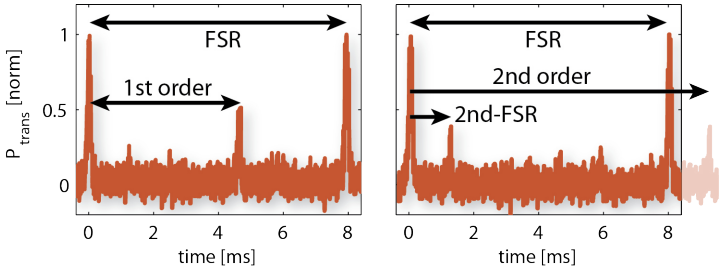

Figure 6.16.: A longitudinal mode scan of the TNI by means of the upper mass actuators shows multiple fundamental modes spaced dependent on the cavity length by an FSR. Higher order modes are separated evenly depending on the mode geometry, i.e. length and mirror curvature. Misaligning a steering mirror in front doesn't change the TNI but introduces first order modes. Shifting a mode matching lens causes second order sidebands to resonate. The ratio of HOM separation and FSR (4.6 ms/8 ms) gives L/R=0.95, so a cavity length 5 mm away from instability for a mirror with ≈100 mm radius of curvature.

When scanning the aligned cavity, multiple, equidistant fundamental resonances show up. Their spacing

$$FSR = c/L_{\mathrm{rt}} \tag{6.23}$$

depends only on the round trip length which can be measured to about 1% with a ruler. An intentional misalignment of either the TNI or the input mirrors induces higher order modes. They resonate at

$$\nu_{qnm} = q\nu + v(m+n+1)\frac{\arccos(\pm\sqrt{g})}{\pi} \quad , \tag{6.24}$$

so their spacing in units of FSRs

$$\frac{\nu_{qnm+1}\nu_{qnm)}}{\nu_{q+1nm} - \nu_{qnm}} = \frac{\arccos(\pm\sqrt{g})}{\pi} \tag{6.25}$$

only depends on the g-factor [38]. The flat end mirror's $g_{\mathrm{TNI\text{-}B}} = 1$ should hold well enough even for small thermally induced deformations. Then the cavity g-factor $g = 1 - L/R_{\mathrm{TNI\text{-}A}}$ is solely defined by the ratio cavity length $L = L_{\mathrm{rt}}/2$ and the incoupler's radius of curvature $R_{\mathrm{TNI\text{-}A}}$. As the suspended mirrors don't always move with a constant speed, the mode scan might not be perfectly linear. Then it helps to measure the spacing of the second order mode relative to the next fundamental mode which approaches zero when tuning closer to instability. In figure 6.13 both spacings agree very well. The accuracy reached for the relative spacing is about 1% which gives 2% L/R-accuracy and gets even better closer to instability.

6.5.5 *Beyond optical instability*

Optical resonators require a certain g-factor $|g|<1$ for stability reasons. However, the spot size on the TNI test mirror is altered by approaching the instability on purpose. Then one may accidentally overshoot as has happened in the past which caused major confusion. Very little is known about passive unstable cavities though active unstable cavities are used with an active medium in high power laser applications.

Figure 6.17.: The light transmitted through an unstable linear cavity shows a distinct circular symmetry. The pattern 'breathes' in- and outwards as the mirrors move differentially. In this case, the measured cavity length is 98 mm with a specified incoupler's radius of curvature of 100 mm. Reducing the length to 85 mm resulted in a stable cavity. The higher order mode spacing hints that the new, now stable length is about 5 mm from optical instability.

In an unstable cavity, the mode slightly expands every round trip. The circulating mode either cannot interfere with the incident one anymore or the accumulated Gouy phase is not constant across the incoupler. If the incident light is well aligned, the transmission shows a circular symmetry. It actually consists of many concentric rings which are 'pumping' in- and outwards with the swing of the cavity mirrors.

If the input light is not well aligned to the cavity, the situation is similar to the stable cavity: two distinct spots can be seen in transmission of the cavity. The position of the first is mostly influenced by the incoupler, the other's by the outcoupler. When collapsing them, they evolve into the above-mentioned circular patterns.

6.6 BEAM STEERING

Two suspended 2" steering mirrors with passive damping as described in chapter 5.6 are used to correct the input beams shift and tilt fluctuations. They are separated by 84° of Gouy phase as showed in figure 6.9. This way both quadratures of beam position can be actuated.

The actuation signal is whitened digitally (f_{zero}=0.33 Hz, f_{pole}=33 Hz) and de-whitened electronically. The signal is controlling a closed loop current driver actuating coils with 200 turns. Four 5 mm ø, 5 mm thick neodymium magnets provide plenty of actuation range.

The mechanical response of both suspensions was characterized in terms of resonance frequency and Q-value in pitch and yaw in figure 6.18. For comparison with the RefC steerings see figure 5.19. The inverse of the transfer function is applied to the digital control signal inside CDS. This way linear actuators with a flat response far beyond the suspension's resonance are synthesized. The drawback of the response compensation and the strong whitening is that care must be taken not to saturate the drivers electronically at high frequencies.

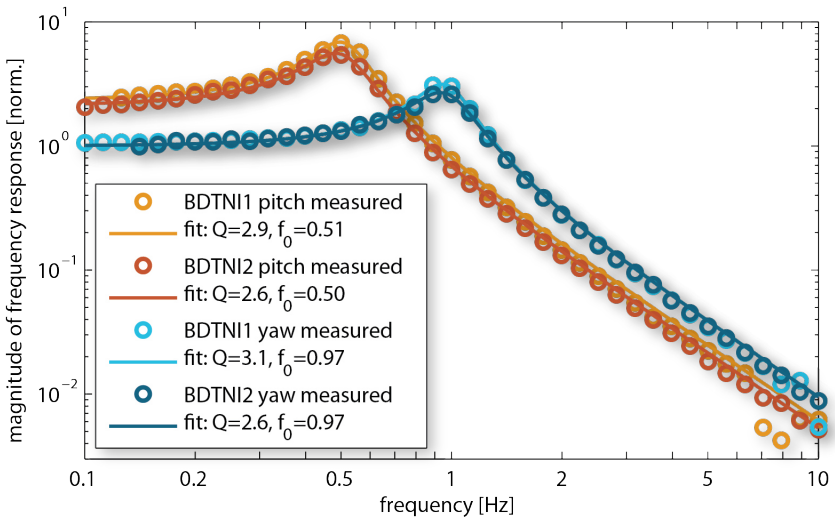

Figure 6.18.: The transfer functions of the TNI's steering mirrors are compared. A swept sine signal was digitally injected in the DOF-coordinates (pitch and yaw) which are used to direct the beam into the TNI cavity. The beam motion was detected by means of in-vacuum QPDs. The Q-value and the eigenfrequency were fitted with the model of a single stage damped harmonic oscillator using the Matlab curve fitting toolbox. The effect of different optical levers was compensated by normalizing to the DC response of yaw to one. Both suspensions match extremely well. The inverse of the fit is used to linearize the actuation signal which simplifies the construction of an auto alignment loop.

6.7 FIXING THE BEAM AT THE SOUTH TABLE

Inside vacuum, the PMC serves as a position reference for the input beam. Therefore, the beam follows any motion of the central bench. Recently, optical levers were installed in addition to the SPI to control the optical benches to behave as one. Yet the steering mirrors lack direct position readouts like BOSEMs. The task of spot position sensors is, to provide a beam position readout directly in front of the TNI. The optimal alignment information can be obtained by means of two sensors which are separated by $\approx 90°$ Gouy phase. For comparable sensitivities and dynamical ranges they should detect similar beam sizes (compare chapter 6.7.2).

6.7.1 *Spot position sensors*

The sensors are placed on top of the south SAS inside vacuum. The associated electronics are located outside the vacuum vessel. They are connected via long ($> 10\,\mathrm{m}$) wires to the bare quadrant photodiodes' casings. This scheme allows only slow signals (i.e. no 8 MHz sidebands) to be detected and requires special care against electromagnetic coupling.

An elaborate transmission scheme (compare chapter C.6) in combination with shielded twisted pair cables provides a strongly increased rejection of noise coupling.

All four quadrants are supplied with the same bias of stabilized and current limited 15 V. The photocurrent is read using a transimpedance amplifier across $3.3\,\mathrm{k}\Omega$ resistance. All quadrant signals are whitened individually (f_{zero}=0.33 Hz, f_{pole}=33 Hz) and sent to CDS differentially. They are digitized individually and the spot position is reconstructed digitally. For now the signals are normalized by the sum signal to reduce the gap effect (see chapter 6.7.4).

Two spot position sensors sense the input beam towards the TNI. Ten percent of the light reflected by the PBS is detected on each photodiode. Three lenses image the beam to 1 mm size with 90° Gouy phase in between the photodiodes to obtain full information about all degrees of freedom (shift and tilt).

6.7.2 *Gouy phase telescopes*

Any spot position photodiode is only capable of sensing a transverse shift of the detected beam while it is completely insensitive to tilt. A differential wavefront sensor, in contrast, can only detect the differential tilt of two beams. It does not show a first order response to differential shifts.

To get access to the non-sensed quadrature, the position of the photodiode needs to be imaged. In geometric optics, this can be understood as applying an optical lever to convert tilt to shift or focusing the beam to transform a shift to tilt in the focus. In Gaussian optics, first order modes can be used to describe beam alignments. Tilt and shift are separated by 90° of Gouy phase [143, 144, 145] plus any multiples of 180° (see equation 2.8..2.11). A lens systems can manipulate any beam to advance the Gouy phase by an arbitrary amount while imaging the beam to a spot with the same size. The same spot size is desired to obtain a similar noise performance. It is noteworthy that the total accumulated Gouy phase must be used in the lens system's design [146].

In principle a single lens can suffice to produce the quadrature shift (see figure 6.19). Then, however, a very specific focal length is required. In most cases a two lens Gouy phase telescope will be unavoidable. Generally speaking, three lenses are required to detect both quadra-

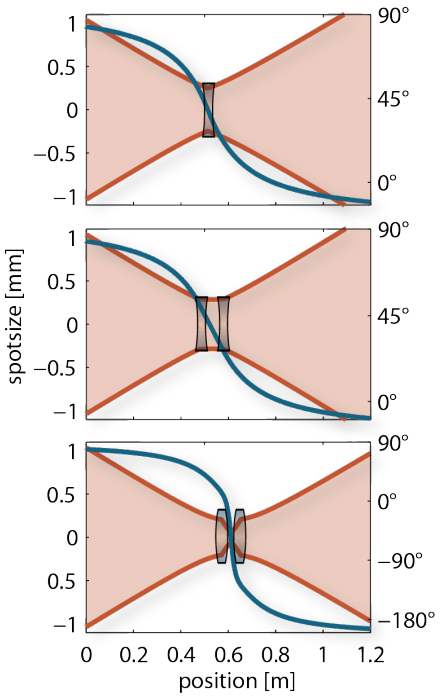

Figure 6.19: An arbitrary beam (x=0) can be imaged to a beam (on the right) of the same size (red) but shifted by 90° Gouy phase (blue). In a lens system there is more freedom of choice for the focal lengths compared to a single lens. In air, any solutions with narrow waists (bottom one) should be avoided to prevent dust particles from being captured.

tures on the PDs in a restricted space: one for creating the correct spot size on the first photodiode and two for the Gouy phase telescope providing 90° shift and 1:1 scaling of the spot.

As an additional requirement, outside of vacuum small waists should be avoided. They tend to act as optical tweezers for dust. Once caught, it causes scattering and absorption.

In practice, the available space is restricted especially in vacuum. It turns out that much shorter solutions can be found compared to figure 6.19. Furthermore, the long optical path of the TNI reflection port requires additional collimation. The search for solutions was automated in Matlab. The script samples available lens positions and focal lengths, and changes distances wherever possible. Solutions are filtered for 1 mm ± 10% spot size on the PD, 90° ± 10% Gouy phase difference, least number of lenses and the smallest consumed space.

6.7.3 *The optimal spot size*

The optimal spot size for the widely used Centronic QD50-3T quadrant photodiode was investigated. This specific sensor type has a wide gap of 200 µm at a total diameter of 8 mm. When using a small beam, a significant fraction of the power is dumped in this insensitive area. In turn, the capacitance between the quadrants is low, allowing for fast readouts.

Theoretically, a small beam results in the most sensitive position signal (steepest signal slope). Yet this is only true as long as all the light is sensed and not dumped in the insensitive gap. Therefore, a

very small beam must be avoided to obtain a steep error signal for spot displacement which is linear over a wide range. A too large beam will result in clipping at the rim of the photodiode. To determine the optimal spot size, the differential power (yaw signal) is calculated for a fundamental Gaussian beam which is statically misplaced by 0.7 mm in vertical (see figure 6.20).

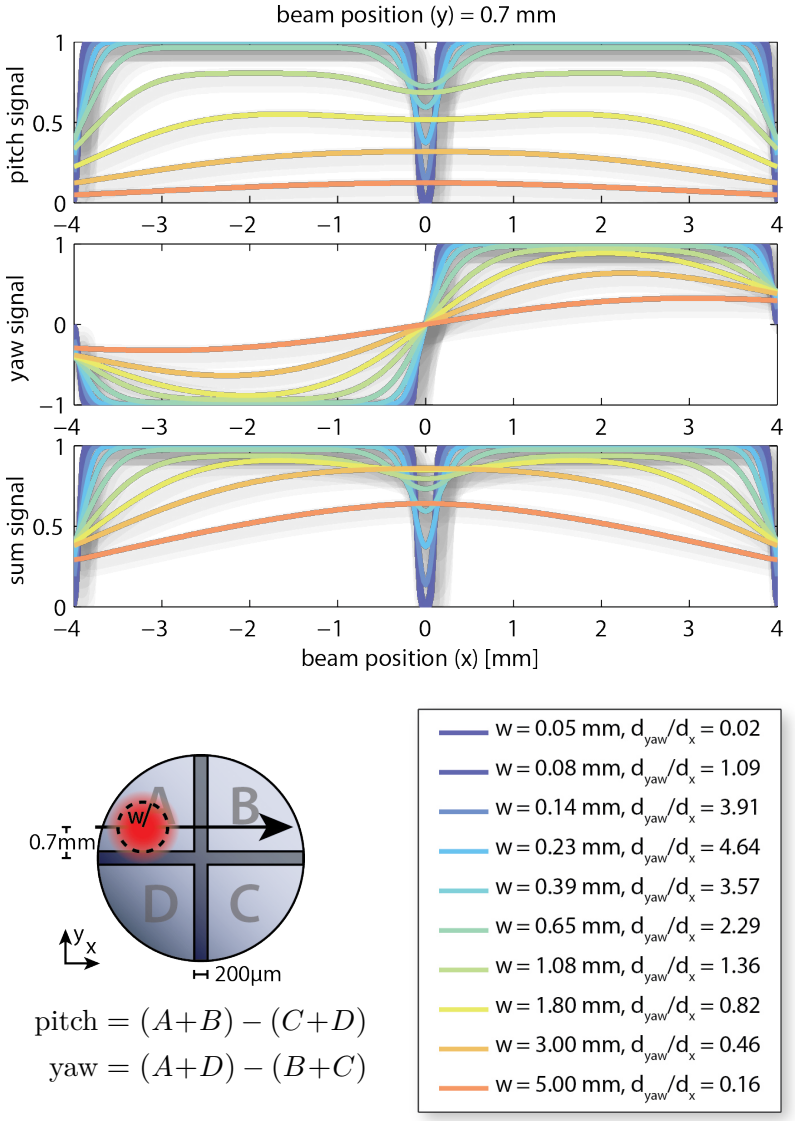

Figure 6.20.: The pitch and yaw signals are calculated by means of differential power for a realistic quadrant photodiode (8 mm diameter, 200 µm gap) for various spot sizes. Smaller beams result in steeper signals when scanning the spot position until the beam size gets of the order of the gap and a significant amount of light is dumped. Large beams, in contrast, result in clipping on the circumference. A static de-centering e.g. in vertical causes coupling to the signal of the other direction. The optimal spot size ($1/e^2$ power radius) is about 1 mm.

It can be seen that in addition to losing steepness of the yaw signal inside the gap, strong couplings between pitch and yaw arise. This will be important when the spot is misplaced intentionally to scan the test mirror's surface for coating thermal noise homogeneity. From the shown plot a target spot size of 1 mm was defined. Remaining nonlinearities and cross couplings are compensated well by the normalization described in the next chapter.

6.7.4 *Position signal normalization*

As described in the last chapter, the gap effect cannot be avoided completely. However, better position information can be obtained when dividing any misalignment signal by the total sensed power, i.e. the sum of all four quadrants. It might appear that extremely small spots are even outperforming the 1 mm target defined in the last sub-section. This is not true, of course, when keeping in mind that in this case the sum signal is getting very small at the center, which causes the normalized signal to get noisy, e.g. from electronic readout noise.

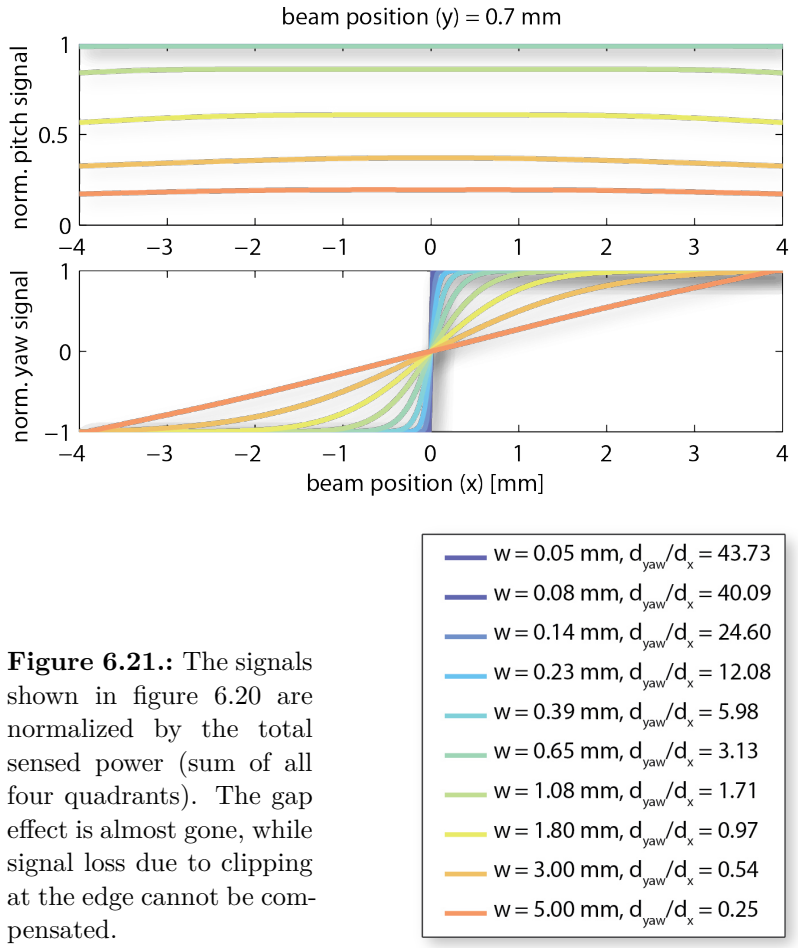

Figure 6.21.: The signals shown in figure 6.20 are normalized by the total sensed power (sum of all four quadrants). The gap effect is almost gone, while signal loss due to clipping at the edge cannot be compensated.

Another positive side effect of the normalization is that the position information is getting less susceptible to power fluctuations in the beam

itself. Therefore, it is not required anymore, to adjust gains in feedback loops when varying the sensed power.

6.8 PDH STABILIZATION

For a length stabilization of a cavity following Pound, Drever and Hall [128], sidebands are created by phase modulating the incident light with the resonant in-vacuum EOM of the RefC. Usually the modulation frequency is chosen such that it is outside of the cavity bandwidth. Then the sidebands are reflected by the cavity, while the carrier enters it and senses the length. For small length fluctuations, the phase of the carrier has a very steep position dependence. Commonly, the error signal is sensed in reflection in a demodulation scheme. RF phase modulation (frequency sidebands) of the laser acts an as optical local oscillator measuring only the optical path length outside the cavity.

A signal could be obtained in transmission as well, but the reflected signal results in a better noise performance and a much more versatile setup. It does not rely on any outcoupler transmission, so that even an opaque substrate can be used. Yet, an impedance matched cavity is desirable if possible. It transmits most of the carrier light which results in a strongly reduced shot noise level on the PD in reflection.

The TNI is designed to have a finesse of ≈3000 at ≈10 cm length. For this design, the 8 MHz modulation is well outside the cavity's linewidth of 0.5 MHz (compare figure 6.22). During initial commissioning, how-

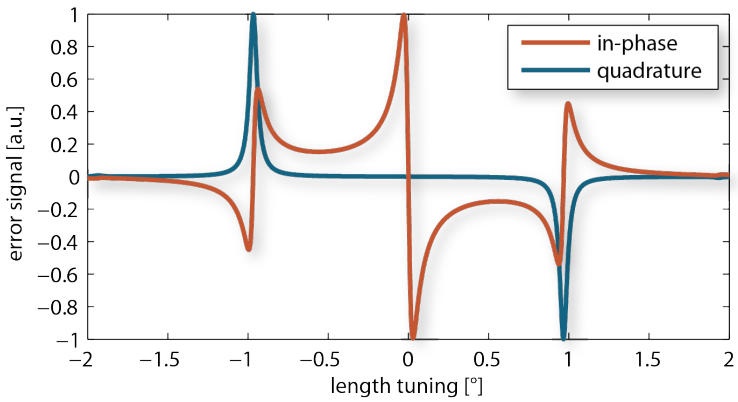

Figure 6.22.: The normalized error signal of the final TNI design is shown for mirror position tunings given in degrees. The bandwidth with a finesse of 3000 is small compared to the modulation frequency. The resulting error signal matches the well known PDH-signal in reflection. The optimal demodulation phase is shifted only by 1.7° with respect to the one for an infinitely small bandwidth.

ever, mirrors with only 98% power reflectivity are installed at a slightly bigger length of approximately 15 cm. This results in a finesse of only 160 which is experimentally easier to handle. In turn, the bandwidth

increases to 6.25 MHz, which is close to the modulation frequency. A significant fraction of the sidebands is entering the TNI and sensing the length as well. In simulations carried out with Finesse [136], it could be shown that the optimal demodulation phase for a maximal error signal slope is still shifted by 90° with respect to the minimal error signal slope. The latter is defined as the new quadrature demodulation while the first one is the new in-phase demodulation. However, the new in-phase demodulation is shifted by 21° with respect to the 'original' in-phase demodulation, the one that would be chosen when using sidebands far beyond the bandwidth (see figure 6.23). The new error signal slope is slightly bigger than the one using the 'original' demodulation phase.

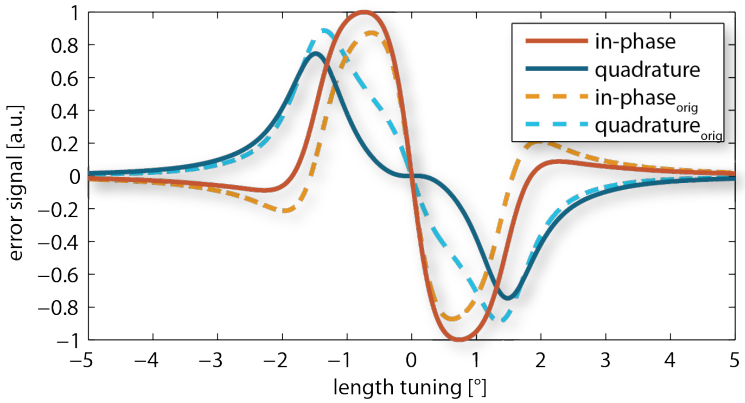

Figure 6.23.: During the commissioning phase a lower finesse of 160 and 1.5 times bigger length is used in the TNI which increases the bandwidth close to the modulation frequency. This mixes the original quadratures and results in a different error signal pattern shown as dashed lines. Yet, a 21° shifted demodulation recovers a steep, linear error signal around the resonance as shown by the solid lines.

In practice, the demodulation phase is tuned to zero slope at the resonance (quadrature demodulation) using a voltage controlled phase shifter described in section 6.8.2. Then it is shifted by exactly 90°. This is verified using an oscilloscope, as the used phase shifter is extremely nonlinear.

In vacuum it would be difficult to detect the 8 MHz signal at a reasonable low noise level. One big advantage of the Pound Drever Hall method is that the local oscillator and the signal beam are superimposed optically right at the incoupling mirror. Thus maximal common mode rejection can be achieved. This allows a detection of the signal out of vacuum and off the SAS platform. The beam leaves the vacuum through a viewport and is detected on a non-suspended detection bench.

A 2 mm ø InGaAs photodiode (Perkin Elmer C30642GH) detects the light with sufficiently high quantum efficiency

$$\eta = \frac{hf}{q\lambda} \cdot R > 80\% \tag{6.26}$$

where $R \approx 0.7\,\mathrm{A/W}$ is the responsivity extrapolated from the datasheet. The readout electronics provide a DC-signal for state recognition and auto-locking and an AC-path with resonant readout at 8.05 MHz. The signal is amplified and demodulated by means of a phase shifted copy of the EOM drive close-by (on the same board). Finally it is low pass filtered to get rid of sideband-sideband beats (twice the modulation frequency) and sent differentially to CDS together with the DC-signal.

6.8.1 *Pound Drever Hall signal refinement*

A detailed analysis of the Pound Drever Hall signal is given by Black in [147, 128]. Yet, the publication only covers the idealized case of a perfectly mode matched and well impedance matched cavity. Any junk-light at the locking photodiode increases the shot noise level (compare figure 6.24). Furthermore, the actual impedance matching changes the slope of the error signal as more light from inside the cavity is reflected to (overcoupled) or transmitted away (undercoupled) from the locking diode located in reflection. This influences the signal equivalent shot noise[3] as well (compare figure 6.11). This discussion is meant as an extension of Black's document and follows the notation closely. However, the following replacements had to be made: $F \rightarrow \mathrm{F}$ in order not to cause confusion with the finesse factor, $P_{\mathrm{in}} \rightarrow P_0$ to account for not mode matched light and $\phi \rightarrow \delta$ to stay consistent with figure 6.5.

Assume a power of P_{in} to be incident onto a non-degenerate optical resonator. Then only a fraction

$$P_0 = \mu \cdot P_{\mathrm{in}} \tag{6.27}$$

is in the actual cavity eigenmode. It can enter the cavity and gather length information. The mismatched light

$$P_{\mathrm{mm}} = (1 - \mu) \cdot P_{\mathrm{in}} \tag{6.28}$$

is reflected to the PDH photodiode without carrying length information. It is assumed to contribute only shot noise. In the case of the Prototype facility this appears valid for most cases, as the laser power is stabilized to the shot noise limited detection of about 250 mW. With this definition, the expressions for the carrier and sideband light remain the same as with Black. The reflection coefficient F is given by

3 The displacement corresponding to the shotnoise limitation of the readout.

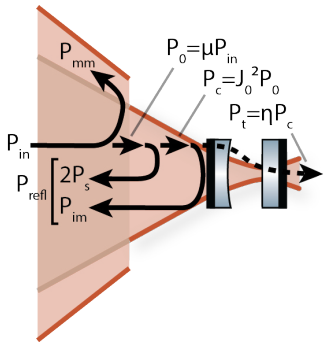

Figure 6.24.: The reflected light components of a non mode matched and not necessarily impedance matched cavity are shown. Only the mode matched fraction μ of the incident light can gather information about the cavity. The two sidebands are assumed to be out of bandwidth being reflected completely. Dependent on the quality of impedance matching, only a fraction η can pass the cavity when on resonance whilst the rest is reflected to the photodetector. All beams contribute shot noise. Yet only a fraction contribute length mismatch information, i.e. the PDH signal.

Black for a symmetric, perfectly impedance matched cavity. It can be generalized to the reflection coefficient

$$\begin{aligned}\frac{E_{\text{refl}}}{E_0} := \mathrm{F}(\delta) &\overset{6.3}{=} \frac{t_1^2 r_2 t_c e^{i\delta}}{1 - r_1 r_2 t_c e^{i\delta}} - r1 \\ &= \frac{(r_1^2 + t_1^2) r_2 t_c e^{i\delta} - r_1}{1 - r_1 r_2 t_c e^{i\delta}} \\ &\approx \frac{r_2 t_c e^{i\delta} - r_1}{1 - r_1 r_2 t_c e^{i\delta}}\end{aligned} \tag{6.29}$$

of the mode matched light without these constraints. Around resonance, this formula can be expanded

$$\lim_{\delta \to 0} F(\delta) = \frac{r_1 - r_2 t_c}{r_1 r_2 t_c - 1} + \frac{(1 - r_1^2) r_2 t_c}{(1 - r_1 r_2 t_2)^2} \cdot i\delta \;+\; \mathcal{O}(\delta^2) \tag{6.30}$$

up to the first order in δ. The quality of the impedance matching

$$\begin{aligned}P_{\text{im}} &= |F(\delta{=}0)|^2 \\ &= \left| \frac{r_1 - r_2 t_c}{r_1 r_2 t_c - 1} \right|^2 \\ &:= (1 - \eta)\end{aligned} \tag{6.31}$$

is limited by the reflected power on resonance, i.e. the constant term in equation 6.30 and represented by the efficiency η according to figure 6.24 in future. The linear slope

$$\frac{(1 - r_1^2) r_2 t_c}{(1 - r_1 r_2 t_2)^2} \cdot i\delta = i \frac{4\mathcal{F}}{\lambda} \delta L \cdot \kappa \tag{6.32}$$

in equation 6.30 can be represented by the finesse given in equation 6.12 and cavity length (not round trip) changes $\delta L = 2 \cdot \delta / (2\pi)\lambda$. It is varied with respect to perfect impedance matching by a correction factor

$$\kappa = \frac{(1 - r_1^2) r_2 t_c}{(1 - r_1 r_2 t_c)\sqrt{r_1 r_2 t_c}} \tag{6.33}$$

ranging from 2 (overcoupled) via 1 (impedance matching) to 0 (undercoupled) dependent on the reflectivity distribution between the in- and outcoupler (compare figure 6.7). Close to the resonance, the reflected power

$$\begin{aligned} P_{\text{refl}} &= P_c \left|F(\omega)\right|^2 \quad + 2P_s \quad - 4\sqrt{P_c P_s}\,\text{Im}\{[F(\omega)]\sin\Omega t\} \\ &\approx (1-\eta) P_c \quad + 2P_s \quad - 16\sqrt{P_c P_s}\frac{\mathcal{F}}{\lambda}\delta L \cdot \kappa \end{aligned} \tag{6.34}$$

in the cavity mode can be added with the mismatched power P_{mm}, as the fields cannot interfere. The error signal and its slope

$$D = -16\sqrt{P_c P_s}\frac{\mathcal{F}}{\lambda} \cdot \kappa \tag{6.35}$$

are both increased by the same correction factor κ.

Compared to Black, the error signal shot noise on resonance

$$\begin{aligned} S_\epsilon &= \sqrt{2\frac{hc}{\lambda}\left[(1-\eta)P_c + 2P_s + (1-\mu)P_{\text{in}}\right]} \\ &= \sqrt{2\frac{hc}{\lambda}P_{\text{in}}\left[\left((1-\eta)J_0^2 + 2J_1^2\right)\mu + (1-\mu)\right]} \end{aligned} \tag{6.36}$$

is increased by non impedance matched and non mode matched light. The equivalent length noise is obtained by dividing the error signal spectrum S_ϵ by the slope D

$$\begin{aligned} S_L &= \frac{\sqrt{2\frac{hc}{\lambda}\left((1-\eta)P_c + 2P_s + (1-\mu)P_{\text{in}}\right)}}{16\sqrt{P_c P_s}\frac{\mathcal{F}}{\lambda}\cdot\kappa} \\ &= \frac{\sqrt{hc}}{8}\frac{\sqrt{\lambda}}{\mathcal{F}} \cdot \sqrt{\frac{\frac{1-\eta}{2}\frac{J_0^2}{J_1^2} + 1 + \frac{1-\mu}{2\mu J_1^2}}{P_c \cdot \kappa^2}} \\ &\overset{\beta \ll 1}{\approx} \frac{\sqrt{hc}}{8}\frac{\sqrt{\lambda}}{\mathcal{F}} \cdot \sqrt{\frac{\frac{2(1-\eta)}{\beta^2} + 1 + \frac{2(1-\mu)}{\mu\beta^2}}{\mu P_{\text{in}} \cdot \kappa^2}}\ , \end{aligned} \tag{6.37}$$

which is arranged in a way that the last $\sqrt{\ }$-term gives the correction compared to the idealized case described by Black. This equation clarifies, why an undercoupled cavity ($\kappa \to 0$) is the least desirable case for length measurements, as the signal equivalent shot noise goes to infinity ($S_L \to \infty$). Furthermore, it is noteworthy that impedance mismatch η and error signal slope κ can be traded against each other. Perfect impedance matching does not yield the lowest possible shot noise anymore.

Whilst η can be calculated easily by the derived equations given the reflectivities and thereby equation 6.33, μ is more difficult to obtain. Either the overlap integral of the ingoing beam and the cavity mode is evaluated analytically, or like in this document, numerically by means of e.g. Finesse [136]. For an impedance matched resonant cavity μ can be measured by means of the transmitted fraction of incident carrier power.

6.8.2 *Voltage controlled phase shifter*

The modulation-demodulation technique used for optical readout utilizes phase modulation. A copy of the drive signal is used to demodulate the detected power later on. This copy needs to have the correct phase. The required phase shift depends mostly on the modulation frequency which is usually fixed, and the optical path length, which is subject to several changes especially in a prototype environment. In principle, the phase shift can be realized by means of a delay line, i.e. cable length, but at low modulation frequencies the required cable is quite long ($\lambda \approx 0.7 \cdot c_0 / f_{mod} = 26\,\mathrm{m}$ for 8 MHz) and might not be fixed.

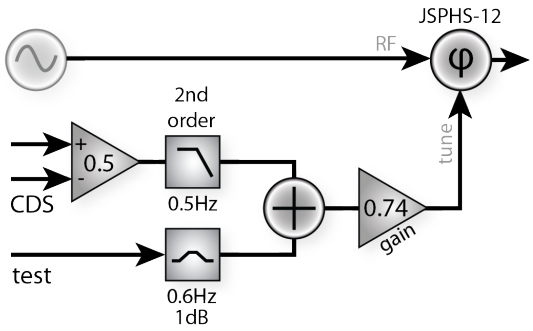

Figure 6.25.: The phase of an RF oscillator is shifted by a JSPHS-12 voltage controlled phase shifter. The differential signal from CDS is converted to single ended and low-passed to avoid oscillator phase noise. A non-filtered test input can be used to introduce oscillator phase noise intentionally in order to characterize couplings to other signals.

A typical suspended cavity needs three differently shifted demodulation signals, the length degree of freedom and two angular quadratures, tilt and shift. A universal phase shifter box was developed. The input signal is split into three paths by an ADPS3-1 three way power splitter (1..300 MHz) and compensated for the overall power loss by means of an AD9009 amplification stage so that each output level equals the input. Each of the paths is receiving its own control signal from CDS differentially. The CDS control signal is divided by two and low pass filtered to avoid excess phase noise. It is applied to a JPSPHS voltage controlled phase shifter (8..12 MHz, so this part needs to be adjusted in case a different modulation frequency is used). The achievable phase

tuning range is approximately 215°. For diagnostic purposes, e.g. investigation of oscillator phase noise coupling, an analog signal, which is not divided by two, can be added on top of the CDS signal.

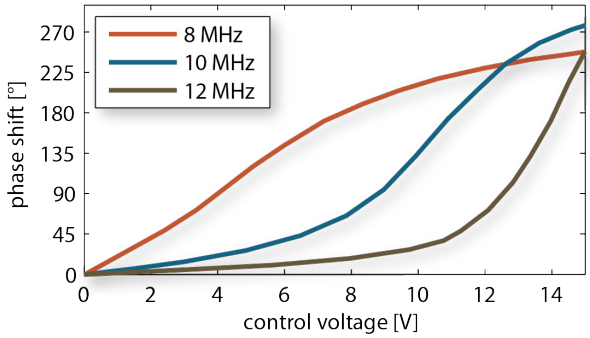

Figure 6.26.: The JSPHS-12 response was obtained from the datasheet. For 8 MHz a tuning range of 215° is available when using 0..10 V control voltage. The voltage dependence is strongly nonlinear and has to be fitted for calibration purposes (equation 6.38). In case the same phase shifter is used for higher frequencies, a bigger control voltage must be applied to achieve the required 180° shift.

Voltage controlled phase shifters are extremely nonlinear as shown in figure 6.26. The voltage response at 8 MHz is taken from the datasheet and fitted by means of a fourth order polynomial. Now the phase

$$\phi = 0.0140 \cdot U^4 - 0.469 \cdot U^3 + 4.15 \cdot U^2 + 12.7 \cdot U \tag{6.38}$$

can be inferred from the control voltage U applied to the phase shifter, i.e. half the CDS voltage, to a few degree accuracy.

6.9 DIFFERENTIAL WAVEFRONT SENSING

Differential wavefront sensing is actually a spatially resolved version of the Pound Drever Hall scheme. Each quadrant of a QPD senses the deviation from resonance of its own quadrant of the beam. The four signals are subtracted in a manner of left minus right (yaw) and top minus bottom (pitch). These signals are zero if the wavefronts of the sidebands being reflected from the cavity and the carrier partially leaking out of the cavity are not tilted against each other. Around this working point they give a linear error signal.

The actual detectors are based on a GEO600 quadcam design. Each quadrant features a DC transimpedance amplifier and a resonant AC readout including onboard demodulation. The two sets of four signals are sent to CDS differentially. An additional whitening stage is under development. Inside CDS, the quadrants' signals are subtracted from each other and normalized by the sum of all quadrants as described in section 6.7.4.

The experience with the 30 m Prototype in Garching already suggested that active centering of the spots onto the photodiodes may be required. This turned out to be the case for the TNI as well. Efforts were started to implement digitally controlled spot centering loops by means of two galvo scanner driven mirrors with orthogonal axes in front of each quadrant photodiode. It is important to remember that such a periscope rotates the coordinate frame of the beam. Hence, the resulting QPD coordinate system is aligned to a synthetic coordinate frame matching that of the TNI by a digital rotation matrix.

6.10 AUTO ALIGNMENT

The idealized Pound Drever Hall signal assumes perfect co-alignment of the ingoing beam and the cavity mode. In reality, a suspended mirror is prone to resonant mechanical enhancement of motion close to the suspension's resonance frequencies as well as slow drifts due to temperature changes and the high susceptibility to small influences due to the softness of the suspension system. Both cause rms deviations from the optimal alignment. These deviations can couple into length noise via clipping on optics, position dependent sensitivity at the locking photodiode or excess power reflection to list only a few.

An active feedback system, called auto alignment, senses and counteractuates misalignments. Two in vacuum spot position sensors measure the alignment of the beam incident onto the TNI. The two steering mirrors in front actuate the beam. The actuation matrix is measured by driving each degree of freedom of the beam directors sinusoidally well below the resonance frequency, one at a time. All responses of the spot sensors are monitored and assembled to form the actuation matrix. This is then inverted to give the sensing matrix and applied to the sensors' signals, so that a virtual pair of sensors is formed, giving the misalignment in terms of required steering mirror actuation. Slow servos were designed to actively center the spots on the mirrors by means of in vacuum spot position sensors with a few Hertz bandwidth. Offsets can be added to the error point in order to misalign the beam intentionally for scanning the input beam across the TNI mode. In the future, the synthesized virtual sensor will be calibrated to beam displacement and tilt on the TNI test mirror.

6.11 DESIGN SENSITIVITY

The TNI's design sensitivity arises from gathering known noise terms. It is calculated by means of a custom Matlab script which was developed initially to predict the Reference Cavity's sensitivity given in chapter 5.7. Analytical noise models are used wherever possible. This eased the design process for the TNI where many parameters could be changed without lengthy tool chain applications.

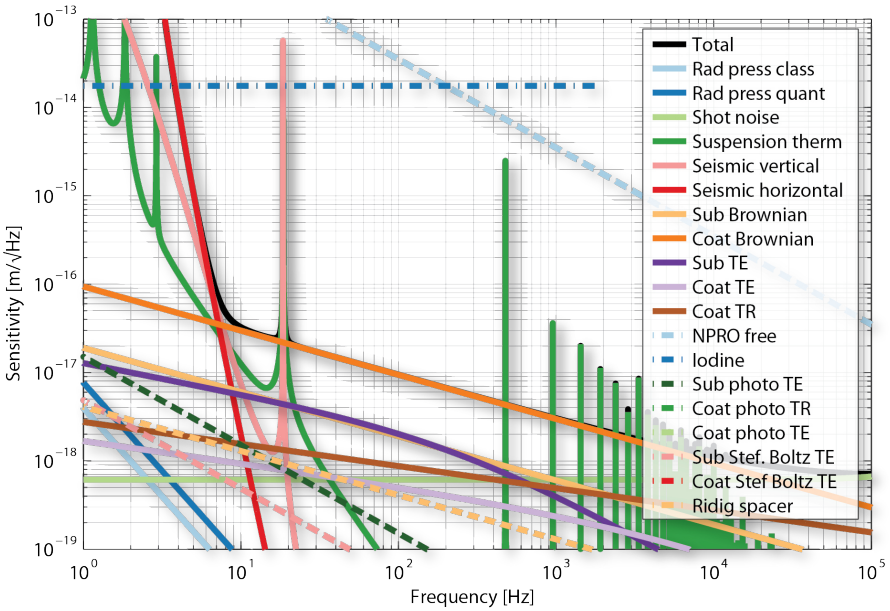

Figure 6.27.: The noise sources discussed in this chapter are projected into length noise of an approximately 10 cm long hemispherical TNI with 850 g mirrors and a finesse of 3000 at a input power of 1 mW. The spot size at the test mirror is 60 µm implying a spot size of 550 µm on the incoupler. This is achieved for a length of 1.1 mm away from optical instability. The thermal noise of the test mirror is dominating the sensitivity over a big range from 20 Hz to 10 kHz.

The simulation includes models for the most common noise terms known from gravitational wave interferometers such as seismic noise, quantum noise and basic thermal noise channels. However, as the TNI enters an uncommon regime with its small spot size, also less common noise terms are included such as photon absorption (photo thermal) and black body radiation (Stefan-Boltzmann noise) while others had to be refined like the coating thermo-elastic noise.

6.11.1 *Cavity geometry*

A linear cavity involves the least number of components. It is not polarization dependent so the light can be split off by means of a quarter wave plate and a polarizing beam splitter[4]. Concerning the cavity geometry itself, coating thermal noise is increased the most, if the test mirror is at the smallest section of the beam, i.e. its waist. As the wavefronts are parallel at this point, the test mirror has to be flat and the cavity is close to hemispherical by definition.

4 This is not true for AlGaAs coatings. Due to the inherent birefringence, a Faraday isolator would be a better choice.

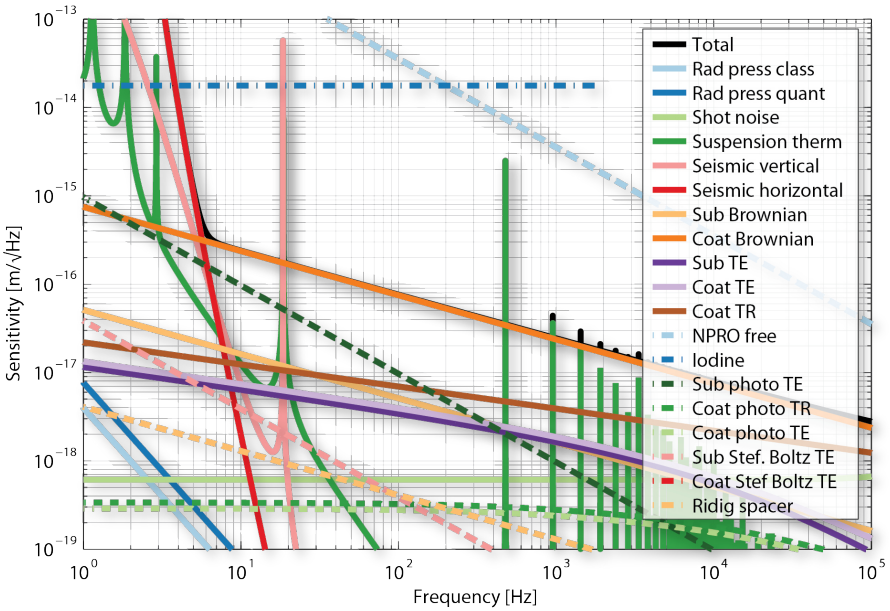

Figure 6.28.: Shown is the same nose projection as in figure 6.27 with a much more extreme spot size of 7.5 µm on the test mirror. An input power of 1 mW this yields an intensity of $2 \cdot 10^{10}\,\mathrm{W/m^2}$ which might be beyond the destruction threshold of an IBS coating. The second spot on the curved mirror is 4.5 mm big and the cavity length is 3 µm from optical instability. With these parameters coating Brownian thermal noise is limiting over an extremely wide frequency range.

Length

According to equation 5.14 a shorter TNI is less susceptible to laser frequency noise. On the other hand, shortening increases the bandwidth so that the sidebands get partly resonant. Furthermore, for the same divergence of the mode the spot size difference decreases, leading to a bigger influence of the curved (non-test-) mirror's coating noise. Although the suspensions are designed to allow sub-cm cavity length in principle, the radius of curvature and thereby the approximate length was fixed to 10 cm.

Finesse

A high finesse enhances any displacement signal which makes it easier to measure thermal noise while it reduces the signal normalized shot noise. Also it keeps the bandwidth reasonably small so that the PDH sidebands (frequency given by the Reference Cavity) are outside the bandwidth. As a drawback a too small bandwidth makes the cavity more difficult to control. A high finesse Furthermore, causes a high power buildup which, due to the small spot size, can damage the coatings. Although the finesse is not exactly fixed, it's design value has been defined to be 3000.

Impedance matching

As seen in chapter 6.8.1, a 'perfect' impedance matching in the sense of section 6.3.1 doesn't necessarily yield the best achievable signal-to-noise ratio. Yet it's least sensitive to technical noise such as intensity noise. In case of a reasonably low finesse, the intra cavity losses are negligible compared to the mirror transmissivity. Therefore (equation 6.16), the reflectivities of in- and outcoupler match ($r_{\mathrm{in}} = r_{\mathrm{out}}$) and can be taken from the same coating run. This is important when the test coating would provide significantly reduced coating noise which would be comparable with that of the bigger spot on the incoupler.

Mirror mass

It was under discussion, whether to suspend a rigid spacer instead of individual mirrors. This appears reasonable when looking at the rigid spacer noise depicted in figure 6.27. The big advantage of individually suspended mirrors, however, is the immense variability in positioning of the spot and tuning the spot size with a basically unchanged TNI (compare section 6.5.1). In this case each mirror requires the full 850 g mass of the lowest stage of the triple pendulum design.

6.11.2 *Seismic noise model*

The seismic noise at the site is described in chapter 3.1. A very crude model of $10^{-7}\,\mathrm{m}/\sqrt{\mathrm{Hz}}$ and a double pole at 1 Hz is assumed in this specific simulation. This appears reasonable, as the seismic barrier is extremely steep: six orders of magnitude suppression per decade from the horizontal pendulum system, another two from the SAS and two more from the seismic itself. A variation of the seismic noise itself will not change the predicted seismic noise vastly, other than shifting the seismic wall by a few Hertz.

6.11.3 *SAS isolation model*

The SAS table is assumed to behave like a damped harmonic oscillator with finite attenuation. According to real measurements, horizontal isolation starts at 70 mHz with a double pole. The double pole of vertical isolation is placed at 150 mHz. Due to center of percussion effects, the isolation levels off in a plateau. In the simulation, this is taken into account by a pessimistic double zero at 7 Hz without any overcompensation. Internal resonances of the suspended tables are neglected. They occur mainly in a frequency range where strong isolation is available from the mirror suspensions.

6.11.4 *Suspension model*

A full state space suspension model is available (more information in chapter 3 and 4). Yet the same argument holds as for the seismic noise model: this simulation focuses on limiting noise sources in the band beyond ten Hertz. The seismic wall, however, is so steep that a minor inaccuracy in the suspension model does not change the band, over which coating thermal noise can be observed, significantly. To reduce the complexity of the simulation, a complex pole pair was placed at the actual longitudinal resonance frequencies of the suspension at 0.6 Hz, 1.4 Hz and 2.6 Hz. The Q-value of these pendulum resonances is determined by the active damping system and was set to five in this case.

The same is true for the vertical isolation, where the frequencies are assumed to be 2 Hz and 3 Hz. The stiffest vertical mode, mainly differential bounce of the lower two masses, is suspected to be around 20 Hz. Hence, it cannot provide significant isolation. Even worse, it decouples from upper mass motion so that it is not observable with the BOSEMs and therefore difficult to damp. This results in a set of high Q modes peaking up in the tens of Hz regime together with the differential lower mass' roll mode which is not included in the model due to unspecified coupling.

According to experience from the past, vertical motion is coupled into horizontal readout with a ratio of $\approx 1:1000$ [63]. It is important to note that the vertical suspension has one stage less than the horizontal suspension. Also, in general, the vertical eigenfrequencies are slightly higher than the horizontal ones. Hence, the relative insensitivity is 'eaten up' in the 5 to 10 Hz range. Above this range vertical seismic noise governs the sensitivity.

6.11.5 *Shot noise*

Photon counting statistics on the photodetector causes a signal indistinguishable from length fluctuations. The shot noise contribution is simulated according to equation 5.33. If not otherwise stated, the mode matching is optimized for a 60 µm waist. A modulation index of $\beta_{\mathrm{mod}} = 0.15$ rad was measured by means of an optical spectrum analyzer using the RefC EOM driven by a 1 W RF amplifier. The cavity is impedance matched $r_1 = r_2$, so according to section 6.11.1, $\kappa = 1$. The mode matching efficiency is determined using Finesse [136] but could be calculated analytically by means of the overlap integral. If the spot size inside the cavity is changed by means of cavity length tuning, the light which is not mode matched contributes additional shot noise (see chapter 6.5.2).

6.11.6 *Radiation pressure noise*

In an arm cavity enhanced Michelson interferometer, the classical laser power fluctuations are correlated between both arms. The common mode rejection is usually high. Quantum noise entering the detection port of the interferometer [148], redistributes the laser power anti-correlated and eventually becomes a limiting noise source for gravitational wave interferometers in the form of quantum radiation pressure noise [149] (compare figure 1.2).

In a single Fabry Perot resonator, there is no common mode rejection at all.[5] The in-vacuum power is stabilized by an intensity stabilization system (ISS) down to the shot noise level of 250 mW detected power [29]. However, only 1..10 mW is assigned to the TNI, which couples in additional vacuum fluctuations (compare appendix D.13). Hence, the power

$$\begin{aligned}\sqrt{S_{\text{shot}}^{\text{power,in}}} &= \sqrt{\frac{2hcP_{\text{in}}}{\Delta f \lambda}} \\ &\overset{1\,\text{mW}}{=} 1\,\text{mW} \cdot 1.9 \cdot 10^{-8} \\ &\overset{10\,\text{mW}}{=} 10\,\text{mW} \cdot \underbrace{6.1 \cdot 10^{-9}}_{\text{RIN}}\end{aligned} \tag{6.39}$$

is shot noise limited at this new level. Within its bandwidth, the cavity coherently amplifies the light, so that power fluctuations with a single sided spectral density of

$$\begin{aligned}\sqrt{S_{\text{shot}}^{\text{power,cav}}} &= \text{pbf} \cdot \sqrt{S_{\text{shot}}^{\text{power,in}}} \\ &= \underbrace{\frac{\mathcal{F}P_{\text{in}}}{\pi}}_{P_{\text{cav}}} \cdot \underbrace{\sqrt{\frac{2hc}{\Delta f \lambda P_{\text{in}}}}}_{\text{RIN}_{\text{in}}}\end{aligned} \tag{6.40}$$

are incident onto both mirrors. The suspension's susceptibility obtained from the state space model translates this into an accurate displacement spectrum. For a coarse estimate at higher frequencies, i.e. above all suspension resonances, two free 850 g-masses can be assumed to be driven coherently.

6.11.7 *Suspension thermal noise*

The suspension system is designed in a way that thermally driven motion of the suspension chain's lowest stage dominates the suspension thermal noise. The simple model [91] of a single, 35 cm long horizontal stage with four 55 µm steel wires of a Q-value of 10^6 gives the correct slope in the high frequency band (well beyond the highest suspension

5 The TNI employs a very different power than the RefC. Radiation pressure is correlated but vastly different in magnitude. Hence, the TNI must be treated as single, independent cavity with uncorrelated noise.

resonance) but overestimates the level (see figure 4.28). Also, it neglects coupling to other modes arising from the triple pendulum multi degree of freedom structure.

For a correct noise prediction, the full state space model is solved to obtain the susceptibility of the lower mass. Applying equation 5.17 gives the expected thermal noise which is then also valid around the highest frequency vertical resonance. In addition to the fundamental resonances, multiple equally spaced violin modes show up in the hundreds of Hz region[6]. Their Q is extremely high, resulting in very narrow lines in the spectrum.

6.11.8 *Substrate Brownian noise*

The beam size is assumed to be small compared to the mirror dimensions. The surface fluctuations can be assumed to be coherent over the read out area. Therefore, Brownian thermal noise is solely defined by material parameters and the achievable Q-value. The latter is guessed to be around 10^6 for Suprasil2 [151]. Under this assumption, Substrate Brownian noise is well (more than a factor of three) below Coating noise for any spot smaller than 100 µm.

6.11.9 *Coating Brownian noise*

For coating Brownian noise the model from [119] is used. It takes into account that the '*material properties of the coating are different from those of the substrate and the mechanical loss angle is anisotropic*' which is important since the coatings have a layer structure. '*The loss angle in the Ta_2O_5 coatings for strains parallel to the surface can be determined from ring-down experiments. [...] Since the coatings experience free boundary conditions, they are not greatly compressed perpendicular to the surface [...]. Therefore, $\phi_\perp$ cannot be easily measured [...] and no measurements of $\phi_\perp$ exists at the present time.*' Until $\phi_\perp$ is measured, the best guess is to assume $\phi_\perp = \phi_\parallel$.

The design of the TNI is chosen that under these assumptions coating Brownian noise of silica-tantala coatings is limiting the sensitivity over a wide range. At the lower end the sensitivity is limited by the seismic wall and the associated feedback noise. At the upper end shot noise is starting to dominate.

For the simulation, ion beam sputtered silica-tantala coatings are assumed (see chapter D.14 for the implications). Recently progress has been made in reducing the loss angle by means of annealing [152] and titania doping [153]. Also the change from amorphous to crystalline structures, e.g. made from GaAs-AlGaAs stacks, seems promising [11]. Due to the big margin between coating Brownian and other

6 This is only an approximation as can be seen from [150] eq. 2.14

noise sources, the TNI is a promising tool also for the new low coating noise technologies.

6.11.10 *Coating thermo optic noise*

Coating thermo elastic noise

According to [106], thermo elastic dissipation of the coating was described to arise from '*the dissimilar thermal and elastic properties of the thin film and the substrate*'. '*In homogeneous solids, thermoelastic dissipation is associated with the irreversible flow of heat driven by temperature gradients associated with strain gradients in the solid*'. In addition, [106] extends this concept to dissipation from temperature gradients caused by a difference of the thermal properties of film and substrate. In earlier calculations[7], '*the thermoelastic properties of the film and the substrate other than the thermal expansion coefficient were assumed to be identical*'. '*After discussions of the authors, the differences have been resolved in favor of the model used here*', i.e. with non-identical elastic properties.

It is shown that the dissipation peak from the inhomogeneity of the dielectric thin film stack is far beyond the frequencies of interest. Therefore, it can be treated as a monofilm of averaged properties.

Furthermore, it is assumed that the '*thermal diffusion lengths for frequencies of interest are short enough compared to [...] the radius of the Gaussian beam interrogating the surface*'. The thermal diffusion length

$$r_T = \sqrt{\frac{\kappa}{\rho C f}} \tag{6.41}$$

is in silica $r_T \approx 39\mu\text{m}$ at 100 Hz [121]. Hence, the assumption is not valid for the more extreme spot sizes in the TNI experiment anymore and the temperature fluctuations in the sensed volumes are not independent anymore. Normally, only dissipation due to heat flow along the direction of the beam into the substrate has to be considered. Now, however, heat can also be transferred efficiently parallel to the surface which opens an additional loss channel. This is completely neglected in the aforementioned models. No deep analysis which takes small readout spots into account could be found.

Coating thermo refractive noise

The laser interferometric readout of a dielectrically coated test mass is not only influenced by real surface fluctuations. As the laser penetrates the first few layers of a coating, thermally induced fluctuations of the refractive index and layer thickness variations cause phase noise which is indistinguishable from real mirror motion. This thermo refrac-

7 [106] refer to their references 7 and 8, i.e. [121, 154].

tive noise[8] was investigated initially in [155]. The effective refractive index was corrected later in [121]. Levin [109] presented a derivation according to the fluctuation-dissipation theorem later on, which was in '*complete agreement with the previous calculations*'.

In the simulation the model from [118] in conjunction with the corrected refractive index [121] is used for the TNI sensitivity prediction.

Substrate thermo elastic noise

In addition to the dissipation induced by the gradient across the dissimilar thermoelastic properties between coating and substrate, solving the elastic equation also leads to a stress gradient inside the substrate. This translates into a temperature gradient leading to dissipation. The associated noise was described first in [123] and generalized for a bigger frequency band in [156] and not only valid in the adiabatic limit. Somiya was able to deduce an analytical form in [157]. It turns out that the transition frequency ω_c between adiabatic and non-adiabatic behavior is right in the TNI detection band which emphasizes the importance of this model (compare equation (9) in [156]).

A unified theory

Recently, the theory became accepted that coating thermo refractive noise and coating thermo elastic noise have opposite signs. Although the specific couplings to reflected phase are different, their origin is similar: the underlying temperature fluctuations are identical for long thermal diffusion lengths (i.e. low frequencies). Therefore, the noise terms are partially correlated and can cancel each other [105]. This can be used intentionally to achieve better cancellation [11]. [157] state that substrate thermal noise is also caused by the same thermodynamical fluctuations and suggest a coherent treatment of all three noise terms.

In [11] it is shown on the example of AlGaAs coatings that the photo thermo elastic and the photo thermo refractive effect can cancel each other. If transferable to the thermo refractive and thermo elastic effect, this could results in a drastically reduced thermo optic noise contribution. In the noise simulation described in this chapter, they are not treated coherently. This has two reasons. Firstly, at the time it was carried out, it was not clear whether the cancellation does actually take place. Secondly, the regime of extreme spots (in particular smaller than the thermal diffusion length) is not well covered by the mentioned theories. Yet, noise cancellation is very sensitive even to minor deviations. Therefore, the pessimistic approach of uncorrelated noise terms is followed. This causes an increased total noise which is still well below the Brownian thermal noise.

8 While both mechanisms together are summarized as 'thermo-refractive', this is somewhat a historically based misnomer.

6.11.11 *Photo thermal noise*

Photo thermal noise is a barely known noise source. Each photon which is absorbed in a mirror decays to approximately 50 thermal phonons. Due to their relatively short free path length of 0.8 nm in silica, any photon absorption leads to a local jump of the temperature. In [123], a shot noise model is used to describe the conversion. The temperature increase leads to optical path length variations from the thermal expansion of the substrate (substrate photo thermo elastic) and from the thermal expansion of the coating (coating photo thermo elastic) as well as it's refractive index change (coating photo thermo refractive). Although the source states that photo thermal noise is only important in the high power regime (megawatts) it is actually strongly spot size dependent and might become important for the TNI due to the small spots with high intensities.

Using the equations given in [118] and an absorption of 2 ppm, the substrate contribution is vastly dominating over the coating in the TNI. Therefore, the individual contributions can not cancel. The positive message is that down to $\approx 5\,\mu$m spot size photo thermal effects will not be dominating the sensitivity. However, it must be kept in mind that any experimental coating or mirror design such as a 1" AlGaAs coated mirror bonded to a large substrate (compound mass) may lead to increased absorption which can bring this noise source closer to or above the Brownian coating thermal noise.

6.11.12 *Stefan Boltzmann thermo elastic noise*

In the aforementioned models, the energy transfer was assumed to happen via thermal conductivity. '*However, thermal radiation as a dissipative process produces additional fluctuations of temperature applied to the mirror*' [118]. This process is included in the simulation since its spot size dependence is stronger than that of coating Brownian noise and might become important for very small spots. The results of the simulation showed that the coating contribution is always negligible and the substrate's contribution stays sufficiently small for reasonable spot sizes as well.

6.12 MEASURED SENSITIVITY

Despite all efforts to lock the laser to the RefC, the TTFSS didn't work. The stringent frequency noise suppression requirements arising from the SQL interferometer result in a barley conditionally stable servo design which is extremely complex to debug and commission. A workaround servo consisting of a digital feedback loop controlling the laser temperature in conjunction with a fast analog servo actuating

onto the laser's piezo can lock the laser to the RefC. Yet, the achieved gain is so low that the lock is unstable on long term scales.

Summarized, no frequency reference was available in the prototype facility. Therefore, in this experiment the laser was locked to the TNI using the actuators of the *workaround* servo with the digital feedback loop shown in figure 6.30. No independent laser frequency or intensity stabilization took place.

6.12.1 *Signal readout*

Interferometric readout requires a certain working condition which is established by a feedback servo. The purpose of the feedback is to suppress any disturbance occurring in the system. This is true for desired signals such as coating thermal noise as well.

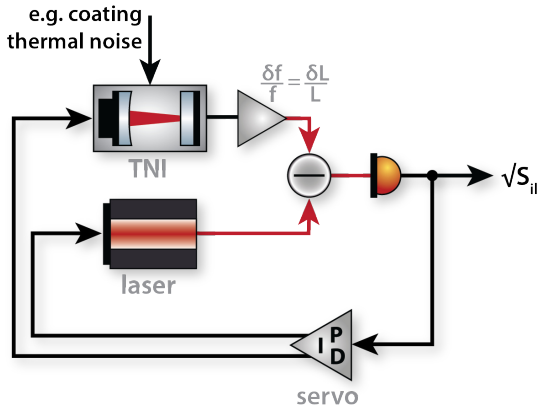

Figure 6.29.: Irrespective whether the servo feeds back to the laser frequency or the TNI length, any differential signal between TNI and laser frequency is measured and suppressed by the feedback loop. The equivalent out of loop signal $\sqrt{S_{\mathrm{ol}}}$ can be inferred by means of the open loop gain G. The results can then be projected back to displacement noise.

Imagine the sensitivity $\sqrt{S_{\mathrm{il}}}$ to be measured inside the loop as shown in figure 6.29. The equivalent out of loop signal, the signal of a virtual system which doesn't have to be held at the working point (i.e. without feedback)

$$\sqrt{S_{\mathrm{ol}}} = \sqrt{S_{\mathrm{il}}} \cdot (1 + G) \tag{6.42}$$

requires the open loop gain G to be known. Directly, this can only be measured in a limited frequency range due to the large loop suppression at low frequencies. The PMC simply cannot follow injected signals that are sufficiently big. Yet for commissioning it is important to have a calibrated signal down to and even below the suspension resonances. What can be measured well enough are the individual transfer functions from actuator drive to laser frequency. As all the other frequency responses are also known to within a scaling factor, the open loop gain can be synthesized.

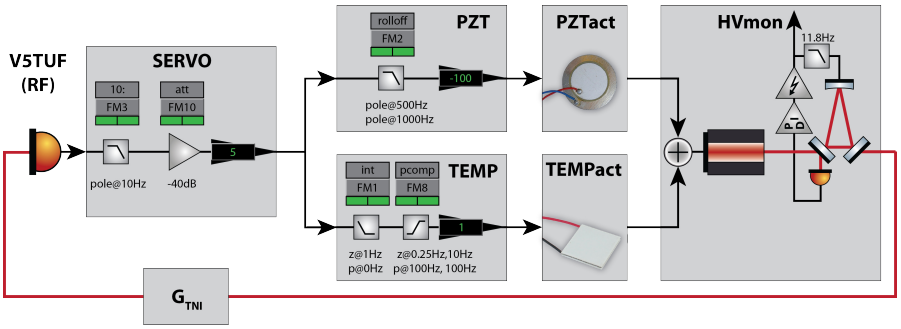

Figure 6.30.: The TNI length is measured relative to the laser frequency by means of the resonant V5TUF-type resonant photodiode. The internally demodulated output is processed by a common SERVO. Its output is split up into a fast PZT actuator path and a slow TEMP actuator. The laser frequency is followed by the PMC feedback loop inside its bandwidth.

6.12.2 *Actuator characterization*

It is rather challenging, to measure individual actuator responses in a multi actuator feedback system as in figure 6.30. With a single actuator, however, the loop won't be robust enough, so another method is required. The PMC can serve as an analyzer for the laser frequency. Its feedback loop tries to follow frequency changes with the end mirror position by means of a voltage applied to the piezo where the mirror is attached to. This voltage can be measured at the high voltage amplifiers monitor port *HVmon* . It is important to consider the finite output impedance of 3.3kΩ in conjunction with the (unbiased) piezo capacitance of 4.08µF. This forms a single pole at 11.8 Hz between *HVmon* and the piezo voltage. As the feedback loop tries to compensate it, this shows up as a zero in the laser frequency to *HVmon* transfer function. Fitting the measured *PZTact* response gives a slightly higher corner frequency of 12.3 Hz compared to the calculated 11.8 Hz (compare figure 6.31). This might arise from biasing the piezo. To compensate this, a pole at 12.3 Hz is multiplied to both the measured actuator responses in order to obtain a response of the laser frequency in units of *HVmon* readout at DC. This is not so clear when looking just at the *TEMPact* response since the measured zero is almost compensated by a close-by pole of the temperature feedback loop built into the laser.

6.12.3 *Sensor characterization*

The coupling of length fluctuations of the TNI to PDH readout signal is determined by the optical transfer function of the cavity plus the electronic conversion inside the photodiode including demodulation. The

9 The star denotes that it is an inferred response which is calibrated in units of *HVmon* DC response per DAC output in counts.

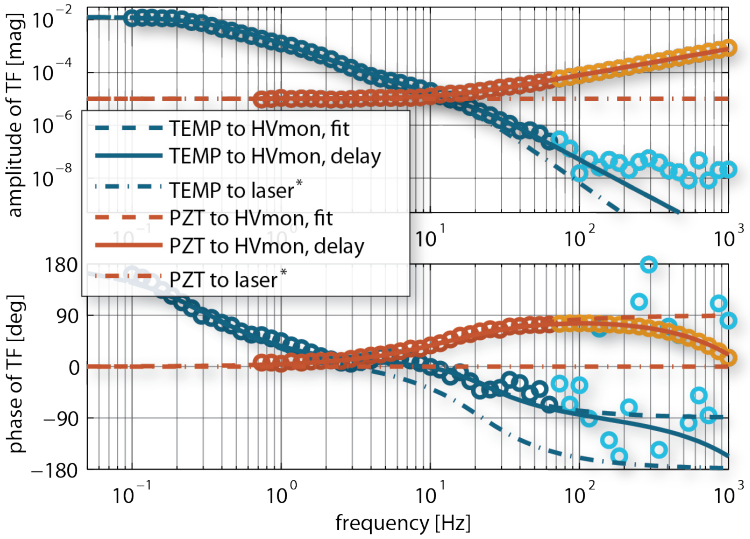

Figure 6.31.: The actuator transfer functions *PZTact* and *TEMPact* are measured from the digital output of the *PZT* and *TEMP* filter to laser frequency by means of the electronic *HVmon* (compare figure 6.30) while the TNI is unlocked. Because of coherence loss in the TEMP and phase loss in both measurements, the light colored data beyond 100 Hz are not fitted in the dashed curve. Including a 190 µs delay, which is in rough agreement with [34] and probably arises from the AA/AI filters and delay in the digital signal processing running at 32 kHz, explains the measured PZT data well as shown in the solid curve. The zero at 12-13 Hz arises from a low-pass in the PMC actuation and is canceled by chance by an unexpected pole in this range in the *TEMP* path. The point-dashed data excludes the *HVmon*-zero and the delay and hence shows the inferred actuator transfer functions to laser frequency *laser**.[9]

optical transfer function is well defined by the cavity pole frequency at ≈3 MHz as given in table 6.1 similar to figure 6.6. This is well beyond the interesting frequency range and can be treated as flat. This might not be completely true for a TNI as proposed in table 6.2.

The opto-electronic transfer function of the photodiode including the first stage was measured. Modulating the current of a laser diode causes a power modulation. Inside the PD electronics, the photocurrent is detected resonantly and its DC contribution is suppressed by an active high-pass filter. The transfer function from laser power to the output of this filter stage is shown in figure 6.32. A manual fit results in a Q of the resonance of 10 at the modulation frequency of 8 MHz. This gives a corner frequency of the pole of ≈400 kHz. For a better understanding, the measurement from the left graph is shown in the right graph again. However, this time the frequency axis has a logarithmic scaling and is centered around the resonance frequency. For comparison, the fitted double pole without any other structure is shown in the right as well.

The fitted response is flat within 0.5 dB up to beyond 110 kHz which is sufficiently flat for the measurement shown in this section.

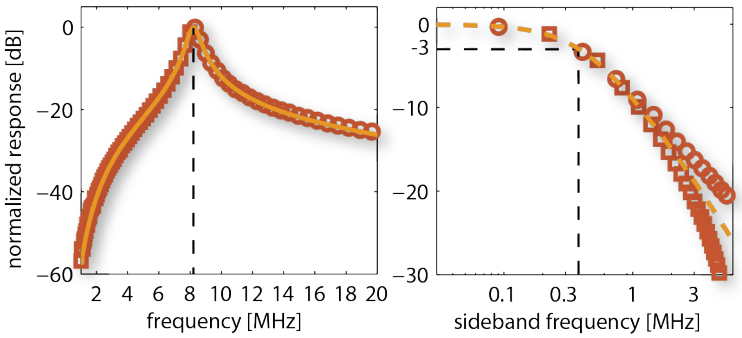

Figure 6.32.: The response of the V5TUF mixer input to optical power fluctuations was measured. The right tile shows the same plot for sideband frequencies around the resonance, i.e. around the TNI's modulation frequency. The -3 dB bandwidth of ≈ 400 kHz should be sufficient for the TNI readout and can be approximated as flat for most applications.

The signal output of this first electronic stage is later on mixed down and filtered by an electronic 4th order Tschebyscheff low-pass with a corner frequency of 500 kHz to suppress leakage at the modulation frequency as well as 2f-signals. Still, the sensor can be assumed flat in the range important for the derivation of the open loop gain shown in figure 6.33, whereas the exact gain is undetermined.

6.12.4 *Open loop gain*

The PDH error signal gets digitized. A common servo determines the overall response of the feedback servo at higher frequencies and creates a robust 1/f slope. This signal is split up into two individual paths. The high bandwidth path acts onto the fast response laser PZT (≅ 1 MHz/V according to the datasheet, 1.5±0.25 MHz/V according to [99]). It is assisted by a small bandwidth path with much bigger tuning range acting on the laser temperature by means of a Peltier element (3 GHz/V according to the datasheet, 2.8±0.3 GHz/V according to [99]). The response of the actuators is shown in figure 6.31. The lasers temperature control actually adds to the error point for a temperature feedback loop inside the Mephisto seed laser, which explains the rather complex response. The *PZT* filter provides a roll-off above unity gain to reduce introduced noise. The *TEMP* filter effectively compensates the response of the lasers temperature loop and thereby widens the possible actuation range. Furthermore, it provides a stable handover between *PZT* and *TEMP* actuation and contains an integrator for improved DC response.

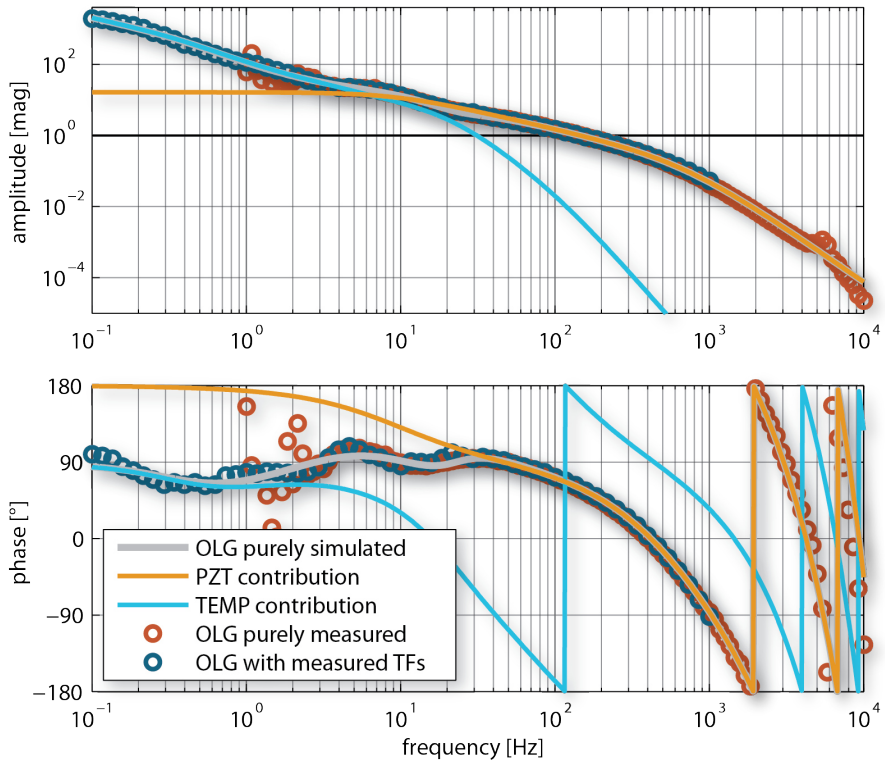

Figure 6.33.: The fits of both actuator paths shown in orange and light blue can be assembled according to figure 6.30 to give the total feedback's loop shape. The optical transfer function G_{TNI} was verified to be flat at about $3 \cdot 10^5$ in the covered frequency range. The actual loop gain could only be measured down to a few Hertz. It is in good agreement with the fully synthetic one besides a 5.5 kHz resonance. The latter might be an artifact of the *PZT* to *HVmon* transfer function due to the PMC's unity gain crossing.

6.12.5 *Results*

The error signal of the TNI is monitored and stored continuously by CDS. A typical spectrum under vacuum is shown in figure 6.34. All graphs are corrected for the loop suppression by means of the open loop gain figure 6.33 and calibrated to equivalent differential TNI mirror displacement.

Above 5 Hz the TNI sensitivity is limited by $1/f$ noise at the expected level of the frequency noise of the unstabilized laser [99]. Below, it is dominated by suspension motion. This residual motion is assumed to fall off with $1/f^6$. Its continuation will pose a low frequency limit in case of decreased laser frequency noise. The calibration is verified by means of the PMC spectrum. Below unity gain the laser follows the TNI's eigenfrequency. The PMC in turn follows the laser, so it can provide an independent readout of the lasers frequency. For comparability, the PMC motion is calibrated in equivalent TNI motion as

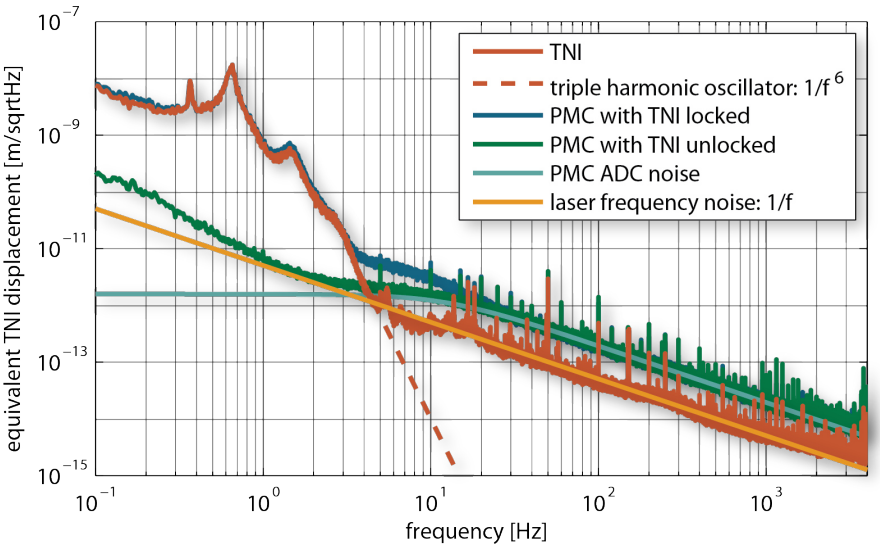

Figure 6.34.: The TNI spectrum can be inferred from the feedback signal by means of the open loop gain (see figure 6.33). At high frequencies it is dominated by the frequency noise of the yet unstabilized laser. Below 5 Hz it is dominated by residual suspension noise. The calibration can be verified independently by means of the PMC following the laser frequency. Its sensitivity was limited by ADC readout noise above 4 Hz at the time of the measurement run, i.e. before whitening was implemented. This is why the signal could not be used for frequency noise suppression in data post processing explained in section 6.12.6. This hurdle should be overcome and a new measurement could deliver a proof of principle. Yet manpower is being assigned to the commissioning of RefC locking instead.

well by means of the geometric round trip length ratio. Below 3 Hz the PMC spectrum is dominated by the TNI's pendulum motion. Beyond, it suffers from ADC readout noise. This is confirmed by its projection as well as the unchanged PMC spectrum in times when the laser doesn't follow the TNI length. However, this limit was improved by implementing whitening/de-whitening to the *HVmon* [158].

6.12.6 *PMC as potential frequency reference*

Until the RefC locking is commissioned, the rigid spacer pre-mode cleaner might be used as independent frequency reference for the TNI but this section might also be of interest when implementing a second loop for the laser frequency stabilization. Now the PMC originally was not optimized for a good noise performance. Its readout noise is above the TNI sensitivity as seen in figure 6.34. After implementing whitening, it should now able to sense frequency noise beyond free running

NPRO noise [158] and thereby allow the subtraction of noise until the RefC is fully operational.

The challenge is that in this scheme the TNI still feeds its length to the laser frequency. The PMC is located inside the optical path from the laser to the TNI forming a nested loop. For frequencies within the PMC servo bandwidth, the PMC can be treated as static and the complicated loop can be unfolded to the easier one shown in figure 6.35. Then the PMC basically serves as an out of loop sensor for the controlled laser frequency.

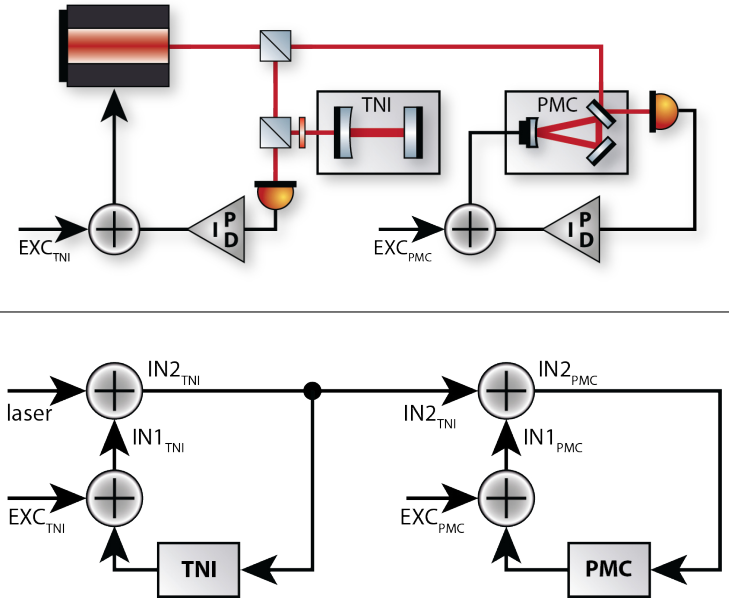

Figure 6.35.: The feedback loop of laser to TNI length is shown. This scheme is equivalent to the one desired for the RefC in future. The PMC has to follow the laser frequency which is determined by the TNI length which will be replaced by the RefC length. For most applications the PMC can be assumed as an independent out of loop sensor for the laser frequency although the TNI is actually supplied by light passing through it. Due to the feedback, the disturbances it has to follow are bigger than free running laser noise in the Hz-region but strongly reduced in the high frequency band.

It is possible to calibrate all shown signals in terms of laser frequency. This eases the calculation as the whole calibration and frequency dependence is shifted to the open loop gains TNI and PMC. To obtain the unknown laser noise

$$laser = IN2_{\mathrm{TNI}} - IN1_{\mathrm{TNI}} \ , \tag{6.43}$$

according to figure 6.35 the two signals before and after its injection are compared. The signal $IN2_{\mathrm{TNI}}$ is unknown and cannot easily be measured with the TNI which was the problem in the last section. The only obtainable information about the laser frequency noise was from

the TNI readout photodiode. This signal, however, already contains added TNI noise, so it is the signal called $IN1_{\mathrm{TNI}}$. However, it can be sensed in the PMC loop in terms of the controlled laser frequency

$$IN2_{\mathrm{TNI}} = IN2_{\mathrm{PMC}} - IN1_{\mathrm{PMC}} \tag{6.44}$$

which shifts the problem to the yet unknown $IN2_{\mathrm{PMC}}$. This, however, can be inferred

$$\begin{aligned} IN1_{\mathrm{PMC}} &= IN2_{\mathrm{PMC}} \cdot PMC + EXC_{\mathrm{PMC}} \\ \rightarrow IN2_{\mathrm{PMC}} &= \left(IN1_{\mathrm{PMC}} - EXC_{\mathrm{PMC}}\right) / PMC \end{aligned} \tag{6.45}$$

from the PMC length readout $IN1_{\mathrm{PMC}}$ taking the PMC's loop gain PMC and the added noise EXC_{PMC} into account. By inserting equation 6.45 into 6.44 one can express the formerly unknown laser noise

$$\begin{aligned} IN2_{\mathrm{TNI}} &= \left(IN1_{\mathrm{PMC}} - EXC_{\mathrm{PMC}}\right)/PMC - IN1_{\mathrm{PMC}} \\ &= \left(IN1_{\mathrm{PMC}} \cdot (1 - PMC) - EXC_{\mathrm{PMC}}\right) / PMC \end{aligned} \tag{6.46}$$

by means of measurable quantities. With this result it is possible to infer the laser noise from the TNI and the PMC signals and even project the PMC noise by inserting equation 6.46 into equation 6.43

$$\begin{aligned} laser = & IN1_{\mathrm{PMC}} \cdot (1 - PMC)/PMC - IN1_{\mathrm{TNI}} \\ & - EXC_{\mathrm{PMC}}/PMC\,. \end{aligned} \tag{6.47}$$

This finally allows the TNI noise to be expressed as

$$\begin{aligned} EXC_{\mathrm{TNI}} &= IN1_{\mathrm{TNI}} - IN2_{\mathrm{TNI}} \cdot TNI \\ &= IN1_{\mathrm{TNI}} - IN1_{\mathrm{PMC}} \cdot \frac{(1-PMC)\cdot TNI}{PMC} \\ &\quad + EXC_{\mathrm{PMC}} \cdot \frac{TNI}{PMC} \end{aligned} \tag{6.48}$$

which is free of laser noise and with the PMC noise suppressed by the factor TNI/PMC.

7

SUMMARY AND OUTLOOK

In the first chapter of the thesis, the AEI 10 m Prototype facility was introduced. It provides an ultra low noise test environment with fast cycling times for interferometric experiments. The first large scale experiment will be the SQL interferometer which aims for a purely quantum noise limited position readout of macroscopic test masses.

A beam jitter requirement for this experiment was deduced in the second chapter. This requirement is so demanding that a pre-mode cleaner (PMC) was designed to reduce mode jitter arising from the photonic crystal fiber which couples the laser into vacuum. This design was realized as a master thesis project. If it turns out that the achieved suppression is not sufficient, a second mode cleaner will have to follow the PMC designed and developed in this thesis. This additional mode cleaner will likely need to be suspended.

The free running laser is by far not able to meet the laser frequency noise requirement of the SQL interferometer. This requires active stabilization of the laser to a frequency reference which needs to be extremely quiet in the hundreds of Hertz band. A 10 m long Reference Cavity (RefC) was presented in the fifth chapter. The design was originally proposed by Fumiko Kawazoe, who also started efforts for a script to predict the cavity's sensitivity. This work was continued in this thesis, which led to the refined sensitivity plot shown in figure 5.20.

Seismic motion spoils the sensitivity of large ground based interferometers by coupling into the optical system due to insufficient mechanical common mode rejection. In the third chapter, the theoretical background behind isolating mirrors from this seismic noise by means of suspension systems was given. Different schemes to damp the suspension resonances, i.e. reducing the resonant enhancement, were presented and discussed.

For the RefC, a triple suspension system was proposed by Robert Taylor. The realization of this design was covered in the fourth chapter. Three suspension systems (plus a 'toy' suspension and a reaction pendulum, which was instead re-purposed as beam splitter suspension recently) were built. They needed to be equipped with damping which was realized by an active feedback system to the upper mass by means of digital control loops. Here the aforementioned RefC sensitivity served as the noise requirement for the suspensions and their control.

All major noise contributions of the developed damping system clear the requirement when projected into cavity length noise. The digital control system of the Prototype allows for an easy conversion from local shadow flag positions into Euler coordinates. This enabled damping in Euler coordinates which in turn can provide reduced feedback noise in the direction along the optical beam. A remote alignment strategy for the in-vacuum cavity was developed. Passively damped, suspended beam directors were designed. Spot positions of the cavity mode are measured by newly developed in-vacuum quadrant photodiodes. Due to their pW DC sensitivity they are capable of detecting leaking light fields even out of a cavity on antiresonance. Initial locking of the suspended cavity was established by means of a workaround servo. First steps towards an auto alignment system could be undertaken. After the early commissioning phase, the upper mass' actuation range will be reduced to provide the full noise performance of the actuation. Incorporating whitened shadow sensor readout will finally allow the ultimate RefC noise to be reached above approximately 10 Hz. Once the cavity can be robustly locked with sufficient gain, the active damping gains can be adapted to the actual seismic noise. The proposed widening of the shadow sensor range could improve the robustness of the damping system beyond the very limited linear range of the BOSEM readout units.

Finally, the script developed to calculate the RefC sensitivity was also used to design a shorter two-mirror twin, to measure Coating Brownian noise. This Thermal Noise Interferometer (TNI) was described in the sixth chapter. The finesse was reduced from the design value to ≈ 150 to ease alignment and locking in the commissioning phase. 1"ø replacement optics were mounted inside a large aluminum ring. This compound structure allows the use of the same suspension system as in the RefC by preserving mass and dimensions. Spot positioning of the cavity's input mode was demonstrated. A full auto-alignment system was set up but could not be used yet because of the missing spot centering on the differential wavefront sensors. In this early stage of the Prototype facility no reliable laser frequency stabilization was available. Therefore, the laser was locked to the TNI. Hence, the achieved preliminary sensitivity was limited by laser frequency noise above a few Hertz. The performance could be verified by using the PMC as an independent frequency reference at low frequencies, i.e. around the suspension resonances. Once the laser can be locked to the RefC, the TNI length in turn needs to be stabilized to the laser frequency. For this, intermediate and lower mass actuation have been prepared. Additional space was reserved for a potential reaction pendulum, should it be required.

A

MECHANICS

A.1 PERISCOPE

The PMC serves as extremely good polarizer and delivers purely s-polarized light. The reference cavity mirrors, in contrast, were coated for p-polarized light. It was decided to place the PMC low above the table (8 cm beam hight) for stability reasons and lift the beam hight up to 10 cm, the beam hight of the reference cavity. A periscope provides by far the cleanest polarization rotation and is independent of thermal effects and beam parameters.

The reference cavity periscope was constructed with emphasis on sturdiness as quasi-monolithic aluminum tower. It houses two 1" optics, which are clamped using peek screws to achieve UHV compatibility. The mirrors are used under an angle of incidence of 45°. They are rotated by 90° with respect to each other around the vertical axis. This way an ingoing horizontal beam is steered up into the vertical and finally to the right (with respect to the ingoing beam) to leave the periscope horizontally but geometrically rotated by 90°. It is lifted by 2 cm which is about the smallest value achievable with 1" mirrors without mechanical interference. The parasitic mirror transmissions are not blocked in order to reduce stray light. This periscope was installed in front of the suspended steering mirrors to ease the diagonalization of the steering (not to have to take the rotation into account).

The periscope was discarded later on. The PMC breadboard was instead lifted by 2 cm and the polarization rotation is currently covered by a less stable $\lambda/2$ waveplate.

A.2 2" STEERING MIRRORS

Remotely controllable mirrors are required to co-align a laser beam with a suspended, and thereby moving eigenmode. At the same time the mirrors may not introduce noise. 2" optics are mounted in an aluminum holder and suspended from a three-legged item cage. The compound mass provides attachment possibilities for the suspension, for dampers, includes pushrods for leveling and increases the moment of inertia to reduce the resonance frequency. The reduced eigenfrequency in turn results in improved high frequency attenuation (compare figure 5.19

and 6.18). A longer suspension would serve the same purpose for displacement DOFs, yet it requires a higher support structure. But the structure's resonance frequency, especially that of the torsional mode, strongly decreases with height. The geometry is chosen such that the resonance frequencies of the frame are beyond the important detection band around 200 Hz. The mirror surface is close to the center in order to get little lateral motion of the beam across the surface when actuating tilt. Furthermore, the mass' suspension point is only slightly above the center of mass in order to get little pitch to long coupling. The separation of the wires at the top and on the compound mass is chosen to be small in order to reduce the yaw frequency.

The wire is clamped using a jig to define the wire length accurately. Once attached to the 'ring mass', it is fed through a set of rods at the top of the cage. These define the wire spacing and allow to adjust roll comfortable before clamping the wire sling at the top. All six rigid body modes are damped by means of six magnets on the mass and eddy current dampers around them attached to the frame (compare figure 5.18). The magnets are oriented pairwise opposite to reduce coupling of magnetic moments to mirror motion. Coils are wound onto the four eddy current dampers, which are behind the mass, to use the corresponding magnets for actuation as well.

A.3 LENS MOUNTS (KENNY)

In contrast to most commercial lens mounts, adjustability was sacrificed in favor of an optimal long term stability. Therefore, the beam needs to be steered through the lens' center externally. The lens mounts provide maximal sturdiness combined with minimal weight and least possible space consumption along the optical axis. A 1" or 2" ø lens (dependent on the mount's version) is placed flat into a recess forming kind of a jig. It is clamped with a single, easy to reach peek screw from the top. The aluminum frame protects the lens' surface from unintentional touching.

The mount design is parametrized and can be changed easily for beam heights which are different from 100 mm. For SQL interferometer heights of 22 cm, however, a different design should be used, as the support would get extremely weak along the beam axis.

A.4 PBS WAVEPLATE ASSEMBLY

The TNI input light is tapped off from the reference cavity path. Defining its input power independently from the reference cavity power requires a continuous power adjustment method. A $\lambda/2$ wave plate followed by a PBS serves this purpose. A $\lambda/4$ wave plate directly behind the PBS circularizes the polarization inside the TNI and strips the reflected beam off from the ingoing beam (compare figure 6.1). The TNI input requires an extremely compact UHV compatible assembly.

A 1" PBS cube is clamped diagonally to provide full accessibility to all four beams. 1" zeroth order wave plates are clamped into a knurled peek ring which can be rotated manually. It is clamped and protected against falling out of its aluminum housing by a thin sheet metal. The ring can be fixed in place by an additional screw from the top. (Care must be taken not to demolish the recess in the peek ring!)

The completely UHV compatible assembly is made for 100 mm beam height and measures only 66 mm end to end.

A.5 IN VACUUM SPOT QPD

DC alignment of beams in a suspended setup requires a form of position sensitive readout. This is usually accomplished via quadrant photo detectors. As the SAS tables are suspended, the sensing needs to take place on top of their surface inside vacuum. Therefore special mounts for commonly used QD50-3T photo detectors were designed and built: The photodiodes' housing is cut open (using the so-called can opener) to vent the trapped volume and to avoid reflexes on the front window.[1] This exposes the silicon area and the sensitive bond wires. To protect them, the bare photodiode is enclosed inside a peek holder consisting of two pieces. It must be isolating as the PD case is connected to bias which would cause shorts to the grounded table otherwise. The peek holder in turn is mounted inside an aluminum base establishing a rigid connection to the table. A piece of sheet metal serves as strain relief for the extremely floppy connector pins. The whole assembly should be placed under an angle to split the parasitic reflected beam off from the incident light in order to dump it. The according cabling and electronics are described in chapter C.6, B.8, and 5.3.2.

A.6 BREAKOUT BOX

In order to clean up the signal redistribution inside vacuum, universal boxes were constructed to hold SubD plugs. Each of the breakout boxes houses single a SubD37 connector which is connected via a straight through cable to the vacuum feedthrough. Six slots for SubD9 connectors are distributed around the other sides of the box. All connectors are fixed with metric screws (M3). A lid closes the box providing mechanical and electrical shielding. Care must be taken with respect to ground loops as all connector shields are locally connected to the box and thereby usually to the table as well.

1 With this type of QPD drilling a hole into the side for venting is not possible as the glass wraps around to the sides of the case.

B

ELECTRONICS

B.1 COIL TESTER

Thin coil wires, for example of the steering mirror actuation, break easily. It turns out to be extremely helpful to test, whether the problem lies on the driver side or on the cabling/coil side. A simple SubD9 plug with resistors serves the purpose. Due to the maximal dissipated power, two $5\,\Omega$ resistors rated for 2 W are used in series for each channel, four sets in total. Another benefit of the tester is the commissioning of the current readback, which gives false values if there are unintentional shorts to ground anywhere in the coil (e.g. abrasion of the wire insulation).

B.2 BOSEM TESTER

The BOSEMs are not only extremely sensitive to flag position changes, but also prone to failure. Their delicate microD9 connector is susceptible for touching of the soldered wires. Therefore, every single unit must be tested for correct signal connections, e.g. by checking resistances in between the according pins and to the aluminum holder. The LEDs stacked in series should cause a voltage drop of about 7.2 V.

Nevertheless, the BOSEM readout boxes need to be checked as well. At several occurrences, the LED current driver tried to push way too much current which destroyed multiple BOSEM units. To reduce this specific risk, several readout boxes were fitted with fast fuses later on. For easy and safe testing of the readout boxes, two SubD9 test plugs were built (one for BOSEMs A..D, one for E, F and LEDs): A Zehner diode simulates the voltage drop from the LEDs while a small resistor simulates their resistive load. The intended current of 35 mA can be checked by means of the voltage drop across the resistor. On each set of photodiode pins, a resistor simulates about half light condition.

It should be mentioned that some problems manifest only by increased noise, so a ‘dark noise’ spectrum should be taken of each channel using the described tester.

B.3 RF DISTRIBUTION

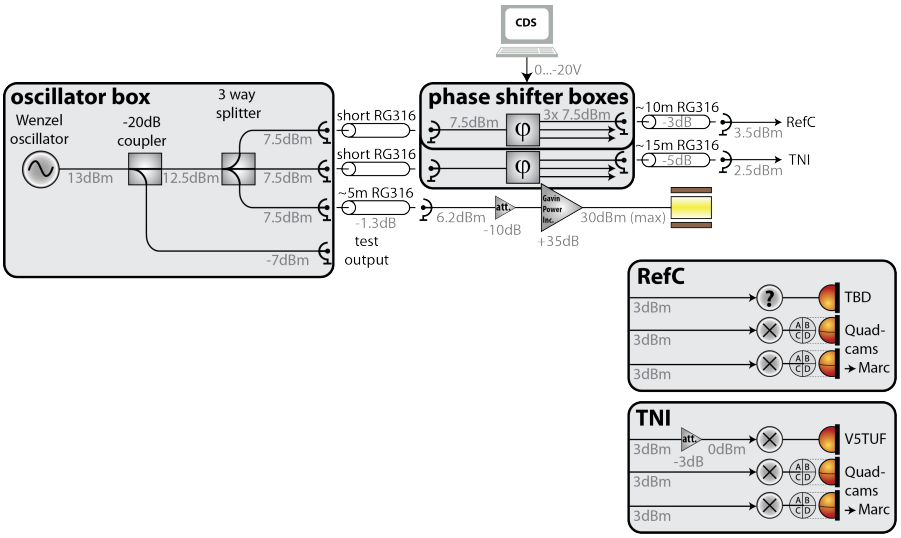

Figure B.1.: The 8 MHz local oscillator distribution for the RefC and the TNI is shown. The highly stable Wenzel oscillator signal is split into several copies, most of which can be shifted in phase electronically. Finally the input power levels to the demodulation electronics must be matched thoroughly.

Wenzel oscillator and power splitting

A Wenzel quartz oscillator provides a highly phase stable 8.047260 MHz signal at a power of 13±2 dBm. The frequency of the oscillator can be tuned electronically by 0.2 µHz/V with ±1 µHz tuning range in total.

A -20 dB coupler (ZX30-13-4S+) splits off a -7 dBm test output. The remaining power is split by means of a balanced 3 way splitter (ZMSC-3-1) and distributed to the three outputs, receiving 7.5 dBm each. All connections are carried out in SMA to achieve good coupling and long term stability.

Phase shifter box

The phase shifter box was designed to accept a signal up to 7.5 dBm power and provide three electronically phase shifted copies.

Due to the limited power handling capabilities of the used JSPHS-12 phase shifter, the RF signal is attenuated slightly in addition to the power splitting into three channels by means of an AD3PS-1. Each phase shifter's output is amplified back to the ingoing power level taking the phase shifter's loss into account. It is important to mention that the output impedance is not 50Ω. This has to be taken into account at the input termination of the following electronics.

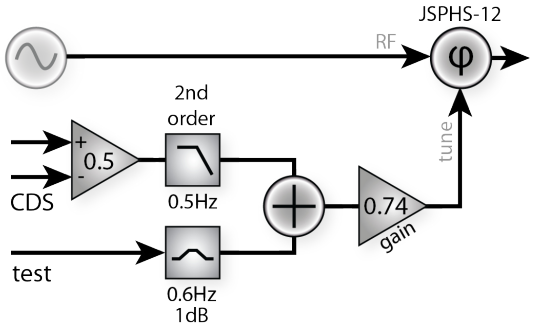

Figure B.2.: The electronic phase shifter takes an RF input power of up to 7.5 dBm. It is separated into three channels, each of which is re-amplified to the original power. Furthermore, each channel can be tuned in phase by means of two inputs, a differential CDS input and a fast test input.

Two inputs can be used to tune each signal in phase. To filter out DAC noise, the differential CDS input path is filtered by a second order 0.5 Hz low-pass. The specific, component saving layout results in a small 1 dB bump in the second, single ended test input. It is not low-passed, as one of its purposes is to measure phase noise coupling later on. Both inputs are summed up and slightly reduced in amplitude, not to exceed the JSPHS-12 voltage input level. The phase shifting performance is described in more detail in chapter 6.8.2, especially in figure 6.26.

RF power levels at PDs

Each mixer used for demodulating error signals requires a specific RF input power. The nominal local oscillator input power to the quadrant photodiodes (described in chapter B.7) is 3 dBm. The TNI photodiode requires an input level of 0 dBm. These values should be well achievable with the ≈ 7.5 dBm delivered by the phase shifter even for long transmission distances.

B.4 BOSEM READOUT BOX

The BOSEM readout box suits several purposes: The shadow sensor photodiodes are supplied with a stable bias, their signals are read out, processed and sent to CDS but also an extremely stable LED current is supplied in the first place. The noise requirement of this electronic box was set by an aLIGO measurement (see figure 4.8), which is thought to be mostly limited by inherent BOSEM noise. The whitened output Furthermore, allows to fulfill the stringent requirements of the RefC regarding injected readout noise.

The stability of the LED current determines the maximal sensitivity of the shadow sensors. The output of an ultra stable 10 V reference

(AD587) is buffered and serves as photodiode bias. Another path is filtered passively by means of a 2nd order low-pass with 0.1 Hz corner frequency and divided to result in an even more stable 2 V set point. It is matched to the voltage drop across a 56.2Ω current sensing resistor which is supplied by a transistor. This resistor doesn't have to be super noise free as the small resistance transforms flicker only to small current noise. Other noise, for example originating from the transistor, is suppressed by the active feedback loop (compare figure 4.9). This results in an extremely stable 35 mA supply for the LEDs. All six LEDs them are stacked in series. Their voltage drop is about 7.2 V in total.

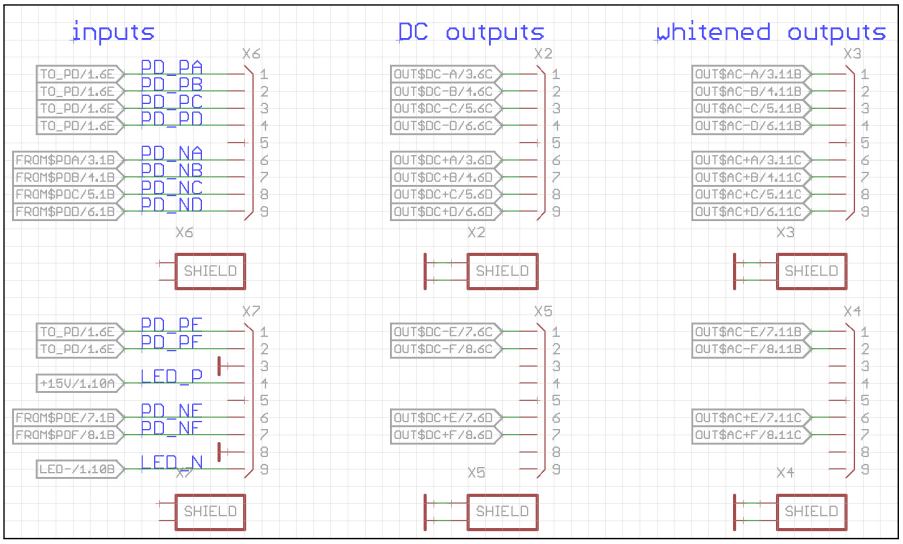

Figure B.3.: The signal connection scheme of the BOSEM readout box is shown: photodiodes A-D are read out at one SubD9 connector, anode and cathode each on adjacent pins. Photodiodes E&F are read out via another SubD9 connector. This also supplies the ultra stable LED current with one signal pair of ground in between. The connection to CDS is established via the same scheme (partly Y cables), as in the case of the BOSEM driver boxes (see below).

The approximately 65 µA of photocurrent are read out by one transimpedance amplifier each. The transimpedance resistor is a 120kΩ low flicker noise resistor. The bandwidth is limited to 6 kHz in the very first stage. The output is sent via a discrete differential line transmitter, which was optimized for low DC noise performance. A second, aggressively whitened output contains a double zero at 0.16 Hz and a double pole at 8 Hz. More detail about the design decisions can be found in chapter 4.5.

B.5 BOSEM DRIVER BOX

The BOSEM driver box supplies the coils of the RefC triples with the currents required for electromagnetic actuation. The CDS' DAC

signals are received by a differential line receiver. The signal is dewhitened aggressively to fulfill the stringent requirements for injected DAC noise (compare figure 4.18) with a double pole at 0.16 Hz and a double zero at 8 Hz. The power for the attached coil is supplied by an OP27 operational amplifier. The actual current is measured by means of the voltage drop across a low flicker noise resistor improving the low frequency performance and actively controlled in a feedback loop. Optionally, the voltage drop is buffered and sent differentially to an ADC (compare figure 4.16). More construction details can be found in chapter 4.5

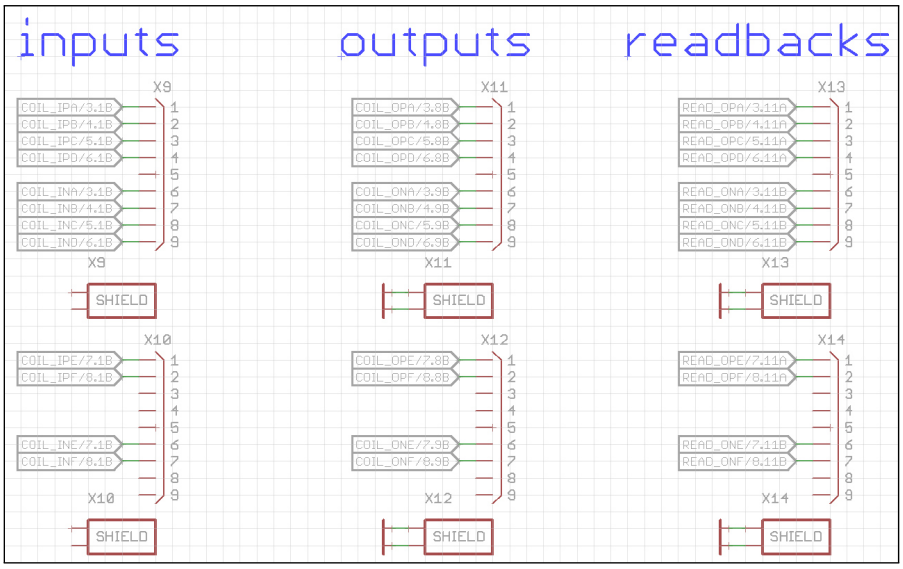

Figure B.4.: The signal connection scheme of the BOSEM driver box is shown: coils A-D are supplied on one SubD9 connector, negative (N) and positive (P) signals located on adjacent pins to ease twisting in the cable. Coils E&F are supplied via another SubD9 connector. This way Y-cables can be used, to feed two BOSEM driver boxes from one quad channel DAC output.

As the coil is part of a feedback loop, it is important that all signals are isolated well. Whenever one of the signals is corrupted (for example by abrasion of the coil wire and shorting to the coil holder, i.e. ground) the feedback loop will not work properly and even the current readback will not show correct readings. Therefore, prior to use each coils resistance must be measured after installation.

In the early times of the RefC commissioning, more actuation force is required than 1kΩ shunt resistors can provide. Hence, smaller 10Ω resistors are used. They just meet the RefC noise requirement beyond 25 Hz. But their noise dominates seismic excitation already above 0.5 Hz.

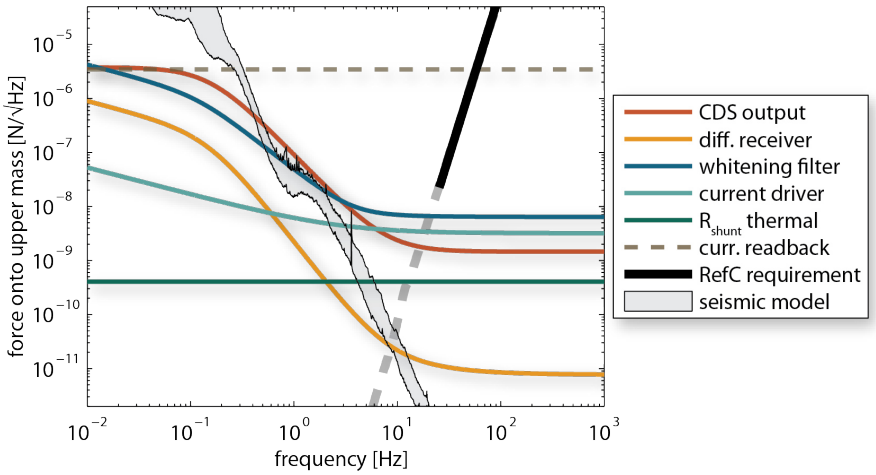

Figure B.5.: The same simulation as in figure 4.18 was carried out for a 10 Ω shunt resistor used in the early commissioning phase. The smaller resistor eases alignment (i.e. it gives more actuation range) but also increases noise.

B.6 COIL DRIVER BOX

This is basically a four channel version of the BOSEM driver box. The de-whitening filters are less aggressive, as the noise requirements for steering mirrors are less stringent. There is a combination of DC force (hold position) and sufficient actuation (fast alignment cannot be carried out at the triple suspensions and must be covered with the steerings) required. Therefore, the de-whitening was changed to a double pole at 1 Hz in conjunction with a double zero at 10 Hz. Furthermore, the sensing resistance was decreased (take figure 4.19 into account) to allow for faster actuation.

B.7 RF QPD AKA QUADCAM

The RF QPD design serves as differential wavefront sensor. It was provided by the GEO600 operators and slightly modified. It features:

- QD50-3T quadrant photodiode
  (note the rather low response of ≈0.2 A/W @ 1064 nm)
- resonant detection at 8 MHz for RF path
- internal 8 MHz demodulation of each quadrant
- balanced 50 Ω LO input (≈3 dBm)
- whitened differential output of demodulated RF for each quadrant
- high-pass filtered sum of all four non-demodulated RF signals

- independent broadband DC readout with whitened differential output for each quadrant
- bias current limitation according to figure B.6 to $\approx 10\,\mathrm{mA}$

It turns out that manual spot positioning is not sufficient to obtain proper differential wavefront signals. For valid DWS signals, faster automatic centering loops using e.g. galvo motor driven mirrors must be implemented.

Some produced quadcam models needed to be rewired internally (exchange quadrant C and D) in order to match the pin numbering of the RF output to that of the DC output.

B.8 QPD READOUT BOX

The purpose of the QPD readout box is to receive current signals from in vacuum spot position photodiodes, and process them for CDS. Due to the relatively long cables in between, only slow (no RF) signals can be detected.

A transimpedance amplifier converts the photo current to a single ended voltage by means of the voltage drop across a $3.3\,\mathrm{k\Omega}$ resistor. The whitening of the signal with a zero at 0.33 Hz and a pole at 33 Hz can be bypassed using a dip switch. In this case the signal is not inverted. Finally the signal is buffered and a copy inverted in a discrete LT1124 differential sender stage, resulting in a differential output with a gain of 2.

Each quadrant's signal is processed individually and only later combined in CDS to give position information. This results in increased noise when compared to electronically subtracted and amplified signals but gives more insight in the case of failures and allows for more range. The latter is important for spot position sensors as the set point often is off-center.

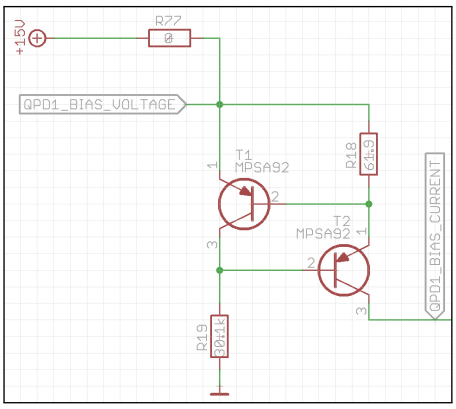

Figure B.6: The bias voltage is current limited. As all quadrants are supplied with the same bias the position sensitivity can be maintained even in this current limit [159].

In case the photocurrent exceeds some limit, the bias voltage of 15 V is reduced to minimize the electronic thermal load. If the voltage drop across R18 exceeds the base-emitter voltage of T1, which is the case

at about 10 mA, the bias drops until the aforementioned condition is reached again. In this case all four quadrants receive the same, reduced bias. Therefore pitch and yaw signals can still be calculated, just at lower sensitivity. The normalized pitch and yaw signals, however, are fully maintained.

B.9 DIGITAL IO OF CDS

There are several CDS channels that require only relatively slow data rates. Custom made DIO field-boxes provide relatively cheap means of eight digital outputs each. Two of such boxes can be supplied by the same controller card. They are interfaced via slow epics channels (16 Hz at most). Each output's state is controlled by one bit of a single 16 bit variable which is responsible for all possible 16 channels. All outputs are galvanically isolated by means of relays lowering the switching rate further.

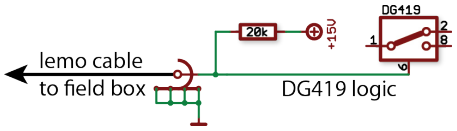

Figure B.7.: The electronics shown above receive a switch state (high or low impedance) from a remote digital IO field box. This is then translated into a path switching applied locally by means of a DG419 solid state switch. The logic table is shown in table B.1.

To use these outputs in practice, a local solid state relay can be used. The DG419 is much faster than it is required in this case but it is convenient as it provides relatively low on resistance combined with high off resistance. Neither current nor voltage noise or coupling between the outputs was observed in extremely sensitive electronics (see section 5.3.2). Applying the scheme presented in figure B.7 yields zero potential on the shield and watches for field-box resistance.

DIO state	DG419 logic	S1 (Pin8)	S2 (Pin2)
off	1	off	on
on	0	on	off

Table B.1.: The DG419 acknowledges < 0.8V as logic 0 and > 2.4V as logic 1.

C

CABLING

C.1 VACUUM FEEDTHROUGHS

In the Prototype facility commercial CF100 vacuum feedthroughs from Allectra are used. It should be mentioned that those have (more robust) male connectors inside and outside vacuum. This results in a mirroring of the pin numbering as shown in figure C.1.

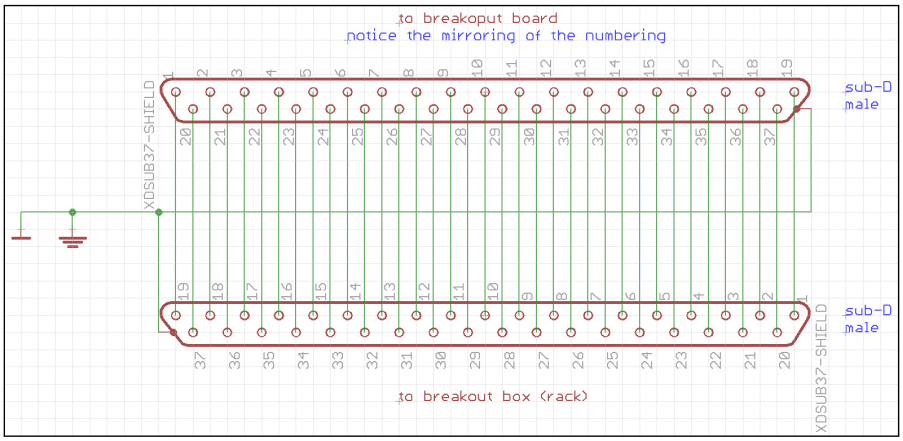

Figure C.1.: The mirroring of the Allectra vacuum feedthroughs is shown.

C.2 REFC BREAKOUT

All signals of each RefC suspension are covered by a single vacuum feedthrough. These signals are grouped after weak/sensitive signals (bias, PD currents) and strong signals (coil currents) all the way from the out of vacuum electronic boxes to the suspension inside vacuum. Close to the upper mass, a breakout board redistributes all the signals into six bundles, one for each BOSEM readout/actuator unit. The LEDs are all sequenced in series, which happens inside the box as well to have six identical, interchangeable cables for the units.

First, the inside of the boxes was wired by hand (crimp connectors). Later, readily routed kapton boards could be added to a bigger order which eases the production of breakout boxes heavily.

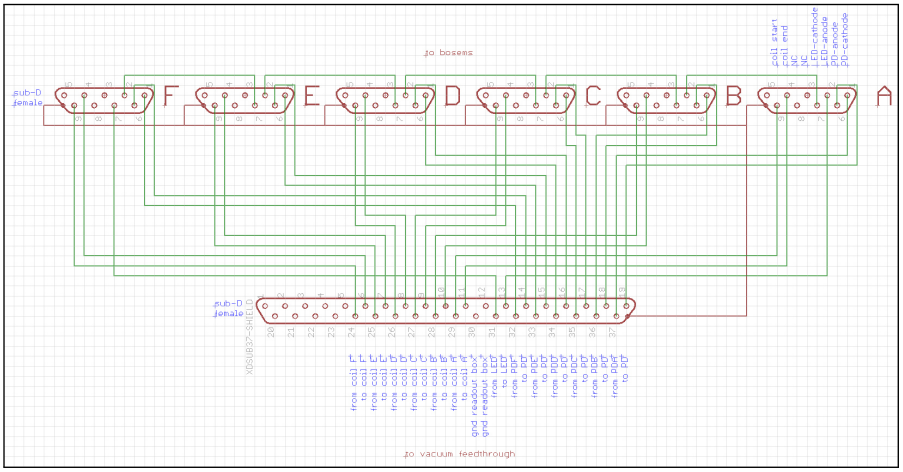

Figure C.2.: One in-vacuum breakout board is located close to every RefC suspension upper mass. It redistributes the signals and stacks the LEDs in series to have standardized straight through (SubD to microD) cables between the box and the BOSEMs.

C.3 REFC OCTOPUS

It was decided that one feedthrough (37 signals possible) would be spent per RefC suspension (26 signals). This results in standardized cables described in the following: Cat7 cables provide four twisted pairs, individually shielded against each other plus a common shield. They are cheaply available. The SubD9 standard provides reliable connections of 8 (+1 unused) signals plus a shield. The transmitted signals are low in frequency (<1 kHz), so 50 Ω impedance is not so essential. The BOSEM (coil) driver box provides six pairs of signals. Coils A..D are routed on one cable, coils E&F on another. The BOSEM readout box deals with seven signals. Again PD A..D are occupying one cable, while PD E&F (pins 1/6, 2/7) are on the second one. The LED current (pins 4/9) is sent via the same cable. It is separated by one set of pins (3/8) to reduce crosstalk. The octopus cable gathers all signals in order in a custom made SubD37 housing. This plug connects to the air side of the vacuum feedthrough.

C.4 9 PIN BREAKOUT FOR EM ACTUATORS, BDS, QPDS ETC.

A SubD9 connector usually supplies four differential signals (pin1/6, 2/7, 3/8, 4/9, while pin5 is left empty). A SubD37 connector as used in the feedthroughs, however, can host five sets of such signals. In contrast to the RefC breakout, no redistribution close to the experiment is required.

Two solutions were developed: octopus cables, separating into bundles of four twisted pair cables at one end while ending in a SubD37 pin connector at the other side, and breakout boxes, which are con-

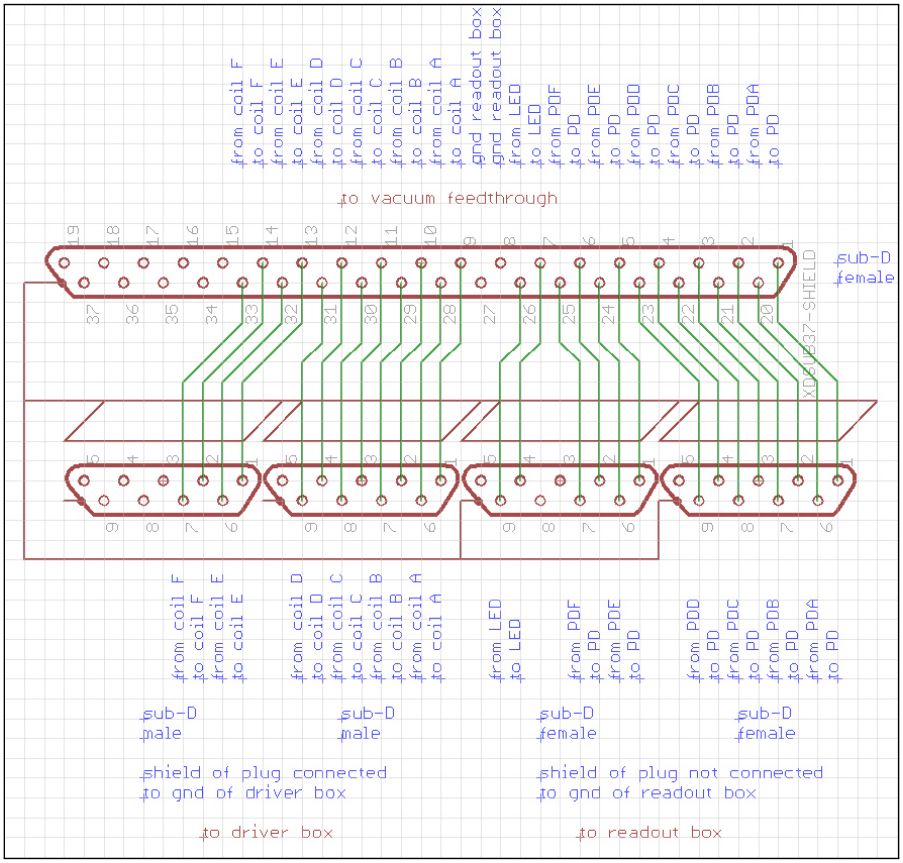

Figure C.3.: The octopus cable collects all signals for a RefC suspension from the BOSEM readout and driver boxes and bundles them onto one vacuum feedthrough.

nected with a straight through cable to the flange (exactly like the RefC breakout box) and splitting into up to six SubD connectors on their circumference.

C.5 9 PIN OCTOPUS FOR EM ACTUATORS, BDS, QPDS ETC.

Outside of vacuum, a standardized octopus cable is used to collect/ distribute four sets of four differential signals to the according electronics (e.g. QPD readout or coil driver).

C.6 SPOT-PD

The DC spot position sensor QPDs (Centroic QD50-3T) are common cathode. Four inside vacuum quadrants must be read out with distant out of vacuum electronics. Additionally, a bias must be supplied into vacuum. [88] talks about electromagnetic incoupling at 60 Hz, so at low frequency. The proposed optimal solution is to have a sense wire tightly twisted around the signal wire. The intentionally picked up

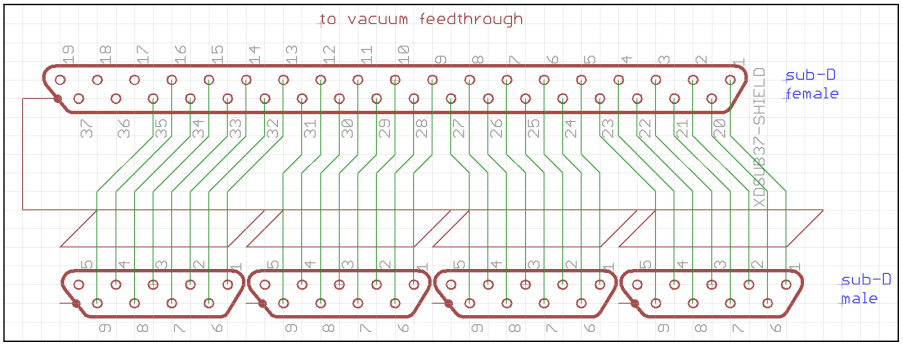

Figure C.4.: Each feedthrough provides 37 connections on a SubD37 connector. Outside vacuum, the signals are bundled in bunches of four signals, each occupying its own twisted pair, on Cat7 cable [88]. For convenience and costs, the Cat-cable connects by means of a SubD9 connector.

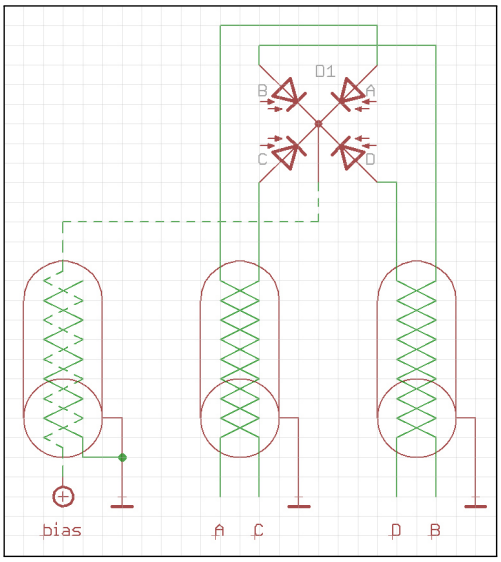

Figure C.5: The cabling of in-vacuum spot position sensors is shown. The specific scheme allows for up to 90 dB suppression of electromagnetic incoupling in the power lines' frequency range into the pitch and yaw signals.

signal is then subtracted from the real signal wire. Together with a grounded shield up to 90 db of 60 Hz rejection could be measured.

With that scheme one witness cable is spent per signal cable. As we are mostly interested in pitch and yaw signals and not at all in butterfly signals, the cabling scheme shown in figure C.5 is used. The signals from diagonally opposing quadrants are used as pickup signals. It is based on the fact that according to

$$\text{pitch/yaw} = (A - C) \pm (B - D) \tag{C.1}$$

pitch and yaw both contain $A-C$ and $B-D$ signals, so differences of diagonally opposing quadrants.

As A and C are (digitally) subtracted (same as B and D) anyway, the tightly twisted pairs in the Gore vacuum cables are used for these signals. The shield is grounded at the feedthrough side. As the photocurrent is less sensitive to bias variations. It can be routed in another,

independent cable strand. For current handling reasons and to give it a defined potential, both signal lines share the bias voltage.

Crosstalk between signals might occur between A and C (or B and D) which again does not influence the pitch and yaw signals. Finally the butterfly signal $(A+C)-(B+D)$ can give information about the effectiveness of the subtraction.

D

OTHER STUFF WORTH MENTIONING

D.1 UHV COMPATIBLE BEAM DUMP

In any complex optical experiment there are many parasitic beams. Proper dumping is crucial, as phase sensitive readouts, i.e. interferometry, are sensitive to the amplitude of stray light. In contrast to out of vacuum, painted materials cannot be used because of outgassing. To avoid this problem, the paint can be encapsulated, e.g. in glass. The described design offers extremely good attenuation performance solely limited by scatter defects on the very first surface and residual s-polarization.

Many cheap 8 mm thick glass plates are available. They don't let any measurable amount of light penetrate at all. The only challenge is to reduce the reflection. For p-pole this is minimized under the Brewster angle. This is not very well known and the index of refraction is unknown as well. It was measured to be about 56° which matches a refractive index of $n = 1.48$.

The described design features three glass blocks in series. The first two are illuminated under the angle of 56°, the third one nearly under normal incidence (2°). The remaining reflex therefore walks off the incident beam and is reflected twice more, this time under 52° and 60°. This leaves an negligible amount of p-polarization. But even residual

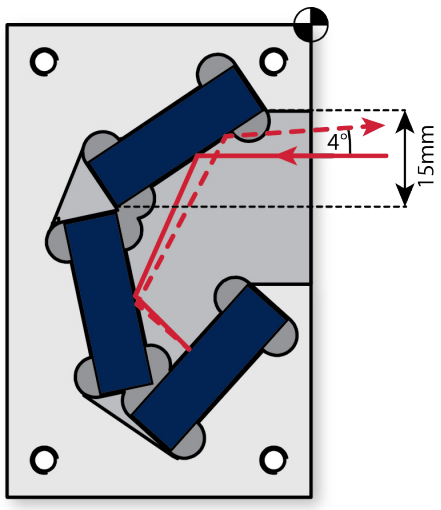

Figure D.1: The high performance UHV compatible beam dump features five reflections off a highly absorptive glass. Four of the reflections are oriented under the Brewster angle. This limits the maximally usable size to ≈15 mm beam size. The remaining 'reflex' is walking off the incident beam by 4°.

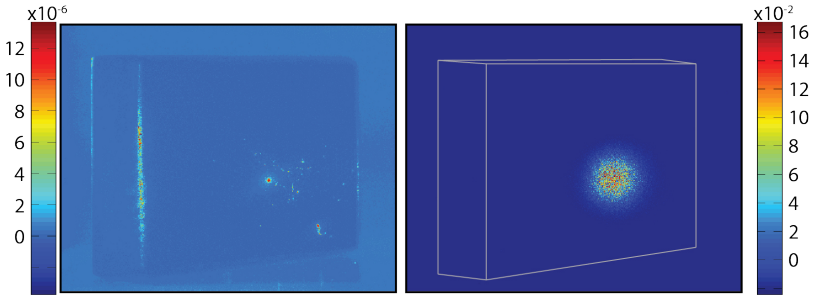

Figure D.2.: To evaluate the beam dump's performance, a glass plate was illuminated under 56°. For reference, the right picture shows the beam scattered off a white surface. The left photo shows that scattering on the glass plate arises from small centers. According to microscopic images, these are inclusions close to the surface. The color scale is calibrated in W/cm^2/sr. The total amount of scattered power integrated across the surface is about 10^{-5}. The performance could not be improved by flame polishing.

s-polarization is attenuated by $2 \cdot 10^{-5}$. According to figure D.2 this is similar to the amount of scattered light in p-pol.

In order to adjust the beam dump for the polarization of the incident light, it can be rotated on its mount by 90° where space allows for this.

D.2 QPD SIGNAL CONVERSION

After being digitized, each QPD quadrants' signal is de-whitened individually.

The digital quadrants signals are combined linearly to give degree of freedom information that can be used for interferometric control. The butterfly degree of freedom should not contain any signals which makes it valuable for debugging. The influence of power being dissipated in the gap is minimized by normalizing the signals with the sum power (compare chapter 6.7.4). Another advantage is that feedback loops relying on these signals, such as spot centering servos, are getting independent of the used laser power. This allows for more aggressive (only conditionally stable) servo designs. Whenever the incident laser beam leaves the horizontal plane, like on the RefC minibench or in the galvo mirror periscopes, it may rotate. This rotation, same as residual mounting inaccuracies, are compensated by a digital (un-)rotation matrix mixing the pitch and yaw signals.

In the RF QPDs' case the normalization with the sum doesn't yield sensible signals anymore. The RF sum is forced to zero by the PDH length lock which would drive the normalized error signal towards infinity. Normalizing with the DC sum doesn't help as well, as the QPD sees the interference of the directly reflected light and the one from inside the cavity. The DWS error signal, in contrast, contains the product of the amplitude of the sidebands and the cavity light. A workaround

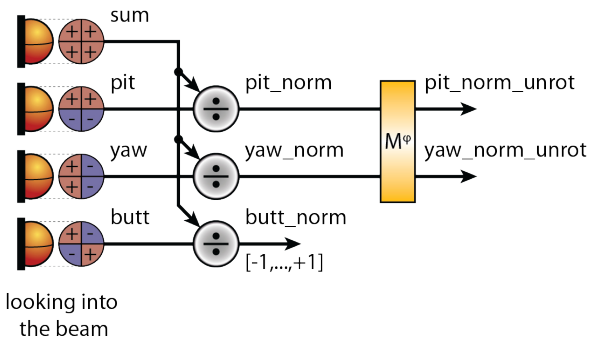

Figure D.3.: After de-whitening and calibrating each QPD's DC signals, the beam degrees of freedom are restored by weighting the quadrants. Positive pitch means the beam points up on the QPD, positive yaw corresponds to hitting to the right side (seen from the beam). Normalizing by the sum creates signals that are independent from power fluctuations. A rotation is applied to pitch and yaw in order to un-rotate residual QPD mounting errors and the 90° caused by the galvo mirror assembly.

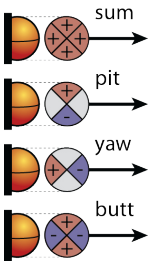

Figure D.4: In the ×-oriented case the pitch and yaw restoration works slightly different. Only two quadrants contribute to each signal resulting in lower noise. However, the signal's slope is reduced by the same amount (compare figure D.6).

might be a set of additional photodiodes: one sensing the input power (assuming a constant modulation depth this is a measure for the sideband amplitude) and one measuring the power circulating inside the cavity. However, this was not tested yet. Hence, all DWS signals remain input power and cavity detuning dependent.

D.3 QPD IN × OR + ORIENTATION

Every once in a while the question is raised, whether it would be better in terms of noise performance to mount QPDs under and angle of 45°, i.e. with the gap in ×-orientation instead of 0°, i.e. with the gap in +-orientation.

Then the pitch and yaw signals are read only from two quadrants each. If the electronic noise of the quadrants is uncorrelated, this reduces noise by $1/\sqrt{2}$. Also only half of the power is dumped on the signal supplying quadrants. This reduces shot noise by the same amount. But at the same time, the slope of the error signal decreases by $1/\sqrt{2}$ as well, so no signal-to-noise ratio can be gained. Even worse, the slope of the error signal gets drastically smaller if the beam is not centered on the QPD anymore (see figure D.6).

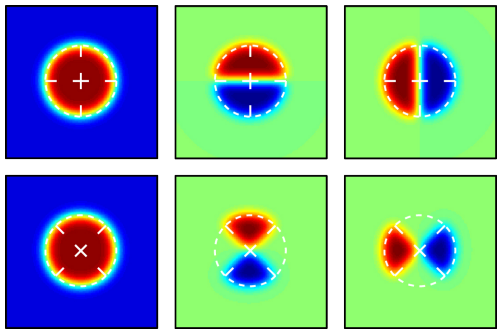

Figure D.5: When mounting a QPD in ×- instead of +-orientation it is more difficult to adjust due to a lack of references. In contrast to the first intuition the signal-to-noise ratio doesn't improve.

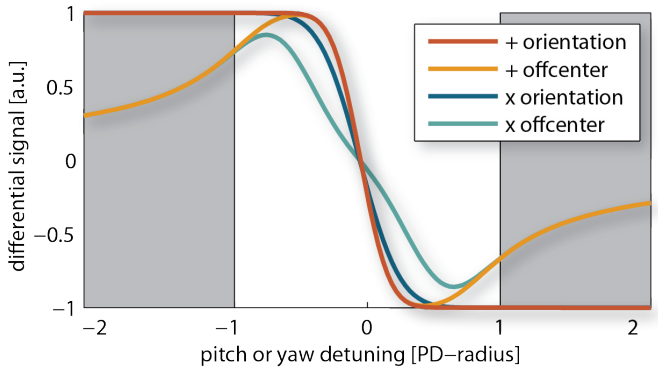

Figure D.6.: The slope of the pitch signal for a QPD oriented in ×- and +-direction are shown. Neither orientation gives benefits in terms of signal-to-noise ratio. But a lot of position information is lost in the case of a not perfectly centered beam on a ×-QPD.

Therefore it was decided to mount all QPDs in +-orientation.

D.4 SUSPENSION WIRE STRENGTH

Mirror suspensions require thin (and light) wire to increase the dilution factor and thereby decrease thermal noise, shift violin modes to higher frequencies and lower the bounce mode frequency. Yet the wire needs to support the suspended mass reliably. The lowest RefC suspension stage requires 0.55 GPA strength for a design diameter of 55 µm not including any safety margin. This already rules out C70 steel with a tensile strength of 0.6..0.7 GPa which was used in suspension designs of early other experiments. Three types of wires were investigated for their potential use in the RefC triples:

- 55 µm music wire from California Fine Wire Company
- hard tempered 50 µm from Goodfellow plus DIY annealing
- 52 µm type 304V high tensile wire from Fort Wayne Metals

Initially, the music wire was used in the triple suspension's lowest stage. In original condition it can withstand 1.72 GPa is not weakened e.g. by kinks. However, the suspension was extremely sensitive and

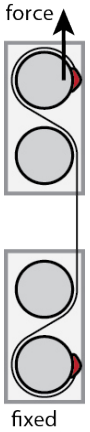

Figure D.7: The wire strength is measured on an improvised test stand. The wire is wound around 10 mm diameter rods on a jig and taped at the end to fix it without reducing the strength from uncontrolled clamping. The pulling force is 'buffered' by means of a coil spring. The actual load is determined by fixing the lower half on a weight scale. The fact that the wire usually breaks in between the jigs, shows that it's strength is not compromised by the measurement process.

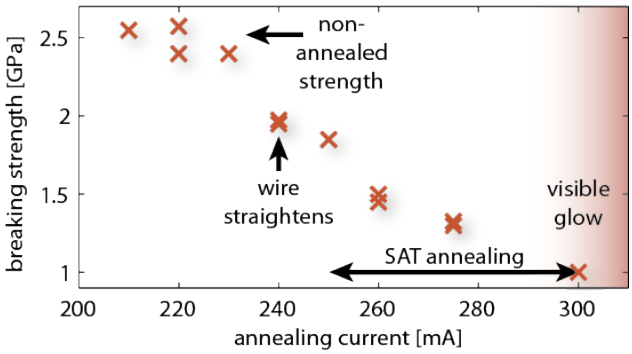

Figure D.8.: The hard tempered wire is annealed by resistive heating. Beyond 210 mA, the temperature is high enough to change the material properties but also to reduce the strength. At 240 mA the wire starts to straighten. The recommendations for the single arm test sacrifice a lot of wire strength. Surprisingly, above 300 mA a glow is visible. This should only occur beyond 600°C.

failed several times. Testing of visually not impaired sections of used wire resulted in only 1.3 GPa strength. Hence, a different wire was searched for.

In the single arm test, hard tempered wire is used instead of the final monolithic suspensions. It is annealed in order to straighten the otherwise extremely curly wire, relieve internal stress and reduce brittleness. For this purpose, a current is sent through the wire heating it up for two minutes. It turns out that the heating duration doesn't make a big difference. The current, however, must be chosen quite accurately (see figure D.8). This is caused by a quite narrow temperature range in which the aimed annealing takes place. Also the dependence of the temperature from current is nonlinear as the resistance increases with temperature.

Beyond 210 mA, the strength of the wire decreases abruptly. At 240 mA the wire begins to straighten completely which is a sign for the relief of strain. Microscopic images taken after the annealing process (see figure D.9) show the temper colors which are in agreement with

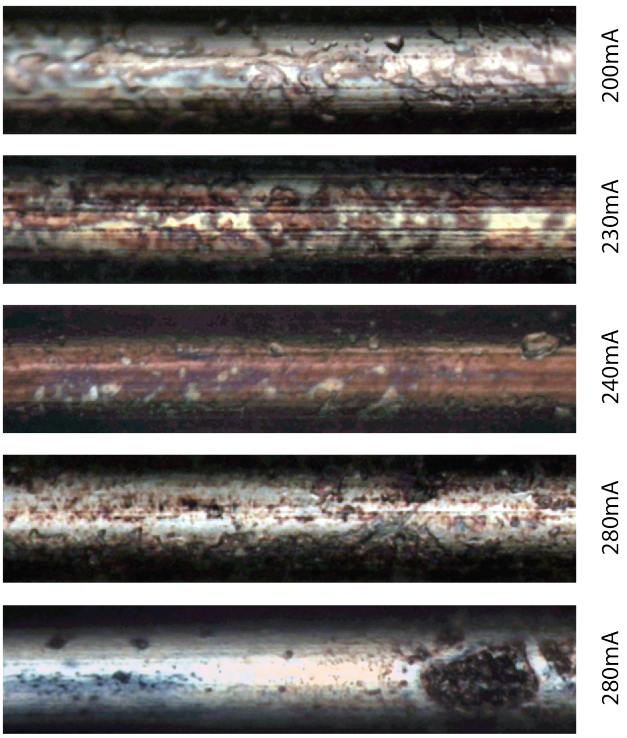

Figure D.9.: Microscopic images of the annealed wire show the onset of coloring at 200 mA. According to the color, 240 mA agrees to 250..290°C. However, the process seems to be very inhomogeneous: there are almost uncolored sections even at 260 mA. At higher currents, dark areas looking like voids occur on the surface and grow significantly with increased current. This suggests that the weakening arises from oxidation processes especially in those areas.

a temperature range of 250..290 °C. The strength, however, is reduced by >20% in comparison to the original wire. The current range recommended for the single arm test results in an extremely wide strength range from 1 to 2 GPa. Here the images suggest that small initial defects at the surface grow due to oxidation processes and result in large voids. For the 100 g mirrors this is not problematic, but in comparison to the music wire the hard tempered DIY annealed wire has no benefits in terms of reliability.

Luckily another company was found producing sufficiently thin high tensile strength wire. Fort Wayne Metals specify their type 304V wire to hold at least 2.932 GPa and provide a diameter of 50 µm ± 2.5 µm. Using a microscope and an etched precision scale the actual diameter was measured to be 52 µm which is well within the tolerances of the wire and measurement. Assuming the specified diameter, the strength was measured to be 2.92..2.97 GPa which gives plenty safety margin compared to the music wire. Therefore, this wire was tested in the TNI suspension.

Even under clamped conditions and running across break-off prisms, the suspensions turned out to be extremely sturdy. From this finding on, every time a RefC suspension chain broke, the new Fort Wayne wire was installed consecutively. With this in place no further breakdowns happened.

D.5 GENERALIZED COMMON MODE REJECTION OF A TRIANGULAR CAVITY

Let the angles of incidence onto the three RefC mirrors be unspecified and named as depicted in figure D.10.

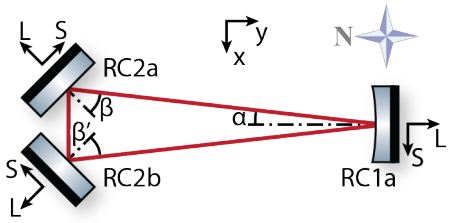

Figure D.10.: Recapitulation of figure 5.9 for convenience.

Equivalent to chapter 5.5, ground motion in the local mirror reference frame

$$\begin{aligned}
L_{2a}^{gnd} &= -\sin(\beta)x - \cos(\beta)y & \partial_{L_{2a}^{mirr}}\Delta_{rt} &= 2\cos(\beta)\\
S_{2a}^{gnd} &= -\cos(\beta)x + \sin(\beta)y & \partial_{S_{2a}^{mirr}}\Delta_{rt} &= 0\\
L_{2b}^{gnd} &= +\sin(\beta')x - \cos(\beta')y & \partial_{L_{2b}^{mirr}}\Delta_{rt} &= 2\cos(\beta')\\
S_{2b}^{gnd} &= -\cos(\beta')x - \sin(\beta')y & \partial_{S_{2b}^{mirr}}\Delta_{rt} &= 0
\end{aligned} \tag{D.1}$$

can be described by motion in the Prototype's reference frame (x,y). Geometry requires that the angle of incidence onto the out-coupler $\beta'=90°-(\alpha+\beta)$ is constrained by the other angles, so that equations 5.7 change to

$$\begin{aligned}
L_{1a}^{gnd} &= y & \partial_{L_{1a}^{mirr}}\Delta_{rt} &= 2\cos(\alpha)\\
S_{1a}^{gnd} &= x & \partial_{S_{1a}^{mirr}}\Delta_{rt} &= 0\\
L_{2a}^{gnd} &= -\sin(\beta)x - \cos(\beta)y & \partial_{L_{2a}^{mirr}}\Delta_{rt} &= 2\cos(\beta)\\
S_{2a}^{gnd} &= -\cos(\beta)x + \sin(\beta)y & \partial_{S_{2a}^{mirr}}\Delta_{rt} &= 0\\
L_{2b}^{gnd} &= +\cos(\alpha+\beta)x - \sin(\alpha+\beta)y & \partial_{L_{2b}^{mirr}}\Delta_{rt} &= 2\sin(\alpha+\beta)\\
S_{2b}^{gnd} &= -\sin(\alpha+\beta)x - \cos(\alpha+\beta)y & \partial_{S_{2b}^{mirr}}\Delta_{rt} &= 0\,.
\end{aligned} \tag{D.2}$$

The round trip deviation as sum of the individual contributions

$$\begin{aligned}\Delta_{\mathrm{rt}} &= 2\cos(\alpha)L_{1\mathrm{a}}^{\mathrm{mirr}} &&+ 2\cos(\beta)L_{2\mathrm{a}}^{\mathrm{mirr}} + 2\sin(\alpha{+}\beta)L_{2\mathrm{b}}^{\mathrm{mirr}}\\ &= 2\cos(\alpha)H_{1\mathrm{a}}^{l}y &&+ 2\cos(\beta)H_{2\mathrm{a}}^{l}\left[-\sin(\beta)x - \cos(\beta)y\right]\\ &&&+ 2\sin\left(\alpha{+}\beta\right)H_{2\mathrm{b}}^{l}\left[\cos\left(\alpha{+}\beta\right)x - \sin\left(\alpha{+}\beta\right)y\right]\\ &= 2\cos(\alpha)H_{1\mathrm{a}}^{l}y &&- \sin(2\beta)H_{2\mathrm{a}}^{l}x - 2\cos^2(\beta)H_{2\mathrm{a}}^{l}y\\ &&&+ \sin\left(2(\alpha{+}\beta)\right)H_{2\mathrm{b}}^{l}x - 2\sin^2\left(\alpha{+}\beta\right)H_{2\mathrm{b}}^{l}y\end{aligned} \tag{D.3}$$

is getting complicated. But the fractional round trip change for ground motion in the x-direction

$$\begin{aligned}\left.\frac{\partial\Delta_{\mathrm{rt}}}{\partial x_{\mathrm{gnd}}}\right|_{y=0} &= \sin\left(2(\alpha{+}\beta)\right)H_{2\mathrm{b}}^{l} - \sin\left(2\beta\right)H_{2\mathrm{a}}^{l}\\ &= H_{2\mathrm{bl}} - H_{2\mathrm{al}} + \mathcal{O}\left(\alpha^2\right) + \mathcal{O}\left((45^\circ{-}\beta)^2\right) + \mathcal{O}\left(\alpha(45^\circ{-}\beta)\right)\end{aligned} \tag{D.4}$$

goes to equation 5.9 sufficiently fast for small α and β close to 45° as it does not have linear terms in α or $\beta{-}45^\circ$. The fractional round trip change for y-motion

$$\begin{aligned}\left.\frac{\partial\Delta_{\mathrm{rt}}}{\partial y_{gnd}}\right|_{x=0} &= 2\cos(\alpha)H_{1\mathrm{a}}^{l} - 2\left[\sin^2(\alpha{+}\beta)H_{2\mathrm{b}}^{l} + \cos^2(\beta)H_{2\mathrm{a}}^{l}\right]\\ &= \ldots\\ &\overset{\substack{\alpha\approx1^\circ\\ \beta\approx\beta'}}{\approx} 2\cos(\alpha)H_{1\mathrm{a}}^{l} - \left[(1{+}\alpha)\cdot\left(H_{2\mathrm{a}}^{l}{+}H_{2\mathrm{b}}^{l}\right)\right]\\ &\qquad + 2(\beta{-}0.777\,\mathrm{rad})\cdot\left(H_{2\mathrm{b}}^{l}{-}H_{2\mathrm{a}}^{l}\right)\\ &\overset{\beta=\beta'}{=} 2\cos(\alpha)H_{1\mathrm{a}}^{l} - (1{+}\alpha)\cdot\left(H_{2\mathrm{a}}^{l}{+}H_{2\mathrm{b}}^{l}\right) \quad [\alpha,\beta\text{ in rad}]\\ &\overset{\alpha=0}{=} 2H_{1\mathrm{a}}^{l} - H_{2\mathrm{b}}^{l} - H_{2\mathrm{a}}^{l}\end{aligned} \tag{D.5}$$

can be simplified around the desired operation point at $\alpha\approx1^\circ$ and $\beta\approx\beta'\approx44.5^\circ=0.777$rad. With perfectly matching transfer functions the imbalance is approximately 2α. Therefore, a small opening angle is good for common mode rejection, while it harms in terms of backscatter. As an example, the common mode rejection of the well aligned RefC is theoretically limited to

$$\begin{aligned}CMR &= 1 - \left|\left.\frac{\partial\Delta_{\mathrm{rt}}}{\partial y_{\mathrm{gnd}}}\right|_{H_{1\mathrm{a}}^{l}=H_{2\mathrm{a}}^{l}=H_{2\mathrm{b}}^{l}}\right|\\ &\approx 1 - \left|2\cos(\alpha) - 2(1+\alpha)\right|\\ &\approx 1{-}2\alpha\\ &= 96.5\%\end{aligned} \tag{D.6}$$

for perfectly matching transfer functions.

In practice, the ground at the two sites probably move less in common. Even the matching of just the SAS platforms is worse on its own.

But the complex structure of the urban environment including building resonances causes spatially uncorrelated seismic motion [160].

Surprisingly, there is no linear coupling between the misalignment of the short, transverse RefC arm along the x-direction even for $\beta \neq \beta'$ as long as the transfer functions of RC2a and RC2b are matched well enough.

D.6 A COMPOUND MIRROR – BONDING SUBSTRATES

The TNI input mirror requires a short radius of curvature of the order of the length of the cavity, which is 10 cm. Yet the suspension was designed for a comparably large mass of 850 g and 10 cm diameter. The realization of such a heavily curved mirror turns out to be challenging. In the case of AlGaAs coatings, the technology isn't even ready to bond a coating onto a 5 cm thick substrate at all.

An alternative approach is to use a flat substrate close to the required mass and bond a small, curved mirror onto its center. As this interface would be inside the input path of the TNI, the optical quality of this bond is important. Some substrates with unknown surface quality were available for testing.

Optical contacting appears to be the optimal method of bonding, as e.g. [161] claims

- Full transparency (bonding layer is '*invisible*')
- No uncontrolled creep/drift under mechanical load (bonding layer is '*stiff*')
- No outgassing at elevated temperatures
- No stress from melting/re-solidification processes or thermal mismatch (for identical materials)
- Assembly of individual parts '*accurate to gage blocks*', bonding layer is '*infinitely thin*'

which suggests superior optical and mechanical qualities. However, optical contacting requires extremely good surface qualities. The surface roughness of the two interfaces should be smaller than 1 nm rms and the surfaces must have a good conformity. The quality of the given substrates was probably not sufficient for this. Even after extended periods of strong pressure no bonding could be observed.

In the hope of assisting the optical contacting by wringing, a drop of deionized water was added to the surface. It is easy to squeeze the water film thin so that Newton fringes appear. The 1" and 2"ø by 1/4" substrates could be deformed by applying decent pressure by more than a whole fringe. This hints that the overall surface figure is probably not the reason why the optical contact did not work. When increasing the pressure, even the last violet fringe eventually disappeared. In that

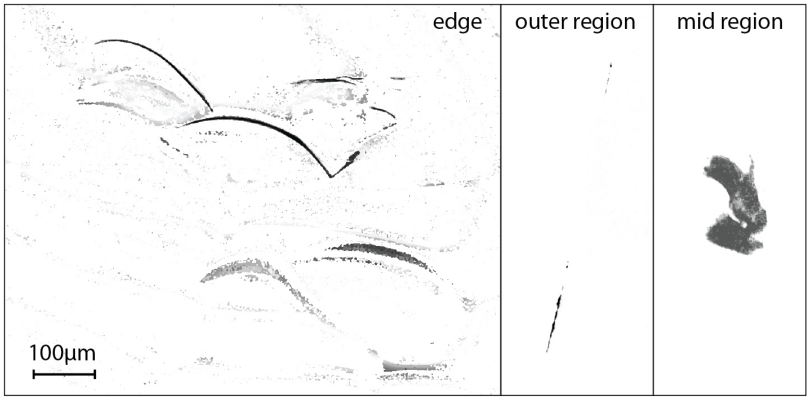

Figure D.11.: The microscopic images of the optocast bond interface are strongly increased in contrast. The conchoidal fractures at the edge probably were in place before the bonding. In the central region a bigger spot, either a particle or a surface defect can be seen. The scratches in the outer region might arise from debris in the glue distribution phase or have been in place before.

case both surfaces should be closer than 150 nm everywhere. Nevertheless, the substrates didn't even make contact over night. Instead, the water started to disappear in the outer 5 mm from the edge. Using isopropanol the same results were obtained with less pressure although the viscosity is twice as high. But this time the same reduction of liquid was observed already after 30 minutes.

Since optical contacting and wringing didn't show the expected success, another thin bonding method was searched for. Optocast 3553-LV-UTF is a UV-curable glue free of any filler. It was tested for vacuum applications by LIGO. The extension LV stands for low viscosity (800 mPas compared to 1 mPas of water). The UTF option means ultra thin film. This version cures in sections smaller than 20 µm. Due to the – with respect to water – increased viscosity, a higher pressure and a bit of sliding was required to squeeze the film between two 1.5" substrates as thin as possible. With this, a 2..4 mm^3 drop of glue was distributed across the whole interface resulting in an theoretical maximum average layer thickness of 1.8..3. µm. That is surprisingly thin. The homogeneity of the film couldn't be judged as no Newton fringes occur. This is because the optocast's index of refraction matches the glass's one pretty well. Optimally, the glue is cured under constant pressure. A jig should be used not to introduce stress and deform the mirror's surface figure.

Aside from a few microscopic defects (see figure D.11) which might arise from imperfect cleanliness or initial defects of the substrates, the bond interface looks very nice with bare eye as well as under the microscope. The test should be redone using high quality mirrors under clean room conditions. The only potential drawback of the UV gluing method is that the extensive pressure might introduce stress and sur-

face deformation to the mirror. However, a part of it can be released before curing the glue.

D.7 SLOW SERVO BEAM SHUTTER

One big challenge in interferometry is the large dynamic range of signals especially in the use of high finesse cavities. Light powers before and after lock acquisition differ by $\mathcal{F}^2$ (compare equation 6.7 or 6.8). Typical signals exceed the dynamic range of CDS. Wherever shot noise performance is not crucial, this can be overcome by inserting optical neutral density filters in front of photodiodes during lock.

It is convenient to insert these filters remotely or even automatically. Toy model servo motors serve as cheap actuators with sub second response time. Such servo motors are supplied with approximately (unstabilized) 5 V. The set position is determined by the pulse width of a TTL signal. The absolute pulse length of $\approx 1..2$ ms (exact values depend on the specific model) determines the angular position within a range of about 0..180°. The pulse is repeated about 50 times a second (usually 40 to 80 Hz will work as well). The ND filter can be glued to the servo arm to be swiped into the beam and out.

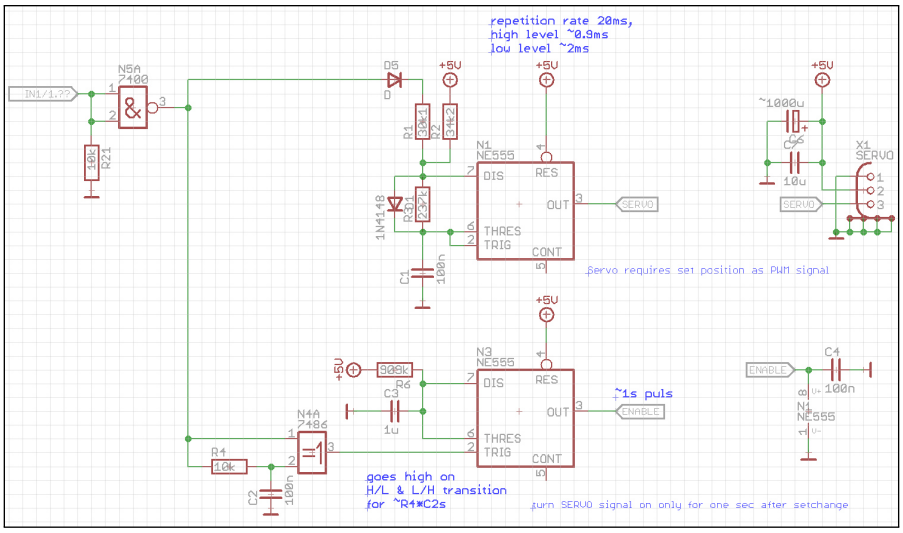

Figure D.12.: An electronic interface controls the position of a cheap model servo motor by means of CDS. This allows mechanical sub-second switching actions such as the attenuation of optical power by means of neutral density filters.

An electronic box was designed to interface the servo. Only two distinct states are available: filter in or filter out. One NE555 timer creates the 50 Hz signal, another sets the pulse length. The state is selected by setting the input for an channel to low or high impedance. This can be done using a switch, but digital IO cards for CDS provide full automation capabilities at 16 Hz switching rate. This is by far sufficient for most applications. To avoid excess electromagnetic radiation,

mechanical disturbances and wear, the servo is switched off automatically one second after any position change by cutting the TTL signal off.

D.8 FAST HDD BEAM SHUTTER

In some special cases, the speed of the shutter described in the last section is not sufficient. When a cavity falls out of lock, the power in reflection rises quickly. The power dissipated in the locking photodiode in this case can exceed the destruction threshold.

Quick mechanical shuttering is extremely challenging. A shading flag, usually a small mirror, must be accelerated into the beam path. Electromagnetic actuation requires high voltages to overcome inductances.

Inspired by [162], a shutter for KAGRA was built from an old hard disk drive. The read/write arm is driven by a core-less coil sitting between two strong magnets. It is meant to move quickly across the hard disk with a positioning time of about 10 ms on average. In the given publication, more emphasis was put onto pulse length (actual speed of motion) than onto reducing the delay of the shuttering action. Nevertheless an average delay of 4.6 ms was achieved. Motivated by this, the fairly simple electronics were modified slightly to achieve improved performance and better reliability.

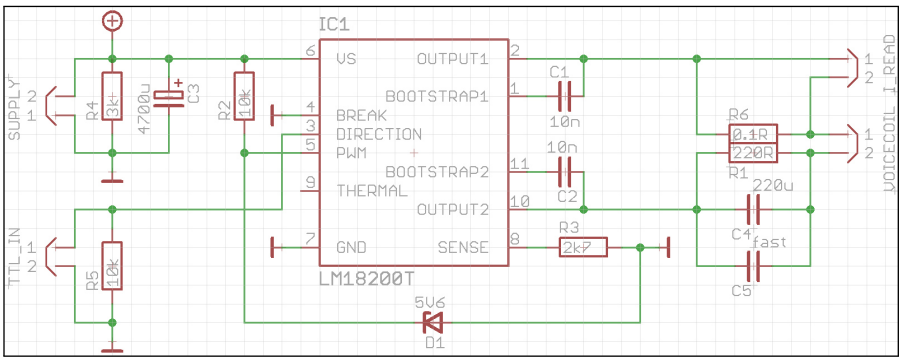

Figure D.13.: A fast but cheap shutter was investigated for the application in KAGRA. A commercially available H-bridge is capable of driving huge currents through a relatively light read/write arm in order to achieve low latency movement. The design can provide twice the supply voltage for a short moment to overcome the inductance of the voice coil.

The basic functionality is the one of the H-bridge LMD18200. The electronics are supplied with a voltage below half of the rating of C_4 and below the rating of C_3. With a change of the TTL input, the LMD changes the polarity of the outputs (2&10). It can deliver high currents, but the voltage is limited by the supply voltage of course. As C_4 is still charged, the effective voltage is doubled in the first moment, overcoming the inductance of the voice coil and rising the current through it

faster. After the acceleration phase, when C_4 is discharged, the current is limited by the resistor R_1 to reduce the thermal load on the shutter coil.

A resistor across C_3 discharges the capacitor in case the electronics are unplugged from the supply. A resistor across the TTL input pulls the input down in case no signal is applied. Before that, the electronics often went into random oscillations which destroyed the shutter after a short while. Two capacitors C_4 in parallel provide even higher speed; a big, slow and a small, fast capacitor. For diagnostic purposes a 0.1 Ω shunt resistor is added in the output path.

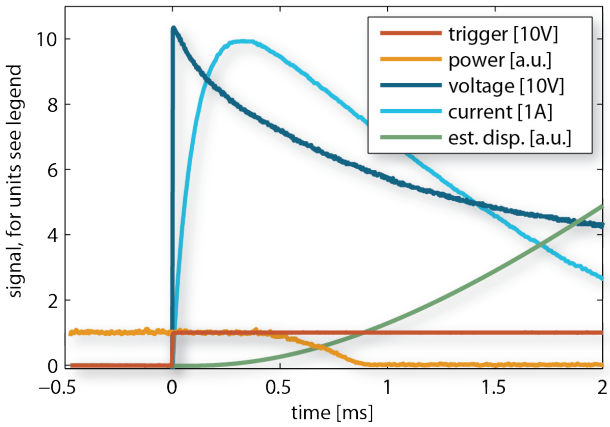

Figure D.14.: The performance of the HDD shutter supplied by 50 V is depicted. It was placed aside an approximately 2 mm diameter beam. Following the TTL signal's edge, the voltage rises to its maximum of twice the supply. The current through the coil follows delayed due to the inductance. After reaching its maximum it falls off almost exponentially. The current is proportional to the exerted force. Integrating it twice gives an estimate for the shutter displacement. After about 0.8 ms the beam is completely blocked.

The TTL input should be differential to prevent ground loops as no differential receiver was implemented into the electronics to maintain simplicity. The circuit was tested for supply voltages up to 50 V successfully.

The achieved 0.8 ms seems to be close to the technical limit of this design. The coil might survive higher currents for a short time, if the exponential tail of the capacitor discharge was clamped by other means to reduce the total deposited thermal energy. With a different mechanical design there is plenty room for improvement left. Already with this poor mans approach a cheap, easy to build shutter with sub-ms closing times for protecting sensitive optical components could be demonstrated successfully. This is comparable to commercially available high end shutters like the fast uniblitz LS shutter series.

D.9 INTERNAL CANTILEVER MODES

In contrast to horizontal seismic isolation, where thin, almost massless wires can be used, vertical isolation relies on more massive cantilever springs. This increases their inertia and thereby lowers internal resonance frequencies into the detection band. The associated Q-factors are usually very high. Yet their frequencies are too high to be damped by upper mass dampers. There are two cases to be considered: The upper stage's blade resonances show up as upper mass motion. Then they are observable and hence dampable by the active feedback system in principle. Their oscillation couples less strongly into test mass motion as it is attenuated by the lower vertical isolation stage(s). But the lower blades' resonances show up in testmass motion almost unfiltered (the lowest stage bounce mode is in the tens of Hertz range). These modes couple to upper mass motion only weakly so they are barely detectable due to BOSEM readout noise and hence not well dampable.

To identify the internal blades' frequencies for the RefC, a simulation was carried out with the FEM tool Ansys. As the whole suspension is too complicated to be simulated, the model was simplified. In the case of the upper stage the root of the flattened out cantilever is assumed to be fixed. This appears reasonable as they are rigidly attached to the cage which in turn is mounted to the table. At the tip a 222.8 mm long spring with a stiffness of 16.8 kN/m is attached. This matches the spring constant of the 150 µm steel suspension wire. The other side of the spring is connected to a mass of 0.55 kg which is free to move vertically. This is half the weight of the upper mass, i.e. the load per upper blade. The lower masses are assumed to decouple due to the soft blades inside the upper mass. The results are shown in figure D.15 and table D.1. It can be seen that many modes involve motion of the tip. The frequencies of these modes could be increased by manufacturing the wire clamp from titanium, i.e. reducing the mass.

Another slightly different model had to be used in case of the RefC lower stage's blades: The blade's root is attached to the 0.55 kg half upper mass which is assumed to be freely movable in vertical due to the softness of the upper blades. The tip is connected via a 220.8 mm long 8.3 kN/m stiff spring to a 0.436 kg mass. This resembles half the load of the vertically free intermediate mass. The lower mass mostly decouples from this resonance due to the few ten Hertz vertical bounce resonance. The results from this simulation are shown in figure D.16 and table D.1

D.10 PHASE MODULATION

In optical experiments, intentional frequency modulation is often achieved by means of periodic phase modulation. The few identities, which help to get a better understanding, are explained this section.

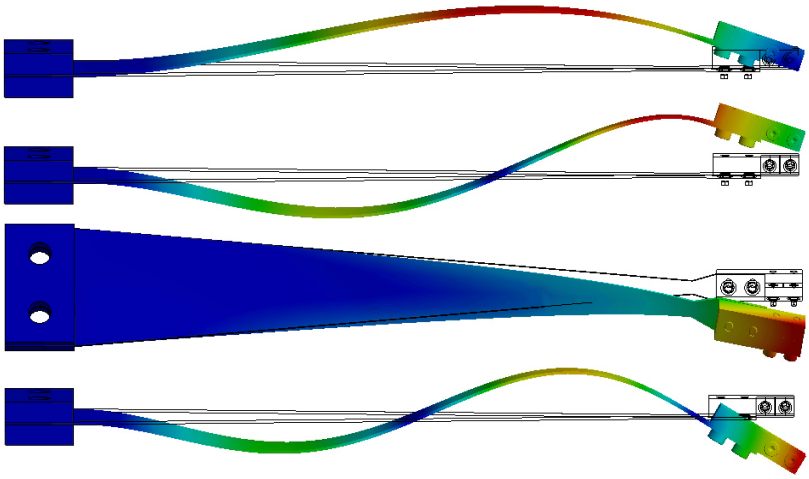

Figure D.15.: An FEM simulation of the upper stage cantilevers was carried out in Ansys to investigate internal modes. The shapes of modes below 300 Hz are shown above. The complex suspension dynamics are replaced with a heavily simplified model. Yet, the attached wire has to be simulated to allow for cantilever tip motion.

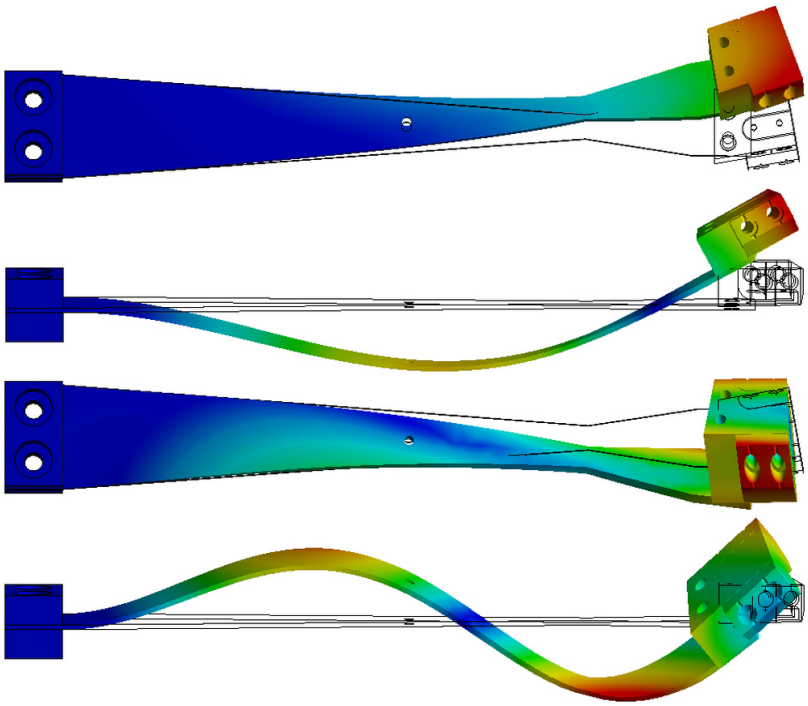

Figure D.16.: The simulation of the upper blades shown in D.15 was repeated with a similarly simplified model for the intermediate blades. In the initial clamp design the effective suspension point was not centered on the blades which caused twisting when loaded. In the final design this was corrected.

mode	upper stage	lower stage
1	76 Hz (v)	186 Hz (v)
2	186 Hz (v)	258 Hz (s)
3	265 Hz (s)	271 Hz (v)
4	285 Hz (v)	571 Hz (s,t)
5	456 Hz (v)	588 Hz (v)
6	545 Hz (t)	
7	739 Hz (v)	
8	818 Hz (t)	

Table D.1.: Simulated frequencies of the internal modes of the RefC's upper and lower stage cantilevers below 1 kHz were obtained from an FEM simulation. The lower stage's modes are higher in frequency because the blade is shorter and stiffer. The strongest involved degrees of freedom of the cantilever tip can be seen in figure D.15 and D.16. They are given in brackets: **v**ertical, **s**ideways, **t**wist.

Imagine an arbitrary carrier

$$E_c = A \cdot \mathrm{e}^{i(\omega_c t + \phi_c)} \tag{D.7}$$

with constant amplitude A and frequency ω_c. Now allow the phase

$$\phi_c(t) = \beta \cdot \sin(\Omega t) \tag{D.8}$$

to be sinusoidally modulated with a frequency Ω and the modulation depth β given in radians. The resulting modulated electrical field

$$E_m = A \cdot \mathrm{e}^{i\omega_c t + i\beta \sin(\Omega t)} \tag{D.9}$$

can be expressed by the Jacobi Anger expansion [163]

$$\begin{aligned} E_m &= A\mathrm{e}^{i\omega_c t} \cdot \sum_{n=-\infty}^{\infty} J_n(\beta)\mathrm{e}^{in\Omega t} \\ &= A\mathrm{e}^{i\omega_c t} \cdot \Bigg(\underbrace{J_0(\beta)}_{\text{carrier}} + \underbrace{\sum_{n=1}^{\infty} J_n(\beta)\mathrm{e}^{in\Omega t}}_{\text{upper sidebands}} + \underbrace{\sum_{n=1}^{\infty} (-1)^n J_n(\beta)\mathrm{e}^{-in\Omega t}}_{\text{lower sidebands}} \Bigg) \end{aligned} \tag{D.10}$$

and separated into different contributions due to the symmetry of the Bessel functions $J(\beta)$. This shows that the phase modulated carrier is reduced in amplitude to $J_0(\beta)$, while frequency sidebands are emerging. For small modulation depth, mainly first order sidebands with amplitude $J_1(\beta)$ each are created at frequencies $\omega_c \pm \Omega$.

D.11 NUMBER OF COATING LAYERS VS. REFLECTIVITY

Often, in experimental design the reflectivity of a given number of coating layers is requested or the number of layers to achieve a certain

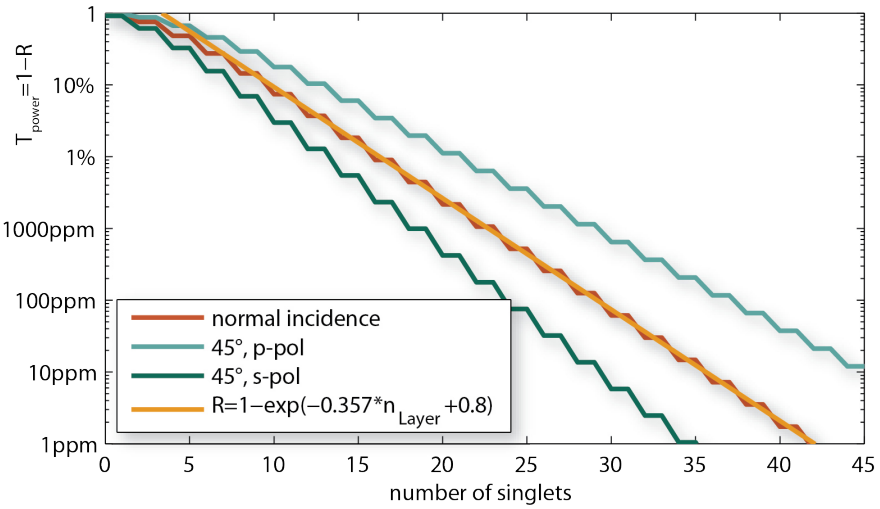

Figure D.17.: The reflectivity of dielectric coatings is based on constructive interference of reflexes from the silica (n=1.47) and tantala (n=2.10) layers (singlets) applied to a quartz substrate. Coatings with optimal constructive interference (quarter wave stack with half wave silica cap) are simulated for common parameters used in the PMC, RefC and TNI. The coatings could be improved in terms of thermal noise performance by changing the silica/tantala thickness ratio.

reflectivity is under question. The reflectivity of a dielectric coating stack arises from constructive interference of Fresnel reflexes on the boundaries between high and low refractive index material. Assuming optimal constructive interference, an upper limit can be given for any number of layers.

mirror	AoI	T_{spec}	layers
RC1a	$\approx 0°$	10 ppm	36
RC2a	$\approx 45°_p$	1000 ppm	28
RC2b	$\approx 45°_p$	600 ppm	30

Table D.2.: Number of coating stack layers for the RefC as deduced from figure D.17 and the specified power transmissivities. The reflectivity of the 45°-RC2-mirrors under s-pol is predicted to be about 100 times closer to one than p-pol.

As the Fresnel formulas are dependent on the angle of incidence, the coating stack reflectivity is as well, even when optimizing the layer thickness for the changed optical path length. The result is shown in figure D.17. From this, a lower bound for coating layers of the RefC can be deduced for usage in thermal noise simulations.

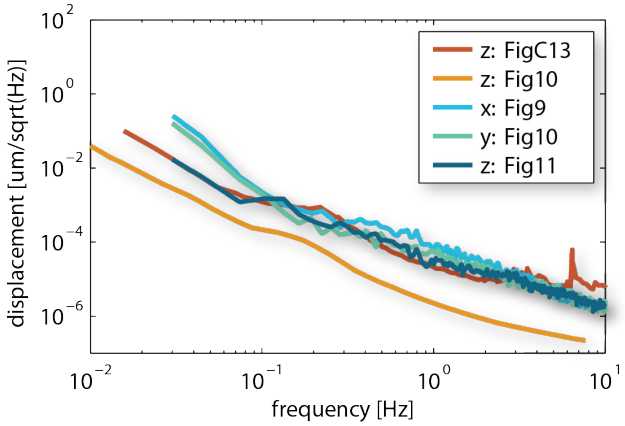

Figure D.18.: Three sources [164, 165, 166] give the vertical (z) self noise of STS2-type seismometers. [165] employed three sensors with special shielding techniques. This seems to increase the sensitivity by a factor 10. The horizontal sensitivity (x,y) given in [166] rises with respect to the vertical noise below 0.1 Hz. Although the source claims the noise to be unidirectional, x shows a twice as high noise from 0.1 to a few Hz.

D.12 STS2 SELF NOISE

The scope of this section is to show that the seismic noise presented in chapter 3.1 is not limited by instrument noise. The self noise is not measurable with a single seismometer, as it's not distinguishable from seismic motion. An estimate can be obtained in a huddle test which requires two sensors of the same kind. The coherent part of the signal is assumed to be signal, the incoherent is supposed to arise from sensor noise.

Since no two sensors were available, four sources are evaluated. [164] gives a power spectrum for vertical acceleration in figure 10. In [165] figure C-13 the '*corrected difference*' of vertical displacement power spectra is given. It is assumed to be corrected by the factor $\sqrt{2}$ to obtain the single instrument's sensor noise. Finally [166] gives measurements for displacement ASDs in horizontal as well as vertical. Surprisingly, the x-noise is a factor 2 worse in the mid-frequency range around 1 Hz than the y-noise.

D.13 COUPLING IN VACUUM NOISE

This section is meant as a quick reminder of how losses transform noise properties of a laser beam. In particular, shot noise can be described by a perfect laser beam E_{in} overlaid with vacuum fluctuations δ_{vac}.

Loss channel

Assume such a shot noise limited laser to be attenuated. This can be described as a beam splitter action.

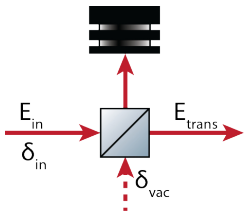

The beam splitter replaces a fraction r of the laser with a fraction r of vacuum. The amplitude of the transmitted light reads

$$E_{\text{trans}} = tE_{\text{in}} + t\delta_{\text{vac}} - r\delta_{\text{vac'}} \quad . \tag{D.11}$$

The fact that the vacuum modes are uncorrelated means that they sum up in quadrature. Hence, the transmitted light

$$\begin{aligned} E_{\text{trans}} &= tE_{\text{in}} + \sqrt{|t\delta_{\text{vac''}}|^2 + |r\delta_{\text{vac''}}|^2} \\ &= tE_{\text{in}} + \sqrt{|t|^2 + |r|^2} \cdot |\delta_{\text{vac''}}| \\ &= tE_{\text{in}} + \delta_{\text{vac''}} \end{aligned} \tag{D.12}$$

is equivalent to a shot noise limited beam with amplitude tE_{in} or $\bar{E}_{\text{trans}}$, the average transmitted amplitude.

Laser intensity stabilization

A laser intensity stabilization picks off a fraction of laser light E_{in} containing amplitude noise δ_{las}.

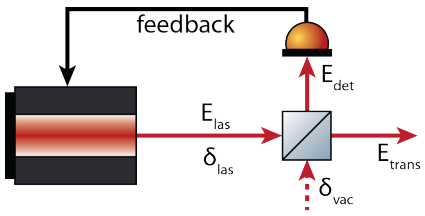

The power

$$|E_{\text{det}}|^2 = |rE_{\text{las}} + r\delta_{\text{las}} + t\delta_{\text{vac}}| \tag{D.13}$$

is detected by a photo diode. The deviation from a set point is fed back to a power actuator of the laser. In the theoretical case of infinite gain, this holds $|E_{\text{det}}|^2$ constant, so that $r\delta_{\text{las}} + t\delta_{\text{vac}} = const.$ Since all DC power is attributed to E_{las},

$$r\delta_{\text{las}} \stackrel{!}{=} -t\delta_{\text{vac}} \tag{D.14}$$

has to hold. Then the laser noise in the transmitted light field

$$E_{\text{trans}} = tE_{\text{las}} + t\delta_{\text{las}} - r\delta_{\text{vac}} \tag{D.15}$$

can be replaced using equation D.14 to obtain

$$\begin{aligned} E_{\text{trans}} &= tE_{\text{las}} - \frac{t^2}{r}\delta_{\text{vac}} - \frac{r^2}{r}\delta_{\text{vac}} \\ &= tE_{\text{las}} - \frac{1}{r}\delta_{\text{vac}} \ . \end{aligned} \tag{D.16}$$

In case the amount of detected power is a big fraction ot the laser power, $P_{\text{det}} \to P_{\text{las}}$ and $r \to 1$, the transmitted light

$$E_{\text{trans}} = tE_{\text{las}} - \delta_{\text{vac}} \tag{D.17}$$

is equivalent to a shot noise limited beam with amplitude $tE_{\text{las}} = \bar{E}_{\text{trans}}$.

If the detected power is only a small fraction of the laser power, $1/r$ goes to infinity. However, it can be replaced using $E_{\text{det}} \approx \bar{E}_{\text{det}} = rE_{\text{las}}$, where $\bar{E}_{\text{det}}$ is the average detected light field, to obtain

$$E_{\text{trans}} \approx tE_{\text{las}} - \frac{E_{\text{las}}}{E_{\text{det}}}\delta_{\text{vac}} \ . \tag{D.18}$$

The noise of the transmitted light is now proportional to the laser amplitude, same as classical laser noise would be and the relative amplitude noise is the same as a shot noise limited detection of E_{det} would give.

D.14 MECHANICAL LOSS OF SILICA/TANTALA COATINGS

material	technology	loss angle	source
SiO_2	e-beam	$6.0 \cdot 10^{-4}$	[152]
SiO_2	e-beam annealed	$0.6 \cdot 10^{-4}$	[152]
SiO_2	IBS	$1.0 \cdot 10^{-4}$	[167]
Ta_2O_5	e-beam annealed	$4.7 \cdot 10^{-4}$	[152]
Ta_2O_5	IBS	$3.8 \cdot 10^{-4}$	[167]
Ta_2O_5	TiO_2 doped	$1.5 \cdot 10^{-4}$	[153]

Table D.3.: The various existent coating technologies yield different mechanical loss angles even for the same materials.

For a long time silica/tantala coatings were the first choice for 1064 nm applications due to their superior mechanical as well as optical quality. In particular, these amorphous thin film structures provide relatively low mechanical loss while optical absorption and scattering are extremely small. Improved coating processes, such as annealing, allow for even lower mechanical loss. Ion beam sputtering (IBS) creates denser films than e-beam evaporation which reduces structural defects. The mechanical performance of tantala, which was hugely dominant for a long time, is shown to improve to levels similar to silica when being doped with titania.

BIBLIOGRAPHY

[1] T. Westphal, G. Bergmann, A. Bertolini, *et al.* Design of the 10 m AEI prototype facility for interferometry studies. *Applied Physics B*, **106**(3):551–557, February 2012.

[2] Thomas Corbitt, Yanbei Chen, Farid Khalili, *et al.* Squeezed-state source using radiation-pressure-induced rigidity. *Physical Review A*, **73**(2):023801, February 2006.

[3] Helge Müller-Ebhardt, Henning Rehbein, Roman Schnabel, Karsten Danzmann, and Yanbei Chen. Entanglement of Macroscopic Test Masses and the Standard Quantum Limit in Laser Interferometry. *Physical Review Letters*, **100**(1):013601, January 2008.

[4] Jasper Chan, T. P. Mayer Alegre, Amir H. Safavi-Naeini, *et al.* Laser cooling of a nanomechanical oscillator into its quantum ground state. *Nature*, **478**(7367):89–92, October 2011.

[5] J. D. Teufel, T. Donner, Dale Li, *et al.* Sideband cooling of micromechanical motion to the quantum ground state. *Nature*, **475**(7356):359–363, July 2011.

[6] Roger Penrose. *The Emperor's New Mind: Concerning Computers, Minds, and the Laws of Physics*. OUP Oxford, March 1999. pp. 475 481.

[7] D.e. McClelland, N. Mavalvala, Y. Chen, and R. Schnabel. Advanced interferometry, quantum optics and optomechanics in gravitational wave detectors. *Laser & Photonics Reviews*, **5**(5):677–696, September 2011.

[8] Kentaro Somiya. Conceptual Design of the Hannover 10m Interferometer for sub SQL measurement, 2009. LIGO-G0900438-v1.

[9] Kentaro Somiya. Conceptual design of an interferometer with a sub-SQL sensitivity ver. 2.0, 2009. LIGO-T0900069.

[10] Garrett D. Cole, Simon Gröblacher, Katharina Gugler, Sylvain Gigan, and Markus Aspelmeyer. Monocrystalline $Al_xGa_{1-x}As$ heterostructures for high-reflectivity high-Q micromechanical resonators in the megahertz regime. *Applied Physics Letters*, **92**(26):261108, June 2008.

[11] Garrett D. Cole, Wei Zhang, Michael J. Martin, Jun Ye, and Markus Aspelmeyer. Tenfold reduction of Brownian noise in high-reflectivity optical coatings. *Nature Photonics*, **7**(8):644–650, August 2013.

[12] Conor Mow-Lowry. Internal logbook page 1441.

[13] Christian Gräf, Stefan Hild, Harald Lück, *et al.* Optical layout for a 10 m Fabry-Perot Michelson interferometer with tunable stability. *Classical and Quantum Gravity*, **29**(7):075003, March 2012.

[14] A. Wanner, G. Bergmann, A. Bertolini, *et al.* Seismic attenuation system for the AEI 10 meter Prototype. *Classical and quantum gravity*, **29**(24):245007, 2012.

[15] Alexander Wanner. *Seismic Attenuation System (AEI-SAS) for the AEI 10 m Prototype.* PhD thesis, University of Hannover, 2013.

[16] Alberto Stochino, Benjamin Abbot, Yoichi Aso, *et al.* The Seismic Attenuation System (SAS) for the Advanced LIGO gravitational wave interferometric detectors. *Nuclear Instruments and Methods in Physics Research Section A: Accelerators, Spectrometers, Detectors and Associated Equipment*, **598**(3):737–753, January 2009.

[17] G Cella, R DeSalvo, V Sannibale, *et al.* Seismic attenuation performance of the first prototype of a geometric anti-spring filter. *Nuclear Instruments and Methods in Physics Research Section A: Accelerators, Spectrometers, Detectors and Associated Equipment*, **487**(3):652–660, July 2002.

[18] A. Takamori, P. Raffai, S. Márka, *et al.* Inverted pendulum as low-frequency pre-isolation for advanced gravitational wave detectors. *Nuclear Instruments and Methods in Physics Research Section A: Accelerators, Spectrometers, Detectors and Associated Equipment*, **582**(2):683–692, November 2007.

[19] Alberto Stochino. Performance Improvement of the Geometric Anti Spring (GAS) Seismic Filter for Gravitational Waves Detectors - SURF report, 2005. T0500239-00-D.

[20] F. Raab and D. Coyne. Effect of Microseismic Noise on a LIGO Interferometer, 1997. T960187-01-D.

[21] K. Dahl, A. Bertolini, M. Born, *et al.* Towards a Suspension Platform Interferometer for the AEI 10 m Prototype Interferometer. *Journal of Physics: Conference Series*, **228**(1):012027, 2010.

[22] Katrin Dahl. *From design to operation: a suspension platform interferometer for the AEI 10 m prototype*. PhD thesis, University of Hannover, 2013.

[23] Coherent Inc. Prometheus ultra-narrow linewidth CW laser.

[24] Euan Morrison, Brian J. Meers, David I. Robertson, and Henry Ward. Automatic alignment of optical interferometers. *Applied Optics*, **33**(22):5041, August 1994.

[25] G. Heinzel, V. Wand, A. García, *et al.* The LTP interferometer and phasemeter. *Classical and Quantum Gravity*, **21**(5):S581, 2004.

[26] Maik Frede, Bastian Schulz, Ralf Wilhelm, *et al.* Fundamental mode, single-frequency laser amplifier for gravitational wave detectors. *Optics Express*, **15**(2):459, January 2007.

[27] Henning Ryll. *Transmission hoher Laserleistung durch optische Fasern*. Diploma thesis, University of Hannover, 2008.

[28] Patrick Oppermann. Personal communication.

[29] Jonas Junker. *Laser power stabilization for the AEI 10m Prototype*. Master thesis, University of Hannover, 2016.

[30] Fumiko Kawazoe, John Robert Taylor, Alessandro Bertolini, *et al.* Designs of the frequency reference cavity for the AEI 10 m Prototype interferometer. *Journal of Physics: Conference Series*, **228**(1):012028, 2010.

[31] Stuart M. Aston. *Optical read-out techniques for the control of test-masses in gravitational wave observatories*. PhD thesis, University of Birmingham, 2011.

[32] F. Kawazoe, R. Schilling, and H. Lück. Eigenmode changes in a misaligned triangular optical cavity. *Journal of Optics*, **13**(5):055504, 2011.

[33] Daniel Sigg and the LIGO Scientific Collaboration. Status of the LIGO detectors. *Classical and Quantum Gravity*, **25**(11):114041, 2008.

[34] Tobin Fricke. Internal logbook page 1606.

[35] ArgonneNationalLaboratory. EPICS - Experimental Physics and Industrial Control System.

[36] Stefan Goßler, Jeff Cumpston, Kirk McKenzie, *et al.* Coating-free mirrors for high precision interferometric experiments. *Physical Review A*, **76**(5):053810, November 2007.

[37] Frank Brückner, Daniel Friedrich, Tina Clausnitzer, *et al.* Realization of a Monolithic High-Reflectivity Cavity Mirror from a Single Silicon Crystal. *Physical Review Letters*, **104**(16):163903, April 2010.

[38] A. E. Siegman. *Lasers*. University Science Books, January 1986.

[39] Thimoteus Alig. *Charakterisierung und Unterdrückung der Strahlgeometriefluktuationen des fasergekoppelten 35W Lasers für das AEI 10m Prototypinterferometer*. Diploma thesis, University of Hannover, 2013.

[40] Guido Mueller. Beam jitter coupling in advanced LIGO. *Optics Express*, **13**(18):7118, 2005.

[41] Patrick Kwee, Frank Seifert, Benno Willke, and Karsten Danzmann. Laser beam quality and pointing measurement with an optical resonator. *Review of Scientific Instruments*, **78**(7):073103, July 2007.

[42] B. Willke, N. Uehara, E. K. Gustafson, *et al.* Spatial and temporal filtering of a 10-W Nd: YAG laser with a Fabry-Perot ring-cavity premode cleaner. *Optics letters*, **23**(21):1704–1706, November 1998.

[43] Fabrice Matichard and Matthew Evans. Review: Tilt-Free Low-Noise Seismometry. *Bulletin of the Seismological Society of America*, **105**(2A):497–510, April 2015.

[44] R. Beauduin, P. Lognonné, J. P. Montagner, *et al.* The effects of the atmospheric pressure changes on seismic signals or how to improve the quality of a station. *Bulletin of the Seismological Society of America*, **86**(6):1760–1769, January 1996.

[45] SURF-forecast. France Surf Map - Wind and Wave forecasts.

[46] P. Bormann. *New manual of seismological observatory practice (NMSOP-2). IASPEI, GFZ German Research Centre for Geosciences, Potsdam*. 2012.

[47] B. Abbott, R. Abbott, R. Adhikari, *et al.* Observation of a kilogram-scale oscillator near its quantum ground state. *New Journal of Physics*, **11**(7):073032, 2009.

[48] S. Wen, R. Mittleman, K. Mason, *et al.* Hydraulic external pre-isolator system for LIGO. *Classical and Quantum Gravity*, **31**(23):235001, November 2014.

[49] Conor Mow-Lowry. Personal communication.

[50] T. Accadia, F. Acernese, F. Antonucci, *et al.* Status of the Virgo project. *Classical and Quantum Gravity*, **28**(11):114002, 2011.

[51] John Bechhoefer. Kramers-Kronig, Bode, and the meaning of zero. *American Journal of Physics*, **79**(10):1053, 2011.

[52] J. R. Leigh. *Control Theory*. IET, The Institution of Engineering and Technology, Michael Faraday House, Six Hills Way, Stevenage SG1 2AY, UK, January 2004. chapter 5.5.

[53] Stefan Gossler. Personal communication.

[54] Kenneth A. Strain. Electrostatic drive (ESD) results from GEO and application in Advanced LIGO, 2006. LIGO-T060015-x0.

[55] E. Goetz, P. Kalmus, S. Erickson, *et al.* Precise calibration of LIGO test mass actuators using photon radiation pressure. *Classical and Quantum Gravity*, **26**(24):245011, November 2009.

[56] Wolfgang Demtröder. *Experimentalphysik 1*. Springer-Lehrbuch. Springer Berlin Heidelberg, Berlin, Heidelberg, 2015.

[57] C Torrie. *Development of Suspenions for the Geo600 Gravitational Wave Detector*. PhD thesis, University of Glasgow, 1999.

[58] Peter R. Saulson. Thermal noise in mechanical experiments. *Physical Review D*, **42**(8):2437–2445, October 1990.

[59] Gregory Harry, Timothy P. Bodiya, and Riccardo DeSalvo. *Optical Coatings and Thermal Noise in Precision Measurement*. Cambridge University Press, January 2012.

[60] David R. M. Crooks. *Mechanical loss and its significance in the test mass mirrors of gravitational wave detectors*. PhD thesis, University of Glasgow, 2002.

[61] A. Gillespie and F. Raab. Suspension losses in the pendula of laser interferometer gravitational-wave detectors. *Physics Letters A*, **190**(3-4):213–220, July 1994.

[62] Rana X. Adhikari. Personal communication.

[63] M. V. Plissi, C. I. Torrie, M. Barton, *et al.* An investigation of eddy-current damping of multi-stage pendulum suspensions for use in interferometric gravitational wave detectors. *Review of Scientific Instruments*, **75**(11):4516–4522, November 2004.

[64] M. Beccaria, M. Bernardini, S. Braccini, *et al.* The creep problem in the VIRGO suspensions: a possible solution using Maraging steel. *Nuclear Instruments and Methods in Physics Research Section A: Accelerators, Spectrometers, Detectors and Associated Equipment*, **404**(2):455–469, 1998.

[65] Jonathan Cripe. Internal logbook page 2269.

[66] Brian Shapiro, Jeffrey Kissel, Nergis Mavalvala, Kenneth Strain, and Kamal Youcef-Toumi. Limitations of Underactuated Modal Damping for Multistage Vibration Isolation Systems. *Mechatronics, IEEE/ASME Transactions on*, **20**(1):393–404, 2015.

[67] L. Carbone, S. M. Aston, R. M. Cutler, *et al.* Sensors and Actuators for the Advanced LIGO Mirror Suspensions. *Classical and Quantum Gravity*, **29**(11):115005, June 2012.

[68] D. I. Robertson, E. Morrison, J. Hough, *et al.* The Glasgow 10 m prototype laser interferometric gravitational wave detector. *Review of Scientific Instruments*, **66**(9):4447–4452, September 1995.

[69] J. Winterflood, D. G. Blair, R. Schilling, and M. Notcutt. Position control system for suspended masses in laser interferometer gravitational wave detectors. *Review of Scientific Instruments*, **66**(4):2763–2776, April 1995.

[70] B. Abbott, R. Abbott, R. Adhikari, *et al.* Detector description and performance for the first coincidence observations between LIGO and GEO. *Nuclear Instruments and Methods in Physics Research Section A: Accelerators, Spectrometers, Detectors and Associated Equipment*, **517**(1):154–179, January 2004.

[71] TTelectronics. datasheet OP23 series.

[72] InfineonTechnologies. datasheet BPX65 Silicon PIN Photodiode.

[73] Matt Evans. BOSEM Flat Magnet Flag, aLIGO SUS, 2011. LIGO-D1100573-v5.

[74] Ron Cutler. Satellite Box Circuit Diagrams, 2009. LIGO-D0901284-v1.

[75] Stuart M. Aston. Personal communication.

[76] David Robertson. GEO LOCAL CONTROL Main Suspension (schematics), 1999.

[77] Frank Seifert. Resistor Current Noise Measurements, 2009. LIGO-T0900200-v1.

[78] G. Heinzel, A. Rüdiger, R. Schilling, *et al.* Automatic beam alignment in the Garching 30-m prototype of a laser-interferometric gravitational wave detector. *Optics Communications*, **160**(4-6):321–334, 1999.

[79] Bernd Schulte. *Untersuchung an mechanischen Aufhängungen und interferometrische Technologien für zukünftige Gravitationswellendetektoren.* Diploma thesis, University of Bremen, 2015.

[80] Dirk Schütte. *Modern Control Approaches for Next-Generation Gravitational Wave Detectors*. PhD thesis, University of Hannover, 2016.

[81] Christoph Affeldt. *Laser power increase for GEO 600*. PhD thesis, University of Hannover, 2014.

[82] Rainer Weiss. Collection of Reports on Barkhausen Noise, 2008. LIGO-T0900061-v1.

[83] Norna Robertson. RODA: Use of SmCo and NdFeB Magnets in Advanced LIGO Suspensions, 2010. LIGO-M0900034-v4.

[84] Bernard Friedland. *Control System Design: An Introduction to State-Space Methods*. Courier Corporation, March 2012.

[85] Mark Barton. Calculation and measurement of the OSEM actuator sweet spot position, 2010. LIGO-T1000164-v3.

[86] Sarah Zuraw. Internal logbook page 1352.

[87] K. A. Strain and B. N. Shapiro. Damping and local control of mirror suspensions for laser interferometric gravitational wave detectors. *Review of Scientific Instruments*, **83**(4):044501, April 2012.

[88] R. Abbott and M. Mageswaran. Photodetector Cable Shielding Analysis, 2010. LIGO-T1000532-v2.

[89] S. Braccini, C. Casciano, F. Cordero, *et al.* The maraging-steel blades of the Virgo super attenuator. *Measurement Science and Technology*, **11**(5):467, February 2000.

[90] Fran Cverna. *ASM Ready Reference: Thermal Properties of Metals*. Materials Data Series. ASM International, 2002.

[91] A. Gillespie and F. Raab. Thermal noise in the test mass suspensions of a laser interferometer gravitational-wave detector prototype. *Physics Letters A*, **178**(5-6):357–363, May 1993.

[92] Patrick Kwee. *Charakterisierung von Lasersystemen für Gravitationswellendetektoren*. Diploma thesis, University of Hannover, 2005.

[93] Christian Gräf. *Optical design and numerical modeling of the AEI 10 m Prototype sub-SQL interferometer*. PhD thesis, University of Hannover, 2013.

[94] Crystalline mirror solutions via Garret Cole. Personal communication.

[95] Andrew Brown, Albert Ogloza, Lucas Taylor, Jeff Thomas, and Joseph Talghader. Continuous-wave laser damage and conditioning of particle contaminated optics. *Applied Optics*, **54**(16):5216, June 2015.

[96] Harald Lück. Personal communication.

[97] Daniel Sigg. TTFSS schmatics, 2009. LIGO-D040105-v1.

[98] Michael Tröbs. *Laser development and stabilization for the spaceborne interferometric gravitational wave detector LISA*. PhD thesis, University of Hannover, 2005.

[99] Patrick Kwee and Benno Willke. Automatic laser beam characterization of monolithic Nd:YAG nonplanar ring lasers. *Applied Optics*, **47**(32):6022, November 2008.

[100] Daniel Sigg. aLIGO TTFSS Revision list.

[101] Fumiko Kawazoe. Internal logbook page 692.

[102] H. Grote, G. Heinzel, A. Freise, *et al.* Alignment control of GEO 600. *Classical and Quantum Gravity*, **21**(5):S441, February 2004.

[103] B. Canuel, E. Genin, M. Mantovani, *et al.* Sub-nanoradiant beam pointing monitoring and stabilization system for controlling input beam jitter in gravitational wave interferometers. *Applied Optics*, **53**(13):2906, May 2014.

[104] Tobin Fricke. Personal communication.

[105] M. Evans, S. Ballmer, M. Fejer, *et al.* Thermo-optic noise in coated mirrors for high-precision optical measurements. *Physical Review D*, **78**(10):102003, November 2008.

[106] M. M. Fejer, S. Rowan, G. Cagnoli, *et al.* Thermoelastic dissipation in inhomogeneous media: loss measurements and displacement noise in coated test masses for interferometric gravitational wave detectors. *Physical Review D*, **70**(8):082003, October 2004.

[107] Patrick Kwee, Benno Willke, and Karsten Danzmann. Shot-noise-limited laser power stabilization with a high-power photodiode array. *Optics Letters*, **34**(19):2912–2914, October 2009.

[108] Herbert B. Callen and Theodore A. Welton. Irreversibility and Generalized Noise. *Physical Review*, **83**(1):34–40, July 1951.

[109] Yuri Levin. Fluctuation-dissipation theorem for thermo-refractive noise. *Physics Letters A*, **372**(12):1941–1944, March 2008.

[110] Fluctuation-dissipation theorem, March 2016. Page Version ID: 709323371.

[111] Kazuhiro Yamamoto, Shinji Miyoki, Takashi Uchiyama, *et al.* Measurement of the mechanical loss of a cooled reflective coating for gravitational wave detection. *Physical Review D*, **74**(2):022002, July 2006.

[112] Ronny Nawrodt. *Kryogene Gütemessung an optischen Substratmaterialien für zukünftige Gravitationswellendetektoren.* PhD thesis, University of Jena, 2008.

[113] Yu. Levin. Internal thermal noise in the LIGO test masses: A direct approach. *Physical Review D*, **57**(2):659–663, January 1998.

[114] Gabriela González. Suspensions thermal noise in the LIGO gravitational wave detector. *Classical and Quantum Gravity*, **17**(21):4409, 2000.

[115] Gabriela I. González and Peter R. Saulson. Brownian motion of a mass suspended by an anelastic wire. *The Journal of the Acoustical Society of America*, **96**(1):207–212, July 1994.

[116] S. Gossler, M. M. Casey, A. Freise, *et al.* The modecleaner system and suspension aspects of GEO 600. *Classical and Quantum Gravity*, **19**(7):1835, 2002.

[117] H. J. Kimble, Benjamin L. Lev, and Jun Ye. Optical Interferometers with Reduced Sensitivity to Thermal Noise. *Physical Review Letters*, **101**(26):260602, December 2008.

[118] Michael L. Gorodetsky. Thermal noises and noise compensation in high-reflection multilayer coating. *Physics Letters A*, **372**(46):6813–6822, November 2008.

[119] Gregory M. Harry, Andri M. Gretarsson, Peter R. Saulson, *et al.* Thermal noise in interferometric gravitational wave detectors due to dielectric optical coatings. *Classical and Quantum Gravity*, **19**(5):897, 2002.

[120] Kentaro Somiya, Keiko Kokeyama, and Ronny Nawrodt. Remarks on thermoelastic effects at low temperatures and quantum limits in displacement measurements. *Physical Review D*, **82**(12):127101, December 2010.

[121] V. B. Braginsky and S. P. Vyatchanin. Thermodynamical fluctuations in optical mirror coatings. *Physics Letters A*, **312**(3-4):244–255, June 2003.

[122] Tara Chalermsongsak, Evan D. Hall, Garrett D. Cole, *et al.* Coherent Cancellation of Photothermal Noise in GaAs/$Al_{0.92}Ga_{0.08}As$ Bragg Mirrors. *arXiv:1506.07088 [physics]*, June 2015.

[123] V. B. Braginsky, M. L. Gorodetsky, and S. P. Vyatchanin. Thermodynamical fluctuations and photo-thermal shot noise in gravitational wave antennae. *Physics Letters A*, **264**(1):1–10, 1999.

[124] A. Gillespie and F. Raab. Thermally excited vibrations of the mirrors of laser interferometer gravitational-wave detectors. *Physical Review D*, **52**(2):577–585, July 1995.

[125] V. B. Braginskii, V. P. Mitrofanov, and O. A. Okhrimenko. Oscillators for free-mass gravitational-wave antennas. *Pisma v Zhurnal Eksperimentalnoi i Teoreticheskoi Fiziki*, **55**:424–426, April 1992.

[126] Kenji Numata. *Direct measurement of mirror thermal noise*. PhD thesis, University of Tokyo, 2002.

[127] Jan Harms and Brian O'Reilly. Velocity and Attenuation Characterization of the LIGO Site near Livingston, Louisiana. *Bulletin of the Seismological Society of America*, **101**(4):1478–1487, August 2011.

[128] Eric D. Black. An introduction to Pound-Drever-Hall laser frequency stabilization. *American Journal of Physics*, **69**(1):79–87, January 2001.

[129] Alexey G. Gurkovsky, Daniel Heinert, Stefan Hild, *et al.* Reducing thermal noise in future gravitational wave detectors by employing Khalili etalons. *Physics Letters A*, **375**(46):4147–4157, November 2011.

[130] A. D. Ludlow, X. Huang, M. Notcutt, *et al.* Compact, thermal-noise-limited optical cavity for diode laser stabilization at 1e-15. *Optics Letters*, **32**(6):641, March 2007.

[131] Y. Y. Jiang, A. D. Ludlow, N. D. Lemke, *et al.* Making optical atomic clocks more stable with 10^{-16}-level laser stabilization. *Nature Photonics*, **5**(3):158–161, March 2011.

[132] Thomas Kessler, Thomas Legero, and Uwe Sterr. Thermal noise in optical cavities revisited. *Journal of the Optical Society of America B*, **29**(1):178, January 2012.

[133] Kenji Numata, Masaki Ando, Kazuhiro Yamamoto, Shigemi Otsuka, and Kimio Tsubono. Wide-Band Direct Measurement of Thermal Fluctuations in an Interferometer. *Physical Review Letters*, **91**(26):260602, December 2003.

[134] Eric D. Black, Akira Villar, Kyle Barbary, *et al.* Direct observation of broadband coating thermal noise in a suspended interferometer. *Physics Letters A*, **328**(1):1–5, July 2004.

[135] Janis Wöhler. Personal communication.

[136] Andreas Freise. Finesse: Frequency domain INterfErometer Simulation SoftwarE.

[137] W. Winkler, K. Danzmann, A. Rüdiger, and R. Schilling. Heating by optical absorption and the performance of interferometric gravitational-wave detectors. *Physical Review A*, **44**(11):7022–7036, December 1991.

[138] Detlev Ristau, editor. *Laser-Induced Damage in Optical Materials*. CRC Press, Boca Raton, 1 edition edition, December 2014.

[139] LMA via Jerome Degallaix. Personal communication.

[140] Haifeng Qi, Qingpu Wang, Xingyu Zhang, *et al.* Investigation on damage process of GaAs induced by 1064nm continuous laser. *Journal of Applied Physics*, **103**(3):033106, February 2008.

[141] Paul Linsay, Peter Saulson, Rai Weiss, and Stan Whitcomb. A study of a long baseline gravitational wave antenna system. 1983.

[142] D. Herriott, H. Kogelnik, and R. Kompfner. Off-axis paths in spherical mirror interferometers. *Applied Optics*, **3**(4):523–526, April 1964.

[143] L. G. Gouy. *Sur une propriété nouvelle des ondes lumineuses*. Gauthier-Villars, 1890.

[144] Robert W. Boyd. Intuitive explanation of the phase anomaly of focused light beams. *Journal of the Optical Society of America*, **70**(7):877, July 1980.

[145] Simin Feng and Herbert G. Winful. Physical origin of the Gouy phase shift. *Optics Letters*, **26**(8):485, April 2001.

[146] M. Fatih Erden and Haldun M. Ozaktas. Accumulated Gouy phase shift in Gaussian beam propagation through first-order optical systems. *Journal of the Optical Society of America A*, **14**(9):2190, September 1997.

[147] Eric Black. Notes on the Pound-Drever-Hall Technique, 1998. LIGO-T980045.

[148] Carlton M. Caves. Quantum-Mechanical Radiation-Pressure Fluctuations in an Interferometer. *Physical Review Letters*, **45**(2):75–79, July 1980.

[149] David Shoemaker. Advanced LIGO anticipated sensitivity curves, 2010. LIGO-T0900288-v3.

[150] Stefan Goßler. *The suspension systems of the interferometric gravitational-wave detector GEO600*. PhD thesis, University of Hannover, 2004.

[151] P. Amico, L. Bosi, L. Carbone, *et al.* Mechanical quality factor of mirror substrates for VIRGO. *Classical and Quantum Gravity*, **19**(7):1663, 2002.

[152] Tianjun Li, Felipe A. Aguilar Sandoval, Mickael Geitner, *et al.* Measurements of mechanical thermal noise and energy dissipation in optical dielectric coatings. *Physical Review D*, **89**(9):092004, May 2014.

[153] Gregory M. Harry, Matthew R. Abernathy, Andres E. Becerra-Toledo, *et al.* Titania-doped tantala/silica coatings for gravitational-wave detection. *Classical and Quantum Gravity*, **24**(2):405, 2007.

[154] V. B Braginsky and A. A Samoilenko. Measurements of the optical mirror coating properties. *Physics Letters A*, **315**(3-4):175–177, August 2003.

[155] V. B. Braginsky, M. L. Gorodetsky, and S. P. Vyatchanin. Thermo-refractive noise in gravitational wave antennae. *Physics Letters A*, **271**(5-6):303–307, July 2000.

[156] M. Cerdonio, L. Conti, A. Heidmann, and M. Pinard. Thermoelastic effects at low temperatures and quantum limits in displacement measurements. *Physical Review D*, **63**(8):082003, March 2001.

[157] Kentaro Somiya and Kazuhiro Yamamoto. Coating thermal noise of a finite-size cylindrical mirror. *Physical Review D*, **79**(10):102004, May 2009.

[158] David Wu. Internal logbook page 2233.

[159] Paul Horowitz and Winfried Hill. *The art of electronics*. Cambridge University Press, 2015.

[160] Marc Kham, Jean-Francois Semblat, Pierre-Yves Bard, and Patrick Dangla. Seismic Site-City Interaction: Main Governing Phenomena through Simplified Numerical Models. *Bulletin of the Seismological Society of America*, **96**(5):1934–1951, October 2006.

[161] G. Kalkowski, S. Risse, C. Rothhardt, M. Rohde, and R. Eberhardt. Optical contacting of low-expansion materials. *Proceedings SPIE 8126*, **8126**, 2011.

[162] R. E. Scholten. Enhanced laser shutter using a hard disk drive rotary voice-coil actuator. *Review of Scientific Instruments*, **78**(2):026101, February 2007.

[163] Michele Zaffalon. Amplitude and Frequency/Phase Modulation Explained, 2011.

[164] C. R. Hutt and A. Ringler. *A Summary of STS-2 Low Noise Installation Methods Tested at the USGS Albuquerque Seismological Laboratory.* unpublished, 2009.

[165] C. Adolphsen, R. Aiello, R. Alley, and others. *Zeroth order design report for the Next Linear Collider.* SLAC-Report, 1996.

[166] Brian Lantz. Sensor Noise Estimates for Advanced LIGO Seismic Isolation Systems, 2009. LIGO-T0900450-v3.

[167] D. R. M. Crooks, G. Cagnoli, M. M. Fejer, *et al.* Experimental measurements of mechanical dissipation associated with dielectric coatings formed using SiO_2, Ta_2O_5 and Al_2O_3. *Classical and Quantum Gravity*, **23**(15):4953, 2006.

ACKNOWLEDGMENTS

I was in the lucky situation to join the project on the exciting voyage from planning the facility to actual suspended interferometric experiments. Working for so long as a member of the 10 m Prototype crew was exiting, instructive, and furthermore great fun.

I would like to thank Karsten Danzmann for creating and leading an institute where I found ideal working conditions. Not only the friendly atmosphere but also the impressive technical support and financial reserves made the daily work very enjoyable.

Being the one who recruited me for this great project, I want to thank Stefan Goßler for his gorgeous mentoring. He always had an open ear and took the time to discuss with me every issue I had during my work.

With his unconventional way of guesstimating and improvising experiments, Harald Lück is the undisputed and unforgettable father of the prototype group.

Whenever there was any question left unanswered, I could count on Ken Strain with his admirable patience.

I'm grateful for Tobin Fricke and Bella accepting me for so long in their office. Subconsciously they taught me to redirect distractibility towards progress.

Yet, without the motivating words from Conor Mow-Lowry[1] and Daniel Eckmann I would still search for sidetracks to procrastinate writing this thesis.

The mechanical workshop is an lovely small island with extraordinary people. Hundreds if not thousands of parts were brought into being here. Especially for the urgent, most urgent and hyperextremyly urgent ones I'm much obliged.

For proofreading of parts of this manuscript I am truly grateful to David Wu, Dirk Schütte, Gerald Bergmann, Harald Lück, Patrick Oppermann, Suresh Doravari, Vaishali Adya and all coffee game participants. All remaining mistakes and typos are entirely my fault.

Almost none of my research was accomplished by me alone. From the beginning of my studies until now I worked together with countless unmentioned people. I hope they had as much fun working with me as I had with them.

I thank my parents for their endurance in supporting and encouraging me all the years. I'm proud to share this with you.

The most cordially thanks go to Hanna and Emil!

1 I wonder, how much of 'Just start writing. The first few pages won't make it into the final manuscript at all anyway...' was actually true.

CURRICULUM VITAE

Personal Data

Name:	Tobias Westphal
Address:	Stüvestraße 30173 Hannover
Nationality:	German
Date and place of birth:	21.06.1983, Hannover

Academic career

02/2009 – 09/2016	PhD Thesis at Leibniz Universität Hannover Institute for gravitational physics *A Coating Thermal Noise Interferometer for the AEI 10 m Prototype facility*
10/2003 – 02/2009	Diploma studies at Leibniz Universität Hannover Diploma thesis at Institute for Gravitational Physics AG Schnabel – Quantum Optics & Optomechanics *Optomechanische Kopplung in Michelson-Sagnac-Interferometern*

Extra curricular activities

2009	DFG Science TV *the Wavehunters*
2010	Public outreach *Christmas lecture*
11/2011	Seminar *Presentation Skills*
01/2012	Seminar *Scientific Writing*
11/2015	Seminar *Good Scientific Practice*

Collaborations

04/2008 – present	Member of *Ligo Scientific Collaboration* (LSC)
01/2011-02/2011	Research stay at IGR Glasgow *Institute for Gravitational Research*
10/2012	Research stay at TITECH *Tokyo Institute for Technology*
03/2013 – present	Modern control of a triple suspension *Control theory and control applications group*

Education

06/1994 – 06/2002	Gymnasium Burgdorf, Abitur
06/1993 – 06/1994	Orientierungsstufe Burgdorf
06/1989 – 06/1994	Grundschule Burgdorf

PUBLICATION LIST

[1] F. Kawazoe, ..., **T. Westphal**, ..., and K. Danzmann. Designs of the frequency reference cavity for the AEI 10 m Prototype interferometer. *Journal of Physics: Conference Series*, **228**:012028, 2010.

[2] K. Dahl, ..., **T. Westphal**, ..., and K. Danzmann. Towards a Suspension Platform Interferometer for the AEI 10 m Prototype Interferometer. *Journal of Physics: Conference Series*, **228**(1):012027, 2010.

[3] K. Yamamoto, ..., **T. Westphal**, ..., and R. Schnabel. Quantum noise of a Michelson-Sagnac interferometer with a translucent mechanical oscillator. *Physical Review A*, **81**(3):033849, March 2010.

[4] S. Goßler, ..., **T. Westphal**, ..., and K. Danzmann. The AEI 10 m prototype interferometer. *Classical and quantum gravity*, **27**(8):084023, April 2010.

[5] D. Friedrich, ..., **T. Westphal**, ..., and R. Schnabel. Laser interferometry with translucent and absorbing mechanical oscillators. *New Journal of Physics*, **13**(9):093017, September 2011.

[6] F. Kawazoe, ..., **T. Westphal**, ..., and K. Danzmann. The AEI 10 m Prototype Interferometer frequency control using the reference cavity and its angular control. *Journal of Physics: Conference Series*, **363**(1):012012, 2012.

[7] **T. Westphal**, *et al.* Design of the 10 m AEI prototype facility for interferometry studies. *Applied Physics B*, **106**(3):551-557, March 2012.

[8] K. Dahl, ..., **T. Westphal**, ..., and K. Danzmann. Status of the AEI 10 m prototype. *Classical and Quantum Gravity*, **29**(14):145005, June 2012.

[9] **T. Westphal**, *et al.* Interferometer readout noise below the standard quantum limit of a membrane. *Physical Review A*, **85**:063806, June 2012.

[10] H. Kaufer, ..., **T. Westphal**, ..., and R. Schnabel. Tomographic readout of an opto- mechanical interferometer. *New Journal of Physics*, **14**(9):095018, September 2012.

[11] J. Bauchrowitz, **T. Westphal**, and R. Schnabel. A graphical description of optical parametric generation of squeezed states of light. *American Journal of Physics*, **81**(10):767, October 2013.

COLLABORATION PUBLICATIONS

[1] J. Abadie, ..., **T. Westphal**, ..., and J. Zweizig. Calibration of the LIGO gravitational wave detectors in the fifth science run. *Nuclear Instruments and Methods in Physics Research Section A*, **624**(1):223–240, December 2010.

[2] J. Abadie, ..., **T. Westphal**, ..., and S. Buchner. Search for gravitational waves associated with the August 2006 timing glitch of the Vela pulsar. *Physical Review D*, **83**(4):042001, February 2011.

[3] J. Abadie, ..., **T. Westphal**, ..., and J. Zweizig. Search for gravitational waves from compact binary coalescence in LIGO and Virgo data from S5 and VSR1. *Physical Review D*, **82**(10):102001, November 2010.

[4] J. Abadie, ..., **T. Westphal**, ..., and K. Yamaoka. Search for Gravitational Wave Bursts from Six Magnetars. *The Astrophysical Journal Letters*, **734**(2):L35, 2011.

[5] J. Abadie, ..., **T. Westphal**, ..., and J. Zweizig. Search for gravitational waves from binary black hole inspiral, merger, and ringdown. *Physical Review D*, **83**(12):122005, June 2011.

[6] J. Abadie, ..., **T. Westphal**, ..., and W. Zheng. Implementation and testing of the first prompt search for gravitational wave transients with electromagnetic counterparts. *Astronomy & Astrophysics*, **539**:A124, March 2012.

[7] J. Abadie, ..., **T. Westphal**, ..., and J. Zweizig. Search for gravitational waves from low mass compact binary coalescence in LIGO's sixth science run and Virgo's science runs 2 and 3. *Physical Review D*, **85**(8):082002, April 2012.

[8] J. Abadie, ..., **T. Westphal**, ..., and J. Zweizig. Upper limits on a stochastic gravitational-wave background using LIGO and Virgo interferometers at 600–1000 Hz. *Physical Review D*, **85**(12):122001, June 2012.

[9] J. Abadie, ..., **T. Westphal**, ..., and M. Was. Implications for the Origin of GRB 051103 from LIGO Observations. *The Astrophysical Journal*, **755**(1):2, 2012.

[10] J. Abadie, ..., **T. Westphal**, ..., and J. Zweizig. Search for gravitational waves from intermediate mass binary black holes. *Physical Review D*, **85**(10):102004, May 2012.

[11] P. A. Evans, ..., **T. Westphal**, ..., and J. Zweizig. Swift Follow-up Observations of Candidate Gravitational-wave Transient Events. *The Astrophysical Journal Supplement Series*, **203**(2):28, 2012.

[12] J. Aasi, ..., **T. Westphal**, ..., and J. Zweizig. Search for gravitational waves from binary black hole inspiral, merger, and ringdown in LIGO-Virgo data from 2009–2010. *Physical Review D*, **87**(2):022002, January 2013.

[13] B. P. Abbott, ..., **T. Westphal**, ..., and Zweizig. Prospects for Observing and Localizing Gravitational-Wave Transients with Advanced LIGO and Advanced Virgo. *Living Reviews in Relativity*, **19**, 2016.

[14] J. Aasi, ..., **T. Westphal**, ..., and J. Zweizig. Parameter estimation for compact binary coalescence signals with the first generation gravitational-wave detector network. *Physical Review D*, **88**(6):062001, September 2013.

[15] J. Aasi, ..., **T. Westphal**, ..., and J. Zweizig. Directed search for continuous gravitational waves from the Galactic center. *Physical Review D*, **88**(10):102002, November 2013.

[16] J. Aasi, ..., **T. Westphal**, ..., and J. Zweizig. Search for long-lived gravitational-wave transients coincident with long gamma-ray bursts. *Physical Review D*, **88**(12):122004, December 2013.

[17] J. Aasi, ..., **T. Westphal**, ..., and J. Zweizig. Search for gravitational wave ringdowns from perturbed intermediate mass black holes in LIGO-Virgo data from 2005–2010. *Physical Review D*, **89**(10):102006, May 2014.

[18] J. Aasi, ..., **T. Westphal**, ..., and A. von Kienlin. Search for Gravitational Waves Associated with γ-ray Bursts Detected by the Interplanetary Network. *Physical Review Letters*, **113**(1):011102, June 2014.

[19] J. Aasi, ..., **T. Westphal**, ..., and J. Zweizig. Search for gravitational radiation from intermediate mass black hole binaries in data from the second LIGO-Virgo joint science run. *Physical Review D*, **89**(12):122003, June 2014.

[20] J. Aasi, ..., **T. Westphal**, ..., and J. Zweizig. Methods and results of a search for gravitational waves associated with gamma-ray bursts using the GEO 600, LIGO, and Virgo detectors. *Physical Review D*, **89**(12):122004, June 2014.

[21] J. Aasi, ..., **T. Westphal**, ..., and J. Zweizig. Improved Upper Limits on the Stochastic Gravitational-Wave Background

from 2009–2010 LIGO and Virgo Data. *Physical Review Letters*, **113**(23):231101, December 2014.

[22] M. G. Aartsen, ..., **T. Westphal**, ..., and J. Zweizig. Multimessenger search for sources of gravitational waves and high-energy neutrinos: Initial results for LIGO-Virgo and IceCube. *Physical Review D*, **90**(10):102002, November 2014.

[23] J. Aasi, ..., **T. Westphal**, ..., and Y. Zlochower. The NINJA-2 project: detecting and characterizing gravitational waveforms modelled using numerical binary black hole simulations. *Classical and Quantum Gravity*, **31**(11):115004, 2014.

[24] J. Aasi, ..., **T. Westphal**, ..., and J. Zweizig. Characterization of the LIGO detectors during their sixth science run. *Classical and Quantum Gravity*, **32**(11):115012, 2015.

[25] J. Aasi, ..., **T. Westphal**, ..., and J. Zweizig. Narrow-band search of continuous gravitational-wave signals from Crab and Vela pulsars in Virgo VSR4 data. *Physical Review D*, **91**(2):022004, January 2015.

[26] J. Aasi, ..., **T. Westphal**, ..., and J. Zweizig. Implementation of an $\mathcal{F}$ -statistic all-sky search for continuous gravitational waves in Virgo VSR1 data. *Classical and Quantum Gravity*, **31**(16):165014, 2014.

[27] J. Aasi, ..., **T. Westphal**, ..., and J. Zweizig. Advanced LIGO. *Classical and Quantum Gravity*, **32**(7):074001, 2015.

[28] J. Aasi, ..., **T. Westphal**, ..., and J. Zweizig. Searches for Continuous Gravitational Waves from Nine Young Supernova Remnants. *The Astrophysical Journal*, **813**(1):39, 2015.

[29] J. Aasi, ..., **T. Westphal**, ..., and J. Zweizig. Search of the Orion spur for continuous gravitational waves using a loosely coherent algorithm on data from LIGO interferometers. *Physical Review D*, **93**(4):042006, February 2016.

[30] B. P. Abbott, ..., **T. Westphal**, ..., and J. Zweizig. Observation of Gravitational Waves from a Binary Black Hole Merger. *Physical Review Letters*, **116**(6):061102, February 2016.

[31] B. P. Abbott, ..., **T. Westphal**, ..., and J. Zweizig. GW150914: The Advanced LIGO Detectors in the Era of First Discoveries. *Physical Review Letters*, **116**(13):131103, March 2016.

[32] B. P. Abbott, ..., **T. Westphal**, ..., and J. Zweizig. The Rate of Binary Black Hole Mergers Inferred from Advanced LIGO Observations Surrounding GW150914. *arXiv:1602.03842*, February 2016.

[33] B. P. Abbott, ..., **T. Westphal**, ..., and J. Zweizig. Observing gravitational-wave transient GW150914 with minimal assumptions. *Physical Review D*, **93**(12):122004, June 2016.

[34] S. Adrián-Martínez, ..., **T. Westphal**, ..., and J. Zweizig. High-energy neutrino follow-up search of gravitational wave event GW150914 with ANTARES and IceCube. *Physical Review D*, **93**(12):122010, June 2016.

[35] B. P. Abbott, ..., **T. Westphal**, ..., and S. Rosswog. Localization and broadband follow-up of the gravitational-wave transient GW150914. *arXiv:1602.08492*, February 2016.

[36] B. P. Abbott, ..., **T. Westphal**, ..., and B. L. Wells. Search for transient gravitational waves in coincidence with short-duration radio transients during 2007–2013. *Physical Review D*, **93**(12):122008, June 2016.

[37] B. P. Abbott, ..., **T. Westphal**, ..., and S. Teukolsky. GW151226: Observation of Gravitational Waves from a 22-Solar-Mass Binary Black Hole Coalescence. *Physical Review Letters*, **116**(24):241103, June 2016.

[38] B. P. Abbott, ..., **T. Westphal**, ..., and J. Zweizig. Binary Black Hole Mergers in the first Advanced LIGO Observing Run. *arXiv:1606.04856*, June 2016.

[39] J. Abadie, ..., **T. Westphal**, ..., and J. Zweizig. Search for Gravitational-wave Inspiral Signals Associated with Short Gamma-ray Bursts During LIGO's Fifth and Virgo's First Science Run. *The Astrophysical Journal*, **715**(2):1453, 2010.

[40] J. Abadie, ..., **T. Westphal**, ..., and J. Zweizig. All-sky search for gravitational-wave bursts in the first joint LIGO-GEO-Virgo run. *Physical Review D*, **81**(10):102001, May 2010.

[41] J. Abadie, ..., **T. Westphal**, ..., and K Belczynski. Predictions for the rates of compact binary coalescences observable by ground-based gravitational-wave detectors. *Classical and Quantum Gravity*, **27**(17):173001, 2010.

[42] J. Abadie, ..., **T. Westphal**, ..., and J. Zweizig. Directional Limits on Persistent Gravitational Waves Using LIGO S5 Science Data. *Physical Review Letters*, **107**(27):271102, December 2011.

[43] J. Abadie, ..., **T. Westphal**, ..., and J. Zweizig. All-sky search for periodic gravitational waves in the full S5 LIGO data. *Physical Review D*, **85**(2):022001, January 2012.

[44] J. Abadie, ..., **T. Westphal**, ..., and J. Zweizig. First low-latency LIGO+Virgo search for binary inspirals and their electromagnetic counterparts. *Astronomy & Astrophysics*, **541**:A155, May 2012.

[45] J. Abadie, ..., **T. Westphal**, ..., and J. Palfreyman. Beating the Spin-down Limit on Gravitational Wave Emission from the Vela Pulsar. *The Astrophysical Journal*, **737**(2):93, 2011.

[46] J. Abadie, ..., **T. Westphal**, ..., and J. Zweizig . A gravitational wave observatory operating beyond the quantum shot-noise limit. *Nature Physics*, **7**(12):962–965, December 2011.

[47] J. Abadie, ..., **T. Westphal**, ..., and J. Zweizig. All-sky search for gravitational-wave bursts in the second joint LIGO-Virgo run. *Physical Review D*, **85**(12):122007, June 2012.

[48] J. Aasi, ..., **T. Westphal**, ..., and J. Zweizig. The characterization of Virgo data and its impact on gravitational-wave searches. *Classical and Quantum Gravity*, **29**(15):155002, 2012.

[49] J. Abadie, ..., **T. Westphal**, ..., and J. Zweizig. First Search for Gravitational Waves from the Youngest Known Neutron Star. *The Astrophysical Journal*, **722**(2):1504, 2010.

[50] J. Abadie, ..., **T. Westphal**, ..., and X.-L. Zhang. Search for Gravitational Waves Associated with Gamma-Ray Bursts during LIGO Science Run 6 and Virgo Science Runs 2 and 3. *The Astrophysical Journal*, **760**(1):12, 2012.

[51] S. Adrián-Martínez, ..., **T. Westphal**, ..., and J. Zweizig. A first search for coincident gravitational waves and high energy neutrinos using LIGO, Virgo and ANTARES data from 2007. *Journal of Cosmology and Astroparticle Physics*, **2013**(06):008, 2013.

[52] J. Aasi, ..., **T. Westphal**, ..., and D. P. Anderson. Einstein@Home all-sky search for periodic gravitational waves in LIGO S5 data. *Physical Review D*, **87**(4):042001, February 2013.

[53] J. Aasi, ..., **T. Westphal**, ..., and J. Zweizig. Enhanced sensitivity of the LIGO gravitational wave detector by using squeezed states of light. *Nature Photonics*, **7**(8):613–619, August 2013.

[54] J. Aasi, ..., **T. Westphal**, ..., and B. W. Stappers. Gravitational Waves from Known Pulsars: Results from the Initial Detector Era. *The Astrophysical Journal*, **785**(2):119, 2014.

[55] J. Aasi, ..., **T. Westphal**, ..., and W. Zheng. First Searches for Optical Counterparts to Gravitational-wave Candidate Events. *The Astrophysical Journal Supplement Series*, **211**(1):7, 2014.

[56] J. Aasi, ..., **T. Westphal**, ..., and J. Zweizig. Constraints on Cosmic Strings from the LIGO-Virgo Gravitational-Wave Detectors. *Physical Review Letters*, **112**(13):131101, April 2014.

[57] J. Aasi, ..., **T. Westphal**, ..., and J. Zweizig. Application of a Hough search for continuous gravitational waves on data from the fifth LIGO science run. *Classical and Quantum Gravity*, **31**(8):085014, 2014.

[58] J. Aasi, ..., **T. Westphal**, ..., and J. Zweizig. First all-sky search for continuous gravitational waves from unknown sources in binary systems. *Physical Review D*, **90**(6):062010, September 2014.

[59] J. Aasi, ..., **T. Westphal**, ..., and J. Zweizig. Searching for stochastic gravitational waves using data from the two colocated LIGO Hanford detectors. *Physical Review D*, **91**(2):022003, January 2015.

[60] J. Aasi, ..., **T. Westphal**, ..., and J. Zweizig. Directed search for gravitational waves from Scorpius X-1 with initial LIGO data. *Physical Review D*, **91**(6):062008, March 2015.

[61] J. Aasi, ..., **T. Westphal**, ..., and J. Zweizig. First low frequency all-sky search for continuous gravitational wave signals. *Physical Review D*, **93**(4):042007, February 2016.

[62] B. P. Abbott, ..., **T. Westphal**, ..., and J. Zweizig. All-sky search for long-duration gravitational wave transients with initial LIGO. *Physical Review D*, **93**(4):042005, February 2016.

[63] B. P. Abbott, ..., **T. Westphal**, ..., and J. Zweizig. GW150914: First results from the search for binary black hole coalescence with Advanced LIGO. *Physical Review D*, **93**(12):122003, June 2016.

[64] B. P. Abbott, ..., **T. Westphal**, ..., and Y. Zlochower. Properties of the Binary Black Hole Merger GW150914. *Physical Review Letters*, **116**(24):241102, June 2016.

[65] B. P. Abbott, ..., **T. Westphal**, ..., and Y. Zlochower. Tests of General Relativity with GW150914. *Physical Review Letters*, **116**(22):221101, May 2016.

[66] B. P. Abbott, ..., **T. Westphal**, ..., and J. Zweizig. Characterization of transient noise in Advanced LIGO relevant to gravitational wave signal GW150914. *Classical and Quantum Gravity*, **33**(13):134001, 2016.

[67] B. P. Abbott, ..., **T. Westphal**, ..., and J. Zweizig. Astrophysical Implications of the Binary Black-hole Merger GW150914. *The Astrophysical Journal Letters*, **818**(2):L22, 2016.

[68] B. P. Abbott, ..., **T. Westphal**, ..., and J. Zweizig. GW150914: Implications for the Stochastic Gravitational-Wave Background from Binary Black Holes. *Physical Review Letters*, **116**(13):131102, March 2016.

[69] B. P. Abbott, ..., **T. Westphal**, ..., and Y. Zlochower. Directly comparing GW150914 with numerical solutions of Einstein's equations for binary black hole coalescence. *arXiv:1606.01262*, June 2016.

[70] B. P. Abbott, ..., **T. Westphal**, ..., and J. Zweizig. A First Targeted Search for Gravitational-Wave Bursts from Core-Collapse Supernovae in Data of First-Generation Laser Interferometer Detectors. *arXiv:1605.01785*, May 2016.

[71] B. P. Abbott, ..., **T. Westphal**, ..., and J. Zweizig. Comprehensive All-sky Search for Periodic Gravitational Waves in the Sixth Science Run LIGO Data. *arXiv:1605.03233*, May 2016.

[72] The LIGO Scientific Collaboration. Calibration of the Advanced LIGO detectors for the discovery of the binary black-hole merger GW150914. *arXiv:1602.03845*, February 2016.

[73] B. P. Abbott, ..., **T. Westphal**, ..., and J. Zweizig. An improved analysis of GW150914 using a fully spin-precessing waveform model. *arXiv:1606.01210*, June 2016.